

**Robust computational procedures
for the nonlinear dynamic analysis of
beam and shell structures**

**Robuste Berechnungsverfahren
zur nichtlinearen dynamischen Analyse von
Balken- und Schalenstrukturen**

Von der Fakultät für Bauingenieurwesen und Geodäsie
der Gottfried Wilhelm Leibniz Universität Hannover
zur Verleihung der Lehrbefugnis für das Fachgebiet

Statik und Dynamik

genehmigte Habilitationsschrift

von

Dr.-Ing. Cristian Guillermo Gebhardt

aus Córdoba, Argentinien

Referenten: Prof. Dr.-Ing. habil. Raimund Rolfes,
Gottfried Wilhelm Leibniz Universität Hannover

Prof. Ignacio Romero Olleros, PhD,
Universidad Politécnica de Madrid

Prof. Dr.-Ing. habil. Jörg Wallaschek,
Gottfried Wilhelm Leibniz Universität Hannover

Tag der Einreichung: 24. Juni 2019

Tag der Habilitation: 5. Februar 2020

Abstract

Existing and new slender structures made of hyperelastic multilayer composite materials subject to highly dynamic loads, *e.g.*, wind turbines, helicopters, cars, speedboats or submarines *inter alia*, are very complex. Their dynamic analysis requires fully nonlinear formulations, at least from the kinematic and geometric point of view, and also to some extent from the material point of view. Thus, simulations in time-domain involving large displacements, rotations and strains could be necessary to predict their mechanical behavior accurately. Numerical procedures to carry out such simulations rely firstly on the partial discretization in space of the governing equations, for instance with finite elements. These semi discrete equations are further discretized in time with an integration scheme. The resulting discrete equations are in fact very stiff and therefore, the computation of the long-term behavior could be problematic. In many applications, the introduction of constraints is also necessary for rendering more complex structures. Besides introducing a new level of complexity, this can sharpen conditioning problems already present in the fully discrete problem. Additionally, we also require procedures able to annihilate the unwanted unresolved high-frequency content without upsetting of the underlying physics. However, the simultaneous satisfaction of all these requirements is a very challenging task.

The main objective of this work is to provide means intended for helping to understand further the nonlinear dynamics of beam and shell structures made of hyperelastic multilayer composite materials subject to highly dynamic loads. To accomplish this main goal, we propose a unifying computational approach that relies on: *i*) a director-based finite-element formulation for geometrically exact beams with general cross-section properties; *ii*) a director-based finite-element formulation for solid-degenerate shells made of hyperelastic multilayer composite materials; *iii*) a unifying description of rigid bodies, geometrically exact beams and solid-degenerate shells and their combination with kinematic pairs, which avoids inherently the necessity of rotational degrees of freedom; and, *iv*) a robust integration scheme based on the *average vector field*. Additionally, we propose: *v*) the particularization of the *principal geodesic analysis* to identify motion patterns exhibited by beam structures in a purely nonlinear setting; and, *vi*) a new conservative/dissipative integration method for general nonlinear mechanical systems, which relies on high-order correction terms that optimally modify the midpoint rule. Moreover, the excellent numerical performance of the proposed unifying framework and procedures is illustrated by means of a good number of examples with different difficulty levels.

Kurzfassung

Gegenwärtige und zukünftige dynamisch beanspruchte, schlanke Strukturen aus mehrschichtig verbundenen, hyperelastischen Werkstoffen, z. B. Windenergieanlagen und Hubschrauber usw., sind sehr komplex. Eine genaue Untersuchung im Zeitbereich erfordert den Einsatz von Methoden, die kinematische, geometrische sowie, bis zu einem gewissen Grad, materielle Nichtlinearitäten berücksichtigen sollten. Daher könnten Simulationen mit Beachtung von großen Verschiebungen, Drehungen und Verzerrungen nötig sein, um das mechanische Verhalten akkurat zu vorhersagen zu vermögen. Zunächst werden die Bewegungsgleichungen räumlich diskretisiert. Dann werden die zum Teil diskretisierten Gleichungen mittels eines Integrationsverfahrens zeitlich diskretisiert. Solche diskreten Gleichungen sind sehr steif, sodass sich die Berechnung der langzeitigen Lösung erschwert. Darüber hinaus ist die Einführung von Nebenbedingungen oft nötig, um komplexere Strukturen aufstellen zu können, wodurch sich die Komplexität erhöht wird und unerwünschte Eigenschaften noch verschärft werden. Um Robustheit zu gewinnen, sollen Berechnungsverfahren hergeleitet werden, die die zugrunde legende Physik in gewissem Maße erhalten können und gleichzeitig den hochfrequenten Anteil der Lösung unterdrücken können. Die Erfüllung dieser Anforderungen stellt sich als sehr herausfordernd dar.

Das Hauptziel dieser Arbeit liegt an der Entwicklung von Berechnungsverfahren zur Vertiefung des Verständnisses des dynamischen Verhaltens von Balken- und Schalenstrukturen. Um dieses Ziel zu erreichen, wird ein umfassender Ansatz vorgeschlagen. Dieser besteht aus: *i*) einer auf Direktoren basierenden, Finite-Elemente-Formulierung für den geometrisch exakten Balken mit allgemeinen Querschnittseigenschaften; *ii*) einer auf Direktoren basierenden, Finite-Elemente-Formulierung für die Kontinuumsmechanik-basierte Schale aus mehrschichtig verbundenen, hyperelastischen Werkstoffen; *iii*) einer vereinheitlichten Beschreibung von Starrkörpern, Balken und Schalen und deren Kopplung mittels kinematischer Nebenbedingungen; und, *iv*) einem robusten Integrationsverfahren basierend auf dem *gemittelten Vektorfeld*. Des Weiteren wird Folgendes ebenfalls vorgeschlagen: *v*) Die Partikularisierung der *Hauptgeodätenanalyse* zur nichtlinearen Identifikation von Bewegungsmoden an Balkenstrukturen; und, *vi*) ein neues konservatives/dissipatives Integrationsverfahren für allgemeine nichtlineare mechanische Systeme basierend auf optimierten Modifizierungen höherer Ordnung, die die Defizite der Mittelpunktsregel beheben. Die sehr gute Leistung des vorgeschlagenen Ansatzes wird durch mehrere Beispiele unterschiedlicher Komplexität nachgewiesen.

Contents

List of Figures	III
List of Articles	V
1 Introduction	1
1.1 Motivation	1
1.2 Literature review	3
1.2.1 Geometrically exact beams	3
1.2.2 Solid-degenerate shells	6
1.2.3 Conservative/dissipative time integration	9
1.3 Main research gaps	11
1.4 Theoretical framework	12
1.4.1 Equilibrium statement	13
1.4.2 Symmetries, momenta and energy	14
1.4.3 Specialization to <i>canonical models</i>	16
1.4.4 Further technical aspects	21
1.5 General objectives	22
1.6 Original contributions	22
1.7 Organization of this work	23
2 Article A	25
3 Article B	43
4 Article C	79
5 Article D	97
6 Closure	121
6.1 Conclusions	121
6.2 Future work	122
A Articles between July 2015 and June 2019	123
Bibliography	125

List of Figures

1-1	Military helicopter during a flight maneuver.	2
1-2	Wind turbine subject to seemly large blade deflections.	2
1-3	The continuum body model.	14
1-4	The rigid body model.	18
1-5	The geometrically exact beam model	20
1-6	The solid-degenerate shell model	21

List of Articles

A	GEBHARDT, C. G., AND ROLFES, R. On the nonlinear dynamics of shell structures: combining a mixed finite element formulation and a robust integration scheme. <i>Thin-Walled Structures</i> 118 (2017), 56–72.	26
B	GEBHARDT, C. G., HOFMEISTER, B., HENTE, C. AND ROLFES, R. Non-linear dynamics of slender structures: a new object-oriented framework. <i>Computational Mechanics</i> 63 (2019), 219–252.	44
C	GEBHARDT, C. G., STEINBACH, M. C., AND ROLFES, R. Understanding the nonlinear dynamics of beam structures: a principal geometric analysis approach. <i>Thin-Walled Structures</i> 140 (2019), 357–372.	80
D	GEBHARDT, C. G., ROMERO, I., AND ROLFES, R. A new conservative/dissipative time integration scheme for nonlinear mechanical systems. <i>Computational Mechanics</i> 65 (2020), 405–427.	98

1. Introduction

1.1. Motivation

Existing and new slender structures made of hyperelastic multilayer composite materials subject to highly dynamic loads, *e.g.*, wind turbines, helicopters, cars, speedboats or submarines, are very complex mainly due to their shape that can be sophisticated, the materials employed for their fabrication, the way in which they carry the loads, *etc.*, see Fig. 1-1¹. The corresponding transient analysis requires the development and application of fully nonlinear formulations (at least from the kinematic point of view, see Fig. 1-2², and also to some extent from the material point of view). One important aspect is that the load-carrying capacity of these structures is given by their geometric shape. Therefore, the correct description of the kinematic and mechanical behavior is of major relevance, specially in the context of their integrated design process supported by transient simulations. Moreover, such simulations are required to be accordingly accompanied by validation tests that usually show large scatter due to a high sensitivity to geometric and material imperfections, the difficulty to set properly boundary conditions and applied loads, and therefore, these are very complicated to prepare and certainly very expensive.

Numerical procedures to carry out transient simulations rely firstly on the discretization in space of the continuous governing equations, for instance with finite elements. Then, the semi discrete equations are further discretized in time with an integration scheme. The resulting fully discrete equations for this kind of structures are very stiff, a feature that is made evident by the large eigenvalue spectrum of the system matrices, *i.e.*, mass and stiffness matrices tend to be not well-conditioned. The computation of long-term convergent responses could be problematic, even using well-established procedures and commercial codes. Many applications require constraints (*e.g.*, supports, joints and junctions) to render more complex structures, introducing a new level of complexity and sharpening the conditioning problems present at the system matrices. Certainly, making the work of the iterative solver even more difficult. Additionally, any acceptable procedure must be able to annihilate the unresolved high-frequency content, while simultaneously avoiding the upsetting of conservation laws, *e.g.*, linear and angular momenta, energy, *etc.* However, dealing with all these aspects at once is rather a very challenging task.

¹Picture made available by Pixabay under Pixabay *Lizenz*.

²Picture by George Becker, made available by Pexels under Pexels License.



Figure 1-1.: Military helicopter during a flight maneuver.



Figure 1-2.: Wind turbine subject to seemingly large blade deflections.

1.2. Literature review

Mostly slender structures can be modeled by means of two specialized structural elements, namely beams and shells. Meanwhile, beams are one-dimensional structural models, *i.e.*, prismatic elements, in which one dimension is much more larger than the two remaining ones. Shells are two-dimensional structural models, *i.e.*, elements described by a mean surface that in general is non flat and whose thickness is relatively very small. Simplifying this idealization further, we can obtain structural elements for plates and membranes as special cases. Even provided that the descriptions of beams and shells strongly differ, they share as a characteristic that their load-carrying capacity is not only given by the material properties, but also by their geometric shape. Moreover, their dynamic behavior is typically described by a set of nonlinear partial differential equations in time and space, a set of initial conditions and a set of boundary conditions. This description can be also complemented by algebraic equations that are necessary to set additional kinematic constraints. As these governing equations are analytically non solvable, we are required to look a solution through the numerical way. For this reason, this work is devoted to develop robust computational procedures to investigate the nonlinear dynamics of beam and shell structures, which will rely on three basic ingredients, *i.e.*, a finite element formulation for geometrically exact beams, a finite element formulation for solid-degenerate shells, and conservative/dissipative time integration methods. On this basis, the remaining of this subsection provides a brief on these three main ingredients, highlighting some critical aspects and the role that they play toward a robust and fully consistent treatment of such kind of structural idealizations.

1.2.1. Geometrically exact beams

Beam-like structural elements can be classified into two main families according to their deformation response. The first one groups non-shearable beams, whose planar cross section remains always flat and perpendicular to the tangent vector associated with the curve that describes the beam axis. In the linear context, we have the Euler-Bernoulli model, and the Rayleigh model. The last one does consider the inertial contribution due to the rotation of the cross section and can be understood as a marginal improvement of the Euler-Bernoulli model. In a nonlinear context, we have the generalization of the Rayleigh beam, the so-called Kirchhoff model. The second one groups shearable beams, whose planar cross section remains always flat as well, but not longer perpendicular to the tangent vector associated with the curve that describes the beam axis. In a linear setting, we have the shear beam model, and the Timoshenko model. The last one does consider the inertial contribution due to the rotation of the cross section. In a nonlinear setting, we have the generalization of the Timoshenko beam, the so-called geometrically exact beam or the Reissner-Simó model. The configuration space related to the geometrically exact beam model, *i.e.*, all admissible positions of the beam axis (three possibilities of

motion) and all admissible orientations of the cross sections (another three possibilities of motion), is very rich, but also very complex mathematically speaking. This is due to the presence of finite rotations that describe the orientation of the cross sections. Since we want to develop methods able to handle the nonlinear dynamics of structures like wind turbine blades or aircraft wings, which in general exhibit arbitrary cross section properties and are prone to undergo shear deformation and shear forces, the most adequate beam model for our purpose is provided by the geometrically exact beam theory. Therefore, this model is one of the main ingredients of this work. Next, we summarize some of the most notable contributions done during the last decades.

REISSNER [74] formulated a one-dimensional large-strain beam theory for the plane case. Such a work can be considered as the first seminal contribution toward the generalization of the Timoshenko beam model. Following a continuum mechanics approach, BATHE AND BOLORUCHI [9] discussed fundamental aspects regarding the formulation of three-dimensional geometrically nonlinear beam elements. SIMÓ [89] extended the concepts considered by REISSNER in [74] to the three-dimensional case, from which resulted the so-called geometrically exact beam theory. CARDONA AND GÉRADIN [25] developed perhaps the first fully objective finite element based on the geometrically exact beam theory and a material description of the rotation group. The concept of *objectivity*, *i.e.*, the invariance of the strain measures under rigid body motions, plays a very critical role. Even, provided that the strain measures in their continuous setting are objective, an inadequate finite-element approximation can easily destroy this crucial property. For instance, the first finite-element approximation proposed by SIMÓ and collaborators was not objective. HODGES [48] proposed a mixed variational formulation for beams that is based on exact intrinsic equations. GRUTTMANN ET AL. [44] developed a three-dimensional beam finite element based on a Timoshenko beam kinematic, where the strain measures are derived from the Green-Lagrange strain tensor as usual in the mechanics of solids. The authors showed also the connection between the proposed strain measures and the standard ones.

ROMERO AND ARMERO [81] derived an objective finite element formulation for geometrically exact beams. Such approach relies on the straightforward interpolation of the *directors* (three orthonormal vectors that describe univocally the orientation of the cross section). BETSCH AND STEINMANN [15] presented a brief overview of the constrained dynamics of nonlinear beams. The authors considered the interpolation of the *directors*, where the mutual orthonormality at the nodes is achieved by imposing holonomic constraints. ZUPAN AND SAJE [106] derived an objective finite element formulation for geometrically exact beams, in which the strain vectors are unknown functions. Motivated by the critical role that rotations play in the context of geometrically exact beams, ROMERO [76] presented an exhaustive review and classification in regard to the parameterization and interpolation of rotations and provided hints regarding their performance

and convergence properties. BOYER AND PRIMAULT [19] proposed a theory specialized for very slender beams. That work can be considered as one of the first attempts toward the formulation of a geometrically exact beam theory for Kirchhoff rods. YU ET AL. [105] considered beams with initially large twisting and large curvature in the context of thin-walled structures. The proposed approximated theory is asymptotically correct and is able to handle material anisotropy. MÄKINEN [61] derived an improved version of the formulation proposed by CARDONA AND GÉRADIN in [25], which, beyond being objective like in its original version, is also path independent. The *path-independence* property, *i.e.*, for conservative loading the work produced through any arbitrary closed path is identically zero, is also a fundamental property of a finite element approximation and can be seriously compromised when updated-Lagrangian formulations are chosen.

AURICCHIO ET AL. [8] emphasized some intrinsic features of the three-dimensional beam model proposed by SIMÓ in [89]. The formulation was also re-derived in a consistent and compact form. PIMENTA ET AL. [71] developed a model for geometrically nonlinear rods equipped with nonlinear material laws, with which the authors achieved the *objectivity* at the discrete level. ROMERO [77] compared the absolute nodal coordinate and geometrically exact formulations. The author covered a wide range of aspects, including implementation effort, performance, robustness, interfacing with material models and other structural members, and accuracy. As a final conclusion, it was not possible to claim the superiority of one approach over the other one. MATA ET AL. [63] generalized the geometrically exact beam theory to take in account material nonlinearities in a dynamic context. GHOSH AND ROY [39] developed an objective scheme using the rotation vector parameterization following an Eulerian formulation approach, which is unusual in the beam context. PAI [69] considered linear and nonlinear shear-deformable beam theories, including Timoshenko's theory and geometrically exact beam theory. Special attention is paid to the order deficiency, shear correction factors, shear locking and nonlinearities. As a follow-up of the previous work, PAI [70] considered an advanced total-Lagrangian displacement-based geometrically exact beam theory without singularities by using a non-conventional description of rotations.

SONNEVILLE ET AL. [96] formulated a geometrically exact beam model on the three-dimensional special Euclidean group. Taking a look on that formulation, one can realize that the equations derived by these authors are equivalent to the equations proposed by HODGES in [48]. EUGSTER ET AL. [34] developed a new three-director-based finite element formulation for geometrically exact beams that considers an adjustment of the variational formulation for dealing with specific features of the director interpolation. Following an alternative path, GENOVESE [38] proposed a two-director-based geometrically exact beam model. However, the mathematical treatment of this approach is tedious in comparison to the three-director approach, since the third director is obtained as

the cross product of other two directors and not as an additional primal director field. YOON AND LEE [104] investigated the performance of a continuum element equipped with a beam kinematics under large twisting. DE MIRANDA ET AL. [30] discussed briefly the constitutive assumptions normally done for linear elastic isotropic and orthotropic materials in the framework of thin-walled beams. ORTIGOSA ET AL. [68] embedded the geometrically exact beam theory in the polyconvex framework. The formulation proposed by PIMENTA ET AL. [71] was enhanced by GAY NETO [36] in the context of mechanisms. And recently, SONNEVILLE ET AL. [95] considered the interpolation of the kinematic fields describing the configuration of geometrically exact beams. Two kinematic representations were investigated: the classical approach that treats the displacement and rotation fields separately and the motion approach that treats those two fields as a unit.

1.2.2. Solid-degenerate shells

Shell-like structural elements can be classified into two main types according to their modeling approach. The first one groups all approaches that are directly derived from a shell theory that is presented in a resultant form, *i.e.*, force and moment resultants that are obtained by analytical integration of stresses across the thickness direction. Moreover, they rely on special strain measures and constitutive laws. In a nonlinear context, the Kirchhoff-Love model, which does not admit transverse shear deformation, and the Reissner-Mindlin, which does consider transverse shear deformations, are the main exponents of this type. The second one groups all approaches that are derived from the continuum mechanics theory after degenerating the solid with allowance of small changes of the thickness. These shell models are also well-known as solid-degenerate shells. They rely on standard strain measures and constitutive laws and therefore, the finite strain setting is straightforward and the knowledge made in the field of material modeling can be spilled on them without any kind of specialization. This fact makes this approach very appealing. Depending on the kinematic description chosen, many sub-models can arise, for instance, the kinematics can be based upon the description of motion of the upper and lower surfaces. Under a certain set of assumptions, this will render an eight-node formulation, in which each node will comprise three degrees of freedom. Another possibility is to employ the kinematics that comes from the standard shell theory, *i.e.*, description of the mean surface and the director field on it. Under a different set of assumptions, this will render a four-node formulation, in which each node will comprise six degrees of freedom. The configuration space based on the description of the mean surface and its director field can become very tedious from the algorithmic point of view, when the enforcement of the non-extensible condition on the director is required. Once again, we want to develop methods able to handle the nonlinear dynamics of structures like wind turbine blades or aircraft wings that are made of hyperelastic multilayer composite materials. In many cases, these structures may undergo moderate or even large deflections within the reversible nonlinear material regime. Due to this fact,

the most adequate shell model for our purpose is then provided by the solid-degenerate shell approach. Therefore, this model is also one of the main ingredients of this work. Next, we summarize some of the most notable contributions done during the last decades.

DVORKIN AND BATHE [31] developed a four-node shell element for general nonlinear analysis, which is applicable to the analysis of thin and thick shells, the well-known MITC4, in which the *assumed natural strain* method was employed to subdue the shear-locking problem very effectively. BATHE AND DVORKIN [10] discussed the requirements for linear and nonlinear analysis. Those works certainly represent a pioneering contribution in the context of solid-degenerate shells. To elucidate the relation among the different formulation approaches, BÜCHTER AND RAMM [22] addressed the controversy between solid-degenerate approaches and shell theories and showed that the formulations based on the same mechanical assumptions differ only in the kind of discretization. The authors paid also special attention to the performance under large rotations and the integration across the thickness. BUCALEM AND BATHE [21] presented two mixed shell finite elements of high order for general nonlinear analysis as extension of the element proposed by DVORKIN AND BATHE in [31]. BÜTCHER ET AL. [23] enabled the introduction of unmodified three-dimensional constitutive laws by means of the *enhanced assumed strain* method proposed by SIMÓ AND RIFAI [90]. As main result, a 7-parameter theory was proposed. Following a similar path, BRAUN ET AL. [20] presented a study on the use of arbitrary complete three-dimensional constitutive equations including composite and laminates without reduction or manipulation in nonlinear analysis. CHOI AND PAIK [27] presented the development of a four-node shell element for the analysis of structures undergoing large deformations, which is free of serious shear and membrane locking problems and undesired spurious kinematic deformation modes. BETSCH AND STEIN [13, 14] developed a four-node shell element that incorporates unmodified three-dimensional constitutive models. This element was improved by means of the *enhanced assumed strain* method proposed by SIMÓ AND ARMERO [91]. BETSCH ET AL. [11] extended the previously developed shell element to deal with hyperelastic materials, specifically the Neo-Hookean and Mooney-Rivlin types were investigated. BISCHOFF AND RAMM [16] formulated a geometrically nonlinear version of the *enhanced assumed strain* approach in terms of Green-Lagrange strains and reduced the underlying three-field formulation to a two-field formulation by imposing the orthogonality condition of the stress field with respect to the assumed strain field. The analysis done confirmed previously observed equivalences among mixed-hybrid elements. During the nineties, research in the field of solid-degenerate shells at the groups in Stuttgart and in Hannover were carried out simultaneously and both groups provided innovative technical solutions in the context of mixed formulations.

HAUPTMANN AND SCHWEIZERHOF [46] proposed a systematic formulation for solid-shell elements with selective reduced integration intended for linear and nonlinear analyses

that only employ displacement degrees of freedom. KLINKEL ET AL. [51] derived a continuum based three-dimensional shell element for the nonlinear analysis of laminated shell structures, where the anisotropic material behavior of layered shells was modeled using a linear elastic orthotropic material law in each layer. SZE ET AL. [98] proposed an eight-node solid-shell element for the nonlinear analysis, in which *assumed natural strains*, modified stiffness and reduced integration were combined to subdue different locking problems. VU-QUOC AND TAN [102] developed an eight-node solid-degenerate shell element and tested it with several integration methods. SANSOUR ET AL. [83] investigated the performance of enhanced strain shell finite elements in large strain deformations for rubber-like materials. TAN AND VU-QUOC [99] presented a low-order solid-shell element for the analysis of large deformable multilayer shell structures with nonlinear materials. The element has only displacement degrees of freedom, and an optimal number of enhancing assumed strain parameters to pass the patch tests (both membrane and out-of-plane bending) and to remedy volumetric locking.

KLINKEL ET AL. [52] improved the behavior of an eight-node solid-shell element by including a displacement field, an assumed strain field and an assumed stress field. In contrast to other formulations, the independent stress and the *enhanced assumed strain* interpolations were not assumed to be orthogonal. That approach represented a major novelty and provided a superior in-plane bending behavior with respect to existing formulations. SCHWARZE AND REESE [86] presented a reduced integration eight-node solid-shell finite element for the linear analysis, which includes the *assumed natural strain* and *enhanced assumed strain* methods and is equipped with an efficient and locking-free hourglass stabilization. CARRERA ET AL. [26] revisited and considered the mixed interpolation of tensorial components (basically, the MITC shell element family proposed by BATHE and collaborators), which was extended to include variable kinematics. MOREIRA ET AL. [65] proposed an approach for the layerwise formulation of composite structures that relies on solid-shell finite elements with enhanced strain variables. That approach is able to deal with large displacements, large deformations and also material nonlinear behavior.

SCHWARZE AND REESE [87] extended the previously developed reduced integration eight-node solid-shell element to the large deformation regime. Those authors claimed that the proposed formulation does not require a co-rotational coordinate system to retain material *objectivity*. VU-QUOC AND TANG [103] derived a hybrid *enhanced assumed stress* element to predict the interlaminar stresses in multilayer beam, plate and shell structures. SUSSMAN AND BATHE [97] investigated the response of an extended version of the MITC4 shell element at large strains. REINOSO AND BLÁZQUEZ [73] developed and validated an eight-node solid-degenerate shell element intended for multilayer composite structures based on the equivalent single layer approach. CALIRI ET AL. [24] presented a very detailed literature review on plate and shell theories for composite structures with

highlights to the finite element method. RAH ET AL. [72] proposed a multilayer locking-free hybrid-stress solid-shell element with high accurate interlaminar stress resolution across the thickness direction, which is restricted to the geometrically linear elastic analysis. And recently, KO ET AL. [53, 54] presented an extensively tested version of the element MITC4, in which the membrane strains components are assumed and tied/obtained from four triangular subdomains, avoiding additional enhanced strain variables.

1.2.3. Conservative/dissipative time integration

A key feature in the numerical approximations intended for the transient analysis of conservative mechanical systems is their ability to exactly preserve the first integrals of their motion (energy, momenta, symplecticity, ...), replicating the properties of the continuous counterparts. This interest in *structure preserving integrators* is hence justified by the qualitative similarity between the dynamical behaviour of a mechanical system and the *discrete dynamics* generated by the time integration scheme. It is not easy to formulate numerical schemes that unconditionally preserve one or more invariants of the discrete motion. Generally speaking, this goal is accomplished by ensuring that some of the abstract mathematical structures that appear in the continuous picture are replicated in the discrete dynamics, which is typically evidenced by the invariance under spatial translations, spatial rotations and time shifts *inter alia*. However, it is well-known that, in general, all invariants cannot be preserved for a fixed time step size scheme. Among the *structure preserving integrators*, we can distinguish two main families. The first one is able to preserve the linear and angular momenta as well as the symplectic structure, and is labeled as symplectic integration. The second one is able to preserve the linear and angular momenta as well as the total energy, and is labeled as energy-momentum integration. The later one has superior performance in the context of stiff equations. In addition to this, the modification of the method to introduce controlled dissipation and to warrant unconditional stability is realizable on the basis of well founded mathematical arguments. Since we want to develop robust procedures to analyze the nonlinear dynamics of beam and shell structures (the later ones normally described by very stiff equations), this family of integration methods provides the most adequate setting for our purpose, being the time integration our third main ingredient. Next, we summarize some of the seminal contributions done during the past decades that deal with this topic.

SIMÓ AND TARNOW [92] developed, in the context of nonlinear elastodynamics, the first energy and momentum conserving algorithms. This pioneering work showed that for Saint Venant-Kirchhoff materials, such structure preserving methods can be easily obtained by a simple modification of the midpoint rule in which the strain, instead of being evaluated at the midpoint instant, should be taken as the average of the strains at the boundaries of the time interval. This simple idea was later applied to the conserving integration of shells by SIMÓ AND TARNOW [93], of rods by SIMÓ ET AL. [94] and ROMERO AND ARMERO [81],

of contact problems by ARMERO AND PETŐCZ [2], of multibody systems by GOICOLEA AND GARCÍA ORDEN [40] and BETSCH ET AL. [12], *etc.* Moreover, it was generalized to hyperelastic materials of arbitrary type including anisotropy by GONZÁLEZ [42] and LAURSEN AND MENG [58]. The key idea for such generalization is the definition of a *discrete gradient* operator, a consistent approximation of the gradient that guarantees the strict conservation of energy in Hamiltonian systems. GOTUSSO [43] proposed an approach to discretize the Lagrange equations that for the conservative case preserves the energy of the system exactly. ITOH AND ABE [50] derived a method for discrete mechanics that does not rely on derivatives, but on difference quotients, with which the preservation of the Hamiltonian was achieved. GONZÁLEZ [41] developed a formalism for the design of conserving time-integration schemes for systems with symmetry, for instance systems that are invariant under certain transformations like spatial translations, spatial rotations and time shifts. Through the formal introduction of the discrete directional derivative implicit second-order conserving schemes can be constructed for general systems which preserve the Hamiltonian along with a certain class of other first integrals arising from affine symmetries.

ROMERO [78] showed that there exist an infinite number of second-order, energy-momentum methods for nonlinear elastodynamics. The existence of infinite second-order approximations relies on the fact that the definition of the *discrete derivative* is very vague. However, finding some of these approximation is generally non trivial. Also it is worth to mention the work of SANSOUR and collaborators [84, 85] in the context of nonlinear dynamics of shells and mixed finite elements. Alternatively, one might derive conserving methods by defining an *average vector field* as proposed by MCLACHLAN ET AL. [64], who followed the work of HARTEN ET AL. [45] in the context of general hyperbolic systems. ROJAS ET AL. [75] employed the *average vector field* for physics-based animations. It is well-known, that many Hamiltonian problems are modeled with stiff differential equations for which conserving integration schemes might not be the most robust. For these problems, numerical methods with controllable numerical dissipation in the high-frequency range provide often a practical solution. KUHLE AND RAMM [56] presented the generalized energy-momentum method for the analysis of shells. That approach was developed within the framework of the generalized- α method, and enforces the preservation of momenta and energy by means of additional algebraic constraints. KUHLE AND CRISFIELD [55] extended the generalized energy-momentum method to allow at the same time guaranteed conservation or decay of total energy and controllable numerical dissipation of unwanted high frequency response. BOTTASSO AND BORRI [17] developed energy conserving/decaying integration methods for the nonlinear dynamics of beams. Relying on the previous work, BOTTASSO AND BORRI [18] derived a general methodology for the dynamic analysis of general nonlinear multibody systems composed of rigid and deformable bodies, the latter under the small strain assumption. While preserving linear and angular momenta, the method can conserve or dissipate energy. Based on a modification of the *discrete gradient* operator, ARMERO AND ROMERO

[3, 4] developed a family of schemes for nonlinear three-dimensional elastodynamics that exhibits this kind of algorithmic dissipation, while preserving the momenta and providing a strict control of the energy, applicable to elastodynamics, as well as rods and shells [5, 80]. IBRAHIMBEGOVIC AND MAUMOURI [49] also presented a conservative/decaying integration scheme for geometrically exact beams with controllable dissipation. NOELS ET AL. [67] investigated the performance of an energy-momentum algorithm at large time-steps in the context of hypoelastic materials. ROMERO [79] described the structure of the most commonly employed integration schemes of this type and focus in their numerical analysis for linear and nonlinear problems. CONDE MARTÍN AND GARCÍA ORDEN [29] investigated the performance of time energy-momentum integration schemes for flexible multibody systems with dissipative physical mechanisms. NGUYEN ET AL. [66] proposed an energy-momentum method for geometrically exact beams, in which the enhanced strain methods was employed to avoid locking problems. LAVRENČIČ AND BRANK [59] showed that due to unresolved high-frequency content, numerical dissipation is absolutely necessary for an efficient implicit dynamic simulation of complex shell buckling and post-buckling behavior. And recently, GARCÍA ORDEN [35] discussed the properties of several formulas for the *discrete derivative* in the field of multibody systems.

1.3. Main research gaps

The previous section shows that a large number of approaches intended for geometrically exact beams, solid-degenerate shells and conservative/dissipative time integration exists and even if classical and well-developed, these research topics are still very meaningful due to: *i*) complex structures or multibody systems that can be represented upon beam-like and shell-like structural elements are of special relevance in the engineering context; and, *ii*) among all the available approaches, the superiority of one approach over the other ones cannot be claimed. Moreover, there is no work available in the literature that deals with the development of a unifying robust computational framework that combines rigid bodies, geometrically exact beams (with general cross section properties, which is very important for instance to describe bend-twist coupling effects of wind turbine blades and/or to capture aeroelastic phenomena like flutter and divergence present at aircraft wings) and solid-degenerate shells (made of hyperelastic multilayer composite materials) with a momentum-preserving, energy-preserving/dissipative integration method. Such an approach requires: *i*) dealing at once with the very different configuration spaces of rigid bodies, geometrically exact beams and solid-degenerate shells; and, *ii*) combining them with integration methods able to strictly retain the conservation/dissipation properties irrespective from the involved configuration spaces. Additionally: *iii*) the identification of motion patterns/modes based on the nonlinear configuration spaces; and, *iv*) the optimal design of robust time integration schemes based on averaged evaluations have not been accomplished before in a formal basis. This work addresses all these four topics.

1.4. Theoretical framework

From the modeling point of view, the present work relies on two basic structural models, *i.e.*, the geometrically exact beam and the solid-degenerate shell. Additionally and due to its great wealth in kinematic concepts, we cannot leave out the rigid body. Along the remaining of this chapter we refer to these three basic idealizations as the *canonical models*. Even, provided that the modeling of these idealizations is rather a classical topic, the consistent treatment and combination within a single framework is far from trivial. This fact is mainly due to the very different kinematic descriptions involved. Typically, in the context of rigid bodies and geometrically exact beams, the description of orientation in space requires to deal with the Lie group

$$SO(3) := \left\{ \mathbf{\Lambda} \in \mathbb{R}^{3 \times 3}, \mathbf{\Lambda}^T \mathbf{\Lambda} = \mathbf{I}, \det(\mathbf{\Lambda}) = 1 \right\}, \quad (1.1)$$

where $\mathbf{\Lambda}$ is the rotation tensor, and its corresponding Lie algebra

$$so(3) := \left\{ \hat{\boldsymbol{\xi}} \in \mathbb{R}^{3 \times 3}, \hat{\boldsymbol{\xi}} = -\hat{\boldsymbol{\xi}}^T \right\}, \quad (1.2)$$

where $\hat{\boldsymbol{\xi}}$ is the skew-symmetric representation of $\boldsymbol{\xi} \in \mathbb{R}^3$. This is a manifold that possesses the very favorable group structure, *i.e.*, it satisfies the group axioms: *i*) the product of two rotations is a rotation; *ii*); there is a neutral element called the identity; and, *iii*) for each rotation, there is a reciprocal element called the inverse (in this particular case, the inverse is computed by means of the transposition). In contrast with this, considering shells requires usually to deal with the unit 2-sphere

$$S^2 := \left\{ \mathbf{d} \in \mathbb{R}^3 \mid \mathbf{d} \cdot \mathbf{d} = 1 \right\}, \quad (1.3)$$

where \mathbf{d} is sometimes referred to as *director*. This manifold does not possess any favorable algebraic structure, specifically like-group structure, see for instance EISENBERG AND GUY [32]. It means that different treatments are required. For instance, a systematic description of rigid bodies and geometrically exact beams can be addressed in a natural way due to the similarities of the kinematic descriptions. Nevertheless, the combination of these two mechanical models with shells requires devoted handling. Along this section, we describe systematically the involved models by means of an unifying approach, which completely circumvents the necessity of incurring to rotational degrees of freedom. The approach starts from the equilibrium statement for a continuum body and after introducing a brief on symmetries, is specialized to the *canonical models*. In a very direct manner, the proposed systematic description allows the combination of the basic mechanical models among them and with the robust integration scheme, topics that are addressed later in the coming four chapters.

For further details on the formal aspects briefly exposed within the scope of this subsection, the reader may refer to TONTI [100], ARNOLD [6], LANDAU AND LIFSHITZ [57], CIARLET [28], MARSDEN AND HUGES [62], SIMMONDS [88], ANTMAN [1], RUBIN [82], LURIE [60], TRUESDELL AND NOLL [101], ARNOLD ET AL. [7], HEARD [47], EPSTEIN [33] and references therein.

1.4.1. Equilibrium statement

As customary, let us consider a continuum body characterized by two reference sets denoted by \mathcal{B}_0 , the original configuration, and by $\mathcal{B}_t = \varphi_t \circ \varphi_0^{-1}(\mathcal{B}_0)$, the current configuration, both open sets of \mathbb{E}^3 (\mathbb{R}^3 with the standard Euclidean structure), see Fig. 1-3. Where $\varphi_t \circ \varphi_0^{-1}$ is merely a smooth regular motion from the original configuration to the current one, *i.e.*, its inverse and derivatives are well defined everywhere, and the symbol \circ denotes the composition rule. Here, a chart is given by the pair $(\boldsymbol{\theta}, \varphi_t)$, where $\boldsymbol{\theta}$ is a subset of \mathbb{R}^3 and the mapping function $\varphi_t : \boldsymbol{\theta} \mapsto \boldsymbol{x}(\boldsymbol{\theta}; t)$. The configuration and velocity fields are described by the vector fields $\boldsymbol{x}(\boldsymbol{\theta}; t) \in \mathcal{X} \subseteq \mathbb{E}^3$ and $\boldsymbol{v}(\boldsymbol{\theta}; t) \in \mathcal{V} \subseteq \mathbb{E}^3$, correspondingly. The dynamics of the system considered can be weakly formulated as

$$\int_{\mathcal{B}_0} (\langle \delta \boldsymbol{v}, \boldsymbol{\pi}(\boldsymbol{v}) - \boldsymbol{p}(\dot{\boldsymbol{x}}) \rangle + \langle \delta \boldsymbol{x}, \dot{\boldsymbol{\pi}}(\boldsymbol{v}) - \boldsymbol{f}^{\text{ext}} + \boldsymbol{H}^T \boldsymbol{\lambda} \rangle + \langle \langle \delta \boldsymbol{E}_b(\boldsymbol{x}), \boldsymbol{S}^\# \rangle \rangle + \langle \delta \boldsymbol{\lambda}, \boldsymbol{h} \rangle) d\mathcal{B}_0 = 0. \quad (1.4)$$

The angle brackets $\langle \cdot, \cdot \rangle : \mathcal{W} \times \mathcal{W}^* \rightarrow \mathbb{R}$ stand for an appropriate dual pairing, in which \mathcal{W} is a vector space (whose elements are called vectors) and \mathcal{W}^* is its algebraic dual space (whose elements are called covectors or one-forms) and the double brackets $\langle \langle \cdot, \cdot \rangle \rangle : (\mathcal{W} \times \mathcal{W}) \times (\mathcal{W}^* \times \mathcal{W}^*) \rightarrow \mathbb{R}$ represent an appropriate double dual pairing. $\delta \boldsymbol{x} \in T_{\boldsymbol{x}(\boldsymbol{\theta}; t)} \mathcal{X}$ and $\delta \boldsymbol{v} \in T_{\boldsymbol{v}(\boldsymbol{\theta}; t)} \mathcal{V}$ are admissible variations of the configuration and velocity fields, respectively. The displacement-based momentum density $\boldsymbol{p}(\dot{\boldsymbol{x}})$ as well as the velocity-based momentum density $\boldsymbol{\pi}(\boldsymbol{v})$ belong to $T_{\boldsymbol{v}(\boldsymbol{\theta}; t)}^* \mathcal{V}$ and are defined as

$$\boldsymbol{p}(\dot{\boldsymbol{x}}) = \rho_0 \dot{\boldsymbol{x}} \quad \text{and} \quad \boldsymbol{\pi}(\boldsymbol{v}) = \rho_0 \boldsymbol{v}, \quad (1.5)$$

correspondingly. Where ρ_0 stands for the mass density in \mathcal{B}_0 . The time rate of the velocity-based momentum density $\dot{\boldsymbol{\pi}}(\boldsymbol{v})$ as well as the external force density $\boldsymbol{f}^{\text{ext}}$ belong to $T_{\boldsymbol{x}(\boldsymbol{\theta}; t)}^* \mathcal{X}$. The Green-Lagrange strain measure, $\boldsymbol{\mathcal{E}} := \{\boldsymbol{E}_b \in T_{\boldsymbol{x}(\boldsymbol{\theta}; 0)}^* \mathcal{X} \times T_{\boldsymbol{x}(\boldsymbol{\theta}; 0)}^* \mathcal{X} \mid \text{skew}(\boldsymbol{E}_b) = \mathbf{0}\}$, is given in the curvilinear setting by

$$\boldsymbol{E}_b(\boldsymbol{\theta}; t) = \frac{1}{2} (\boldsymbol{G}(\boldsymbol{\theta}; t) - \boldsymbol{G}(\boldsymbol{\theta}; 0)). \quad (1.6)$$

The pullback of the metric tensor at \mathcal{B}_t through the regular motion $\varphi_t \circ \varphi_0^{-1}$, *i.e.*, $\boldsymbol{G}(\boldsymbol{\theta}; t) : T_{\boldsymbol{x}(\boldsymbol{\theta}; 0)}^* \mathcal{X} \times T_{\boldsymbol{x}(\boldsymbol{\theta}; 0)}^* \mathcal{X} \rightarrow \mathbb{R}_{>0}$, is defined as

$$\mathbf{G}(\boldsymbol{\theta}; t) = \delta_{ij} \frac{\partial x^i(\boldsymbol{\theta}; t)}{\partial \theta^a} \frac{\partial x^j(\boldsymbol{\theta}; t)}{\partial \theta^b} \mathbf{g}^a(\boldsymbol{\theta}; 0) \otimes \mathbf{g}^b(\boldsymbol{\theta}; 0), \quad (1.7)$$

where δ_{ij} are the components of the Euclidean metric tensor, $\mathbf{g}_a \in T_{\mathbf{x}(\boldsymbol{\theta}; 0)}\mathcal{X}$ defined as $\mathbf{g}_a = \frac{\partial x^i}{\partial \theta^a} \mathbf{i}_i$ with \mathbf{i}_i for i from 1 to 3 standing for the elements of the standard orthonormal basis in \mathbb{E}^3 , *i.e.*, the space of column vectors, and the elements of the covariant basis $\mathbf{g}^a \in T_{\mathbf{x}(\boldsymbol{\theta}; 0)}^*\mathcal{X}$ defined in the usual form, that is, $\langle \mathbf{g}^b, \mathbf{g}_a \rangle = \delta_b^a$, the elements of the contravariant basis. The symbol \otimes stands for the outer product. The admissible variation of the Green-Lagrange strain tensor is denoted by $\delta \mathbf{E}_b$. The specific strain measure chosen here is accompanied by the appropriate stress definition, $\mathcal{S} := \{\mathbf{S}^\sharp \in T_{\mathbf{x}(\boldsymbol{\theta}; 0)}\mathcal{X} \times T_{\mathbf{x}(\boldsymbol{\theta}; 0)}\mathcal{X} \mid \text{skew}(\mathbf{S}^\sharp) = \mathbf{0}\}$, the second Piola-Kirchhoff stress tensor, which in the case of general hyperelastic materials is given by $\mathbf{S}^\sharp = \frac{\partial W^{\text{int}}(\mathbf{E}_b)}{\partial \mathbf{E}_b}$, where $W^{\text{int}}(\mathbf{E}_b)$ stands for the associated strain energy. Additionally, we have that

$$\langle\langle \delta \mathbf{E}_b(\mathbf{x}), \mathbf{S}^\sharp \rangle\rangle = \langle \delta \mathbf{x}, \mathbf{f}^{\text{int}}(\mathbf{x}, \mathbf{S}^\sharp) \rangle, \quad (1.8)$$

where $\mathbf{f}^{\text{int}} \in T_{\mathbf{x}(\boldsymbol{\theta}; t)}^*\mathcal{X}$ represents the vector density of internal forces. Such alternative representation will result very convenient in the remaining of this section. Finally, $\mathbf{H} \in \mathbb{R}^n \times T_{\mathbf{x}(\boldsymbol{\theta}; t)}^*\mathcal{X}$ is the Jacobian matrix of $\mathbf{h} = \mathbf{0} \in \mathbb{R}^n$, a finite-dimensional field of holonomic restrictions and $\delta \boldsymbol{\lambda}$ is an admissible variation of the Lagrange multipliers $\boldsymbol{\lambda} : \mathcal{B}_t \times [0, T] \rightarrow \mathbb{R}^n$.

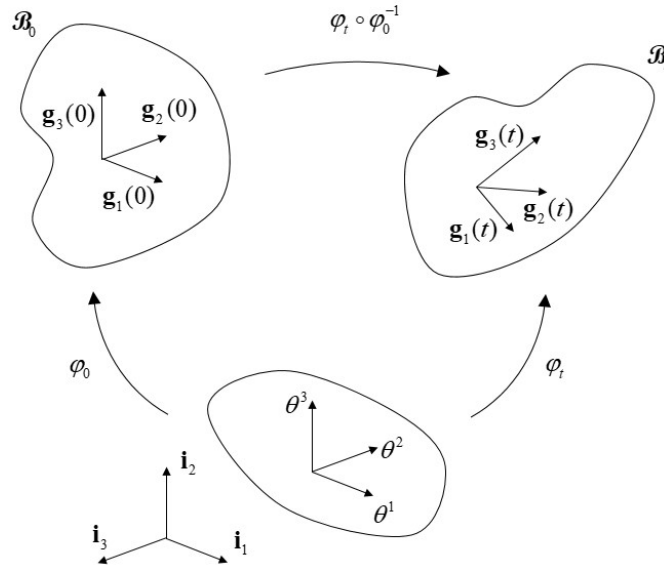


Figure 1-3.: The continuum body model.

1.4.2. Symmetries, momenta and energy

We would like to introduce next the implications that symmetry (the invariance of the Lagrangian function of a given mechanical system under certain transformations, *e.g.*, spa-

tial translations, spatial rotations and time shifts) has on the form of the internal forces and the appropriate notions of linear and angular momentum in the space \mathcal{X} . For that, the relation between the configuration space \mathcal{X} and the ambient space \mathbb{E}^3 has to be carefully considered. We start by defining $\Phi : \mathbb{E}^3 \times \mathcal{X} \rightarrow \mathcal{X}$ to be a smooth action of \mathbb{E}^3 on the configuration space such that $\Phi(\boldsymbol{\xi}, \mathbf{x})$ is the configuration of the system after all its points have been translated in space by constant vector $\boldsymbol{\xi}$. The infinitesimal generator of this translation at \mathbf{x} is the vector $\boldsymbol{\tau}_{\boldsymbol{\xi}}(\mathbf{x}) \in T_{\mathbf{x}}\mathcal{X}$ defined as

$$\boldsymbol{\tau}_{\boldsymbol{\xi}}(\mathbf{x}) = \left. \frac{\partial}{\partial \iota} \right|_{\iota=0} \Phi(\iota \boldsymbol{\xi}, \mathbf{x}), \quad (1.9)$$

with $\iota \in \mathbb{R}$. Let us now assume that the strain energy is invariant under translations, *i.e.*,

$$W^{\text{int}} = W^{\text{int}} \circ \Phi. \quad (1.10)$$

Then, choosing a one parameter curve of translations $\Phi(\iota \boldsymbol{\xi}, \cdot)$ in Eq. (1.10) and differentiating with respect to ι , it follows that a translation invariant strain energy implies that the internal forces satisfy

$$0 = \left. \frac{\partial}{\partial \iota} \right|_{\iota=0} W^{\text{int}}(\Phi(\iota \boldsymbol{\xi}, \mathbf{x})) = \left\langle \frac{\partial W^{\text{int}}(\mathbf{x})}{\partial \mathbf{x}}, \boldsymbol{\tau}_{\boldsymbol{\xi}}(\mathbf{x}) \right\rangle = -\langle \mathbf{f}^{\text{int}}(\mathbf{x}), \boldsymbol{\tau}_{\boldsymbol{\xi}}(\mathbf{x}) \rangle. \quad (1.11)$$

To study the conservation of angular momentum, we must repeat the same argument but considering now a second smooth action $\Psi : \mathbb{E}^3 \times \mathcal{X} \rightarrow \mathcal{X}$ such that $\Psi(\boldsymbol{\xi}, \mathbf{x})$ is the configuration of the system after all its points have been rotated in ambient space by the application of a rotation $\exp[\hat{\boldsymbol{\xi}}]$. Defining, as before, the infinitesimal generator of this action to be the vector $\boldsymbol{\rho}_{\boldsymbol{\xi}}(\mathbf{x}) \in T_{\mathbf{x}}\mathcal{X}$ calculated as

$$\boldsymbol{\rho}_{\boldsymbol{\xi}}(\mathbf{x}) = \left. \frac{\partial}{\partial \iota} \right|_{\iota=0} \Psi(\iota \boldsymbol{\xi}, \mathbf{x}), \quad (1.12)$$

again with $\iota \in \mathbb{R}$. If the strain energy is now rotation invariant, *i.e.*,

$$W^{\text{int}} = W^{\text{int}} \circ \Psi. \quad (1.13)$$

Then the internal forces must also satisfy

$$0 = \left. \frac{\partial}{\partial \iota} \right|_{\iota=0} W^{\text{int}}(\Psi(\iota \boldsymbol{\xi}, \mathbf{x})) = \left\langle \frac{\partial W^{\text{int}}(\mathbf{x})}{\partial \mathbf{x}}, \boldsymbol{\rho}_{\boldsymbol{\xi}}(\mathbf{x}) \right\rangle = -\langle \mathbf{f}^{\text{int}}(\mathbf{x}), \boldsymbol{\rho}_{\boldsymbol{\xi}}(\mathbf{x}) \rangle. \quad (1.14)$$

The precise notion of linear and angular momentum for the system defined in this section is provided as follows: Consider a mechanical system with configuration space $\mathcal{X} \subseteq \mathbb{E}^3$ and vanishing external forces. Let $\Phi(\boldsymbol{\xi}, \cdot), \Psi(\boldsymbol{\xi}, \cdot)$ be the translation and rotation actions on the configuration space with infinitesimal generators $\boldsymbol{\tau}_{\boldsymbol{\xi}}$ and $\boldsymbol{\rho}_{\boldsymbol{\xi}}$, respectively, and define the linear momentum $\mathbf{l} \in \mathbb{E}^3$ and the angular momentum $\mathbf{j} \in \mathbb{E}^3$ as the two quantities

that verify

$$\langle \boldsymbol{\xi}, \boldsymbol{l} \rangle = \left\langle \boldsymbol{\xi}, \int_{\mathcal{B}_0} \boldsymbol{\pi}(\boldsymbol{v}) d\mathcal{B}_0 \right\rangle = \int_{\mathcal{B}_0} \langle \boldsymbol{\tau}_\xi(\boldsymbol{x}), \boldsymbol{\pi}(\boldsymbol{v}) \rangle d\mathcal{B}_0 \quad (1.15)$$

and

$$\langle \boldsymbol{\xi}, \boldsymbol{j} \rangle = \left\langle \boldsymbol{\xi}, \int_{\mathcal{B}_0} \boldsymbol{x} \times \boldsymbol{\pi}(\boldsymbol{v}) d\mathcal{B}_0 \right\rangle = \int_{\mathcal{B}_0} \langle \boldsymbol{\rho}_\xi(\boldsymbol{x}), \boldsymbol{\pi}(\boldsymbol{v}) \rangle d\mathcal{B}_0. \quad (1.16)$$

Then, the linear momentum is conserved if the strain energy is invariant with respect to translations. Similarly, if the strain energy is invariant under rotations, the angular momentum is a constant of the motion. Moreover, the total energy

$$H = \int_{\mathcal{B}_0} \left(\frac{1}{2} \langle \boldsymbol{v}, \boldsymbol{\pi}(\boldsymbol{v}) \rangle + W^{\text{int}}(\boldsymbol{x}) \right) d\mathcal{B}_0 \quad (1.17)$$

is preserved by the motion, due to its time invariance.

The proof of momenta conservation follows from taking the derivative of these quantities and using the argument of the time integral in Eq. (1.4) with admissible variations $(\delta \boldsymbol{x}, \delta \boldsymbol{v}) = (\boldsymbol{\tau}_\xi(\boldsymbol{x}), \mathbf{0})$ and $(\boldsymbol{\rho}_\xi(\boldsymbol{x}), \mathbf{0})$, respectively. The conservation of energy property follows similarly by choosing $(\delta \boldsymbol{x}, \delta \boldsymbol{v}) = (\boldsymbol{v}, \mathbf{0})$ for $\boldsymbol{v} = \dot{\boldsymbol{x}}$.

1.4.3. Specialization to *canonical models*

First *canonical model*: the rigid body

The position of any given point of the rigid body shown in Fig. 1-4 can be written as

$$\boldsymbol{x}(\boldsymbol{\theta}; t) = \bar{\boldsymbol{x}}(t) + \theta^1 \boldsymbol{d}_1(t) + \theta^2 \boldsymbol{d}_2(t) + \theta^3 \boldsymbol{d}_3(t), \quad (1.18)$$

in which $\bar{\boldsymbol{x}} \in \bar{\mathcal{X}} \subseteq \mathbb{E}^3$ is the position vector of a reference point and \boldsymbol{d}_1 , \boldsymbol{d}_2 and \boldsymbol{d}_3 in S^2 are three mutually orthonormal vectors, *i.e.*, *directors*. On that basis, the rotation tensor can be simply obtained as $\boldsymbol{\Lambda} = \boldsymbol{d}_i \otimes \boldsymbol{i}^i \in SO(3)$, in which \boldsymbol{i}^i for i from 1 to 3 stands for the elements of the dual basis of \mathbb{E}^3 (\mathbb{R}^3 with the standard Euclidean structure), *i.e.*, the space of row vectors. $\boldsymbol{\theta} = (\theta^1, \theta^2, \theta^3)$ is a set of parameters chosen in the way that $\bar{\boldsymbol{\theta}} = \theta^1 \boldsymbol{d}_1 + \theta^2 \boldsymbol{d}_2 + \theta^3 \boldsymbol{d}_3$ describes the position of any given point of the body relative to the reference point described by $\bar{\boldsymbol{x}}$. Analogously, the velocity can be written as

$$\boldsymbol{v}(\boldsymbol{\theta}; t) = \bar{\boldsymbol{v}}(t) + \theta^1 \boldsymbol{w}_1(t) + \theta^2 \boldsymbol{w}_2(t) + \theta^3 \boldsymbol{w}_3(t), \quad (1.19)$$

in which $\bar{\boldsymbol{v}} \in \bar{\mathcal{V}} \subseteq \mathbb{E}^3$ is the translational velocity of the adopted reference point and \boldsymbol{w}_1 , \boldsymbol{w}_2 and \boldsymbol{w}_3 are three director velocity vectors. Then Eq. (1.4) takes the form

$$\int_{\mathcal{B}_0} (\langle \delta \boldsymbol{v}, \boldsymbol{\pi}(\boldsymbol{v}) - \boldsymbol{p}(\boldsymbol{x}) \rangle + \langle \delta \boldsymbol{x}, \dot{\boldsymbol{\pi}}(\boldsymbol{v}) - \boldsymbol{f}^{\text{ext}} + \boldsymbol{H}^T \boldsymbol{\lambda} \rangle + \langle \delta \boldsymbol{\lambda}, \boldsymbol{h} \rangle) d\mathcal{B}_0 = 0. \quad (1.20)$$

After performing the integration over the entire volume, the governing equation for the rigid body, in its weak form, becomes

$$\begin{aligned}
& \langle \delta \bar{\mathbf{v}}, \boldsymbol{\pi}^0(\bar{\mathbf{v}}, \mathbf{w}_1, \mathbf{w}_2, \mathbf{w}_3) - \mathbf{p}^0(\bar{\mathbf{x}}, \mathbf{d}_1, \mathbf{d}_2, \mathbf{d}_3) \rangle + \\
& \langle \delta \mathbf{w}_i, \boldsymbol{\pi}^i(\bar{\mathbf{v}}, \mathbf{w}_1, \mathbf{w}_2, \mathbf{w}_3) - \mathbf{p}^i(\bar{\mathbf{x}}, \mathbf{d}_1, \mathbf{d}_2, \mathbf{d}_3) \rangle + \\
& \langle \delta \bar{\mathbf{x}}, \dot{\boldsymbol{\pi}}^0(\bar{\mathbf{v}}, \mathbf{w}_1, \mathbf{w}_2, \mathbf{w}_3) - \mathbf{f}^{0,\text{ext}} + \mathbf{H}_0^T \boldsymbol{\lambda} \rangle + \\
& \langle \delta \mathbf{d}_i, \dot{\boldsymbol{\pi}}^i(\bar{\mathbf{v}}, \mathbf{w}_1, \mathbf{w}_2, \mathbf{w}_3) - \mathbf{f}^{i,\text{ext}} + \mathbf{H}_i^T \boldsymbol{\lambda} \rangle + \langle \delta \boldsymbol{\lambda}, \mathbf{h} \rangle = 0,
\end{aligned} \tag{1.21}$$

with i from 1 to 3. Given the mass density ρ_0 , the generalized velocity-based momentum $\boldsymbol{\pi}^i(\bar{\mathbf{v}}, \mathbf{w}_1, \mathbf{w}_2, \mathbf{w}_3)$ is defined as $\mathcal{E}_{i0}\bar{\mathbf{v}} + \mathcal{E}_{i1}\mathbf{w}_1 + \mathcal{E}_{i2}\mathbf{w}_2 + \mathcal{E}_{i3}\mathbf{w}_3$ and the generalized displacement-based momentum $\mathbf{p}^i(\bar{\mathbf{x}}, \mathbf{d}_1, \mathbf{d}_2, \mathbf{d}_3)$ as $\mathcal{E}_{i0}\dot{\bar{\mathbf{x}}} + \mathcal{E}_{i1}\dot{\mathbf{d}}_1 + \mathcal{E}_{i2}\dot{\mathbf{d}}_2 + \mathcal{E}_{i3}\dot{\mathbf{d}}_3$, where the symmetric mass inertia coefficients \mathcal{E}_{ij} are computed by means of $\int_{\mathcal{B}_0} \rho_0 \theta^i \theta^j d\mathcal{B}_0$ for i and j from 0 to 3. For the case i (j) equal to zero, θ^i (θ^j) takes a constant unit value. This setting allows to consider zeroth-order inertia \mathcal{E}_{00} , first-order inertia \mathcal{E}_{0i} for i greater than zero, and second-order inertia \mathcal{E}_{ij} for i and j greater than zero. It enables the handling of rigid bodies, in which the reference point does not coincide with the center of mass. \mathbf{H}_0 and \mathbf{H}_i (for $i = 1, 2, 3$) stand for $\frac{\partial \mathbf{h}}{\partial \bar{\mathbf{x}}}$ and $\frac{\partial \mathbf{h}}{\partial \mathbf{d}_i}$, respectively. Finally, the mutual orthonormality condition among the *directors* is simply included by considering

$$\mathbf{h}^{\text{int}}(t) = \left\{ \begin{array}{l} \mathbf{d}_1(t) \cdot \mathbf{d}_1(t) - \mathbf{d}_1(0) \cdot \mathbf{d}_1(0) \\ \mathbf{d}_2(t) \cdot \mathbf{d}_2(t) - \mathbf{d}_2(0) \cdot \mathbf{d}_2(0) \\ \mathbf{d}_3(t) \cdot \mathbf{d}_3(t) - \mathbf{d}_3(0) \cdot \mathbf{d}_3(0) \\ \mathbf{d}_2(t) \cdot \mathbf{d}_3(t) - \mathbf{d}_2(0) \cdot \mathbf{d}_3(0) \\ \mathbf{d}_1(t) \cdot \mathbf{d}_3(t) - \mathbf{d}_1(0) \cdot \mathbf{d}_3(0) \\ \mathbf{d}_1(t) \cdot \mathbf{d}_2(t) - \mathbf{d}_1(0) \cdot \mathbf{d}_2(0) \end{array} \right\} = \mathbf{0}, \tag{1.22}$$

which is in fact the internal constraint that completes the dynamic description. Be aware that this type of internal constraint will be also employed for the geometrically exact beam formulation.

Second *canonical model*: the geometrically exact beam

The position of any given point of the beam shown in Fig. 1-5 can be written as

$$\mathbf{x}(\boldsymbol{\theta}; t) = \bar{\mathbf{x}}(\boldsymbol{\theta}^3; t) + \theta^1 \mathbf{d}_1(\boldsymbol{\theta}^3; t) + \theta^2 \mathbf{d}_2(\boldsymbol{\theta}^3; t), \tag{1.23}$$

in which $\bar{\mathbf{x}} \in \bar{\mathcal{X}} \subseteq \mathbb{E}^3$ is the position vector of the beam axis and \mathbf{d}_1 and \mathbf{d}_2 together with \mathbf{d}_3 in S^2 are three mutually orthonormal directors. $\boldsymbol{\theta} = (\theta^1, \theta^2, \theta^3)$ is a set of parameters chosen in the way that $\bar{\boldsymbol{\theta}} = \theta^1 \mathbf{d}_1 + \theta^2 \mathbf{d}_2$ describes the cross section at the station $\mathcal{L}(\boldsymbol{\theta}^3)$, which intersects the beam and $\mathbf{x} = \mathbf{x}(\boldsymbol{\theta}; t)$ is the given parametrization rule in time and space. In the context of geometrically exact beams, the Green-Lagrange strain tensor can be specialized after eliminating quadratic strain yielding

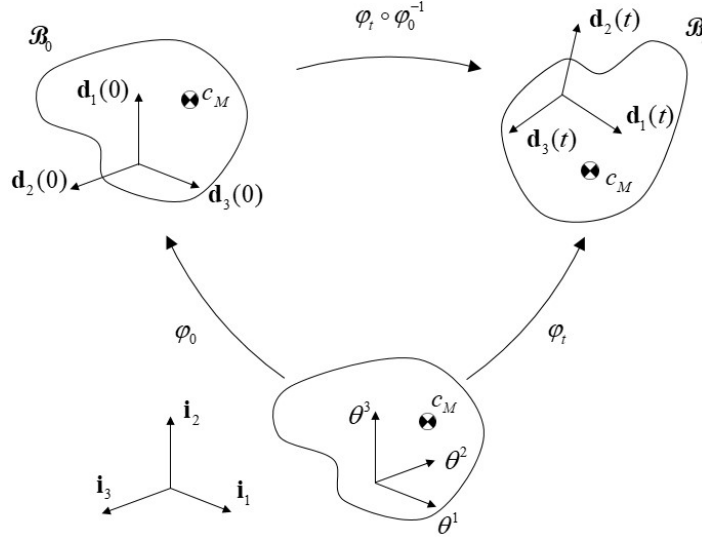


Figure 1-4.: The rigid body model.

$$\bar{E}_{ij}(\boldsymbol{\theta}, \boldsymbol{\Gamma}, \boldsymbol{\Omega}; t) \approx \text{symm} \left(\delta_{i3} \delta_{jk} \left(\Gamma^k(\boldsymbol{\theta}^3; t) - \varepsilon_{lm}^k \bar{\theta}^l \Omega^m(\boldsymbol{\theta}^3; t) \right) \right), \quad (1.24)$$

where $\text{symm}(\cdot)$ denotes symmetrization, $\Gamma^i(\boldsymbol{\theta}^3; t)$ defined as $\mathbf{d}_i(\boldsymbol{\theta}^3; t) \cdot \bar{\mathbf{x}}'(\boldsymbol{\theta}^3; t) - \mathbf{d}_i(\boldsymbol{\theta}^3; 0) \cdot \bar{\mathbf{x}}'(\boldsymbol{\theta}^3; 0)$ is a first strain measure (for shear refer to first and second components and for elongation refer to the third one), $\Omega^i(\boldsymbol{\theta}^3; t)$ defined as $\frac{1}{2} \varepsilon_{jk}^i [\mathbf{d}_k(\boldsymbol{\theta}^3; t) \cdot \mathbf{d}'_j(\boldsymbol{\theta}^3; t) - \mathbf{d}_k(\boldsymbol{\theta}^3; 0) \cdot \mathbf{d}'_j(\boldsymbol{\theta}^3; 0)]$ is a second strain measure (for bending refer to first and second components and for torsion refer to the third one) and ε_{ijk}^l is the alternating symbol that appears in the computation of the cross product in the three-dimensional Euclidean space.

Analogously, the velocity can be written as

$$\mathbf{v}(\boldsymbol{\theta}; t) = \bar{\mathbf{v}}(\boldsymbol{\theta}^3; t) + \theta^1 \mathbf{w}_1(\boldsymbol{\theta}^3; t) + \theta^2 \mathbf{w}_2(\boldsymbol{\theta}^3; t), \quad (1.25)$$

in which $\bar{\mathbf{v}} \in \bar{\mathcal{V}} \subseteq \mathbb{E}^3$ is the translational velocity of the beam axis and $\mathbf{w}_1, \mathbf{w}_2$ together with \mathbf{w}_3 are three director velocity vectors. Now Eq. (1.4) takes the form

$$\int_{\mathcal{L}_0} \int_{\mathcal{A}_0} (\langle \delta \mathbf{v}, \boldsymbol{\pi}(\mathbf{v}) - \mathbf{p}(\mathbf{x}) \rangle + \langle \delta \mathbf{x}, \dot{\boldsymbol{\pi}}(\mathbf{v}) + \mathbf{f}^{\text{int}}(\mathbf{x}, \mathbf{S}^\sharp) - \mathbf{f}^{\text{ext}} + \mathbf{H}^T \boldsymbol{\lambda} \rangle + \langle \delta \boldsymbol{\lambda}, \mathbf{h} \rangle) d\mathcal{A}_0 d\mathcal{L}_0 = 0, \quad (1.26)$$

where \mathcal{A}_0 represents the cross-sectional area and \mathcal{L}_0 stands for the arc length in the original configuration. Given two mutually orthonormal directors \mathbf{d}_1 and \mathbf{d}_2 , a third director \mathbf{d}_3 could be simply computed as $\mathbf{d}_1 \times \mathbf{d}_2$. This description would lead to a two-director formulation. An alternative to this formulation results from the additional consideration of \mathbf{d}_3 in combination with the mutual orthonormality condition for the three directors as already introduced by Eq (1.22). The resulting representation is a so-called three-director formulation, which we adopt to facilitate the combination among beams

and rigid bodies and evenly to avoid special treatment of the third director, *i.e.*, \mathbf{d}_3 . After introducing explicitly \mathbf{d}_3 in the variational principle and performing the integration over the cross section, the governing equations for the geometrically exact beam, in its weak form, becomes

$$\begin{aligned}
& \int_{\mathcal{L}_0} (\langle \delta \bar{\mathbf{v}}, \boldsymbol{\pi}^0(\bar{\mathbf{v}}, \mathbf{w}_1, \mathbf{w}_2) - \mathbf{p}^0(\bar{\mathbf{x}}, \mathbf{d}_1, \mathbf{d}_2) \rangle + \\
& \langle \delta \mathbf{w}_i, \boldsymbol{\pi}^i(\bar{\mathbf{v}}, \mathbf{w}_1, \mathbf{w}_2) - \mathbf{p}^i(\bar{\mathbf{x}}, \mathbf{d}_1, \mathbf{d}_2) \rangle + \langle \delta \mathbf{w}_3, \mathbf{w}_3 - \dot{\mathbf{d}}_3 \rangle + \\
& \langle \delta \bar{\mathbf{x}}, \dot{\boldsymbol{\pi}}^0(\bar{\mathbf{v}}, \mathbf{w}_1, \mathbf{w}_2) + \mathbf{f}^{0,\text{int}}(\mathbf{d}_1, \mathbf{d}_2, \mathbf{d}_3, \mathbf{N}) - \mathbf{f}^{0,\text{ext}} + \mathbf{H}_0^T \boldsymbol{\lambda} \rangle + \\
& \langle \delta \mathbf{d}_i, \dot{\boldsymbol{\pi}}^i(\bar{\mathbf{v}}, \mathbf{w}_1, \mathbf{w}_2) + \mathbf{f}^{i,\text{int}}(\bar{\mathbf{x}}, \mathbf{d}_1, \mathbf{d}_2, \mathbf{d}_3, \mathbf{N}, \mathbf{M}) - \mathbf{f}^{i,\text{ext}} + \mathbf{H}_i^T \boldsymbol{\lambda} \rangle + \\
& \langle \delta \mathbf{d}_3, \mathbf{f}^{3,\text{int}}(\bar{\mathbf{x}}, \mathbf{d}_1, \mathbf{d}_2, \mathbf{d}_3, \mathbf{N}, \mathbf{M}) - \mathbf{f}^{3,\text{ext}} + \mathbf{H}_3^T \boldsymbol{\lambda} \rangle + \langle \delta \boldsymbol{\lambda}, \mathbf{h} \rangle) d\mathcal{L}_0 = 0,
\end{aligned} \tag{1.27}$$

with i from 1 to 2. The generalized velocity-based momentum $\boldsymbol{\pi}^i(\bar{\mathbf{v}}, \mathbf{w}_1, \mathbf{w}_2)$ is defined as $\mathcal{E}_{i0} \bar{\mathbf{v}} + \mathcal{E}_{i1} \mathbf{w}_1 + \mathcal{E}_{i2} \mathbf{w}_2$ and the generalized displacement-based momentum $\mathbf{p}^i(\bar{\mathbf{x}}, \mathbf{d}_1, \mathbf{d}_2)$ as $\mathcal{E}_{i0} \dot{\bar{\mathbf{x}}} + \mathcal{E}_{i1} \dot{\mathbf{d}}_1 + \mathcal{E}_{i2} \dot{\mathbf{d}}_2$, where \mathcal{E}_{ij} is computed by means of $\int_{\mathcal{A}_0} \varrho_0 \theta^i \theta^j d\mathcal{A}_0$ for i and j from 0 to 2. This consideration allows the handling of cross sections with arbitrary shape and material properties, which exactly applies to the case of modern slender structures made of hyperelastic multilayer composite materials. Given the beam strain energy density per unit length W^{beam} defined as

$$W^{\text{beam}}(\boldsymbol{\theta}^3, \boldsymbol{\Gamma}, \boldsymbol{\Omega}; t) = \int_{\mathcal{A}_0} W^{\text{int}}(\bar{\mathbf{E}}_b(\boldsymbol{\theta}, \boldsymbol{\Gamma}, \boldsymbol{\Omega}; t)) d\mathcal{A}_0, \tag{1.28}$$

the force and moment resultants are respectively

$$\mathbf{N} = \frac{\partial W^{\text{beam}}}{\partial \boldsymbol{\Gamma}} \quad \text{and} \quad \mathbf{M} = \frac{\partial W^{\text{beam}}}{\partial \boldsymbol{\Omega}}. \tag{1.29}$$

The components of the cross-sectional tangent constitutive matrices are in principle computed as

$$\begin{aligned}
(\boldsymbol{\mathfrak{C}}_{\boldsymbol{\Gamma}\boldsymbol{\Gamma}})_{ij} &= \int_{\mathcal{A}_0} \boldsymbol{\mathfrak{C}}^{IJKL} \frac{\partial \bar{E}_{IJ}}{\partial \Gamma^i} \frac{\partial \bar{E}_{KL}}{\partial \Gamma^j} d\mathcal{A}_0, \quad (\boldsymbol{\mathfrak{C}}_{\boldsymbol{\Gamma}\boldsymbol{\Omega}})_{ij} = \int_{\mathcal{A}_0} \boldsymbol{\mathfrak{C}}^{IJKL} \frac{\partial \bar{E}_{IJ}}{\partial \Gamma^i} \frac{\partial \bar{E}_{KL}}{\partial \Omega^j} d\mathcal{A}_0, \\
(\boldsymbol{\mathfrak{C}}_{\boldsymbol{\Omega}\boldsymbol{\Gamma}})_{ij} &= \int_{\mathcal{A}_0} \boldsymbol{\mathfrak{C}}^{IJKL} \frac{\partial \bar{E}_{IJ}}{\partial \Omega^i} \frac{\partial \bar{E}_{KL}}{\partial \Gamma^j} d\mathcal{A}_0, \quad (\boldsymbol{\mathfrak{C}}_{\boldsymbol{\Omega}\boldsymbol{\Omega}})_{ij} = \int_{\mathcal{A}_0} \boldsymbol{\mathfrak{C}}^{IJKL} \frac{\partial \bar{E}_{IJ}}{\partial \Omega^i} \frac{\partial \bar{E}_{KL}}{\partial \Omega^j} d\mathcal{A}_0.
\end{aligned} \tag{1.30}$$

Where $\boldsymbol{\mathfrak{C}}^{IJKL}$ represents the components of the tangent elasticity tensor and \bar{E}_{IJ} stands for the components of the strain tensor presented by Eq. (1.24). For thin-walled structures, additional assumptions about the strain and stress states may be necessary. At this point, warping effects are completely neglected. In the case of the blade of a wind turbine, which is in some regions far away from the thin-walled structure hypothesis and also non-negligible variations of the cross section may take place, the primary warping due to torsion ought to be combined with the consideration of secondary warping due to shear.

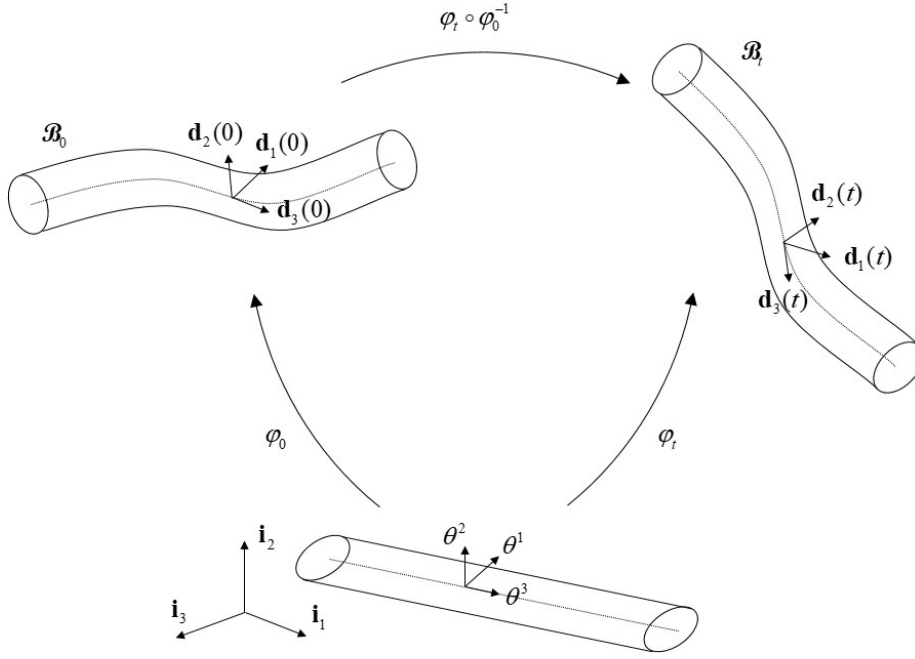


Figure 1-5.: The geometrically exact beam model

This would require to include additional displacements fields, see for example GEBHARDT ET AL. [37]. Therefore, standard assumptions regarding warping effects may result not adequate. However, a detailed discussion and treatment of this aspect is beyond the scope of the current work. The acting internal load densities are indicated as follows:

$$\begin{aligned} \mathbf{f}^{0,\text{int}}(\mathbf{d}_1, \mathbf{d}_2, \mathbf{d}_3, \mathbf{N}) &= \left(\frac{\partial \Gamma}{\partial \bar{\mathbf{x}}}(\mathbf{d}_1, \mathbf{d}_2, \mathbf{d}_3) \right)^T \mathbf{N}, \\ \mathbf{f}^{i,\text{int}}(\bar{\mathbf{x}}, \mathbf{d}_1, \mathbf{d}_2, \mathbf{d}_3, \mathbf{N}, \mathbf{M}) &= \left(\frac{\partial \Gamma}{\partial \bar{\mathbf{d}}_i}(\bar{\mathbf{x}}, \mathbf{d}_1, \mathbf{d}_2, \mathbf{d}_3) \right)^T \mathbf{N} + \left(\frac{\partial \Omega}{\partial \bar{\mathbf{d}}_i}(\mathbf{d}_1, \mathbf{d}_2, \mathbf{d}_3) \right)^T \mathbf{M}. \end{aligned} \quad (1.31)$$

Third *canonical model*: the solid-degenerate shell

The position of any given point of the shell shown in Fig. 1-6 can be written as

$$\mathbf{x}(\boldsymbol{\theta}; t) = \bar{\mathbf{x}}(\theta^1, \theta^2; t) + \theta^3 \frac{\vartheta}{2} \mathbf{d}(\theta^1, \theta^2; t), \quad (1.32)$$

in which $\bar{\mathbf{x}} \in \bar{\mathcal{X}} \subseteq \mathbb{E}^3$ is the position vector of the midsurface, ϑ represents the thickness of the shell and $\mathbf{d} \in \mathcal{D} \subseteq \mathbb{R}_{\neq 0}^3$ is an extensible director field, which admits multiplicative decomposition, *i.e.*, $\mathbf{d} = d \hat{\mathbf{d}}$ with $d \in \mathbb{R}_{>0}$ and $\hat{\mathbf{d}} \in S^2$. $\boldsymbol{\theta} = (\theta^1, \theta^2, \theta^3)$ is a set of parameters chosen in the way that $\bar{\boldsymbol{\theta}} = (\theta^1, \theta^2, 0)$ describes the midsurface. For instance, we can choose $\boldsymbol{\theta}$ to span the domain \mathfrak{B} , such as $\mathfrak{B} := \{[-1, 1] \times [-1, 1] \times [-1, 1]\}$. The spatial metric structure induced by this construction agrees with Eq. (1.7).

Analogously, the velocity can be written as

$$\mathbf{v}(\boldsymbol{\theta}; t) = \bar{\mathbf{v}}(\theta^1, \theta^2; t) + \theta^3 \frac{\vartheta}{2} \mathbf{w}(\theta^1, \theta^2; t), \quad (1.33)$$

in which $\bar{\mathbf{v}} \in \bar{\mathcal{V}} \subseteq \mathbb{E}^3$ is the translational velocity of the midsurface and $\mathbf{w} \in \mathcal{W} \subseteq \mathbb{R}^3$ is the director velocity. By employing the same idea applied already for the rigid body and the geometrically exact beam, the governing equation for the solid-degenerate shell, in its weak form, becomes

$$\int_{\mathfrak{B}} (\langle \delta \mathbf{v}, \boldsymbol{\pi}(\mathbf{v}) - \mathbf{p}(\mathbf{x}) \rangle + \langle \delta \mathbf{x}, \dot{\boldsymbol{\pi}}(\mathbf{v}) + \mathbf{f}^{\text{int}}(\mathbf{x}, \mathbf{S}^\sharp) - \mathbf{f}^{\text{ext}} + \mathbf{H}^T \boldsymbol{\lambda} \rangle + \langle \delta \tilde{\mathbf{E}}_b, \mathbf{S}^\sharp \rangle + \langle \delta \boldsymbol{\lambda}, \mathbf{h} \rangle) \sqrt{\det[\mathbf{G}(\boldsymbol{\theta}; 0)]} d\mathfrak{B} = 0, \quad (1.34)$$

where the enhanced part of the Green-Lagrange strain tensor is defined by convenience as $\tilde{\mathbf{E}}_b \in T_{\mathbf{x}(\boldsymbol{\theta}; 0)}^* \mathcal{X} \times T_{\mathbf{x}(\boldsymbol{\theta}; 0)}^* \mathcal{X}$ such that $\text{skew}(\tilde{\mathbf{E}}_b) = \mathbf{0}$ and $\langle \int_{\mathfrak{B}} \tilde{\mathbf{E}}_b \sqrt{\det[\mathbf{G}(\boldsymbol{\theta}; 0)]} d\mathfrak{B}, \mathbf{S}^\sharp \rangle = 0$ for all non-trivial constant stress \mathbf{S}^\sharp , and $\sqrt{\det[\mathbf{G}(\boldsymbol{\theta}; 0)]} d\mathfrak{B}$ is the volume element. And finally, $\delta \tilde{\mathbf{E}}_b$ is an admissible variation of the enhanced part of the Green-Lagrange strain tensor.

Note that this model, the solid-degenerated shell, is a solid in itself and no devoted handling is required, as in case of rigid bodies and geometrically exact beams.

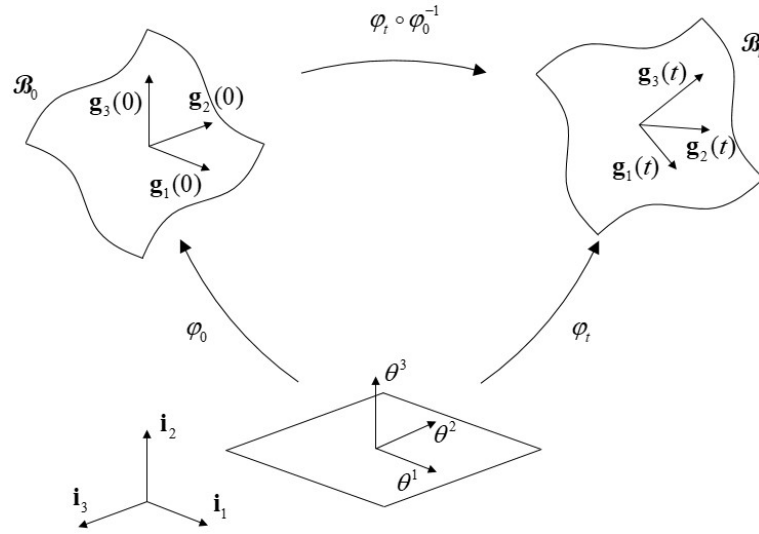


Figure 1-6.: The solid-degenerate shell model

1.4.4. Further technical aspects

Formulations derived with the Hamiltonian setting rely on the description of motion in the *phase space*, *i.e.*, the variables are generalized coordinates and generalized momenta. This kind of approaches is very elegant and allows to exploit the very rich underlying

mathematical structure, specially in the case of conservative systems. In contrast to this, the mechanical framework adopted here is intended for general non-conservative systems that may arise in the presence of dissipation functions and/or non-integrable constraints (restrictions that are path-dependent, *e.g.*, non-slip condition at the contact point of a sphere rolling on the floor), which are highly relevant for industrial applications. Therefore, we follow a complementary path, in which the description of motion takes place in the *state space*, *i.e.*, the variables are generalized coordinates and generalized velocities. Such a kind of representations were introduced by Poincaré, see for instance HEARD [47]. This description allows to introduce dissipation functions as well as nonholonomic constraints in a very natural way, since both can be easily stated in terms of velocities, but not in terms of momenta. For the general non-conservative case, the resulting governing equations can be reverted to the Lagrange-D'Alembert equations, which are non-variational. For the conservative case, the resulting governing equations can be reverted to the Euler-Lagrange equations, which are variational. Thus, it can be regarded as a very general setting and this is why we chose it.

1.5. General objectives

This research effort provides means intended for helping to understand further the nonlinear dynamics of beam and shell structures made of hyperelastic multilayer composite materials subject to highly dynamic loads that can take place in modern engineering applications, *e.g.*, wind turbines, helicopters, cars, speedboats or submarines *inter alia*. This general objective is materialized through the development and posterior employment of highly-robust and -reliable, computational procedures that warrant affordable time expenditures. It is apparent that the development of such methods promotes not only the improvement of the current understanding, but also provides sound foundations that are necessary for the design and analysis of future generations of high-performance slender structures.

1.6. Original contributions

We summarize next the original contributions of this work:

1. A director-based finite-element formulation for nonlinear dynamics of geometrically exact beams with general cross-section properties embedded in a momentum-preserving, energy-preserving/dissipative setting. This is intended for general non-conservative beam structures/mechanisms that may arise in the presence of dissipation functions and/or non-integrable constraints, which are very relevant for industrial applications.
2. A director-based finite element formulation for nonlinear dynamics of solid-degenerate shells made of hyperelastic multilayer composite materials embedded in a momentum-

preserving, energy-preserving/dissipative setting. Following the same philosophy than before, this is also intended for general non-conservative shell structures/mechanisms that may arise in the context of industrial applications.

3. Combination of rigid bodies, geometrically exact beams and solid-degenerate shells with robust time integration techniques into a single common object-oriented framework. This is highly extensible and very suitable for structural engineering and inherits all advantages of the basic ingredients, *e.g.*, *objectivity*, *path-independence*, unconditional stability, robustness, *etc.*
4. A comprehensive framework to analyze the nonlinear dynamics of beam structures that relies on the *principal geodesic analysis* and thus goes beyond classical procedures, which assume that every motion takes place in the three-dimensional ambient space, *i.e.*, the configuration space is considered to be linear.
5. A new conservative/dissipative time integration scheme relying on a collection of linearly constrained quadratic programs intended to optimally modify the classical midpoint rule so as to guarantee the strict energy conservation/dissipation properties.

1.7. Organization of this work

This work is a compilation of four journal articles. Following the chronological order of publication and not a thematic sequence, the remaining of this work is organized in chapters as indicated below. Additionally, we provide hints regarding the main innovations that are partially or completely addressed within the scope of each chapter.

Chapter 2 considers the nonlinear dynamics of shell structures made of single- or multilayer elastic materials (an extension of the linear elastic material model to the large deformation setting), in which a mixed finite element formulation for solid-degenerate shells and a robust integration scheme are consistently combined. To render more complicated structures, this formulation also includes algebraic constraints and their treatment by means of a null-space method. This addresses (partially) the second main innovation.

Chapter 3 presents a new object-oriented framework for the nonlinear dynamics of slender structures made of multilayer composite and hyperelastic materials, in which each mechanical system is modeled as a collection of stiff and flexible components, *e.g.*, rigid bodies, geometrically exact beams and solid-degenerate shells. The adopted robust time integration scheme relies on the *average vector field*, which ensures the preservation of momenta and the conservation or controlled dissipation of energy. This addresses (partially) the first, (partially) the second and (completely) the third main innovations.

Chapter 4 provides, by means of the *principal geodesic analysis*, a new approach to investigate the nonlinear dynamics of beam structures that is presented in a fully nonlinear setting and exploits the underlying mathematical structure provided by the configuration space. Additionally, we also provide hints regarding the further model order reduction. This addresses (partially) the first and (completely) the fourth main innovations.

Chapter 5 considers a new conservative/dissipative time integration in the context of both, reduced-order models and finite elasticity models, where a new systematic approach for the derivation of algorithmic internal forces and generalized velocities is presented and analyzed. Such algorithmic force and velocity approximations warrant strictly the desired conservation/dissipation properties and are very easy to implement into existing codes. This addresses (completely) the fifth main innovation.

Finally, *Chapter 6* culminates this work with conclusions and suggests future work.

For sake of completeness, *Appendix A* presents a lists of journal articles written between July 2015 and June 2019. Period, in which this work took place. All these fall directly or indirectly within the field of structural analysis (*Statik und Dynamik*).

2. Article A: On the nonlinear dynamics of shell structures: combining a mixed finite element formulation and a robust integration scheme

This article presents an approach to analyze the nonlinear dynamics of shell structures, which relies on the combination of a mixed finite element formulation and a robust integration scheme that is presented in a differential-algebraic setting. The structure is spatially discretized with extensible-director-based solid-degenerate shells. The shear locking and the artificial thickness strains are cured by means of the *assumed natural strain* method, but the enhancement of the strain field in the thickness direction and the cure of the membrane locking are achieved by means of the *enhanced assumed strain* method. This director-based approach allows to consider unmodified three-dimensional constitutive laws by only improving the director field. Due to the adopted kinematic description, the treatment of folded shells is very simple. The resulting semi-discrete equations are temporally discretized by means of a momentum-preserving, energy-preserving/decaying method, which allows to mitigate the undesirable effect due to unresolved high-frequency content providing robustness without destroying the precision of the solution. To render more complicated structures by means of junctions, some interesting constraints are introduced together with their null-space treatment. In few words, from a methodological point of view, the novelty of this work is the combination of a mixed finite element for shells, the time integration with a momentum-preserving, energy-preserving/decaying method and a null-space method into a single common unifying framework, which may be used very effectively to analyze wind turbine blades or aircraft wings.

This article is published in *Thin-Walled Structures* 118 (2017), 56–72. The main work was done by the author of this *Habilitationsschrift*. Raimund Rolfes contributed with technical suggestions and supporting work.

Permanent link: <http://doi.org/10.1016/j.tws.2017.05.001>



Contents lists available at ScienceDirect

Thin-Walled Structures

journal homepage: www.elsevier.com/locate/tws

Full length article

On the nonlinear dynamics of shell structures: Combining a mixed finite element formulation and a robust integration scheme



Cristian Guillermo Gebhardt*, Raimund Rolfes

Institute of Structural Analysis, Leibniz Universität Hannover, Appelstraße 9A, Hannover 30167, Germany

ARTICLE INFO

Keywords:

Nonlinear dynamics
Shell structures
Mixed finite element formulation
Robust integration scheme
Differential-algebraic equations

ABSTRACT

In this work, we present an approach to analyze the nonlinear dynamics of shell structures, which combines a mixed finite element formulation and a robust integration scheme. The structure is spatially discretized with extensible-director-based solid-degenerate shells. The semi-discrete equations are temporally discretized with a momentum-preserving, energy-preserving/decaying method, which allows to mitigate the effects due to unresolved high-frequency content. Additionally, kinematic constraints are employed to render structural junctions. Finally, the method, which can be used to analyze blades of wind turbines or wings of airplanes effectively, is tested and its capabilities are illustrated by means of examples.

1. Introduction

The complexity of current and new shell structures in combination with the increased computation capacity encouraged the development and application of fully nonlinear shell formulations. In this context, time-domain analysis involving large displacements, large rotations and large strains due to dynamic loads plays a major role. The discrete equations of shells are in fact very stiff and therefore, the calculation of long-term response could be very problematic, even for well-established commercial codes. Achieving robustness requires the development of new methods that must annihilate the unresolved high-frequency content, warranting evenly the preservation of the underlying physics. Certainly, the accomplishment of these features is very challenging.

Dvorkin and Bathe [1] developed a four-node shell element for general nonlinear analysis, which is applicable to the analysis of thin and thick shells. Bathe and Dvorkin [2] discussed the requirements for linear and nonlinear analysis. Büchter and Ramm [3] addressed the controversy between solid-degenerate approaches and shell theories. Büchter et al. [4] enabled the introduction of unmodified three-dimensional constitutive laws by means of the enhanced assumed strain method proposed by Simo and Rifai [5]. Simo and Tarnow [6,7] developed a time integration scheme for the dynamics of elastic solids and shells, which preserves, independently of the time step size, the linear momentum, the angular momentum and the total energy. Choi and Paik [8] presented the development of a four-node shell element for the analysis of structures undergoing large deformations. Betsch and Stein [9,10] developed a four-node shell element that incorporates unmodified three-dimensional constitutive models. This element was

improved by means of the enhanced assumed strain method proposed by Simo and Armero [11]. Bischoff and Ramm [12] formulated a geometrically nonlinear version of the enhanced assumed strain approach in terms of Green-Lagrange strains. Sansour et al. [13] combined a geometric exact shell theory and an integration scheme that preserves the linear momentum, the angular momentum and the total energy. Kuhl and Ramm [14] developed a generalization of the energy-momentum method developed within the framework of the generalized α method. Armero and Romero [15,16] developed a family of schemes for nonlinear three-dimensional elastodynamics that exhibits controllable numerical dissipation in the high-frequency range. For a fixed and finite time step, the method produces a correct picture of the phase space even in the presence of dissipation. Sansour et al. [17] dealt with a dynamic formulation of shells and the development of a robust energy-momentum integration scheme. Romero and Armero [18] extended the previously introduced method for the dynamics of geometrically exact shells. Proofs of the numerical properties in the full nonlinear range were also provided. Bauchau et al. [19] developed energy-preserving/decaying schemes for the simulation of multibody systems including shell components. Vu-Quoc and Tan [20] developed an eight-node solid-degenerate shell element and tested it with several integration methods. Sansour et al. [21] modified an existent method to deal with material nonlinearities. Ozkul [22] presented a finite element for dynamic analysis of shells of general shape. Ziemčík [23] presented a four-node shell element to analyze lightweight smart structures. Leyendecker et al. [24] extended a framework for the computational treatment of rigid bodies and nonlinear beams to the realm of nonlinear shells. Vaziri [25] studied the response of shell structures under large

* Corresponding author.

E-mail address: c.gebhardt@isd.uni-hannover.de (C.G. Gebhardt).

deformations and presented a review of the current state-of-the-art with practical suggestions. Carrera et al. [26] considered the mixed interpolation of tensorial components, which was extended to model shells with variable kinematics. Wu [27] described the nonlinear dynamic behavior of shell structures by means of a vector form intrinsic formulation. Ahmed and Sluys [28] presented a three-dimensional shell element for the dynamic analysis of laminated composites. Pietraszkiewicz and Konopińska [29] reviewed different theoretical, numerical, and experimental approaches to model, analyze and design compound shell structures with junctions. Reinoso and Blázquez [30] developed an eight-node solid-degenerate shell element, which was reformulated in the context of composite structures. Recently, Caliri et al. [31] presented a very detailed literature review on plate and shell theories for composite structures with highlights to the finite element method.

In this work, we present an approach to analyze the nonlinear dynamics of shell structures, which relies on the combination of a mixed finite element formulation and a robust integration scheme that is presented in a differential-algebraic setting. The structure is spatially discretized with extensible-director-based solid-degenerate shells. The shear locking and the artificial thickness strains are cured by means of the assumed natural strain method, but the enhancement of the strain field in the thickness direction and the cure of the membrane locking are achieved by means of the enhanced assumed strain method. This director-based approach allows to consider unmodified three-dimensional constitutive laws by only improving the director field. Due to the adopted kinematic description, the treatment of folded shells is very simple and the combination with rigid bodies and beams is straightforward (this is valid for rotationless frameworks). Similar approaches for eight-node solid-degenerate shells would require to reparametrize the director field in terms of the upper and lower displacement fields, which would be surely effective, but certainly more elaborate. However, objective and comprehensive comparisons between the four-node extensible-director-based solid-degenerate shell and the eight-node displacement-based solid degenerate shell are not part of this work. The resulting semi-discrete equations are temporally discretized by means of a momentum-preserving, energy-preserving/decaying method, which allows to mitigate the undesirable effect due to unresolved high-frequency content providing robustness without destroying the precision of the solution. Finally, some interesting constraints to render more complicated structures by means of junctions are introduced, and its null-space treatment is briefly described. In few words, from a methodological point of view, the novelty of this work is the combination of a mixed finite element for shells, the time integration with a momentum-preserving, energy-preserving/decaying method and the null-space projection method into a single common unifying framework, which may be used very effectively to analyze blades of wind turbines or wings of airplanes. To our best knowledge, there is not a single work, in which all these three topics are combined with a similar setting in the context of shell structures.

The remaining is organized as follows: Section 2 presents the adopted mechanical framework, comprising a general description, the spatial discretization that relies on a mixed formulation, the temporal discretization that relies on a robust scheme, the treatment of various interesting constraints and the presentation of the discrete equations. In Section 3, we present five examples taken from literature, which were chosen to show the potentialities and capabilities of the exposed ideas. Finally, concluding remarks and future work are given in the Section 4.

2. Mechanical framework

In this section, we present the necessary mathematical tools to deal, from a purely mechanical point of view, with shell structures. First, we roughly outline the fundamentals that are needed to establish a starting point. Second, we introduce the shell kinematics and the spatial discretization based on a mixed finite element formulation. Third, we introduce the temporal discretization starting from the energy-momen-

tum-conserving algorithm and the modifications needed to build a momentum-preserving, energy-preserving/decaying algorithm. Fourth, we provide a brief exposition of some interesting constraints, which are used to render more complicated structures. And lastly, we present the governing equations for the fully discretized problem in their final implementation form.

2.1. Generalities

Let us assume a continuum body characterized by a chosen reference set denoted by \mathcal{B}_0 , this is an open set of \mathbb{R}^3 , whose configuration and velocity are described at time t by the vectors $\mathbf{x}(t) \in \mathcal{X}_t \subseteq \mathbb{R}^3$ and $\mathbf{v}(t) \in \mathcal{V}_t \subseteq \mathbb{R}^3$, respectively. In addition, let us assume that the body is subjected to a finite-dimensional set of constraints $\mathbf{h}(\mathbf{x}) = \mathbf{0} \in \mathbb{R}^n$, with $n \in \mathbb{N}$, that only accounts for integrable restrictions. The dynamic behavior of the flexible system within the bounded time interval $[t_1, t_2] \subset \mathbb{R}_0^+$ can be formulated with the Hamilton principle as

$$\delta \bar{\mathcal{S}} = \int_{t_1}^{t_2} \int_{\mathcal{B}_0} \{ \langle \delta \mathbf{v}, \mathbf{l}(\mathbf{x}) - \mathbf{l}(\mathbf{v}) \rangle - \langle \delta \mathbf{x}, \mathbf{f}^{\text{int}}(\mathbf{x}, \mathbf{S}^\sharp) + \dot{\mathbf{l}}(\mathbf{v}) - \mathbf{f}^{\text{ext}}(\mathbf{x}) + \mathbf{H}(\mathbf{x})^T \boldsymbol{\lambda} \rangle - \langle \delta \bar{\mathbf{E}}_b, \mathbf{S}^\sharp \rangle - \langle \delta \boldsymbol{\lambda}, \mathbf{h}(\mathbf{x}) \rangle \} d\mathcal{B} dt = 0, \quad (1)$$

where $\delta \bar{\mathcal{S}}$ is merely the infinitesimal increment of the action functional, which may be not an actual variation due to the presence of non-conservative external fields, and $\langle \cdot, \cdot \rangle$ is an appropriate dual pairing. $\delta \mathbf{x} \in T_{\mathbf{x}(t)} \mathcal{X}_t$ and $\delta \mathbf{v} \in T_{\mathbf{v}(t)} \mathcal{V}_t$ are admissible variations of the configuration and velocity vectors, respectively. The displacement-based momentum density $\mathbf{l}(\mathbf{x})$ and the velocity-based momentum density $\mathbf{l}(\mathbf{v})$ map elements of $T_{\mathbf{x}(t)} \mathcal{X}_t$ to elements of \mathbb{R} . The time rate of the velocity-based momentum density $\dot{\mathbf{l}}(\mathbf{v})$, the internal force density $\mathbf{f}^{\text{int}}(\mathbf{x}, \mathbf{S}^\sharp)$ and the external force density $\mathbf{f}^{\text{ext}}(\mathbf{x})$ map elements of $T_{\mathbf{x}(t)} \mathcal{X}_t$ to elements of \mathbb{R} . $\mathbf{H}: \mathbb{R}^n \times T_{\mathbf{x}(t)} \mathcal{X}_t \rightarrow \mathbb{R}$ is the Jacobean matrix of $\mathbf{h}(\mathbf{x})$, $\boldsymbol{\lambda}: [t_1, t_2] \rightarrow \mathbb{R}^n$ belongs to the space of curves with no boundary conditions, the well-known Lagrange's multipliers, and $\delta \boldsymbol{\lambda}$ represents an admissible variation of the multipliers. The strain $\bar{\mathbf{E}}_b \in \bar{\mathcal{E}} := \{ \bar{\mathbf{E}}_b \in T_{\mathbf{x}(0)}^* \mathcal{X}_0 \times T_{\mathbf{x}(0)}^* \mathcal{X}_0 | 2\bar{\mathbf{E}}_b = [\boldsymbol{\phi}_t \circ (\boldsymbol{\phi}_0)^{-1}]^* \mathbf{G}[\mathbf{x}(t)] - \mathbf{G}[\mathbf{x}(0)] \}$ is the displacement-based part of the Green-Lagrange strain tensor, in which $\mathbf{G}[\mathbf{x}(0)]$ is the metric tensor in the original configuration, $\mathbf{G}[\mathbf{x}(t)]$ is the metric tensor in the current configuration and $[\boldsymbol{\phi}_t \circ (\boldsymbol{\phi}_0)^{-1}]^*(\cdot)$ denotes the pullback from the current configuration to the original one by means of the regular motion $\boldsymbol{\phi}_t \circ (\boldsymbol{\phi}_0)^{-1}$. The strain $\bar{\mathbf{E}}_b \in \bar{\mathcal{E}} := \{ \bar{\mathbf{E}}_b \in T_{\mathbf{x}(0)}^* \mathcal{X}_0 \times T_{\mathbf{x}(0)}^* \mathcal{X}_0 | \text{skew}(\bar{\mathbf{E}}_b) = \mathbf{0}, \int_{\mathcal{B}_0} \langle \bar{\mathbf{E}}_b, \mathbf{S}^\sharp \rangle d\mathcal{B} = 0 \}$ is an enhancement and $\delta \bar{\mathbf{E}}_b \in T_{\bar{\mathbf{E}}_b(t)} \bar{\mathcal{E}}_t$ represents an admissible variation, assuming that the strain space possesses a manifold structure. From the linear combination of both parts, i.e. $\bar{\mathbf{E}}_b + \bar{\mathbf{E}}_b$, results the Green-Lagrange strain tensor \mathbf{E}_b , which is energetically conjugated by an appropriate stress definition $\mathbf{S}^\sharp(t) \in \mathcal{S} := \{ \mathbf{S}^\sharp \in T_{\mathbf{x}(0)} \mathcal{X}_0 \times T_{\mathbf{x}(0)} \mathcal{X}_0 | \mathbf{S}^\sharp = \partial_{\mathbf{E}_b} \Psi(\mathbf{E}_b) \}$, the second Piola-Kirchhoff stress tensor, and $\Psi(\mathbf{E}_b)$ is the material law. The symbol $\flat(\sharp)$ indicates that a second-rank tensor is doubly covariant (contravariant).

2.2. Shell kinematics and spatial discretization

The position at time t of any given point belonging to the shell can be written as

$$\mathbf{x}(\boldsymbol{\theta}; t) = \bar{\mathbf{x}}(\boldsymbol{\theta}^1, \boldsymbol{\theta}^2; t) + \boldsymbol{\theta}^3 \frac{\partial}{2} \mathbf{d}(\boldsymbol{\theta}^1, \boldsymbol{\theta}^2; t), \quad (2)$$

in which $\bar{\mathbf{x}} \in \mathbb{R}^3$ is the position vector of the middle surface, ∂ represents the thickness of the shell and \mathbf{d} is an extensible director, which admits multiplicative decomposition, i.e. $\mathbf{d} = d \hat{\mathbf{d}}$ with $d \in \mathbb{R}^+$ and $\hat{\mathbf{d}} \in S^2$. $\boldsymbol{\theta} = (\boldsymbol{\theta}^1, \boldsymbol{\theta}^2, \boldsymbol{\theta}^3)$ is a set of parameters chosen in the way that $\bar{\boldsymbol{\theta}} = (\boldsymbol{\theta}^1, \boldsymbol{\theta}^2, 0)$ describes the middle surface and $\mathbf{x} = \mathbf{x}(\boldsymbol{\theta}; t)$ is the given parameterization rule in time and space, see Fig. 1. For instance, we can choose $\boldsymbol{\theta}$ to span the domain \square such as

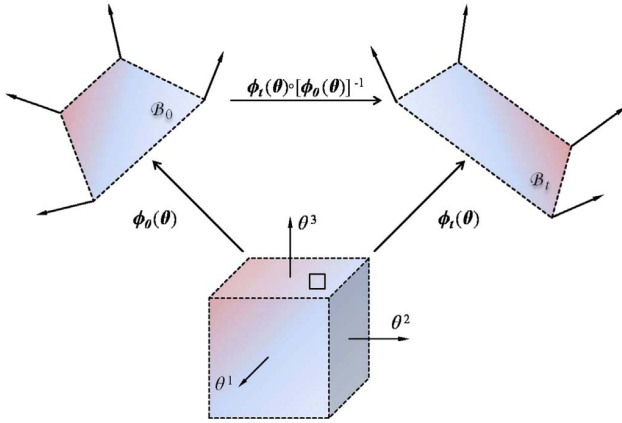


Fig. 1. The extensible-director-based solid-degenerated shell concept.

$\square := \{[-1, 1] \times [-1, 1] \times [-1, 1]\}$. The spatial metric structure induced by this construction is

$$G = \delta_{ij} \frac{\partial x^i}{\partial \theta^a} \frac{\partial x^j}{\partial \theta^b} g^a \otimes g^b, \quad (3)$$

where δ_{ij} are the components of the Euclidean metric tensor, $g_a \in T_\theta \mathcal{X}$ defined as $g_a = \frac{\partial x^i}{\partial \theta^a} \hat{i}_i$ with \hat{i}_i for i from 1 to 3 standing for the elements of the standard orthonormal basis in \mathbb{E}^3 , i.e. \mathbb{R}^3 with the standard Euclidean structure, are the elements of the covariant basis and $g^a \in T_\theta^* \mathcal{X}$ defined in the usual form $\langle g^b, g_a \rangle = \delta_b^a$ are the elements of the contravariant basis. δ_{ij} and δ_b^a are simply Kronecker deltas. At this point, it is certain that $G: T_\theta \mathcal{X} \times T_\theta \mathcal{X} \rightarrow \mathbb{R}^+$. Then the displacement-based part of the Green-Lagrange strain tensor is simply

$$\bar{E}_b(\theta; t) = \frac{1}{2} \{G[x(\theta; t)] - G[x(\theta; 0)]\}, \quad (4)$$

which is expressed directly in terms of θ and t . Analogously, the velocity at time t can be written as

$$v(\theta; t) = \bar{v}(\theta^1, \theta^2; t) + \theta^3 \frac{\partial}{\partial t} w(\theta^1, \theta^2; t), \quad (5)$$

in which $\bar{v} \in \mathbb{R}^3$ is the translational velocity of the middle surface and $w \in \mathbb{R}^3$ is the director velocity.

By following the adopted setting, the argument of the temporal integration of Eq. (1) yields

$$\int_{\square} \{\delta v \cdot [I(v) - I(x)] + \delta x \cdot [f^{\text{int}}(x, S) + \dot{l}(v) - f^{\text{ext}}(x) + H(x)^T \lambda] + \delta \bar{E} \cdot S + \delta \lambda \cdot h(x)\} \sqrt{\det[G(\theta; 0)]} d^3\theta = 0, \quad (6)$$

where \cdot is the interior product of first order Cartesian-like tensors, S and \bar{E} are the Voigt forms of $S^\#$ and \bar{E}_b , respectively, and $\sqrt{\det[G(\theta; 0)]} d^3\theta$ is the volume element at time $t=0$. Without losing generality, the dependencies on θ and t are indicated only when the specification of given time-space locations is necessary.

For an initial mass density ρ_0 and the already implicitly introduced Cartesian framework, the velocity-based and displacement-based linear momentum densities and the internal force density are respectively defined as

$$I(v) = \rho_0 v, \quad I(x) = \rho_0 \dot{x} \quad \text{and} \quad f^{\text{int}}(x, S) = \bar{B}^T(x) S, \quad (7)$$

in which $\bar{B}(x)$ is the matrix representation of the operator

$$\bar{B}(x)(\cdot) = \begin{bmatrix} \delta_{ij} \frac{\partial x^i}{\partial \theta^1} \left[\frac{\partial}{\partial \theta^1}(\cdot) \right]^j \\ \delta_{ij} \frac{\partial x^i}{\partial \theta^2} \left[\frac{\partial}{\partial \theta^2}(\cdot) \right]^j \\ \delta_{ij} \frac{\partial x^i}{\partial \theta^3} \left[\frac{\partial}{\partial \theta^3}(\cdot) \right]^j \\ \delta_{ij} \frac{\partial x^i}{\partial \theta^2} \left[\frac{\partial}{\partial \theta^3}(\cdot) \right]^j + \delta_{ij} \frac{\partial x^i}{\partial \theta^3} \left[\frac{\partial}{\partial \theta^2}(\cdot) \right]^j \\ \delta_{ij} \frac{\partial x^i}{\partial \theta^1} \left[\frac{\partial}{\partial \theta^3}(\cdot) \right]^j + \delta_{ij} \frac{\partial x^i}{\partial \theta^3} \left[\frac{\partial}{\partial \theta^1}(\cdot) \right]^j \\ \delta_{ij} \frac{\partial x^i}{\partial \theta^1} \left[\frac{\partial}{\partial \theta^2}(\cdot) \right]^j + \delta_{ij} \frac{\partial x^i}{\partial \theta^2} \left[\frac{\partial}{\partial \theta^1}(\cdot) \right]^j \end{bmatrix}. \quad (8)$$

Now let us assume a four-node element, in which the displacement and velocity fields as well as their admissible variations are discretized by means of the usual approach, i.e.:

$$x(\theta; t) \approx N^A(\bar{\theta}) \left[\bar{x}_A(t) + \theta^3 \frac{\partial}{\partial t} d_A(t) \right] = N(\theta) \hat{x}(t), \quad (9)$$

$$v(\theta; t) \approx N^A(\bar{\theta}) \left[\bar{v}_A(t) + \theta^3 \frac{\partial}{\partial t} w_A(t) \right] = N(\theta) \hat{v}(t), \quad (10)$$

$$\delta x(\theta) \approx N^A(\bar{\theta}) \left[\delta \bar{x}_A + \theta^3 \frac{\partial}{\partial t} \delta d_A \right] = N(\theta) \delta \hat{x}, \quad (11)$$

$$\delta v(\theta) \approx N^A(\bar{\theta}) \left[\delta \bar{v}_A + \theta^3 \frac{\partial}{\partial t} \delta w_A \right] = N(\theta) \delta \hat{v} \quad (12)$$

with A running from 1 to 4. The functions $N^A(\bar{\theta})$ are the following Lagrange-type shape functions:

$$N^1(\bar{\theta}) = \frac{1}{2}(1 + \theta^1)(1 + \theta^2), \quad (13)$$

$$N^2(\bar{\theta}) = \frac{1}{2}(1 - \theta^1)(1 + \theta^2), \quad (14)$$

$$N^3(\bar{\theta}) = \frac{1}{2}(1 - \theta^1)(1 - \theta^2), \quad (15)$$

$$N^4(\bar{\theta}) = \frac{1}{2}(1 + \theta^1)(1 - \theta^2). \quad (16)$$

Although higher order approximations are still possible, we chose the bilinear approach in concordance with the ‘‘Effective Finite Elements’’ philosophy proposed by Bucalem and Bathe [32]. The matrix $N(\theta)$ is the interpolation matrix, whose rows are dual vectors constructed as

$$N^i(\theta) = \left[N^1(\bar{\theta}) \hat{i}^i, \theta^3 \frac{\partial}{\partial t} N^1(\bar{\theta}) \hat{i}^i, N^2(\bar{\theta}) \hat{i}^i, \theta^3 \frac{\partial}{\partial t} N^2(\bar{\theta}) \hat{i}^i, N^3(\bar{\theta}) \hat{i}^i, \theta^3 \frac{\partial}{\partial t} N^3(\bar{\theta}) \hat{i}^i, N^4(\bar{\theta}) \hat{i}^i, \theta^3 \frac{\partial}{\partial t} N^4(\bar{\theta}) \hat{i}^i \right], \quad (17)$$

in which \hat{i}^i for i from 1 to 3 stands for the elements of the dual basis of \mathbb{E}^3 , which is the space of row vectors. The nodal variables and their admissible variations are then stored as:

$$\hat{x}^T(t) := \{\bar{x}_1^T(t), d_1^T(t), \bar{x}_2^T(t), d_2^T(t), \bar{x}_3^T(t), d_3^T(t), \bar{x}_4^T(t), d_4^T(t)\}, \quad (18)$$

$$\hat{v}^T(t) := \{\bar{v}_1^T(t), w_1^T(t), \bar{v}_2^T(t), w_2^T(t), \bar{v}_3^T(t), w_3^T(t), \bar{v}_4^T(t), w_4^T(t)\}, \quad (19)$$

$$\delta \hat{x}^T := \{\delta \bar{x}_1^T, \delta d_1^T, \delta \bar{x}_2^T, \delta d_2^T, \delta \bar{x}_3^T, \delta d_3^T, \delta \bar{x}_4^T, \delta d_4^T\}, \quad (20)$$

$$\delta \hat{v}^T := \{\delta \bar{v}_1^T, \delta w_1^T, \delta \bar{v}_2^T, \delta w_2^T, \delta \bar{v}_3^T, \delta w_3^T, \delta \bar{v}_4^T, \delta w_4^T\}. \quad (21)$$

It means that $\hat{x}(t) \in \hat{\mathcal{X}}_t \subseteq \mathbb{R}^{24}$, $\hat{v}(t) \in \hat{\mathcal{V}}_t \subseteq \mathbb{R}^{24}$, $\delta \hat{x} \in T_{\hat{x}(t)} \hat{\mathcal{X}}_t$ and $\delta \hat{v} \in T_{\hat{v}(t)} \hat{\mathcal{V}}_t$. To follow the next calculations, we think it to be

convenient to introduce equivalent expressions for the displacement field, namely

$$\mathbf{x}(\boldsymbol{\theta}; t) \approx \mathbf{N}(\boldsymbol{\theta})\hat{\mathbf{x}}(t) = \langle \mathbf{N}^i(\boldsymbol{\theta}), \hat{\mathbf{x}}(t) \rangle \hat{\mathbf{i}}_i = N_A^i(\boldsymbol{\theta})\hat{\mathbf{x}}^A(t)\hat{\mathbf{i}}_i. \quad (22)$$

For the adopted discretization, the approximation for the metric tensor at a time t can be computed as

$$G_{ab}[\mathbf{x}(\boldsymbol{\theta}; t)] \approx G_{ab}[\boldsymbol{\theta}, \hat{\mathbf{x}}(t)] = \delta_{ij} \frac{\partial N_A^i(\boldsymbol{\theta})}{\partial \theta^a} \frac{\partial N_B^j(\boldsymbol{\theta})}{\partial \theta^b} \hat{\mathbf{x}}^A(t)\hat{\mathbf{x}}^B(t), \quad (23)$$

which implies that the displacement-based part of the Green-Lagrange strain tensor is approximated as

$$\begin{aligned} \bar{E}_{ab}[\mathbf{x}(\boldsymbol{\theta}; t)] &\approx \bar{E}_{ab}[\boldsymbol{\theta}, \hat{\mathbf{x}}(t), \hat{\mathbf{x}}(0)] = \frac{\delta_{ij}}{2} \frac{\partial N_A^i(\boldsymbol{\theta})}{\partial \theta^a} \frac{\partial N_B^j(\boldsymbol{\theta})}{\partial \theta^b} \\ &[\hat{\mathbf{x}}^A(t)\hat{\mathbf{x}}^B(t) - \hat{\mathbf{x}}^A(0)\hat{\mathbf{x}}^B(0)]. \end{aligned} \quad (24)$$

Having already introduced the spatial approximation, the discrete version of $\bar{\mathbf{B}}[(\hat{\mathbf{x}})](\cdot)$ given by Eq. (8) becomes

$$\bar{\mathbf{B}}_d[(\hat{\mathbf{x}})](\cdot) = \begin{bmatrix} \delta_{ij} \frac{\partial N_A^i}{\partial \theta^1} \hat{\mathbf{x}}^A \frac{\partial N^j}{\partial \theta^1}(\cdot) \\ \delta_{ij} \frac{\partial N_A^i}{\partial \theta^2} \hat{\mathbf{x}}^A \frac{\partial N^j}{\partial \theta^2}(\cdot) \\ \delta_{ij} \frac{\partial N_A^i}{\partial \theta^3} \hat{\mathbf{x}}^A \frac{\partial N^j}{\partial \theta^3}(\cdot) \\ \delta_{ij} \frac{\partial N_A^i}{\partial \theta^2} \hat{\mathbf{x}}^A \frac{\partial N^j}{\partial \theta^3}(\cdot) + \delta_{ij} \frac{\partial N_A^i}{\partial \theta^3} \hat{\mathbf{x}}^A \frac{\partial N^j}{\partial \theta^2}(\cdot) \\ \delta_{ij} \frac{\partial N_A^i}{\partial \theta^1} \hat{\mathbf{x}}^A \frac{\partial N^j}{\partial \theta^3}(\cdot) + \delta_{ij} \frac{\partial N_A^i}{\partial \theta^3} \hat{\mathbf{x}}^A \frac{\partial N^j}{\partial \theta^1}(\cdot) \\ \delta_{ij} \frac{\partial N_A^i}{\partial \theta^1} \hat{\mathbf{x}}^A \frac{\partial N^j}{\partial \theta^2}(\cdot) + \delta_{ij} \frac{\partial N_A^i}{\partial \theta^2} \hat{\mathbf{x}}^A \frac{\partial N^j}{\partial \theta^1}(\cdot) \end{bmatrix}. \quad (25)$$

Note that quadratic terms in θ^3 are retained. However, the validity of the current formulation for moderately thick-walled structures would require special attention, which is beyond the scope of this work.

It is well-known that purely displacement-based formulations suffer from some pathologies, e.g. shear locking, artificial thickness strains and membrane locking. These deficiencies are caused by the adopted simplified kinematics and the chosen discretization that lead to a poor representation of the involved quantities that are necessary to set properly the finite-dimensional version of the equilibrium. To cure the shear locking and the artificial thickness strains, we use the assumed natural strain method. To complete the strain field in the thickness direction and to cure the membrane locking, we use the enhanced assumed strain method.

The assumed natural strain method allows to cure some locking issues without introducing additional degrees of freedom and is very easy to implement, since it involves only redefinition of some terms based on those originally computed from the displacement-based ones. Here, we use the assumed natural strain formulation developed by Dvorkin and Bathe [1] to remove the shear-locking issue. To remove the artificial thickness strain issue, we use the assumed natural strain formulation developed by Betsch and Stein [10] and similarly introduced by Bischoff and Ramm [12], which should be typically combined with an enhancement that is described next. For this aim, let us assume some tying points laying in the middle surface of the shell, which are summarized in Table 1.

The tying points $\bar{\boldsymbol{\theta}}_A, \bar{\boldsymbol{\theta}}_B, \bar{\boldsymbol{\theta}}_C$ and $\bar{\boldsymbol{\theta}}_D$ are employed to cure the shear locking. We redefine $\bar{E}_{23}(\bar{\boldsymbol{\theta}})$ and $\bar{E}_{13}(\bar{\boldsymbol{\theta}})$ as

$$\bar{E}_{23}(\bar{\boldsymbol{\theta}}) = \frac{1}{2}(1 - \theta^1)\bar{E}_{23}(\boldsymbol{\theta}_B) + \frac{1}{2}(1 + \theta^1)\bar{E}_{23}(\boldsymbol{\theta}_D) \quad (26)$$

Table 1
Tying points for the assumed natural strain method.

	A	B	C	D	1	2	3	4
θ^1	0	-1	0	1	1	-1	-1	1
θ^2	1	0	-1	0	1	1	-1	-1

and

$$\bar{E}_{13}(\bar{\boldsymbol{\theta}}) = \frac{1}{2}(1 - \theta^2)\bar{E}_{13}(\boldsymbol{\theta}_C) + \frac{1}{2}(1 + \theta^2)\bar{E}_{13}(\boldsymbol{\theta}_A). \quad (27)$$

The tying points $\bar{\boldsymbol{\theta}}_1, \bar{\boldsymbol{\theta}}_2, \bar{\boldsymbol{\theta}}_3$ and $\bar{\boldsymbol{\theta}}_4$ are employed to cure the artificial thickness strain. We redefine $\bar{E}_{33}(\bar{\boldsymbol{\theta}})$ as

$$\bar{E}_{33}(\bar{\boldsymbol{\theta}}) = N^1(\bar{\boldsymbol{\theta}})\bar{E}_{33}(\boldsymbol{\theta}_1) + N^2(\bar{\boldsymbol{\theta}})\bar{E}_{33}(\boldsymbol{\theta}_2) + N^3(\bar{\boldsymbol{\theta}})\bar{E}_{33}(\boldsymbol{\theta}_3) + N^4(\bar{\boldsymbol{\theta}})\bar{E}_{33}(\boldsymbol{\theta}_4). \quad (28)$$

Immediately, the original strain components, $\bar{E}_{23}(\bar{\boldsymbol{\theta}}), \bar{E}_{13}(\bar{\boldsymbol{\theta}})$ and $\bar{E}_{33}(\bar{\boldsymbol{\theta}})$, are replaced by the new redefinitions, $\bar{E}_{23}(\bar{\boldsymbol{\theta}}), \bar{E}_{13}(\bar{\boldsymbol{\theta}})$ and $\bar{E}_{33}(\bar{\boldsymbol{\theta}})$, respectively.

The enhanced assumed strain method allows to improve the strain field and to cure some locking issues as well, but this time, the introduction of additional elemental degrees of freedom is necessary. The method proposed by Simo and Rifai [5] enables the definition of enhanced strains, which are spanned by outer products of the elements of the dual basis at the center of the element, which is at $\boldsymbol{\theta} = \boldsymbol{\theta}$. Then the enhanced strain fields are computed everywhere by

$$\begin{aligned} \tilde{E}_{ab}(\boldsymbol{\theta}; t)\mathbf{g}^a(\boldsymbol{\theta}; 0) \otimes \mathbf{g}^b(\boldsymbol{\theta}; 0) &= \sqrt{\frac{\det[\mathbf{G}(\boldsymbol{\theta}; 0)]}{\det[\mathbf{G}(\boldsymbol{\theta}; 0)]}} \tilde{E}_{ab}[\boldsymbol{\theta}; \tilde{\boldsymbol{\epsilon}}(t)]\mathbf{g}^a(\boldsymbol{\theta}; 0) \\ &\otimes \mathbf{g}^b(\boldsymbol{\theta}; 0), \end{aligned} \quad (29)$$

in which \tilde{E}_{ab} are the enhancements and where “by design” $\tilde{E}_{ab}(\boldsymbol{\theta}, 0)$ is set equal to zero. For the membrane strain state, it is possible to identify that due to the assumed approximations some terms proportional to θ^1 and to θ^2 are missing at the strain components $\bar{E}_{11}, \bar{E}_{22}$ and \bar{E}_{12} . This lack can be addressed by adopting:

$$\tilde{E}_{11}[\boldsymbol{\theta}; \tilde{\boldsymbol{\epsilon}}(t)] \approx \theta^1 \frac{\partial \tilde{E}_{11}}{\partial \theta^1}(\boldsymbol{\theta}; t) = \theta^1 \tilde{\epsilon}_{111}(t), \quad (30)$$

$$\tilde{E}_{22}[\boldsymbol{\theta}; \tilde{\boldsymbol{\epsilon}}(t)] \approx \theta^2 \frac{\partial \tilde{E}_{22}}{\partial \theta^2}(\boldsymbol{\theta}; t) = \theta^2 \tilde{\epsilon}_{222}(t), \quad (31)$$

$$\tilde{E}_{12}[\boldsymbol{\theta}; \tilde{\boldsymbol{\epsilon}}(t)] \approx \theta^1 \frac{\partial \tilde{E}_{12}}{\partial \theta^1}(\boldsymbol{\theta}; t) + \theta^2 \frac{\partial \tilde{E}_{12}}{\partial \theta^2}(\boldsymbol{\theta}; t) = \frac{1}{2}\theta^1 \tilde{\epsilon}_{121}(t) + \frac{1}{2}\theta^2 \tilde{\epsilon}_{122}(t). \quad (32)$$

The main motivation for improving the strain component \bar{E}_{33} is to give the element the capability of handling unmodified three-dimensional material laws. This is achieved by considering some terms proportional to $\theta^3, \theta^1\theta^3, \theta^2\theta^3$ and $\theta^1\theta^2\theta^3$ that can be addressed by adopting the following enhancement:

$$\begin{aligned} \tilde{E}_{33}[\boldsymbol{\theta}; \tilde{\boldsymbol{\epsilon}}(t)] &\approx \theta^3 \frac{\partial \tilde{E}_{33}}{\partial \theta^3}(\boldsymbol{\theta}; t) + \theta^1\theta^3 \frac{\partial^2 \tilde{E}_{33}}{\partial \theta^1 \partial \theta^3}(\boldsymbol{\theta}; t) + \theta^2\theta^3 \frac{\partial^2 \tilde{E}_{33}}{\partial \theta^2 \partial \theta^3}(\boldsymbol{\theta}; t) \\ &+ \theta^1\theta^2\theta^3 \frac{\partial^3 \tilde{E}_{33}}{\partial \theta^1 \partial \theta^2 \partial \theta^3}(\boldsymbol{\theta}; t) \end{aligned} \quad (33)$$

$$= \theta^3 \tilde{\epsilon}_{333}(t) + \theta^1\theta^3 \tilde{\epsilon}_{3313}(t) + \theta^2\theta^3 \tilde{\epsilon}_{3323}(t) + \theta^1\theta^2\theta^3 \tilde{\epsilon}_{33123}(t), \quad (34)$$

which is based on the ideas proposed by Büchter et al. [4]. This can be supported by considering high-order shell kinematics with infinite directors and by truncating higher order terms of the infinite expansion, see [10]. Finally, the array of elemental degrees of freedom is given by

$$\tilde{\boldsymbol{\epsilon}} = (\tilde{\epsilon}_{111}, \tilde{\epsilon}_{222}, \tilde{\epsilon}_{121}, \tilde{\epsilon}_{122}, \tilde{\epsilon}_{333}, \tilde{\epsilon}_{3313}, \tilde{\epsilon}_{3323}, \tilde{\epsilon}_{33123}). \quad (35)$$

Notice that the condition $\int_{\mathcal{B}_0} (\bar{\mathbf{E}}_v, \mathbf{S}^\#) d\mathcal{B} = 0$ was implicitly replaced by

$$\left\langle \int_{\mathcal{B}_0} \bar{\mathbf{E}}_v d\mathcal{B}, \mathbf{S}_{\text{const}}^\# \right\rangle = 0, \text{ which is a more restrictive condition and in}$$

which $\mathbf{S}_{\text{const}}^\#$ represents a constant nominal stress state. This constant nominal stress state condition is closely related to the satisfaction of the patch test in its nonlinear form, see Simo and Armero [11]. By design, the adopted enhancements fulfill the constant nominal stress state condition.

Now it is possible to define the discrete operator related to the enhanced strain as the multiplicative composition of a “left” operator and a “right” operator:

$$\tilde{\mathbf{B}}_d[(\theta; 0)](\cdot) = \{\tilde{\mathbf{B}}_l[(\theta; 0)] \circ \tilde{\mathbf{B}}_r[(\theta; 0)]\}(\cdot), \quad (36)$$

where $\tilde{\mathbf{B}}_l$ is merely a transformation rule for the enhanced strains in its Voigt form. The matrix representation of the “left” operator is

$$\tilde{\mathbf{B}}_l(\theta; 0) = \sqrt{\frac{\det[\mathbf{G}(\theta; 0)]}{\det[\mathbf{G}(\theta; 0)]}} \begin{bmatrix} \tilde{G}_1^1 \tilde{G}_1^1 & \tilde{G}_1^2 \tilde{G}_1^2 & \tilde{G}_1^3 \tilde{G}_1^3 & \tilde{G}_1^2 \tilde{G}_1^3 & \tilde{G}_1^1 \tilde{G}_1^3 & \tilde{G}_1^1 \tilde{G}_1^2 \\ \tilde{G}_2^1 \tilde{G}_2^1 & \tilde{G}_2^2 \tilde{G}_2^2 & \tilde{G}_2^3 \tilde{G}_2^3 & \tilde{G}_2^2 \tilde{G}_2^3 & \tilde{G}_2^1 \tilde{G}_2^3 & \tilde{G}_2^1 \tilde{G}_2^2 \\ \tilde{G}_3^1 \tilde{G}_3^1 & \tilde{G}_3^2 \tilde{G}_3^2 & \tilde{G}_3^3 \tilde{G}_3^3 & \tilde{G}_3^2 \tilde{G}_3^3 & \tilde{G}_3^1 \tilde{G}_3^3 & \tilde{G}_3^1 \tilde{G}_3^2 \\ 2\tilde{G}_2^1 \tilde{G}_3^1 & 2\tilde{G}_2^2 \tilde{G}_3^2 & 2\tilde{G}_2^3 \tilde{G}_3^3 & \tilde{G}_2^2 \tilde{G}_3^3 + \tilde{G}_2^3 \tilde{G}_3^2 & \tilde{G}_2^1 \tilde{G}_3^3 + \tilde{G}_2^3 \tilde{G}_3^1 & \tilde{G}_2^1 \tilde{G}_3^2 + \tilde{G}_2^2 \tilde{G}_3^1 \\ 2\tilde{G}_1^1 \tilde{G}_3^1 & 2\tilde{G}_1^2 \tilde{G}_3^2 & 2\tilde{G}_1^3 \tilde{G}_3^3 & \tilde{G}_1^2 \tilde{G}_3^3 + \tilde{G}_1^3 \tilde{G}_3^2 & \tilde{G}_1^1 \tilde{G}_3^3 + \tilde{G}_1^3 \tilde{G}_3^1 & \tilde{G}_1^1 \tilde{G}_3^2 + \tilde{G}_1^2 \tilde{G}_3^1 \\ 2\tilde{G}_1^1 \tilde{G}_2^1 & 2\tilde{G}_1^2 \tilde{G}_2^2 & 2\tilde{G}_1^3 \tilde{G}_2^3 & \tilde{G}_1^2 \tilde{G}_2^3 + \tilde{G}_1^3 \tilde{G}_2^2 & \tilde{G}_1^1 \tilde{G}_2^3 + \tilde{G}_1^3 \tilde{G}_2^1 & \tilde{G}_1^1 \tilde{G}_2^2 + \tilde{G}_1^2 \tilde{G}_2^1 \end{bmatrix}, \quad (37)$$

in which the coefficients \tilde{G}_b^a are computed as

$$\tilde{G}_b^a(\theta; 0) = \langle \mathbf{g}^b(\theta; 0), \mathbf{g}_a(\theta; 0) \rangle. \quad (38)$$

The matrix representation of the “right” operator is

$$\tilde{\mathbf{B}}_r(\theta) = \begin{bmatrix} \theta^1 & 0 & 0 & 0 & 0 & 0 & 0 & 0 \\ 0 & \theta^2 & 0 & 0 & 0 & 0 & 0 & 0 \\ 0 & 0 & 0 & 0 & \theta^3 & \theta^1 \theta^3 & \theta^2 \theta^3 & \theta^1 \theta^3 \theta^3 \\ 0 & 0 & 0 & 0 & 0 & 0 & 0 & 0 \\ 0 & 0 & 0 & 0 & 0 & 0 & 0 & 0 \\ 0 & 0 & \theta^1 & \theta^2 & 0 & 0 & 0 & 0 \end{bmatrix}, \quad (39)$$

which allows the computation of $\tilde{\mathbf{E}}$ as $\tilde{\mathbf{E}}[\theta; \tilde{\mathbf{e}}(t)] = \{\tilde{\mathbf{B}}_l(\theta)\}[\tilde{\mathbf{e}}(t)]$ that renders a separation of variables. This construction allows to systematically include further enhancements, if necessary, just by adding more columns to the matrix representation of $\tilde{\mathbf{B}}_r$, since no separate treatment of the enhancements was made in the sense of Eq. (29). Of course, particular considerations are necessary to justify the necessity of including specific non-trivial columns into $\tilde{\mathbf{B}}_r$, but this discussion is beyond the scope of the current work. In contrast with the type of approach employed by Reinoso and Blázquez [30], where the definition of three matrices is necessary to define the enhancements, the current approach requires just one single matrix.

2.3. Temporal discretization and robust integration scheme

The preservation of mechanical invariants like the linear momentum, the angular momentum, the total energy or even the symplectic form is very important to produce acceptable numerical results, which at least do not violate the underlying physical essence. The construction of numerical schemes showing the conservation of one or several of these properties consists in finding discrete versions of the continuous terms, which after their corresponding evaluation at the time-quadrature points and in combination with appropriate admissible variations of the position and velocity vectors yield to the desired preservation rules. These preservation rules are typically materialized in terms of the continuous invariant quantities evaluated only at the boundaries of the time interval. For nonlinear systems, this is not directly achieved just by evaluating the continuous terms at the temporal collocation points, because the consistency and directionality of the discrete partial derivatives are not *per se* satisfied. Therefore, the discrete setting ought to parallel the continuous framework. Moreover, not all mechanical invariants can be discretely preserved for a fixed time step h . The preservation of the linear momentum, the angular momentum in combination with the preservation of the total energy and the symplectic form is only achieved by adaptation of the time step, whose size is obtained by solving a minimization problem subjected to inequality constraints, see [33].

In this work, we chose the family of integration schemes that is obtained by direct discretization of the equations of motion, which are derived from the continuous variational principle. Thus, the properties to be preserved are the linear momentum, the angular momentum and the total energy without the necessity of imposing additional algebraic constraints, see [7]. This choice is an alternative to variational integration schemes that preserve typically the linear momentum, the angular momentum and the symplectic form of the underlying Hamiltonian system. In contrast with our choice, this second family of integration schemes is obtained by direct discretization of the action integral followed by the discrete minimization of the discrete action. The variational integration in its standard form is less robust for highly stiff problems that typically arise in the context of beams and shells, being for the last case extremely critical. Therefore, this is not an effective alternative for the present work.

Next, we summarize the three conditions that must be fulfilled to achieve the desired preservation properties. For this purpose, we require to introduce an arbitrary non-trivial vector $\xi \in \mathbb{R}^3$, which does not have temporal or spatial dependency.

First, to ensure the preservation of the linear momentum l , for the load-free case, the discrete version of the time rate of the linear momentum $\dot{l}_d(v_n, v_{n+1})$ must, for a virtual displacement of the form $\delta x_{n+\frac{1}{2}} = \xi$, satisfy

$$\delta x_{n+\frac{1}{2}} \cdot \dot{l}_d(v_n, v_{n+1}) = \xi \cdot \dot{l}_d(v_n, v_{n+1}) = \frac{\xi}{h} \cdot [l(v_{n+1}) - l(v_n)], \quad (40)$$

and at the same time, the discrete version of the stress S_d ought to warrant the vanishment of the virtual work done by the internal loads, *i.e.*

$$\delta x_{n+\frac{1}{2}} \cdot [f_d^{\text{int}}(x_n, x_{n+1}, S_d)] = \xi \cdot \left[\bar{\mathbf{B}}^T(x_{n+\frac{1}{2}}) S_d \right] = 0. \quad (41)$$

Once these two requirements are fulfilled, the linear momentum is exactly preserved, *ergo*

$$l(v_{n+1}) = l(v_n). \quad (42)$$

Second, to ensure the preservation of the angular momentum j , for the load-free case, the discrete version of the time rate of the linear momentum $\dot{j}_d(v_n, v_{n+1})$ must, for a virtual displacement of the form $\delta x_{n+\frac{1}{2}} = \xi \times x_{n+\frac{1}{2}}$, satisfy

$$\delta x_{n+\frac{1}{2}} \cdot \dot{j}_d(v_n, v_{n+1}) = \left(\xi \times x_{n+\frac{1}{2}} \right) \cdot \dot{j}_d(v_n, v_{n+1}) = \frac{\xi}{h} \cdot [j(x_{n+1}, v_{n+1}) - j(x_n, v_n)], \quad (43)$$

and at the same time, the discrete version of the stress S_d ought to warrant the vanishment of the virtual work done by the internal loads, *i.e.*

$$\delta x_{n+\frac{1}{2}} \cdot [f_d^{\text{int}}(x_n, x_{n+1}, S_d)] = \left(\xi \times x_{n+\frac{1}{2}} \right) \cdot \left[\bar{\mathbf{B}}^T(x_{n+\frac{1}{2}}) S_d \right] = 0. \quad (44)$$

Once that these two requirements are satisfied, the angular momentum is identically preserved, which is

$$j(x_{n+1}, v_{n+1}) = j(x_n, v_n). \quad (45)$$

Third, to ensure the preservation of total energy, H defined as $T + U$, for the load-free case, the discrete version of the time rate of the linear momentum $\dot{H}_d(v_n, v_{n+1})$ must, for a virtual displacement of the form $\delta x_{n+\frac{1}{2}} = \frac{1}{h}(x_{n+1} - x_n)$, satisfy

$$\delta x_{n+\frac{1}{2}} \cdot \dot{H}_d(v_n, v_{n+1}) = \frac{1}{h}(x_{n+1} - x_n) \cdot \dot{H}_d(v_n, v_{n+1}) = \frac{1}{h} [T(v_{n+1}) - T(v_n)], \quad (46)$$

which is the rate of kinetic energy, and at the same time, the discrete version of the stress S_d ought to warrant

$$\begin{aligned}\delta \mathbf{x}_{n+\frac{1}{2}} \cdot [\mathbf{f}_d^{\text{int}}(\mathbf{x}_n, \mathbf{x}_{n+1}, \mathbf{S}_d)] &= \frac{1}{h}(\mathbf{x}_{n+1} - \mathbf{x}_n) \cdot \left[\overline{\mathbf{B}}^T(\mathbf{x}_{n+\frac{1}{2}}) \mathbf{S}_d \right] \\ &= \frac{1}{h} [U(\mathbf{E}_{n+1}) - U(\mathbf{E}_n)],\end{aligned}\quad (47)$$

which is the rate of potential energy. Once these two requirements are fulfilled, the total energy is exactly preserved, *ergo*

$$H(\mathbf{v}_{n+1}, \mathbf{E}_{n+1}) = H(\mathbf{v}_n, \mathbf{E}_n). \quad (48)$$

The aforementioned conditions are satisfied, for example, by the following second-order definitions

$$\mathbf{l}_d(\mathbf{v}_n, \mathbf{v}_{n+1}) := \frac{Q_0}{2}(\mathbf{v}_{n+1} + \mathbf{v}_n), \quad (49)$$

$$\dot{\mathbf{l}}_d(\mathbf{v}_n, \mathbf{v}_{n+1}) := \frac{Q_0}{h}(\mathbf{v}_{n+1} - \mathbf{v}_n), \quad (50)$$

$$\mathbf{S}_d(\mathbf{E}_n, \mathbf{E}_{n+1}) := \frac{\mathfrak{C}}{2}(\mathbf{E}_{n+1} + \mathbf{E}_n), \quad (51)$$

in which the algorithmic stress $\mathbf{S}_d(\mathbf{E}_n, \mathbf{E}_{n+1})$ is valid only for Saint Venant-Kirchhoff elastic materials and \mathfrak{C} is the Voigt form of the elasticity tensor. In case of considering other material laws, the introduction of a new definition for the algorithmic stress is necessary, see [7], which can be circumvented by means of a discrete derivative in the sense of Gonzalez [34]. However, Romero [35] proved that there are infinite second-order approximations.

The preservation of linear momentum and the angular momentum in combination with the conservation of the total energy does not warrant the robustness of the integration scheme. It means that the presence of unresolved high frequencies could trigger the failure of the Newton-Raphson algorithm. One remedy to alleviate this problem is adding some artificial dissipation to the system. However, the dissipation proportional to discrete rate of strain *per se* is not able to damp the unresolved high-frequency content; therefore, the addition of some damping proportional to the discrete rate of velocity module is necessary. Following the ideas presented in [15,16,18,36], the velocity-based discrete linear momentum and the discrete stress are modified to achieve the desired dissipation properties preserving at the same time the objectivity of the formulation.

The velocity-based discrete linear momentum density can be redefined as the additive combination of a conservative part and a dissipative part, *i.e.*

$$\mathbf{l}_d(\mathbf{v}_n, \mathbf{E}_n, \mathbf{v}_{n+1}, \mathbf{E}_{n+1}) := \mathbf{l}_d^{\text{cons}}(\mathbf{v}_n, \mathbf{v}_{n+1}) + \mathbf{l}_d^{\text{diss}}(\mathbf{v}_n, \mathbf{E}_n, \mathbf{v}_{n+1}, \mathbf{E}_{n+1}) \quad (52)$$

where the conservative part is

$$\mathbf{l}_d^{\text{cons}}(\mathbf{v}_n, \mathbf{v}_{n+1}) = \frac{Q_0}{2}(\mathbf{v}_{n+1} + \mathbf{v}_n), \quad (53)$$

and the dissipative one must, for a virtual velocity of the form $\delta \mathbf{v}_{n+\frac{1}{2}} = \mathbf{v}_{n+1} - \mathbf{v}_n$, satisfy

$$\delta \mathbf{v}_{n+\frac{1}{2}} \cdot \mathbf{l}_d^{\text{diss}}(\mathbf{v}_n, \mathbf{E}_n, \mathbf{v}_{n+1}, \mathbf{E}_{n+1}) = (\mathbf{v}_{n+1} - \mathbf{v}_n) \cdot \mathbf{l}_d^{\text{diss}}(\mathbf{v}_n, \mathbf{E}_n, \mathbf{v}_{n+1}, \mathbf{E}_{n+1}) = \quad (54)$$

$$= \mathcal{D}_T(\|\mathbf{v}_n\|, \mathbf{E}_n, \|\mathbf{v}_{n+1}\|, \mathbf{E}_{n+1}) \geq 0, \quad (55)$$

in which the dissipation function, \mathcal{D}_T , allows cross definitions of some objective quantities. Therefore, the dependency on $\|\mathbf{v}_n\|$, \mathbf{E}_n , $\|\mathbf{v}_{n+1}\|$ and \mathbf{E}_{n+1} , is implicitly introduced. This condition implies

$$\mathbf{l}_d^{\text{diss}}(\mathbf{v}_n, \mathbf{E}_n, \mathbf{v}_{n+1}, \mathbf{E}_{n+1}) = 2 \frac{\mathcal{D}_T(\|\mathbf{v}_n\|, \mathbf{E}_n, \|\mathbf{v}_{n+1}\|, \mathbf{E}_{n+1})}{\|\mathbf{v}_{n+1}\|^2 - \|\mathbf{v}_n\|^2} \mathbf{v}_{n+\frac{1}{2}}. \quad (56)$$

The discrete stress can also be redefined as the additive combination of a conservative part and a dissipative part, *i.e.*

$$\mathbf{S}_d(\mathbf{v}_n, \mathbf{E}_n, \mathbf{v}_{n+1}, \mathbf{E}_{n+1}) := \mathbf{S}_d^{\text{cons}}(\mathbf{E}_n, \mathbf{E}_{n+1}) + \mathbf{S}_d^{\text{diss}}(\mathbf{v}_n, \mathbf{E}_n, \mathbf{v}_{n+1}, \mathbf{E}_{n+1}) \quad (57)$$

where the conservative part is

$$\mathbf{S}_d^{\text{cons}}(\mathbf{E}_n, \mathbf{E}_{n+1}) = \frac{\mathfrak{C}}{2}(\mathbf{E}_{n+1} + \mathbf{E}_n), \quad (58)$$

and the dissipative one must, for a virtual velocity of the form $\delta \mathbf{x}_{n+\frac{1}{2}} = \mathbf{x}_{n+1} - \mathbf{x}_n$, satisfy

$$\delta \mathbf{x}_{n+\frac{1}{2}} \cdot \left[\overline{\mathbf{B}}^T(\mathbf{x}_{n+\frac{1}{2}}) \mathbf{S}_d^{\text{diss}}(\mathbf{v}_n, \mathbf{E}_n, \mathbf{v}_{n+1}, \mathbf{E}_{n+1}) \right] = (\mathbf{E}_{n+1} - \mathbf{E}_n) \cdot \mathbf{S}_d^{\text{diss}}(\mathbf{v}_n, \mathbf{E}_n, \mathbf{v}_{n+1}, \mathbf{E}_{n+1}) \quad (59)$$

$$= \mathcal{D}_U(\|\mathbf{v}_n\|, \mathbf{E}_n, \|\mathbf{v}_{n+1}\|, \mathbf{E}_{n+1}) \geq 0, \quad (60)$$

in which the dissipation function, \mathcal{D}_U , allows cross definitions as well. This condition implies

$$\mathbf{S}_d^{\text{diss}}(\|\mathbf{v}_n\|, \mathbf{E}_n, \|\mathbf{v}_{n+1}\|, \mathbf{E}_{n+1}) = \frac{\mathcal{D}_U(\|\mathbf{v}_n\|, \mathbf{E}_n, \|\mathbf{v}_{n+1}\|, \mathbf{E}_{n+1})}{\|\mathbf{E}_{n+1} - \mathbf{E}_n\|_{\mathfrak{C}}^2} \mathfrak{C}(\mathbf{E}_{n+1} - \mathbf{E}_n). \quad (61)$$

After the consideration of $\mathbf{l}_d^{\text{diss}}(\mathbf{v}_n, \mathbf{E}_n, \mathbf{v}_{n+1}, \mathbf{E}_{n+1})$ and $\mathbf{S}_d^{\text{diss}}(\|\mathbf{v}_n\|, \mathbf{E}_n, \|\mathbf{v}_{n+1}\|, \mathbf{E}_{n+1})$, Eq. (48) becomes

$$H(\mathbf{v}_{n+1}, \mathbf{E}_{n+1}) + \mathcal{D}_V(\|\mathbf{v}_n\|, \mathbf{E}_n, \|\mathbf{v}_{n+1}\|, \mathbf{E}_{n+1}) = H(\mathbf{v}_n, \mathbf{E}_n), \quad (62)$$

for a positive semi-definite dissipation function density

$$\mathcal{D}_V = \mathcal{D}_T + \mathcal{D}_U \geq 0. \quad (63)$$

$\mathbf{l}_d^{\text{diss}}$ and $\mathbf{S}_d^{\text{diss}}$ must be as small as possible to avoid severe distortions in the physical behavior.

2.4. Kinematic constraints

The introduction of kinematic constraints represents an effective and less intrusive alternative to render, for example, structures with intersections and/or ply-drop-offs. The implementation of this technique requires the solution of differential-algebraic equations, which are originated through the combination of differential equations that describe the motion of the modeled flexible bodies in the three-dimensional space and algebraic equations that describe the enforced conditions. These restrictions can be either internal, which come on the scene in the case of parameterizing the configuration manifold of a system with a number of parameters larger than its intrinsic dimension, *e.g.* by using unit quaternions, $\mathbf{q} \in \mathbb{H}_1$, to describe actual rotations, $\mathbf{R} \in SO(3)$, or external ones, which come on the scene in the case of constraining bodies by means of joints, connections or supports. Inspired by the usual practices done in the field of multibody dynamics, we present and discuss briefly some important aspects of three kinematic constraints that are important for the structural analysis of very complex shell structures. The first one is the continuous connection, that could arise in the context of smoothly connected shells. The second one is the discontinuous connection, which could arise in the context of intersecting plates. The last one is the layer connection, which typically arises in the context of multi-layered composite structures.

The differential-algebraic framework requires concomitantly the introduction of Lagrange's multipliers. It means that beside the increased number of unknowns due to redundant nodes and their corresponding coordinates, it is necessary to take into account the additional unknowns represented by the multipliers. The additional cost due to the explicit computation of the constraint forces in joints, connections or supports can be saved. Some techniques to avoid the calculation of Lagrange's multipliers are available, *e.g.* by means of the definition of a new connection in the sense of transporting information along a curve over the configuration manifold, by partitioning the vector of coordinates and computing a reduced form of the governing equations, or by finding a suitable projection that eliminates the contribution coming from the constraint forces. These three approaches are briefly introduced and discussed in [37]. In this work, we chose the third one in a slightly different setting as proposed in [38,39,24]. The rows of the projection $\mathbf{P}: \mathbb{R}^n \rightarrow \mathbb{R}^{m-n}$ are then completely spanned by a

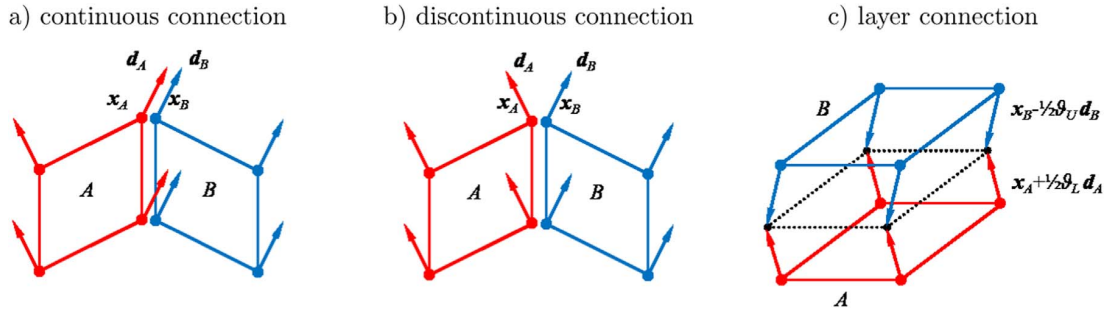


Fig. 2. Three kinematic constraints that can be used to carry out the analysis of shell structures.

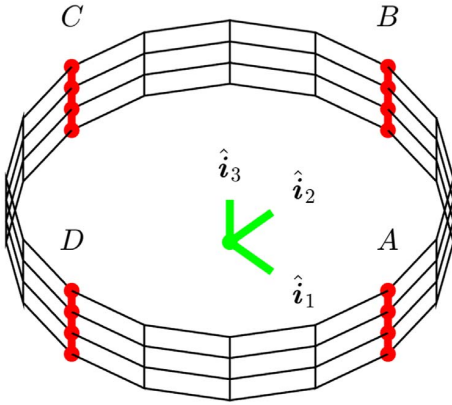


Fig. 3. Tumbling cylinder – finite element representation.

Table 2

Tumbling cylinder – spatial loads per length unit in N/m.

	A	B	C	D
f_1	0	1	1	0
f_2	-1	1	1	-1
f_3	-1	1	1	-1

given basis of the kernel of the constraint Jacobean matrix in its transposed form, where $\text{kernel}(H^T) = \{k \in \mathbb{R}^m | k \neq 0, H^T k = 0 \in \mathbb{R}^n\}$, and therefore $\text{rank}(P) = \text{nullity}(H^T)$. This construction warrants $PH^T = 0$. Once the solution is computed, Lagrange's multipliers are easily recovered by a discrete version of

$$\lambda = -(HH^T)^{-1} H [f^{\text{int}}(x, S) + \dot{l}(v) - f^{\text{ext}}(x)]. \quad (64)$$

The continuous connection allows the joining of two shells by introducing constraints at their interfacing edges, see Fig. 2a. Then the positions and extensible directors are set to be equal. This is $h_{CC} = 0 \in \mathbb{R}^6$, in which

$$h_{CC} := \begin{Bmatrix} \bar{x}_A(t) - \bar{x}_B(t) \\ \bar{d}_A(t) - \bar{d}_B(t) \end{Bmatrix}, \quad (65)$$

and A and B stand for the pair of interfacing nodes belonging to the surfaces A and B, respectively. Realize that no restriction over the magnitude of the extensible directors was introduced, meaning that the component $\bar{E}_{33} = \frac{1}{2}[\bar{d}(t) \cdot \bar{d}(t) - \bar{d}(0) \cdot \bar{d}(0)]$ of the displacement-based part of the Green-Lagrange strain tensor is able to change with the time. The corresponding Jacobean matrix takes the following form

$$H_{CC} = \begin{bmatrix} I_{3 \times 3} & \mathbf{0}_{3 \times 3} & -I_{3 \times 3} & \mathbf{0}_{3 \times 3} \\ \mathbf{0}_{3 \times 3} & I_{3 \times 3} & \mathbf{0}_{3 \times 3} & -I_{3 \times 3} \end{bmatrix}. \quad (66)$$

A visual inspection of H_{CC}^T permits to find a basis for its null space. Having found these vectors, the construction of the corresponding

projection operator is straightforward, whose final form is

$$P_{CC} = \begin{bmatrix} I_{3 \times 3} & \mathbf{0}_{3 \times 3} & I_{3 \times 3} & \mathbf{0}_{3 \times 3} \\ \mathbf{0}_{3 \times 3} & I_{3 \times 3} & \mathbf{0}_{3 \times 3} & I_{3 \times 3} \end{bmatrix}. \quad (67)$$

The three uppermost rows show that movements with an identical increment of translation at both nodes are present in the projection operator. The three lowermost rows show that movements with an identical increment of director motion are present as well. This means that neither relative translation nor relative director motion will occur and the directors will suffer an identical variation in their length direction.

The discontinuous connection allows to deal with folded shells by introducing constraints at the junction, see Fig. 2b. Then the positions are set to be equal, the directors are set to be inextensible and the projection between directors is set to be constant. This is $h_{DC} = 0 \in \mathbb{R}^6$, in which

$$h_{DC} = \begin{Bmatrix} \bar{x}_A(t) - \bar{x}_B(t) \\ \frac{1}{2}[\bar{d}_A(t) \cdot \bar{d}_A(t) - \bar{d}_A(0) \cdot \bar{d}_A(0)] \\ \frac{1}{2}[\bar{d}_B(t) \cdot \bar{d}_B(t) - \bar{d}_B(0) \cdot \bar{d}_B(0)] \\ \bar{d}_A(t) \cdot \bar{d}_B(t) - \bar{d}_A(0) \cdot \bar{d}_B(0) \end{Bmatrix}, \quad (68)$$

and A and B stand for the pair of intersecting nodes belonging to the surfaces A and B, respectively. Realize that now the directors are no longer extensible, meaning that the component $\bar{E}_{33} = \frac{1}{2}[\bar{d}(t) \cdot \bar{d}(t) - \bar{d}(0) \cdot \bar{d}(0)]$ of the displacement/director-based part of the Green-Lagrange strain tensor is identically zero at every time step, which is required to avoid discontinuities in the change of thickness along the intersection. An extensive discussion of this topic can be found in [40]. The corresponding Jacobean matrix takes the following form

$$H_{DC} = \begin{bmatrix} I_{3 \times 3} & \mathbf{0}_{3 \times 3} & -I_{3 \times 3} & \mathbf{0}_{3 \times 3} \\ \mathbf{0}_{1 \times 3} & \bar{d}_A^T(t) & \mathbf{0}_{1 \times 3} & \mathbf{0}_{1 \times 3} \\ \mathbf{0}_{1 \times 3} & \mathbf{0}_{1 \times 3} & \mathbf{0}_{1 \times 3} & \bar{d}_B^T(t) \\ \mathbf{0}_{1 \times 3} & \bar{d}_B^T(t) & \mathbf{0}_{1 \times 3} & \bar{d}_A^T(t) \end{bmatrix}. \quad (69)$$

A visual inspection of H_{DC}^T permits to find a basis for its null space. Having found these vectors, the construction of the corresponding projection operator is straightforward, whose final appearance is

$$P_{DC} = \begin{bmatrix} I_{3 \times 3} & \mathbf{0}_{3 \times 3} & I_{3 \times 3} & \mathbf{0}_{3 \times 3} \\ \mathbf{0}_{1 \times 3} & [\bar{d}_A(t) \times \bar{d}_B(t)]^T & \mathbf{0}_{1 \times 3} & \mathbf{0}_{1 \times 3} \\ \mathbf{0}_{1 \times 3} & \mathbf{0}_{1 \times 3} & \mathbf{0}_{1 \times 3} & [\bar{d}_A(t) \times \bar{d}_B(t)]^T \\ \mathbf{0}_{1 \times 3} & [\tilde{d}_A(t)]^T & \mathbf{0}_{1 \times 3} & [\tilde{d}_B(t)]^T \end{bmatrix}, \quad (70)$$

for $\tilde{d}^T = (d^3 - d^2)\hat{i}^1 + (d^1 - d^3)\hat{i}^2 + (d^2 - d^1)\hat{i}^3$, such as $\tilde{d}^T \in T_d^* S^2$ and then $\tilde{d}^T d = 0$. The newly introduced co-vector \tilde{d}^T was inspired by the rotor of a vector field. As it can be observed, the current construction of the projection radically differs from the one proposed in [41]. The three uppermost rows show that movements with an identical increment of translation at both nodes are present in the

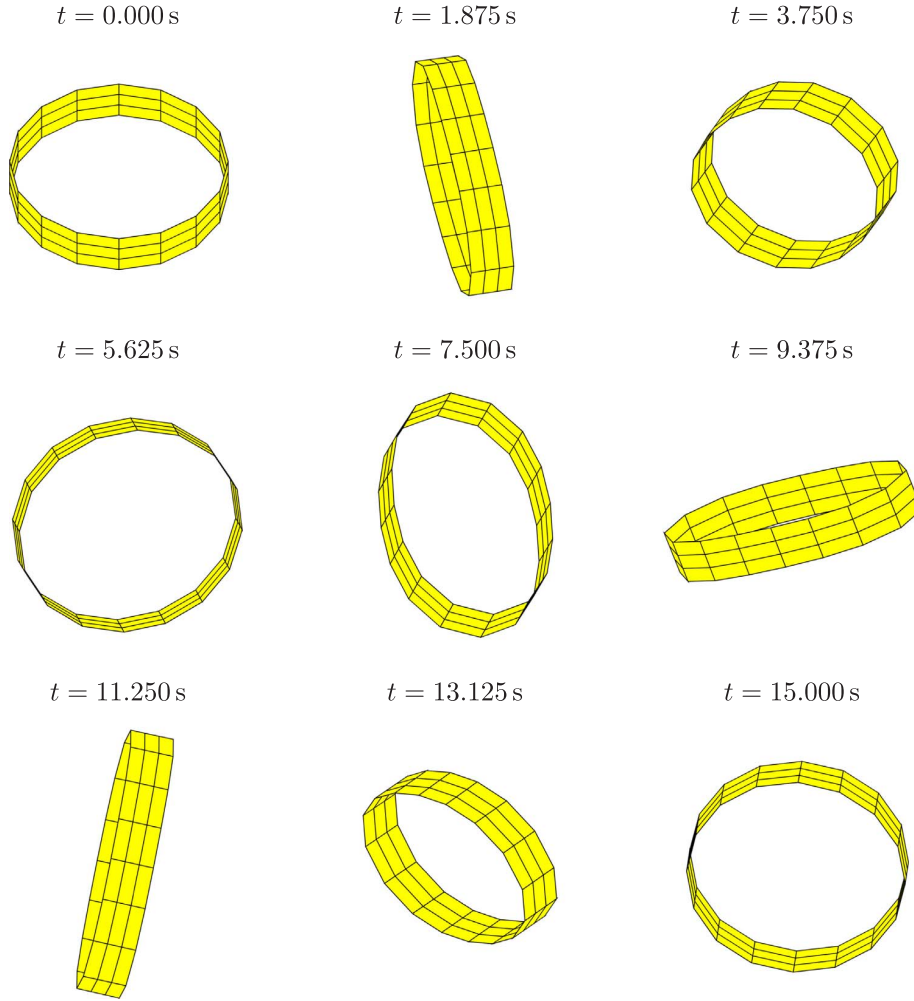


Fig. 4. Tumbling cylinder – motion sequence.

Table 3
Tumbling cylinder – verification of stationary values.

$t > t_{\text{load}}$	[41]	Present
l_1	20.0	20.0
l_2	0.0	0.0
l_3	0.0	0.0
j_1	124.4	122.0
j_2	-148.9	-147.2
j_3	-182.2	-178.3
H	440.0	445.2

projection operator. The fourth and fifth rows show that movements with identical director motion in the perpendicular plane to both directors are permitted. The lowermost row shows that movements simultaneously perpendicular to each director are present as well. This means that no relative motion will occur between the intersecting nodes. The absence of motion along the directors confirms the preservation of the initial lengths. A further observation with respect to the applicability of this constraint ought to be done. In the limit case, in which the directors have the same direction, meaning that the angle between directors is identically zero, the two unit length constraints become linearly dependent.

The layer connection allows to stack two single shells by introducing constraints at a single fictitious interfacing surface, which lies at a relative position equal to half the thickness of the lower layer, $\frac{\partial U}{2}$, times

its extensible director, which is seen from the middle surface of the lower shell, and at a relative position equal to minus half the thickness of the upper layer, $-\frac{\partial U}{2}$, times its extensible director, which is seen from the middle surface of the upper shell, see Fig. 2c. Then the positions at the interfacing surface from both sides is set to be equal. This is $\mathbf{h}_{LC} = \mathbf{0} \in \mathbb{R}^3$, in which

$$\mathbf{h}_{LC} = \left\{ \bar{\mathbf{x}}_A(t) + \frac{\partial U}{2} \mathbf{d}_A(t) - \bar{\mathbf{x}}_B(t) + \frac{\partial U}{2} \mathbf{d}_B(t) \right\}. \quad (71)$$

This constraint enables to account situations in which the displacement field across two adjacent layers is C^0 . The corresponding Jacobean matrix takes the following form

$$\mathbf{H}_{LC} = \begin{bmatrix} \mathbf{I}_{3 \times 3} & \frac{\partial U}{2} \mathbf{I}_{3 \times 3} & -\mathbf{I}_{3 \times 3} & \frac{\partial U}{2} \mathbf{I}_{3 \times 3} \end{bmatrix}. \quad (72)$$

A visual inspection of \mathbf{H}_{LC}^T permits to find a basis for its null space. Having found these vectors, the construction of the corresponding projection operator is straightforward, whose final form is

$$\mathbf{P}_{LC} = \begin{bmatrix} \mathbf{I}_{3 \times 3} & \mathbf{0}_{3 \times 3} & \mathbf{I}_{3 \times 3} & \mathbf{0}_{3 \times 3} \\ -\frac{\partial U}{2} \mathbf{I}_{3 \times 3} & \mathbf{0}_{3 \times 3} & \mathbf{0}_{3 \times 3} & \mathbf{I}_{3 \times 3} \\ -\frac{\partial U}{2} \mathbf{I}_{3 \times 3} & \mathbf{I}_{3 \times 3} & \mathbf{0}_{3 \times 3} & \mathbf{0}_{3 \times 3} \end{bmatrix}. \quad (73)$$

The three uppermost rows show that movements with an identical increment of translation at both nodes are present in the projection

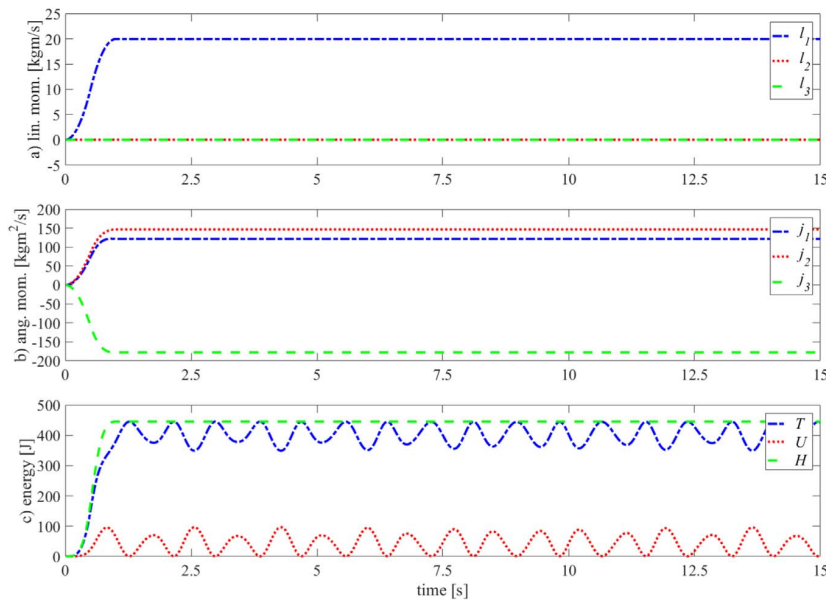


Fig. 5. Tumbling cylinder – linear momentum (lin. mom.), angular momentum (ang. mom.) and total energy.

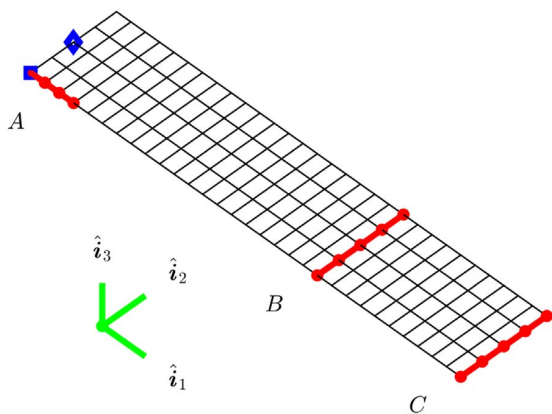


Fig. 6. Free-flying single-layer plate – finite element representation.

Table 4

Free-flying single-layer plate – force density per length unit in N/m.

	A	B	C
f_1	0	0	40,000
f_2	40,000	0	0
f_3	40,000	-40,000	40,000

operator. The three central rows show that movements, which couple translation of the lower shell with the director motion of the upper shell, are permitted. Finally, the three lowermost rows show that movements, which couple translation with the director motion within a single shell, are present as well. This means that in addition to the rigid body motion, some relative motion will occur. The resultant number of equations to determine the solution is comparable to the one obtained with the assembly of brick-shell elements.

2.5. Final equations

The combination of Sections 2.2–2.4 yields the full discrete formulation of the equilibrium for the extensible-director-based solid-degenerate shell. This is comprised by four residuals, one for each field, that must be minimized at every time step. The governing differential-

algebraic equations in their implementation form are given as follows:

$$r_{\hat{v}} = \int_{\square} N^T \{ [I_d^{\text{cons}}(\mathbf{v}_n, \mathbf{v}_{n+1}) + I_d^{\text{diss}}(\mathbf{v}_n, \mathbf{E}_n, \mathbf{v}_{n+1}, \mathbf{E}_{n+1})] - I_d(\mathbf{x}_n, \mathbf{x}_{n+1}) \} \sqrt{\det[G(\boldsymbol{\theta}, 0)]} d^3\boldsymbol{\theta}, \quad (74)$$

$$r_{\hat{x}} = P_d(\hat{\mathbf{x}}_n, \hat{\mathbf{x}}_{n+1}) \int_{\square} \tilde{\mathbf{B}}_d^T(\mathbf{x}_{n+\frac{1}{2}}) [S_d^{\text{cons}}(\mathbf{E}_n, \mathbf{E}_{n+1}) + S_d^{\text{diss}}(\mathbf{v}_n, \mathbf{E}_n, \mathbf{v}_{n+1}, \mathbf{E}_{n+1})] + N^T \left[\dot{\mathbf{I}}_d(\mathbf{v}_n, \mathbf{v}_{n+1}) - \mathbf{f}^{\text{ext}}(\mathbf{x}_{n+\frac{1}{2}}) \right] \sqrt{\det[G(\boldsymbol{\theta}, 0)]} d^3\boldsymbol{\theta}, \quad (75)$$

$$r_{\hat{e}} = \int_{\square} \{ \tilde{\mathbf{B}}_d^T [S_d^{\text{cons}}(\mathbf{E}_n, \mathbf{E}_{n+1}) + S_d^{\text{diss}}(\mathbf{v}_n, \mathbf{E}_n, \mathbf{v}_{n+1}, \mathbf{E}_{n+1})] \} \sqrt{\det[G(\boldsymbol{\theta}, 0)]} d^3\boldsymbol{\theta}, \quad (76)$$

$$r_{\lambda} = \mathbf{h}(\hat{\mathbf{x}}_{n+1}). \quad (77)$$

This set of equations is solved by means of the full Newton-Raphson algorithm. As we employ a rotationless framework, there is no necessity of applying a hybrid combination of the additive and multiplicative procedures to actualize the unknowns, which is standard in frameworks that employ rotation matrices to describe the orientation of the directors. Instead, we use the simplest additive actualization.

In Eq. (75) Lagrange's multipliers were eliminated by means of a null-space projection. It means that $r_{\hat{x}} \in \mathbb{R}^{m-n}$, in which m represents the dimension of the configuration manifold and n stays for the rank associated with the restriction sub-manifold. For this purpose, the null-space projection in its discrete form arises after direct evaluation at $\hat{\mathbf{x}}_{n+\frac{1}{2}}$, which means that $P_d(\hat{\mathbf{x}}_n, \hat{\mathbf{x}}_{n+1})$ is identically equal to $P(\hat{\mathbf{x}}_{n+\frac{1}{2}})$. In our case, this is valid because the constraints that we consider are in the worst case quadratic functions of the nodal coordinates. If higher-order dependencies on the nodal coordinates are considered, the introduction of a discrete derivative is necessary to compute the Jacobean of the constraints, which has to satisfy the consistency and directionality conditions. An example is the nonstandard quadrature proposed in [34] and employed for multibody systems in [42].

3. Results

In this section, we present some numerical examples, which were chosen to show the potentialities of the proposed approach. The first

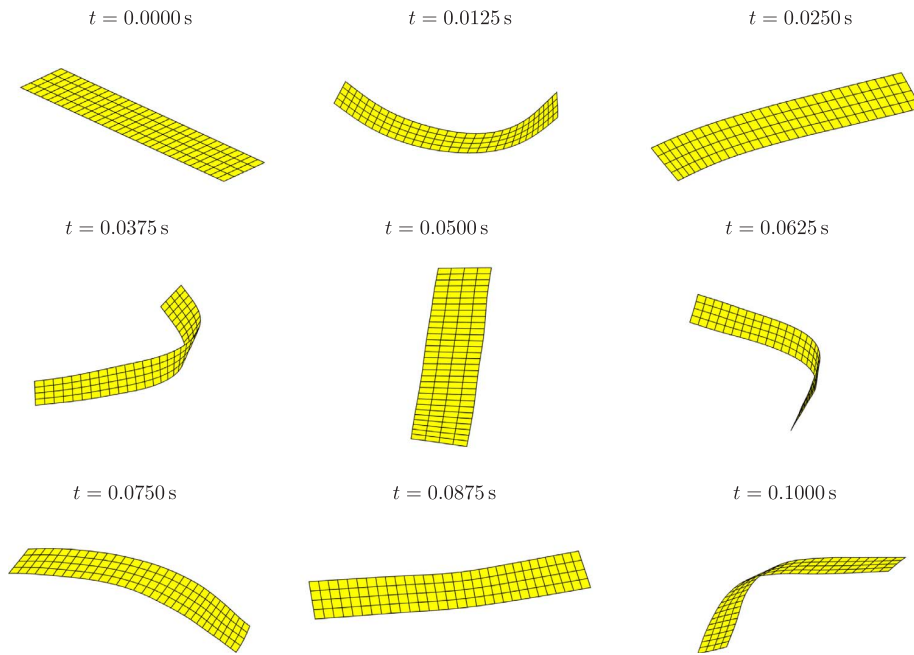


Fig. 7. Free-flying single-layer plate – motion sequence.

Table 5
Free-flying single-layer plate – verification of stationary values.

$t > t_{load}$	[14] at \diamond	Present at \diamond	[20] at \square	Present at \square
l_1	4.8	4.8	4.8	4.8
l_2	3.2	3.2	3.2	3.2
l_3	3.2	3.2	3.2	3.2
j_1	-0.069	-0.067	0.027	0.029
j_2	-0.386	-0.387	-0.381	-0.387
j_3	-0.109	-0.108	-0.036	-0.036
H	247.9	246.5	246.8	246.5

example is a tumbling cylinder. The second case considers a free-flying single-layer plate. As an extension of the previous example, the third one comprises a free-flying three-layer plate with ply-drop-offs. The fourth case consists of three-intersecting plates, and the last example considers the dynamic snap-through of a cylindrical panel. All the results presented here are contrasted with results obtained by other authors. Although the results from literature show some scattering due to the theory employed, the time and space discretizations, which are rather coarse, among others, the agreement with our results is indeed very good.

We implemented Eqs. (74)–(77) in the straight manner. The model was coded in Fortran 2008, and object-oriented programming was adopted. Further improvements are still possible to reduce the computational effort and to increment the numerical efficiency, e.g. by

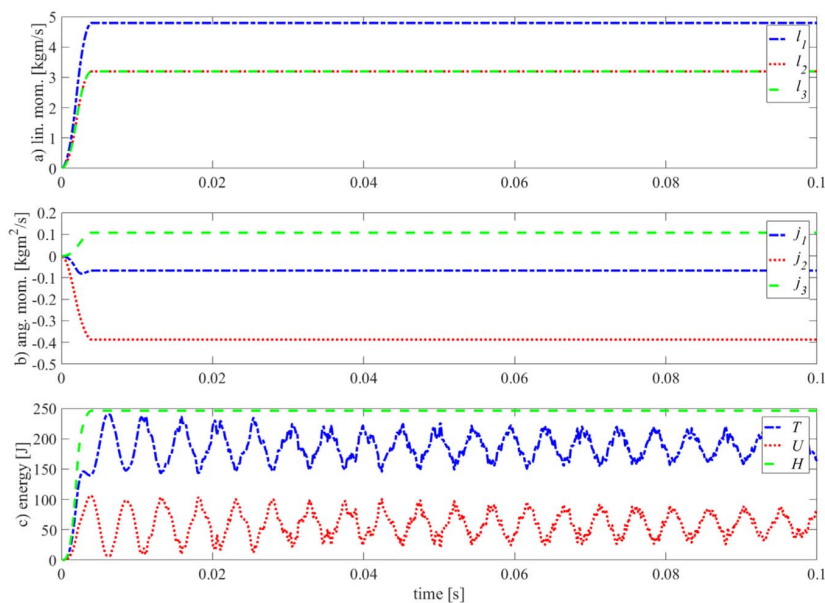


Fig. 8. Free-flying single-layer plate – linear momentum, angular momentum and total energy.

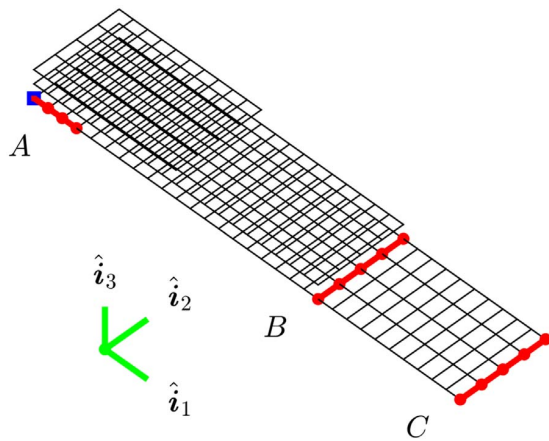


Fig. 9. Free-flying three-layer plate – finite element representation.

implementation of a nested procedure to compute I^{diss} and S^{diss} , scaling of the directors to improve the condition number of the iteration matrix [43], implementation of an hyper-reduction method [44], consideration of occasionally rigid sub-domains [45] and off-line precomputation of coefficients for Saint Venant-Kirchhoff elastic materials. Since the involved equations are very stiff, the second-order predictions to initialize the Newton-Raphson method are not appropriate. The presence of unresolved high-frequency content in the acceleration and velocity terms can lead to predictions outside the basin of attraction of the iterative method, which is only locally stable, and thus, implicate instability issues. Then, it is strongly recommended to employ the solution of the previous step. Moreover, no line-search algorithm is necessary to globalize properties of convergence.

Table 6

Free-flying three-layer plate with ply-drop-offs – verification of stationary values.

$t > t_{\text{load}}$	[20]	Present
l_1	4.8	4.8
l_2	3.2	3.2
l_3	3.2	3.2
j_1	0.0266	0.0285
j_2	-0.2236	-0.2254
j_3	-0.0659	-0.0656
H	195.0	195.6

3.1. Tumbling cylinder

The tumbling cylinder was largely studied, see for instance [7,41]. This structure is a cylindrical shell subjected to spatial loads with a prescribed time variation. The geometrical and material properties are the following: mean radius 7.5 m, height 3.0 m, thickness 0.02 m, longitudinal elastic modulus 2.0×10^8 Pa, Poisson's ratio 0.25 and mass density per volume unit 1.0 kg/m^3 . The cylinder is discretized with 48 elements, in which 16 elements are located along the circumference and 3 elements along the height. The total number of nodes is 68, so it means that the mesh has a seam, which was modeled by means of the continuous connection. Moreover, no further kinematic boundary condition is enforced and no dissipation is considered.

Fig. 3 shows the finite element representation of the tumbling cylinder. Additionally, the line segments A, B, C and D, to which the spatial loads are applied, are indicated. The seam is located along the line segment A, which joins the first and last rows of nodes. Table 2 presents the values for the spatial loads that are applied to the structure. The loads are then multiplied with a function that describes the variation of the applied force over the time, which is defined in Eq. (78). Then $f_0^{\text{ext}} = f_1 \hat{i}^1 + f_2 \hat{i}^2 + f_3 \hat{i}^3$ and $f^{\text{ext}}(t) = f(t) \cdot f_0^{\text{ext}}$, in which the last expression is the acting load.

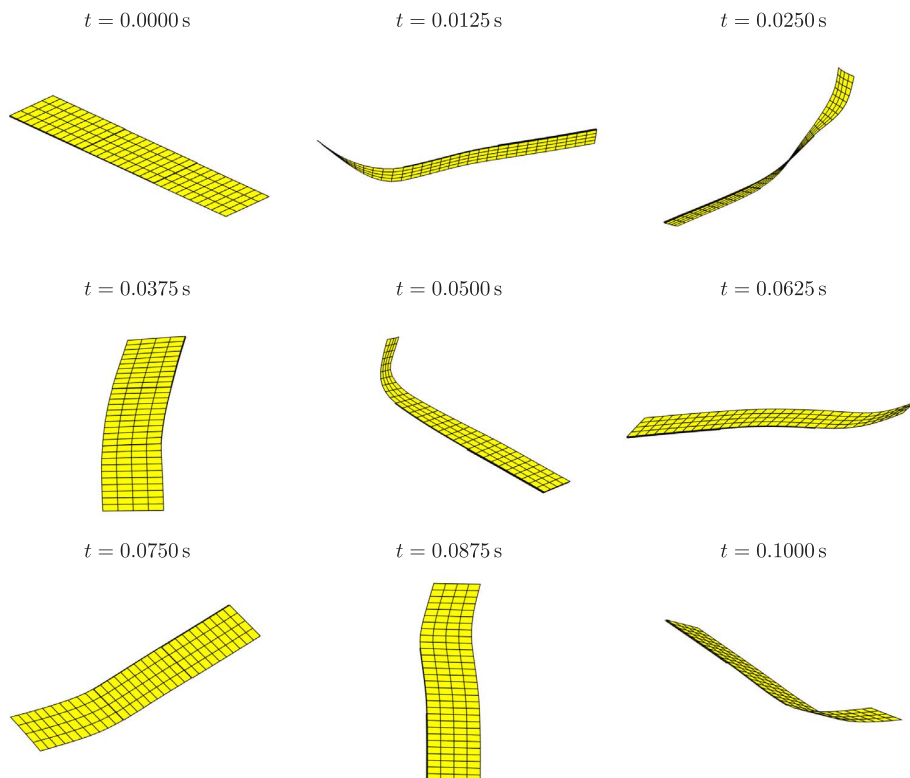


Fig. 10. Free-flying three-layer plate – motion sequence.

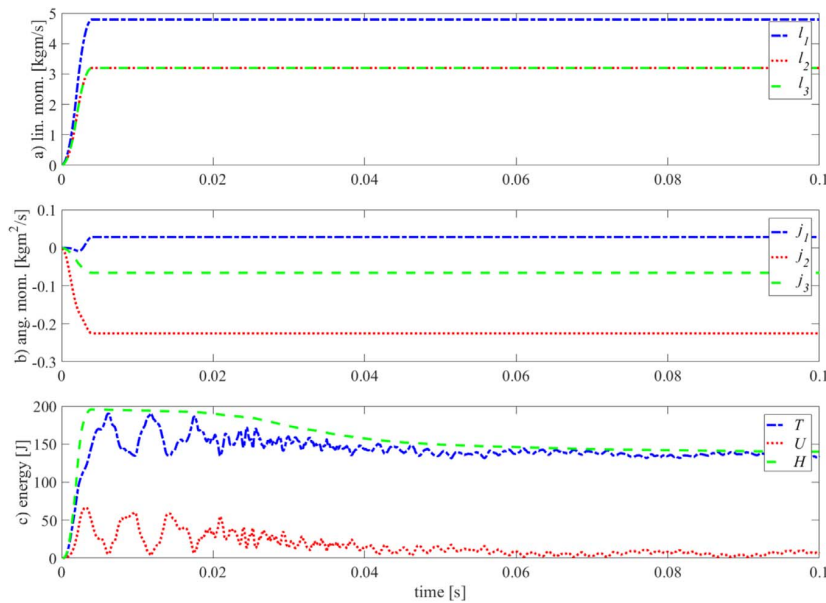


Fig. 11. Free-flying three-layer plate – linear momentum, angular momentum and total energy.

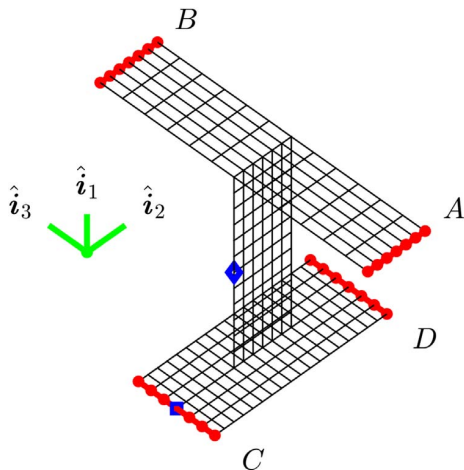


Fig. 12. Three-intersecting plates – finite element representation.

Table 7

Three-intersecting plates – force density per length unit in N/m.

	A	B	C	D
f_1	2	-2	1	10
f_2	0	-4	-1	6
f_3	-2	2	-1	-1

$$f(t) = \begin{cases} 10t & \text{for } 0 \leq t < 0.5 \\ 5 - 10t & \text{for } 0.5 \leq t < 1 \\ 0 & \text{for } t \geq 1 \end{cases} \quad (78)$$

Fig. 4 shows a motion sequence, where the original configuration is located at the upper-left corner of the plot, and some deformed configurations are sequentially shown from left to right and from top to bottom. As it can be observed, the tumbling cylinder exhibits large displacements and large rotations, therefore the nonlinear kinematic behavior is apparent. Table 3 presents a verification of the stationary values for the linear momentum, angular momentum and total energy. The results obtained with the present approach are then compared with those results published in [41], whose values were taken directly from

the PDF file by mean of a point-capture technique. Therefore, they should be considered just as references for comparison, but not as exact values. Although some small differences can be appreciated, the agreement is indeed very good. The main source of scattering can be attributed to the modeling approaches, which are substantially different. As already mentioned, the current model is based on an extensible-director-based solid-degenerate shell, which can accommodate stresses in the thickness direction, whereas the reference model presented in [41] is based on a standard shell theory with an inextensible director, which is not able to accommodate stresses in the thickness direction.

Fig. 5 shows the time history for the linear momentum, angular momentum and energy. It can be observed that the linear momentum, angular momentum and total energy vary during the time in which the external load is active, i.e. the first 1 s. After the vanishment of the external load, all these three invariant quantities are identically preserved through the time. These results prove numerically that the adopted integration scheme preserves momenta and energy. Although the total energy remains constant, the potential and kinematic energies vary in the course of time, complementing each other in such a way that the total energy is perfectly constant. As a final comment, this particular case shows no unresolved high-frequency content, therefore no dissipation is necessary to compute a convergent long-term response of the system.

3.2. Free-flying single-layer plate

The free-flying single-layer plate was proposed by Kuhl and Ramm [14] and studied later by Vu-Quoc and Tan [20] among others. The structure is a rectangular flat plate, which comprises a single material layer and is subjected to spatial loads with a prescribed time variation. The geometrical and material properties are the following: length 0.3 m, width 0.06 m, thickness 0.002 m, longitudinal elastic modulus 2.06×10^{11} Pa, Poisson's ratio 0.0 and mass density per volume unit 7.3×10^3 kg/m³. The flat plate is then discretized with 120 elements, 30 elements being located along the largest dimension and 4 elements along the smallest dimension. The total amount of nodes is 155 and no dissipation is considered.

Fig. 6 shows the finite element representation of the free-flying single-layer plate. The line segments A, B and C, to which the spatial loads are applied, are indicated as well. Additionally, the points of

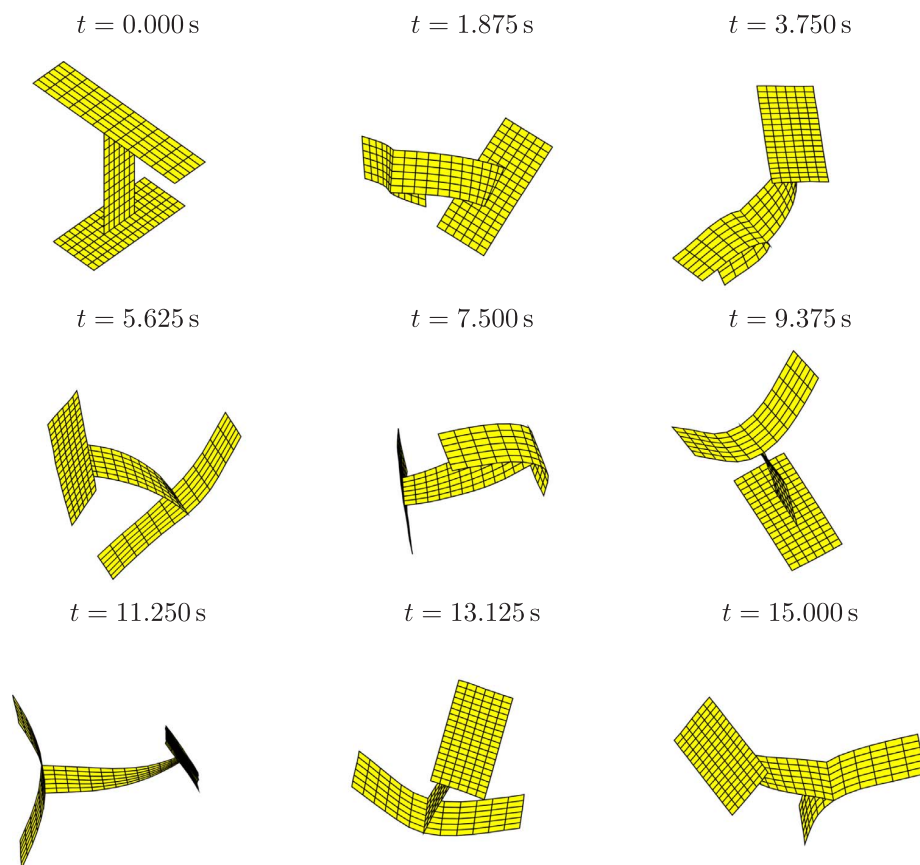


Fig. 13. Three-intersecting plates – motion sequence.

Table 8
Three-intersecting plates – verification of stationary values.

$t > t_{\text{load}}$	[46] at \diamond	Present at \diamond	[41] at \square	Present at \square
l_1	4.125	4.125	4.125	4.125
l_2	-0.125	-0.125	-0.125	-0.125
l_3	-0.75	-0.75	-0.75	-0.75
j_1	-5.880	-5.913	-8.199	-8.163
j_2	22.39	22.463	26.238	26.213
j_3	25.68	25.712	12.733	12.712
H	59.51	59.326	59.164	59.326

origin denoted by the symbols \diamond and \square are indicated, which are necessary to perform the verification of the stationary angular momentum. Table 4 presents the values for the spatial loads that are applied to the structure. The loads are then amplified with a function, which is defined in Eq. (79).

$$f(t) = \begin{cases} 500t & \text{for } 0 \leq t < 0.002 \\ 2 - 500t & \text{for } 0.002 \leq t < 0.004 \\ 0 & \text{for } t \geq 0.004 \end{cases} \quad (79)$$

Fig. 7 shows a motion sequence. Table 5 presents a verification of the stationary values for the linear momentum, angular momentum and total energy. The results obtained with the present approach are compared with those results published in [14], whose authors used the initial location of the material point \diamond as origin of the global coordinate system, and with the results presented in [20], whose authors used the initial location of the material point \square as origin of the global coordinate system. Both authors consider eight-node solid-degenerate shell elements, which do belong to the same family of finite elements. In [14], a generalized energy-momentum method based on

the generalized α method with adaptive time step was employed, whereas in [20] the Bossak α algorithm with fixed time step was applied. The values were taken from the PDF. Very small differences can be appreciated, but the agreement is indeed very good, even provided that the computed results are slightly sensitive to the time step.

Fig. 8 shows the time history for the linear momentum, angular momentum and total energy. These three quantities vary during the time in which the external load is active, *i.e.* the first 0.004 s. After the vanishment of the external load, they are identically preserved over the time. As a final comment, this particular case does show unresolved high-frequency content, which for very long simulations could trigger the fail of the Newton-Raphson method. Although the adopted numerical method is indeed unconditionally stable, if initial guess of the solution falls outside the basin of the attraction, the stability is not longer warranted and therefore, some dissipation would provide robustness for computing a convergent long-term response of the system.

3.3. Free-flying three-layer plate with ply-drop-offs

The free-flying three-layer plate with ply-drop-offs was originally proposed by Vu-Quoc and Tan [20] to analyze the dynamic behavior of thin-walled structures with ply-drop-offs. The structure is comprised by three rectangular flat plates, which are stacked one over the other. The lowermost plate is subjected to the same loads that are considered for the free-flying single-layer plate. The properties are as follows: length of the lowermost plate 0.3 m, length of the middle plate 0.2 m, length of the uppermost plate 0.1 m, width 0.06 m, thickness 0.001 m, longitudinal modulus 2.06×10^{11} Pa, Poisson's ratio 0.0 and mass density per volume unit 7.3×10^3 kg/m³. The largest plate is discretized with

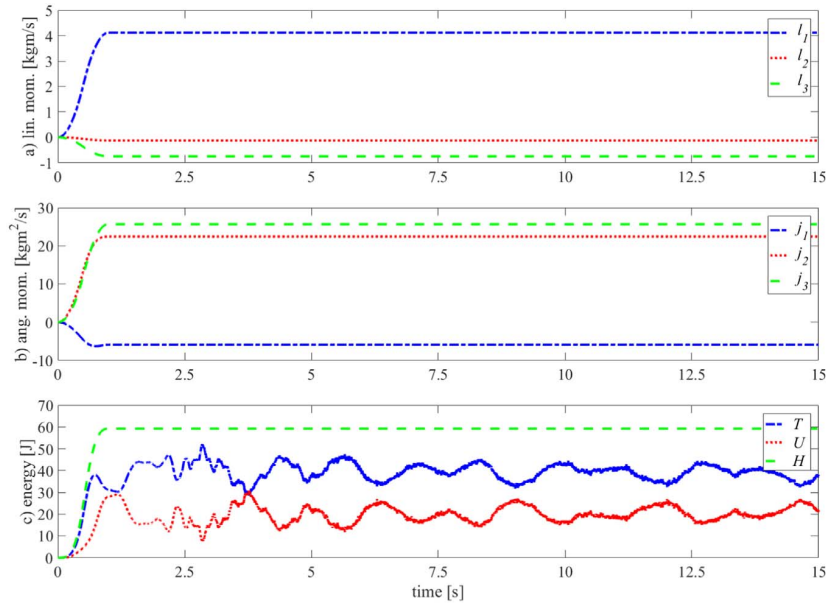


Fig. 14. Three-intersecting plates – linear momentum, angular momentum and total energy.

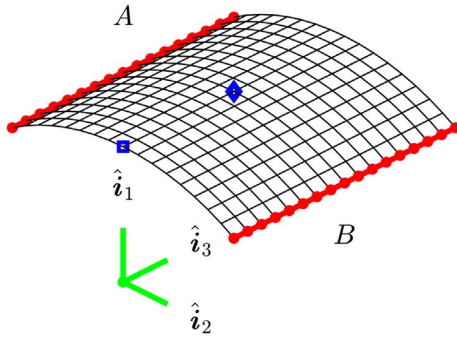


Fig. 15. Cylindrical panel – finite element representation.

120 elements. The middle plate comprises 80 elements. And finally, the smallest plate is discretized with 40 elements. The plates are stacked by means of the layer connection. At one edge, all the plates coincide in the in-plane location. From this one to the other edge along the longitudinal direction, the difference in length of the plates materializes itself as ply-drop-offs. Moreover, no further kinematic boundary condition is enforced. For the comparison of stationary values, no damping was utilized, although convergence problems, due to the high-frequency content, were present after few multiples of the load time duration. This fact was also observed in [20]. Finally, to compute a convergent long-term response, a dissipation factor of $\alpha = 0.05$ was employed.

Fig. 9 shows the finite element representation. The line segments A, B and C at the lowermost plate, to which the spatial loads are applied, are indicated as well. Additionally, the point \square in the original configuration is indicated, which is necessary to perform the verification of the stationary angular momentum. Fig. 10 shows a motion sequence. The region containing the ply-drop-offs exhibits larger deformations than the stiffer region containing all the three layers. Table 6 presents a verification of the stationary values. The results obtained with the present approach are contrasted with those results published in [20]. In the aforementioned publication, the authors consider eight-node degenerated-solid shell elements and the Bossak α algorithm with fixed time step.

Fig. 11 shows the time history for the linear momentum, angular momentum and energy. After the vanishment of the external load, *i.e.*

$t > 0.004$ s, the momenta are identically preserved. Due to the presence of unresolved high-frequency content, the introduction of numerical dissipation was necessary to obtain a convergent long-term response. Although the energy is not preserved, it always decays in a controlled form by means of a suitable definition of the non-conservative parts of the linear momentum and stress. The reduction of energy is always warranted for positive-definite dissipation functions even in the non-linear case. Standard integration methods do not provide this feature, and the desired dissipation characteristics are only warranted for the linear case.

3.4. Three-intersecting plates

This example is very complicated. For instance [46], presented a deep study of the discrepancies shown in literature. The structure comprises three flat plates and is subjected to spatial loads. The properties are the following: length and width of the lowermost plate 9.0 m and 4.0 m, respectively, length and width of the middle plate 10.0 m and 3.0 m, correspondingly, length and width of the uppermost plate 14.0 m and 3.0 m, respectively, thickness of each plate 0.02 m, longitudinal modulus 2.0×10^7 Pa, Poisson's ratio 0.23 and mass density per volume unit 1.0 kg/m^3 . The lowermost plate is discretized with 108 elements, from which 18 elements are located along the largest direction and 6 elements along the smallest dimension. The plate in the middle comprises 72 elements, from which 12 elements are located along the largest direction and 6 elements along the smallest dimension. The uppermost plate is discretized in 72 elements, from which 12 elements are located along the largest direction and 6 elements along the smallest dimension. The plates are connected by means of the discontinuous connection. Moreover, no further kinematic boundary condition is enforced and no dissipation is considered.

Fig. 12 shows the finite element representation of the three-intersecting plates. The line segments A, B, C and D, to which the spatial loads are applied, are indicated as well. Additionally, the points of origin denoted by the symbols \diamond and \square are indicated, which are necessary to perform the verification of the stationary angular momentum. Table 7 presents the values for the spatial loads that are applied to the structure. The loads are then multiplied with a temporal function that describes the time variation, which is defined in Eq. (80).

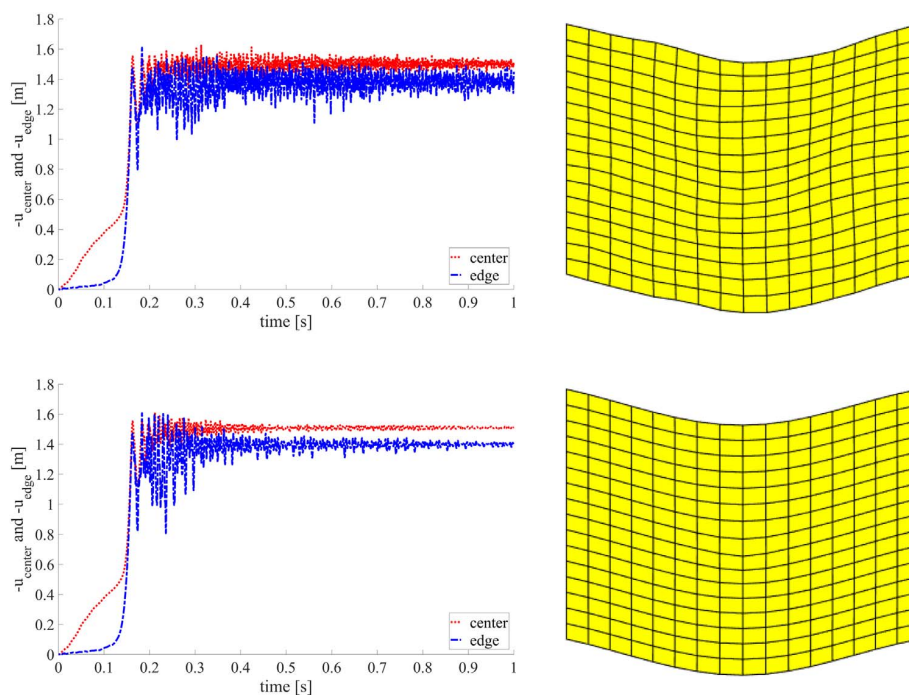


Fig. 16. Snap-through of a cylindrical panel – displacement and mesh quality.

$$f(t) = \begin{cases} 0.5t & \text{for } 0 \leq t < 0.5 \\ 0.25 - 0.5t & \text{for } 0.5 \leq t < 1 \\ 0 & \text{for } t \geq 1 \end{cases} \quad (80)$$

Fig. 13 shows a motion sequence. As it can be observed, the three-intersecting plates exhibits large displacements and large rotations, therefore the nonlinear kinematic behavior is evident. Table 8 presents a verification of the stationary values for the linear momentum, angular momentum and total energy. The results obtained with the present approach are then compared with those results published in [46], whose authors used the initial location of the material point \diamond as origin of the global coordinate system, and with the results in [41], whose authors used the initial location of the material point \square as origin of the global coordinate system. In both publications, the authors consider four-node shell elements, which do belong to the same family of finite elements, but to a different one with respect to our modeling approach. The values were taken directly from the PDF. Although some small differences can be appreciated, the agreement with the references is indeed very good. Due to this good agreement, it is not possible to attribute the differences to the modeling approach.

Fig. 14 shows the time history for the linear momentum, angular momentum and total energy. After the vanishment of the external load, i.e. $t > 1$ s, all these quantities are exactly preserved. This particular case shows unresolved high-frequency content, which for very long simulations could trigger the fail of the numerical method and therefore, some dissipation would provide robustness.

3.5. Dynamic snap-through of a cylindrical panel

Here, we investigate the dynamic snap-through of a cylindrical panel, originally proposed by Kuhl and Ramm [14] in the context of solid-degenerate shell elements and studied later by Romero and Armero [18] in the context of a geometrically exact shell theory. The structure is a shell with constant curvature along the traversal direction. It is subjected to a concentrated normal load that is applied to the point, which is located at the geometric center of the panel. The properties are the following: radius 5.0 m, half-angle 30.0° , dimension in the longitudinal direction 5.0 m, thickness 0.01 m, longitudinal modulus

2.0×10^{11} Pa, Poisson's ratio 0.25 and mass density per volume unit 1.0×10^4 kg/m³. The structure was completely modeled instead of using symmetries to reduce the computation time. The cylindrical panel is then discretized in 256 elements, from which 16 elements are located along the longitudinal direction and 16 elements along the transversal direction. The total amount of nodes is 289, both longitudinal edges are simply supported and no further kinematic boundary condition is enforced. For the convergent long-term response, two cases are considered, one without dissipation and one with dissipation factor $\alpha = 0.1$. Fig. 15 shows the finite element representation. At the edges A and B, the simply supported boundary condition is applied. The geometric center of the shell is indicated with a \diamond symbol. Additionally, with a \square symbol an interesting point located in the middle of one of the free edges is indicated. The concentrated load is defined as $f^{\text{ext}}(t) = -200000f(t)\hat{i}^1$, which is expressed in N, and the time variation is given by

$$f(t) = \begin{cases} 5t & \text{for } 0 \leq t < 0.2 \\ 1 & \text{for } t \geq 0.2. \end{cases} \quad (81)$$

Fig. 16 presents to the left the vertical displacement of the points located at \diamond and at \square , and to the right the mesh geometry at time 1 s. The upper row corresponds to the case where no dissipation was introduced and the lower row corresponds to the case where dissipation was considered. Considering the results presented at the left, it can be observed that for the time interval between 0 s and 0.2 s the distinction of both cases is practically impossible. Taking a carefully look at the long-term responses, it is possible to confirm that the results presented at the bottom correspond to the case with dissipation. At the right, it is possible to appreciate the long-term resulting mesh geometry for both cases. The mesh that corresponds to the case without dissipation shows distortions and lack of symmetry. As this case is purely symmetric, with respect to two planes, in geometry, material, loads and boundary conditions, this fact is unacceptable. The mesh, which corresponds to the case with dissipation, shows neither distortion nor lack of symmetry. This fact confirms that by considering a small dissipation, the robustness of the long-term response can be improved, not only by removing the unresolved high-frequency content, but also by annihilat-

ing their unwanted effects on the quality of the mesh. Finally, the static solution published in [14] indicates a displacement of the center point of -1.5111 m, and the stationary response obtained with the current approach is -1.5093 m. Moreover, the dynamic behavior for both cases shows the same unsteady features as those obtained by Kuhl and Ramm [14]. On the contrary, the results obtained by Romero and Armero [18] in the context of a geometrically exact shell theory show that the cylindrical panel develops a nearly vibration steady-state about the static solution immediately after reaching the maximal load. Although the source of this discrepancy could be attributed to the modeling approaches, the explanation requires more investigations that are beyond the scope of this work.

4. Concluding remarks

This work presented a framework for simulating the nonlinear dynamics of shell structures that relies on the combination of a mixed finite element formulation, a robust integration scheme and a null-space projection method. This unifying approach, which can deal with large displacements, large rotations and large strains, was successfully verified. Moreover, it inherits the advantages of all involved basic ingredients (e.g. objectivity, unconditional stability, robustness, etc) and is relatively easy to implement. We can claim that the approach is able to handle highly-unsteady nonlinear cases and the robustness-precision relation is well balanced.

However, the current methodology ought to be enhanced, for example, by implementation of a hyper-reduction method, off-line precomputation of coefficients for Saint Venant-Kirchhoff elastic materials, implementation of multi-layer laminated materials and, enrichment of the displacement field with zig-zag functions.

Acknowledgements

We greatly acknowledge the financial support of the Lower Saxony Ministry of Science and Culture that enabled this work by means of the Project *Ventus Efficiens* (FKZ ZN3024).

We also thank Eelco Jansen for the fruitful discussions about the nonlinear dynamics of shells, Leandro Cagliero due to the comments about the mathematical aspects exposed in the current work and Ignacio Romero for the hints regarding the implementation of the robust integration scheme.

References

- [1] E.N. Dvorkin, K.-J. Bathe, A continuum mechanics based four-node shell element for general non-linear analysis, *Eng. Comput.* 1 (1984) 77–88, <http://dx.doi.org/10.1108/eb023562>.
- [2] K.-J. Bathe, E.N. Dvorkin, A formulation of general shell elements—the use of mixed interpolation of tensorial components, *Int. J. Numer. Methods Eng.* 22 (1986) 697–722, <http://dx.doi.org/10.1002/nme.1620220312>.
- [3] N. Büchter, E. Ramm, Shell theory versus degeneration – a comparison in large rotation finite element analysis, *Int. J. Numer. Methods Eng.* 34 (1992) 39–59, <http://dx.doi.org/10.1002/nme.1620340105>.
- [4] N. Büchter, E. Ramm, D. Roehl, Three-dimensional extension of non-linear shell formulation based on the enhanced assumed strain concept, *Int. J. Numer. Methods Eng.* 37 (1994) 2551–2568, <http://dx.doi.org/10.1002/nme.1620371504>.
- [5] J.C. Simo, M.S. Rifai, A class of mixed assumed strain methods and the method of incompatible modes, *Int. J. Numer. Methods Eng.* 29 (1990) 1595–1638, <http://dx.doi.org/10.1002/nme.1620290802>.
- [6] J.C. Simo, N. Tarnow, The discrete energy-momentum method. Conserving algorithms for nonlinear elastodynamics, *Z. Angew. Math. Phys.* 43 (1994) 757–792, <http://dx.doi.org/10.1007/BF00913408>.
- [7] J.C. Simo, N. Tarnow, A new energy and momentum conserving algorithm for the non-linear dynamics of shells, *Int. J. Numer. Methods Eng.* 37 (1994) 2527–2549, <http://dx.doi.org/10.1002/nme.1620371503>.
- [8] C.K. Choi, J.G. Paik, An effective four node degenerated shell element for geometrically nonlinear analysis, *Thin-Walled Struct.* 24 (1996) 261–283, [http://dx.doi.org/10.1016/0263-8231\(95\)00037-2](http://dx.doi.org/10.1016/0263-8231(95)00037-2).
- [9] P. Betsch, E. Stein, An assumed strain approach avoiding artificial thickness straining for a non-linear 4-node shell element, *Commun. Numer. Methods Eng.* 11 (1995) 899–909, <http://dx.doi.org/10.1002/cnm.1640111104>.
- [10] P. Betsch, E. Stein, A nonlinear extensible 4-node shell element based on continuum theory and assumed strain interpolations, *J. Nonlinear Sci.* 6 (1996) 169–199, <http://dx.doi.org/10.1007/BF02434053>.
- [11] J.C. Simo, F. Armero, Geometrically non-linear enhanced strain mixed methods and the method of incompatible modes, *Int. J. Numer. Methods Eng.* 33 (1992) 1413–1449, <http://dx.doi.org/10.1002/nme.1620330705>.
- [12] M. Bischoff, E. Ramm, Shear deformable shell elements for large strains and rotations, *Int. J. Numer. Methods Eng.* 40 (1997) 4427–4449, [http://dx.doi.org/10.1002/\(SICI\)1097-0207\(19971215\)40:233.0.CO;2-9](http://dx.doi.org/10.1002/(SICI)1097-0207(19971215)40:233.0.CO;2-9).
- [13] C. Sansour, P. Wriggers, J. Sansour, Nonlinear dynamics of shells: theory, finite element formulation, and integration schemes, *Nonlinear Dyn.* 13 (1997) 279–305, <http://dx.doi.org/10.1023/A:1008251113479>.
- [14] D. Kuhl, E. Ramm, Generalized energy-momentum method for non-linear adaptive shell dynamics, *Comput. Methods Appl. Mech. Eng.* 178 (1999) 343–366, [http://dx.doi.org/10.1016/S0045-7825\(99\)00024-9](http://dx.doi.org/10.1016/S0045-7825(99)00024-9).
- [15] F. Armero, I. Romero, On the formulation of high-frequency dissipative time-stepping algorithms for nonlinear dynamics. Part I: low-order methods for two model problems and nonlinear elastodynamics, *Comput. Methods Appl. Mech. Eng.* 190 (2001) 2603–2649, [http://dx.doi.org/10.1016/S0045-7825\(00\)00256-5](http://dx.doi.org/10.1016/S0045-7825(00)00256-5).
- [16] F. Armero, I. Romero, On the formulation of high-frequency dissipative time-stepping algorithms for nonlinear dynamics. Part II: second-order methods, *Comput. Methods Appl. Mech. Eng.* 190 (2001) 6783–6824, [http://dx.doi.org/10.1016/S0045-7825\(01\)00233-X](http://dx.doi.org/10.1016/S0045-7825(01)00233-X).
- [17] C. Sansour, W. Wagner, P. Wriggers, J. Sansour, An energy-momentum integration scheme and enhanced strain finite elements for the non-linear dynamics of shells, *Int. J. Non-Linear Mech.* 37 (2002) 951–966, [http://dx.doi.org/10.1016/S0020-7462\(01\)00108-1](http://dx.doi.org/10.1016/S0020-7462(01)00108-1).
- [18] I. Romero, F. Armero, Numerical integration of the stiff dynamics of geometrically exact shells: an energy-dissipative momentum-conserving scheme, *Int. J. Numer. Methods Eng.* 54 (2002) 1043–1086, <http://dx.doi.org/10.1002/nme.463>.
- [19] O.A. Bauchau, J.-Y. Choi, C.L. Bottasso, On the modeling of shells in multibody dynamics, *Multibody Syst. Dyn.* 8 (2002) 459–489, <http://dx.doi.org/10.1023/A:1021109015553>.
- [20] L. Vu-Quoc, X.G. Tan, Optimal solid shells for non-linear analyses of multilayer composites. II. Dynamics, *II Comput. Methods Appl. Mech. Eng.* 192 (2003) 1017–1059, [http://dx.doi.org/10.1016/S0045-7825\(02\)00336-5](http://dx.doi.org/10.1016/S0045-7825(02)00336-5).
- [21] C. Sansour, P. Wriggers, J. Sansour, On the design of energy-momentum integration schemes for arbitrary continuum formulations. applications to classical and chaotic motion of shells, *Int. J. Numer. Methods Eng.* 60 (2004) 2419–2440, <http://dx.doi.org/10.1002/nme.931>.
- [22] T.Aksu Ozkul, A finite element formulation for dynamic analysis of shells of general shape by using the wilson- θ method, *Thin-Walled Struct.* 42 (2004) 497–513, <http://dx.doi.org/10.1016/j.tws.2003.12.008>.
- [23] R. Zemčík, R. Rolfes, M. Rose, J. Teßmer, High-performance four-node shell element with piezoelectric coupling for the analysis of smart laminated structures, *Int. J. Numer. Methods Eng.* 70 (2007) 934–961, <http://dx.doi.org/10.1002/nme.1909>.
- [24] S. Leyendecker, P. Betsch, P. Steinmann, The discrete null space method for the energy-consistent integration of constrained mechanical systems. Part. III: flexible multibody dynamics, *Multibody Syst. Dyn.* 19 (2008) 45–72, <http://dx.doi.org/10.1007/s11044-007-9056-4>.
- [25] A. Vaziri, Mechanics of highly deformed elastic shells, *Thin-Walled Struct.* 47 (2009) 692–700, <http://dx.doi.org/10.1016/j.tws.2008.11.009>.
- [26] E. Carrera, M. Cinefra, P. Nali, MITC technique extended to variable kinematic multilayered plate elements, *Compos. Struct.* 92 (2010) 1888–1895, <http://dx.doi.org/10.1016/j.compstruct.2010.01.009>.
- [27] T.-Y. Wu, Dynamic nonlinear analysis of shell structures using a vector form intrinsic finite element, *Eng. Struct.* 56 (2013) 2028–2040, <http://dx.doi.org/10.1016/j.engstruct.2013.08.009>.
- [28] A. Ahmed, L.J. Sluys, Implicit/explicit elastodynamics of isotropic and anisotropic plates and shells using a solid-like shell element, *Eur. J. Mech. – A/Solids* 43 (2015) 118–132, <http://dx.doi.org/10.1016/j.euromechsol.2013.09.009>.
- [29] W. Pietraszkiewicz, V. Konopińska, Junctions in shell structures: a review, *Thin-Walled Struct.* 95 (2015) 310–334, <http://dx.doi.org/10.1016/j.tws.2015.07.010>.
- [30] J. Reinoso, A. Blázquez, Application and finite element implementation of 7-parameter shell element for geometrically nonlinear analysis of layered CFRP composites, *Compos. Struct.* 139 (2016) 263–276, <http://dx.doi.org/10.1016/j.compstruct.2015.12.009>.
- [31] M.F. Caliri Jr., A.J.M. Ferreira, V. Tita, A review on plate and shell theories for laminated and sandwich structures highlighting the finite element method, *Compos. Struct.* 156 (2016) 63–77, <http://dx.doi.org/10.1016/j.compstruct.2016.02.036>.
- [32] M.L. Buecalem, K.-J. Bathe, *The Mechanics of Solids and Structures – Hierarchical Modeling and the Finite Element Solution*, Springer Science & Business Media, 2011, <http://dx.doi.org/10.1007/978-3-540-26400-2>.
- [33] C. Kane, J.E. Marsden, M. Ortiz, Symplectic-energy-momentum preserving variational integrators, *J. Math. Phys.* 40 (1999) 3353–3371, <http://dx.doi.org/10.1063/1.532892>.
- [34] O. Gonzalez, Time integration and discrete Hamiltonian systems, *J. Nonlinear Sci.* 6 (1996) 449, <http://dx.doi.org/10.1007/BF02440162>.
- [35] I. Romero, An analysis of the stress formula for energy-momentum methods in nonlinear elastodynamics, *Comput. Mech.* 50 (2012) 603–610, <http://dx.doi.org/10.1007/s00466-012-0693-y>.
- [36] F. Armero, I. Romero, Energy-dissipative momentum-conserving time-stepping algorithms for the dynamics of nonlinear Cosserat rods, *Comput. Mech.* 31 (2003) 3–26, <http://dx.doi.org/10.1007/s00466-002-0389-9>.
- [37] W.B. Heard, *Rigid Body Mechanics: Mathematics, Physics and Applications*, Wiley-

- VCH Verlag GmbH & Co. KGaA, Weinheim, 2005. <http://dx.doi.org/10.1002/9783527618811>.
- [38] P. Betsch, The discrete null space method for the energy consistent integration of constrained mechanical systems: part I: holonomic constraints, *Comput. Methods Appl. Mech. Eng.* 194 (2005) 5159–5190, <http://dx.doi.org/10.1016/j.cma.2005.01.004>.
- [39] P. Betsch, S. Leyendecker, The discrete null space method for the energy consistent integration of constrained mechanical systems. Part II: multibody dynamics, *Int. J. Numer. Methods Eng.* 67 (2006) 499–552, <http://dx.doi.org/10.1002/nme.1639>.
- [40] J.C. Simo, On a stress resultant geometrically exact shell model. Part VII: shell intersections with 56-DOF finite element formulations, *Comput. Methods Appl. Mech. Eng.* 108 (1993) 319–339, [http://dx.doi.org/10.1016/0045-7825\(93\)90008-L](http://dx.doi.org/10.1016/0045-7825(93)90008-L).
- [41] P. Betsch, N. Sanger, On the use of geometrically exact shells in a conserving framework for flexible multibody dynamics, *Comput. Methods Appl. Mech. Eng.* 198 (2009) 1609–1630, <http://dx.doi.org/10.1016/j.cma.2009.01.016>.
- [42] P. Betsch, S. Uhlar, Energy-momentum conserving integration of multibody dynamics, *Multibody Syst. Dyn.* 17 (2007) 243–289, <http://dx.doi.org/10.1007/s11044-007-9043-9>.
- [43] T. Kloppel, M.W. Gee, W.A. Wall, A scaled thickness conditioning for solid- and solid-shell discretizations of thin-walled structures, *Comput. Methods Appl. Mech. Eng.* 200 (2011) 1301–1310, <http://dx.doi.org/10.1016/j.cma.2010.11.001>.
- [44] C. Farhat, T. Chapman, P. Avery, Structure-preserving, stability, and accuracy properties of the energy-conserving sampling and weighting method for the hyper reduction of nonlinear finite element dynamic models, *Int. J. Numer. Methods Eng.* 102 (2015) 1077–1110, <http://dx.doi.org/10.1002/nme.4820>.
- [45] B. Gottlicher, K. Schweizerhof, Analysis of flexible structures with occasionally rigid parts under transient loading, *Comput. Struct.* 83 (2005) 2035–2051, <http://dx.doi.org/10.1016/j.compstruc.2005.03.007>.
- [46] J. Chro´sacielewski, W. Witkowski, Discrepancies of energy values in dynamics of three intersecting plates, *International, J. Numer. Methods Biomed. Eng.* 26 (2010) 1188–1202, <http://dx.doi.org/10.1002/cnm.1208>.

3. Article B: Nonlinear dynamics of slender structures: a new object-oriented framework

This article presents a new object-oriented framework to study the nonlinear dynamics of slender structures made of hyperelastic multilayer composite materials that relies on finite element method and multibody system formalism with a robust integration scheme and is presented in a differential-algebraic setting. Each mechanical system under consideration is represented as a collection of infinitely stiff components, such as rigid bodies, and flexible components like geometrically exact beams and solid-degenerate shells. The current approach employs directors instead of standard angle-based parametrizations to describe the orientation of the involved components in combination with the total-Lagrangian description. This setting allows to preserve by design the *objectivity* of the discrete strain measures under rigid space transformations and the *path-independence* of the formulation under the action of conservative loading. The semi-discrete equations are temporally discretized for a fixed time increment with a momentum-preserving, energy-preserving/dissipative method, which allows the annihilation of undesirable effects due to unresolved high-frequency content and provides robustness without compromising the precision of the solution. Some interesting constraints to render more complicated structures without modifying the underlying finite element formulation are introduced. In few words, from a methodological point of view, the novelty of this work is the combination of rigid bodies, geometrically exact beams and solid-degenerate shells, and the time integration with a momentum-preserving, energy-preserving/dissipative method into a single common unifying framework, which is implemented by using the object-oriented programming philosophy. The resulting approach may be used very effectively, for example, in wind energy and aeronautics.

This article is published in *Computational Mechanics* 63 (2019), 219–252. The main work was done by the author of this *Habilitationschrift*. Benedikt Hofmeister and Christian Hente contributed mainly with the preparation and simulation of examples. Raimund Rolfes contributed with technical suggestions and supporting work.

Permanent link: <https://doi.org/10.1007/s00466-018-1592-7>



Nonlinear dynamics of slender structures: a new object-oriented framework

Cristian Guillermo Gebhardt¹ · Benedikt Hofmeister¹ · Christian Hente¹ · Raimund Rolfes¹

Received: 27 February 2018 / Accepted: 12 June 2018 / Published online: 2 July 2018
© Springer-Verlag GmbH Germany, part of Springer Nature 2018

Abstract

With this work, we present a new object-oriented framework to study the nonlinear dynamics of slender structures made of composite multilayer and hyperelastic materials, which combines finite element method and multibody system formalism with a robust integration scheme. Each mechanical system under consideration is represented as a collection of infinitely stiff components, such as rigid bodies, and flexible components like geometrically exact beams and solid-degenerate shells, which are spatially discretized into finite elements. The semi-discrete equations are temporally discretized for a fixed time increment with a momentum-preserving, energy-preserving/dissipative method, which allows the systematic annihilation of unresolved high-frequency content. As usual in multibody system dynamics, kinematic constraints are employed to render supports, joints and structural connections. The presented ideas are implemented following the object-oriented programming philosophy. The approach, which is perfectly suitable for wind energy or aeronautic applications, is finally tested and its potential is illustrated by means of numerical examples.

Keywords Nonlinear dynamics of slender structures · Finite elements · Multibody systems · Robust integration · Object-oriented programming

1 Introduction

Existing and new slender structures made of composite multilayer materials, e.g. wind turbines or airplanes, are very complex and the corresponding dynamic analysis requires a vast computational capacity as well as the development and application of fully nonlinear formulations (at least from the geometrical and kinematic point of view). Simulations in time-domain involving large displacements, large rotations and even large strains due to dynamic loads could be mandatory. The resulting discrete equations for this kind of structures are in fact very stiff and therefore, the computation of long-term convergent responses could be very problematic, even for well-established commercial codes. Achieving robustness requires the development of procedures able to annihilate the unwanted unresolved high-frequency content, while warranting simultaneously preservation of the under-

lying physics. For further development and enhancement of these procedures, it is equally important to take into account implementation aspects regarding source-code reusability and extension. However, the accomplishment of these features is rather effortful.

Reissner [1] formulated a one-dimensional large-strain beam theory for plane deformations of plane beams. Bathe and Boloruchi [2] discussed fundamental aspects regarding the formulation of three-dimensional geometrically nonlinear beam elements. Simo [3] extended the concepts considered by Reissner in [1] to the three-dimensional case, from which resulted the so-called geometrically exact beam theory. Cardona and G eradin [4] developed an objective beam finite element based on the geometrically exact beam theory and a material description of the rotation group, whose composition is performed to the right. Romero and Armero [5] presented a finite element formulation for geometrically exact beams, which is frame-indifferent. Relying on the straightforward interpolation of the directors, the authors provided a detailed derivation of the spatial and temporal discretization. The proposed framework allowed the development of an unconditionally stable time-stepping algorithm that preserves first integrals of motion. Armero and

Cristian Guillermo Gebhardt
c.gebhardt@isd.uni-hannover.de

¹ Institute of Structural Analysis, Leibniz Universit at Hannover and ForWind Hannover, Appelstr. 9A, 30167 Hannover, Germany

Romero [6,7] developed a family of schemes for nonlinear three-dimensional elastodynamics that exhibits controllable numerical dissipation in the high-frequency range. Armero and Romero [8] particularized that integration approach to the Cosserat rod case. In the energy-preserving context, Betsch and Steinmann [9] presented a brief overview of the constrained dynamics of nonlinear beams. In contrast to the standard formulations based on rotational degrees of freedom, the authors proposed the interpolation of a triad consisting of three orthonormal directors, where the mutual orthonormality is achieved by imposing holonomic constraints. Yu et al. [10] considered geometrically exact beams with initially large twisting and large curvature in the context of thin-walled structures. Mäkinen [11] derived an improved version of the formulation proposed by Cardona and G eradin in [4], which, beyond being objective like in its original version, is also path independent. Auricchio et al. [12] emphasized some intrinsic features of the three-dimensional beam model proposed by Simo in [3]. The formulation was also re-derived in a consistent and compact form. Pimenta et al. [13] developed a fully conserving algorithm for the integration of the equations of motion in nonlinear rod dynamics. Romero [14] compared the absolute nodal coordinate and geometrically exact formulations. Pai [15] discussed occurrent problems for different beam theories under large deformations. De Miranda et al. [16] discussed briefly the constitutive assumptions normally done for linear elastic isotropic and orthotropic materials in the framework of thin-walled beams. And very recently, the aero-hydro-servo-elastic simulation framework FAST [17], which employs a multibody formulation based on a predictor-corrector scheme and loose coupling, was enhanced with an angle-based geometrically exact beam finite element for blade calculations [18].

Dvorkin and Bathe [19] developed a four-node shell element for general nonlinear analysis, which is applicable to the analysis of thin and thick shells. In [20], the authors discussed the requirements concerning linear and nonlinear analysis. Choi and Paik [21] presented the development of a four-node shell element for the analysis of structures undergoing large deformations. Betsch and Stein [22,23] developed a four-node shell element that incorporates unmodified three-dimensional constitutive models. This element was improved by means of the enhanced assumed strain method proposed by Simo and Armero [24]. Bischoff and Ramm [25] formulated a geometrically nonlinear version of the enhanced assumed strain approach in terms of Green–Lagrange strains. Sansour et al. [26] combined a geometrically exact shell theory and an integration scheme that preserves first integrals of motion. Betsch et al. [27] exposed a classification of concepts regarding the parametrization of finite rotations in the context of smooth shells. Sansour et al. [28] dealt with a dynamic formulation of shells and the development

of a robust energy-momentum integration scheme. Romero and Armero [29] extended the previously introduced method to the dynamics of geometrically exact shells. Proofs of the numerical properties in the full nonlinear range were also provided. Bauchau et al. [30] developed energy preserving/dissipative schemes for the simulation of multibody systems including shell components. Ozkul [31] presented a finite element for dynamic analysis of shells with general shape. Betsch and S anger [32] dealt with the design of energy-momentum conserving schemes for flexible multibody dynamics by extending the ideas proposed by the same authors in [9]. The approach is based on nonlinear finite element methods for the space discretization of flexible bodies, particularly geometrically exact shells. Vaziri [33] studied the response of shell structures under large deformations and presented a review of the current state-of-the-art with practical suggestions. Campello et al. [34] extended the fully conserving algorithm presented in [13] for the integration of motion in nonlinear shell dynamics. Wu [35] described the nonlinear dynamic behavior of shell structures by means of a vector form intrinsic formulation. Ahmed and Sluys [36] presented a three-dimensional shell element for the dynamic analysis of laminated composites. Pietraszkiewicz and Konopińska [37] reviewed different theoretical, numerical, and experimental approaches to model, analyze and design compound shell structures with junctions. Reinoso and Bl azquez [38] developed an eight-node solid-degenerate shell element, which was reformulated in the context of composite structures by means of the single-layer concept. Caliri et al. [39] presented a very detailed literature review on plate and shell theories for composite structures with remarks regarding the finite element implementation. Ota et al. [40] considered the nonlinear dynamics of thin foldable curved structures that may go through many snapping transitions from a stable configuration to another. And very recently, Gebhardt and Rolfes [41] dealt, in the context of shell structures, with the combination of a mixed finite element and a robust integration scheme, featuring a well-balanced robustness-precision relation.

In this work, we present a new object-oriented framework to study the nonlinear dynamics of slender structures made of composite multilayer materials combining finite element method and multibody system formalism with a robust integration scheme that is presented in a differential-algebraic setting. Each mechanical system under consideration is represented as a collection of infinitely stiff components, such as rigid bodies, and flexible components like geometrically exact beams and solid-degenerate shells. The current approach employs directors instead of standard angle-based parametrizations to describe the orientation of the involved components in combination with the total-Lagrangian description. This setting allows to preserve “by design” the objectivity of the discrete strain measures under rigid space transformations and the path

independence of the formulation under the action of conservative loading. For the spatial discretization, we use low-order interpolations following the “Effective Finite Elements” philosophy proposed by Bucalem and Bathe [42]. The semi-discrete equations are temporally discretized for a fixed time increment with a momentum-preserving, energy-preserving/dissipative method, which allows the annihilation of undesirable effects due to unresolved high-frequency content and provides robustness without compromising the precision of the solution. Some interesting constraints to render more complicated structures without modifying the underlying finite element formulation are introduced. In few words, from a methodological point of view, the novelty of this work is the combination of rigid bodies, geometrically exact beams and solid-degenerate shells, and the time integration with a momentum-preserving, energy-preserving/dissipative method into a single common unifying framework, which is implemented by using the object-oriented programming philosophy. The resulting approach may be used very effectively, for example, in wind energy and aeronautics. To our best knowledge, there is no comprehensive work available in the literature, where all these ingredients are consistently combined with a similar setting in the context of slender structures made of composite multilayer and hyperelastic materials.

The article is organized as follows: Sect. 2 presents the basic mechanical models, comprising a general description and some details of the spatial discretization into finite elements. Section 3 is devoted to the temporal discretization based on a robust scheme. Section 4 presents several constraints that allow to render complex structures. Section 5 presents some examples to show the potential of the framework proposed. Finally, Sect. 6 is dedicated to concluding remarks, limitations and future work. Additionally, “Appendix” presents a summary of the numerical implementation.

2 Basic mechanical models

The current work relies on three basic mechanical models, i.e. rigid bodies, geometrically exact beams and solid-degenerate shells. Even, provided that the modeling of these idealizations is rather a classical topic, the consistent combination within a single framework is still far from trivial. This is mainly due to the very different kinematic descriptions involved. Typically, in the context of rigid bodies and geometrically exact beams, the orientation problem requires to deal with the Lie group $SO(3)$ and its corresponding Lie algebra $\mathfrak{so}(3)$. In the context of director-based shells on the contrary, it is required to deal with the unit 2-sphere S_1^2 , a manifold that does not possess Lie group structure (this is a consequence of the hairy ball theorem [43]). It means that different treatments are required. For instance, a systematic descrip-

tion of rigid bodies and geometrically exact beams can be addressed in a natural way due to the similarities of the kinematic descriptions. However, the combination of these two mechanical models with shells requires devoted handling. Along this section, we describe systematically all the three basic mechanical models by means of unifying approach without the necessity of incurring to rotational degrees of freedom. In a very direct manner, the proposed systematic description allows the combination of the basic mechanical models among them and with the robust integration scheme, which is presented later. Therefore, the present summarized exposure is considered essential for the subsequent steps.

2.1 Rigid body

2.1.1 Kinematic description and weak form of the governing equations

The position at time t , for $t \in [t_1, t_2] \subset \mathbb{R}^+$, of any given point belonging to the rigid body shown in Fig. 1, namely $\mathbf{x}(t) \in \mathcal{X}_t \subseteq \mathbb{R}^3$, can be written as

$$\mathbf{x}(\boldsymbol{\theta}; t) = \bar{\mathbf{x}}(t) + \theta^1 \mathbf{d}_1(t) + \theta^2 \mathbf{d}_2(t) + \theta^3 \mathbf{d}_3(t), \quad (1)$$

in which $\bar{\mathbf{x}} \in \bar{\mathcal{X}} \subseteq \mathbb{R}^3$ is the position vector of a reference point and $\mathbf{d}_1, \mathbf{d}_2$ and \mathbf{d}_3 are three mutually orthonormal directors. On that basis, the rotation tensor can be simply obtained as $\mathbf{R} = \mathbf{d}_i \otimes \mathbf{i}^i \in SO(3)$, in which \mathbf{i}^i for i from 1 to 3 stands for the elements of the dual basis of \mathbb{E}^3 (\mathbb{R}^3 with the standard Euclidean structure), i.e. the space of row vectors. $\boldsymbol{\theta} = (\theta^1, \theta^2, \theta^3)$ is a set of parameters chosen in the way that $\bar{\boldsymbol{\theta}} = \theta^1 \mathbf{d}_1 + \theta^2 \mathbf{d}_2 + \theta^3 \mathbf{d}_3$ describes the position of any given point of the body relative to the reference point described by $\bar{\mathbf{x}}$. Analogously, the velocity, namely $\mathbf{v}(t) \in \mathcal{V}_t \subseteq \mathbb{R}^3$, can be written as

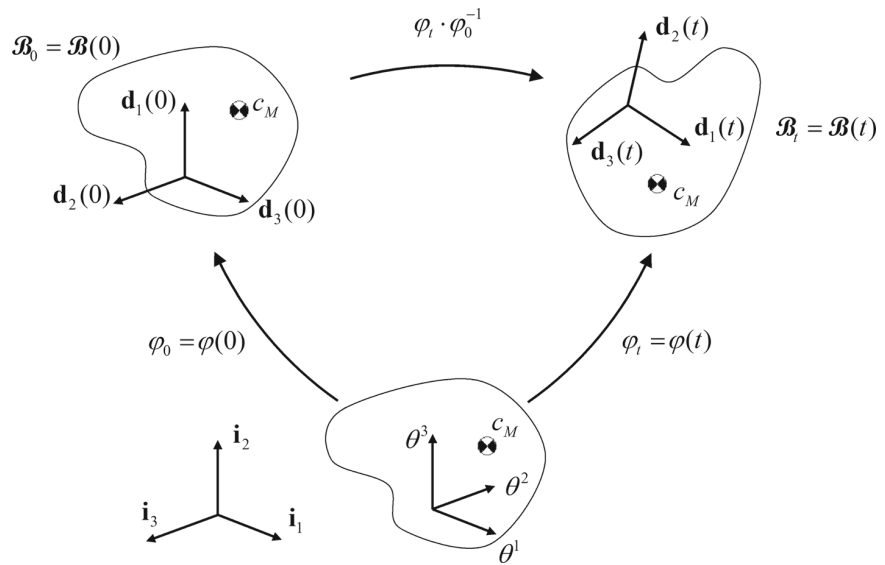
$$\mathbf{v}(\boldsymbol{\theta}; t) = \bar{\mathbf{v}}(t) + \theta^1 \mathbf{w}_1(t) + \theta^2 \mathbf{w}_2(t) + \theta^3 \mathbf{w}_3(t), \quad (2)$$

in which $\bar{\mathbf{v}} \in \bar{\mathcal{V}} \subseteq \mathbb{R}^3$ is the translational velocity of the adopted reference point and $\mathbf{w}_1, \mathbf{w}_2$ and \mathbf{w}_3 are three director velocity vectors. The dynamic behavior of the rigid body can be formulated as

$$\int_{\mathcal{B}_0} \{ \langle \delta \mathbf{v}, \mathbf{I}(\mathbf{v}) - \mathbf{I}(\mathbf{x}) \rangle + \langle \delta \mathbf{x}, \dot{\mathbf{I}}(\mathbf{v}) - \mathbf{f}^{\text{ext}} + \mathbf{H}^T \cdot \boldsymbol{\lambda} \rangle + \langle \delta \boldsymbol{\lambda}, \mathbf{h} \rangle \} d\mathcal{B}_0 = 0, \quad (3)$$

where \mathcal{B}_0 is an open subset of \mathbb{R}^3 and $\langle \cdot, \cdot \rangle : V \times V^* \rightarrow \mathbb{R}$ is a dual pairing, in which V is a vector space (whose elements are called vectors) and V^* is its algebraic dual space (whose elements are called covectors or one-forms). $\delta \mathbf{v} \in T_{\mathbf{v}}\mathcal{V}$ and $\delta \mathbf{x} \in T_{\mathbf{x}}\mathcal{X}$ are admissible variations of the position and the velocity vectors, respectively. $\mathbf{I}(\mathbf{v})$ and

Fig. 1 The rigid body concept—time evolution among configurations through the regular motion $\varphi_t \circ \varphi_0^{-1}$



$l(\mathbf{x})$, both in $T_v^* \mathcal{V}$, are the velocity-based momentum and the displacement-based momentum densities, correspondingly. $\dot{l}(\mathbf{v})$ and $\mathbf{f}^{\text{ext}}(\mathbf{x})$, both in $T_x^* \mathcal{X}$, are the time rate of the velocity-based momentum and the external force densities, respectively. $\mathbf{H} : \mathbb{R}^n \times T_x \mathcal{X} \rightarrow \mathbb{R}$ is the Jacobian matrix of $\mathbf{h} = \mathbf{0} \in \mathbb{R}^n$, a finite-dimensional set of holonomic restrictions and $\delta \lambda$ is an admissible variation of the corresponding Lagrange multipliers $\lambda : [t_1, t_2] \rightarrow \mathbb{R}^n$. At this point, it should be clear that a state-space description is adopted instead a phase-state description. This setting (in contrast to approaches based only on generalized coordinates) is necessary to include in a natural way the dissipation of energy at the level of the generalized velocities for the flexible bodies that are described along the next section. Further details on the geometrical aspects introduced above can be found in [44,45] within the context of classical mechanics or in [46,47] within an engineering context. After performing the integration over the entire volume, the governing equation for the rigid body, in its weak form, becomes

$$\begin{aligned}
 & \langle \delta \bar{\mathbf{v}}, l^0(\bar{\mathbf{v}}, \mathbf{w}_1, \mathbf{w}_2, \mathbf{w}_3) - l^0(\bar{\mathbf{x}}, \mathbf{d}_1, \mathbf{d}_2, \mathbf{d}_3) \rangle \\
 & + \langle \delta \bar{\mathbf{x}}, l^0(\bar{\mathbf{v}}, \mathbf{w}_1, \mathbf{w}_2, \mathbf{w}_3) - \mathbf{f}^{0,\text{ext}} + \mathbf{H}_0^T \cdot \lambda \rangle \\
 & + \langle \delta \mathbf{w}_1, l^1(\bar{\mathbf{v}}, \mathbf{w}_1, \mathbf{w}_2, \mathbf{w}_3) - l^1(\bar{\mathbf{x}}, \mathbf{d}_1, \mathbf{d}_2, \mathbf{d}_3) \rangle \\
 & + \langle \delta \mathbf{d}_1, l^1(\bar{\mathbf{v}}, \mathbf{w}_1, \mathbf{w}_2, \mathbf{w}_3) - \mathbf{f}^{1,\text{ext}} + \mathbf{H}_1^T \cdot \lambda \rangle \\
 & + \langle \delta \mathbf{w}_2, l^2(\bar{\mathbf{v}}, \mathbf{w}_1, \mathbf{w}_2, \mathbf{w}_3) - l^2(\bar{\mathbf{x}}, \mathbf{d}_1, \mathbf{d}_2, \mathbf{d}_3) \rangle \\
 & + \langle \delta \mathbf{d}_2, l^2(\bar{\mathbf{v}}, \mathbf{w}_1, \mathbf{w}_2, \mathbf{w}_3) - \mathbf{f}^{2,\text{ext}} + \mathbf{H}_2^T \cdot \lambda \rangle \\
 & + \langle \delta \mathbf{w}_3, l^3(\bar{\mathbf{v}}, \mathbf{w}_1, \mathbf{w}_2, \mathbf{w}_3) - l^3(\bar{\mathbf{x}}, \mathbf{d}_1, \mathbf{d}_2, \mathbf{d}_3) \rangle \\
 & + \langle \delta \mathbf{d}_3, l^3(\bar{\mathbf{v}}, \mathbf{w}_1, \mathbf{w}_2, \mathbf{w}_3) - \mathbf{f}^{3,\text{ext}} + \mathbf{H}_3^T \cdot \lambda \rangle \\
 & + \langle \delta \lambda, \mathbf{h} \rangle = 0.
 \end{aligned} \tag{4}$$

Given the mass density ϱ_0 , the generalized velocity-based momentum $l^i(\bar{\mathbf{v}}, \mathbf{w}_1, \mathbf{w}_2, \mathbf{w}_3)$ is defined as $\mathcal{E}_{i0} \bar{\mathbf{v}} + \mathcal{E}_{i1} \mathbf{w}_1 + \mathcal{E}_{i2} \mathbf{w}_2 + \mathcal{E}_{i3} \mathbf{w}_3$ and the generalized displacement-based momentum $l^i(\bar{\mathbf{x}}, \mathbf{d}_1, \mathbf{d}_2, \mathbf{d}_3)$ as $\mathcal{E}_{i0} \bar{\mathbf{x}} + \mathcal{E}_{i1} \mathbf{d}_1 + \mathcal{E}_{i2} \mathbf{d}_2 + \mathcal{E}_{i3} \mathbf{d}_3$, where the symmetric mass inertia coefficients \mathcal{E}_{ij} are computed by means of $\int_{\mathcal{B}_0} \varrho_0 \theta^i \theta^j d\mathcal{B}_0$ for i and j from 0 to 3. For the case i (j) equal to zero, θ^i (θ^j) takes a constant unit value. This setting allows to consider zeroth-order inertia \mathcal{E}_{00} , first-order inertia \mathcal{E}_{0i} for i greater than zero, and second-order inertia \mathcal{E}_{ij} for i and j greater than zero. It enables the handling of rigid bodies, in which the reference point does not coincide with the center of mass. \mathbf{H}_0 and \mathbf{H}_i (for $i = 1, 2, 3$) stand for $\frac{\partial \mathbf{h}}{\partial \bar{\mathbf{x}}}$ and $\frac{\partial \mathbf{h}}{\partial \mathbf{d}_i}$, respectively. Finally, the mutual orthogonality condition among the directors is simply included by considering

$$\mathbf{h}^{\text{int}}(t) = \begin{Bmatrix} \mathbf{d}_1(t) \cdot \mathbf{d}_1(t) - \mathbf{d}_1(0) \cdot \mathbf{d}_1(0) \\ \mathbf{d}_2(t) \cdot \mathbf{d}_2(t) - \mathbf{d}_2(0) \cdot \mathbf{d}_2(0) \\ \mathbf{d}_3(t) \cdot \mathbf{d}_3(t) - \mathbf{d}_3(0) \cdot \mathbf{d}_3(0) \\ 2[\mathbf{d}_2(t) \cdot \mathbf{d}_3(t) - \mathbf{d}_2(0) \cdot \mathbf{d}_3(0)] \\ 2[\mathbf{d}_1(t) \cdot \mathbf{d}_3(t) - \mathbf{d}_1(0) \cdot \mathbf{d}_3(0)] \\ 2[\mathbf{d}_1(t) \cdot \mathbf{d}_2(t) - \mathbf{d}_1(0) \cdot \mathbf{d}_2(0)] \end{Bmatrix} = \mathbf{0}, \tag{5}$$

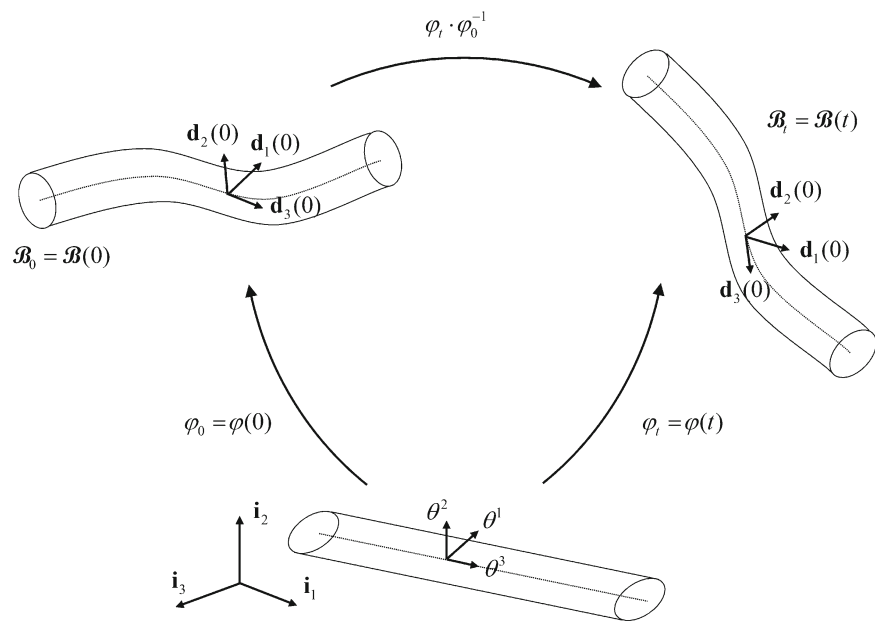
which is in fact the internal constraint that completes the dynamic description, for more details see [48].

2.2 Geometrically exact beam

2.2.1 Kinematic description and weak form of the governing equations

The position at time t of any given point belonging to the beam shown in Fig. 2 can be written as

Fig. 2 The geometrically exact beam concept—time evolution among configurations through the regular motion $\varphi_t \circ \varphi_0^{-1}$



$$\mathbf{x}(\boldsymbol{\theta}; t) = \bar{\mathbf{x}}(\theta^3; t) + \theta^1 \mathbf{d}_1(\theta^3; t) + \theta^2 \mathbf{d}_2(\theta^3; t), \quad (6)$$

in which $\bar{\mathbf{x}} \in \bar{\mathcal{X}} \subseteq \mathbb{R}^3$ is the position vector of the middle curve and \mathbf{d}_1 and \mathbf{d}_2 together with \mathbf{d}_3 are three mutually orthonormal directors. $\boldsymbol{\theta} = (\theta^1, \theta^2, \theta^3)$ is a set of parameters chosen in the way that $\bar{\boldsymbol{\theta}} = \theta^1 \mathbf{d}_1 + \theta^2 \mathbf{d}_2$ describes the cross section at the station $\mathcal{L}(\theta^3)$, which intersects the middle curve and $\mathbf{x} = \mathbf{x}(\boldsymbol{\theta}; t)$ is the given parametrization rule in time and space. The spatial metric structure induced by this construction is

$$\mathbf{G} = \delta_{ij} \frac{\partial x^i}{\partial \theta^a} \frac{\partial x^j}{\partial \theta^b} \mathbf{g}^a \otimes \mathbf{g}^b, \quad (7)$$

where δ_{ij} are the components of the Euclidean metric tensor, $\mathbf{g}_a \in T_{\boldsymbol{\theta}} \mathcal{X}$ defined as $\mathbf{g}_a = \frac{\partial x^i}{\partial \theta^a} \mathbf{i}_i$ with \mathbf{i}_i for i from 1 to 3 standing for the elements of the standard orthonormal basis in \mathbb{R}^3 , i.e. the space of column vectors, and the elements of the covariant basis $\mathbf{g}^a \in T_{\boldsymbol{\theta}}^* \mathcal{X}$ defined in the usual form, this is $\mathbf{g}^b(\mathbf{g}_a) = \delta_b^a$, the elements of the contravariant basis. δ_{ij} and δ_b^a are simply Kronecker deltas. At this point, it is certain that $\mathbf{G} : T_{\boldsymbol{\theta}} \mathcal{X} \times T_{\boldsymbol{\theta}} \mathcal{X} \rightarrow \mathbb{R}^+$. Then the displacement-based doubly-covariant Green–Lagrange strain tensor is

$$\bar{\mathbf{E}}_b(\boldsymbol{\theta}; t) = \frac{1}{2} \{ \mathbf{G}[\mathbf{x}(\boldsymbol{\theta}; t)] - \mathbf{G}[\mathbf{x}(\boldsymbol{\theta}; 0)] \}, \quad (8)$$

which in the context of geometrically exact beams can be reduced after eliminating quadratic strain terms as

$$\bar{\mathbf{E}}_{ij}(\boldsymbol{\theta}; t) \approx \mathbb{S} \{ \delta_{i3} \delta_{jk} [\Gamma^k(\theta^3; t) - \varepsilon_{lm}^k \bar{\theta}^l \Omega^m(\theta^3; t)] \}. \quad (9)$$

where $\mathbb{S}(\cdot)$ denotes symmetrization, $\Gamma^i(\theta^3; t)$ defined as $\mathbf{d}_i(\theta^3; t) \cdot \bar{\mathbf{x}}'(\theta^3; t) - \mathbf{d}_i(\theta^3; 0) \cdot \bar{\mathbf{x}}'(\theta^3; 0)$ is a first strain measure (for shear refer to first and second components and for elongation refer to the third one), $\Omega^i(\theta^3; t)$ defined as $\frac{1}{2} \varepsilon_{ijk} [\mathbf{d}_k(\theta^3; t) \cdot \mathbf{d}'_j(\theta^3; t) - \mathbf{d}_k(\theta^3; 0) \cdot \mathbf{d}'_j(\theta^3; 0)]$ is a second strain measure (for bending refer to first and second components and for torsion refer to the third one) and ε_{ijk} is the alternating symbol that allows the computation of the cross product in the three-dimensional Euclidean space. Analogously, the velocity can be written as

$$\mathbf{v}(\boldsymbol{\theta}; t) = \bar{\mathbf{v}}(\theta^3; t) + \theta^1 \mathbf{w}_1(\theta^3; t) + \theta^2 \mathbf{w}_2(\theta^3; t), \quad (10)$$

in which $\bar{\mathbf{v}} \in \bar{\mathcal{V}} \subseteq \mathbb{R}^3$ is the translational velocity of the middle curve and $\mathbf{w}_1, \mathbf{w}_2$ together with \mathbf{w}_3 are three director velocity vectors. The dynamic behavior of the geometrically exact beam can be formulated as

$$\int_{\mathcal{L}_0} \int_{\mathcal{A}_0} \{ \langle \delta \mathbf{v}, \mathbf{l}(\mathbf{v}) - \mathbf{l}(\mathbf{x}) \rangle + \langle \delta \mathbf{x}, \mathbf{f}^{\text{int}}(\mathbf{x}, \mathbf{S}^{\sharp}) \rangle + \langle \dot{\mathbf{l}}(\mathbf{v}) - \mathbf{f}^{\text{ext}} + \mathbf{H}^T \cdot \boldsymbol{\lambda} \rangle + \langle \delta \boldsymbol{\lambda}, \mathbf{h} \rangle \} d\mathcal{A}_0 d\mathcal{L}_0 = 0, \quad (11)$$

where \mathcal{A}_0 represents the cross-sectional area and \mathcal{L}_0 stands for the arc length in the original configuration, $\mathbf{f}^{\text{int}}(\mathbf{x}, \mathbf{S}^{\sharp}) \in T_{\mathbf{x}}^* \mathcal{X}$ is the internal force and $\mathbf{S}^{\sharp} \in T_{\mathbf{x}(0)} \mathcal{X}_0 \times T_{\mathbf{x}(0)} \mathcal{X}_0$ is an appropriate stress definition, here the second Piola–Kirchhoff stress tensor.

Given two mutually orthonormal directors \mathbf{d}_1 and \mathbf{d}_2 , a third director \mathbf{d}_3 could be simply computed as $\mathbf{d}_1 \times \mathbf{d}_2$. This description would lead to a two-director formulation. An alternative to this formulation results from the additional consideration of \mathbf{d}_3 in combination with the mutual

orthonormality condition for the three directors as already introduced by Eq. (5). The resulting representation is a so-called three-director formulation, which we adopt to facilitate the combination among beams and rigid bodies. After introducing explicitly \mathbf{d}_3 in the variational principle and performing the integration over the cross section, the governing equations for the geometrically exact beam, in its weak form, becomes

$$\int_{\mathcal{L}_0} \{ \langle \delta \bar{\mathbf{v}}, \mathbf{l}^0(\bar{\mathbf{v}}, \mathbf{w}_1, \mathbf{w}_2) - \mathbf{l}^0(\bar{\mathbf{x}}, \mathbf{d}_1, \mathbf{d}_2) \rangle + \langle \delta \bar{\mathbf{x}}, \mathbf{f}^{0,\text{int}}(\mathbf{d}_1, \mathbf{d}_2, \mathbf{d}_3, N) + \mathbf{l}^0(\bar{\mathbf{v}}, \mathbf{w}_1, \mathbf{w}_2) - \mathbf{f}^{0,\text{ext}} + \mathbf{H}_0^T \cdot \boldsymbol{\lambda} \rangle + \langle \delta \mathbf{w}_1, \mathbf{l}^1(\bar{\mathbf{v}}, \mathbf{w}_1, \mathbf{w}_2) - \mathbf{l}^1(\bar{\mathbf{x}}, \mathbf{d}_1, \mathbf{d}_2) \rangle + \langle \delta \mathbf{d}_1, \mathbf{f}^{1,\text{int}}(\bar{\mathbf{x}}, \mathbf{d}_2, \mathbf{d}_3, N, \mathbf{M}) + \mathbf{l}^1(\bar{\mathbf{v}}, \mathbf{w}_1, \mathbf{w}_2) - \mathbf{f}^{1,\text{ext}} + \mathbf{H}_1^T \cdot \boldsymbol{\lambda} \rangle + \langle \delta \mathbf{w}_2, \mathbf{l}^2(\bar{\mathbf{v}}, \mathbf{w}_1, \mathbf{w}_2) - \mathbf{l}^2(\bar{\mathbf{x}}, \mathbf{d}_1, \mathbf{d}_2) \rangle + \langle \delta \mathbf{d}_2, \mathbf{f}^{2,\text{int}}(\bar{\mathbf{x}}, \mathbf{d}_1, \mathbf{d}_3, N, \mathbf{M}) + \mathbf{l}^2(\bar{\mathbf{v}}, \mathbf{w}_1, \mathbf{w}_2) - \mathbf{f}^{2,\text{ext}} + \mathbf{H}_2^T \cdot \boldsymbol{\lambda} \rangle + \langle \delta \mathbf{d}_3, \mathbf{f}^{3,\text{int}}(\bar{\mathbf{x}}, \mathbf{d}_1, \mathbf{d}_2, N, \mathbf{M}) - \mathbf{f}^{3,\text{ext}} + \mathbf{H}_3^T \cdot \boldsymbol{\lambda} \rangle + \langle \delta \boldsymbol{\lambda}, \mathbf{h} \rangle \} d\mathcal{L}_0 = 0. \tag{12}$$

The generalized velocity-based momentum $\mathbf{l}^i(\bar{\mathbf{v}}, \mathbf{w}_1, \mathbf{w}_2)$ is defined as $\mathcal{E}_{i0}\bar{\mathbf{v}} + \mathcal{E}_{i1}\mathbf{w}_1 + \mathcal{E}_{i2}\mathbf{w}_2$ and the generalized displacement-based momentum $\mathbf{l}^i(\bar{\mathbf{x}}, \mathbf{d}_1, \mathbf{d}_2)$ as $\mathcal{E}_{i0}\dot{\bar{\mathbf{x}}} + \mathcal{E}_{i1}\dot{\mathbf{d}}_1 + \mathcal{E}_{i2}\dot{\mathbf{d}}_2$, where \mathcal{E}_{ij} is computed by means of $\int_{\mathcal{A}_0} \varrho_0 \theta^i \theta^j d\mathcal{A}_0$ for i and j from 0 to 2. This consideration allows the handling of cross sections with arbitrary shape and material properties, which exactly applies to the case of modern slender structures made of composite multilayer materials. Given the beam potential energy density per unit length V^{beam} , the internal force and moment densities per unit length are $\mathbf{N} = \frac{\partial V^{\text{beam}}}{\partial \boldsymbol{\Gamma}}$ and $\mathbf{M} = \frac{\partial V^{\text{beam}}}{\partial \boldsymbol{\Omega}}$, respectively. The components of the cross-sectional tangent constitutive matrices are in principle computed as

$$\begin{aligned} (\mathfrak{C}_{\Gamma\Gamma})_{ij} &= \int_{\mathcal{A}_0} \mathfrak{C}^{IJKL} \frac{\partial \bar{E}_{IJ}}{\partial \Gamma^i} \frac{\partial \bar{E}_{KL}}{\partial \Gamma^j} d\mathcal{A}_0, \\ (\mathfrak{C}_{\Gamma\Omega})_{ij} &= \int_{\mathcal{A}_0} \mathfrak{C}^{IJKL} \frac{\partial \bar{E}_{IJ}}{\partial \Gamma^i} \frac{\partial \bar{E}_{KL}}{\partial \Omega^j} d\mathcal{A}_0, \\ (\mathfrak{C}_{\Omega\Gamma})_{ij} &= \int_{\mathcal{A}_0} \mathfrak{C}^{IJKL} \frac{\partial \bar{E}_{IJ}}{\partial \Omega^i} \frac{\partial \bar{E}_{KL}}{\partial \Gamma^j} d\mathcal{A}_0, \\ (\mathfrak{C}_{\Omega\Omega})_{ij} &= \int_{\mathcal{A}_0} \mathfrak{C}^{IJKL} \frac{\partial \bar{E}_{IJ}}{\partial \Omega^i} \frac{\partial \bar{E}_{KL}}{\partial \Omega^j} d\mathcal{A}_0. \end{aligned} \tag{13}$$

where \mathfrak{C}^{IJKL} represents the components of the tangent elasticity tensor and \bar{E}_{IJ} stands for the components of the strain tensor presented by Eq. (9). For thin-walled structures, additional assumptions about the strain and stress states may

be necessary. At this point, warping effects are completely neglected. In the case of the blade of a wind turbine, which is in some regions far away from the thin-walled structure hypothesis and also non-negligible variations of the cross section may take place, the primary warping due to torsion ought to be combined with the consideration of secondary warping due to shear. This would require to include additional displacements fields, see for example [49]. Therefore, standard assumptions regarding warping effects may result not adequate. However, a detailed discussion and treatment of a this aspect is beyond the scope of the current work. The acting internal load densities are indicated as follows:

$$\begin{aligned} \mathbf{f}^{0,\text{int}}(\mathbf{d}_1, \mathbf{d}_2, \mathbf{d}_3, N) &= \left[\frac{\partial \boldsymbol{\Gamma}}{\partial \bar{\mathbf{x}}}(\mathbf{d}_1, \mathbf{d}_2, \mathbf{d}_3) \right]^T \cdot \mathbf{N}, \\ \mathbf{f}^{1,\text{int}}(\bar{\mathbf{x}}, \mathbf{d}_2, \mathbf{d}_3, N, \mathbf{M}) &= \left[\frac{\partial \boldsymbol{\Gamma}}{\partial \mathbf{d}_1}(\bar{\mathbf{x}}, \mathbf{d}_2, \mathbf{d}_3) \right]^T \cdot \mathbf{N} \\ &\quad + \left[\frac{\partial \boldsymbol{\Omega}}{\partial \mathbf{d}_1}(\mathbf{d}_2, \mathbf{d}_3) \right]^T \cdot \mathbf{M}, \\ \mathbf{f}^{2,\text{int}}(\bar{\mathbf{x}}, \mathbf{d}_1, \mathbf{d}_3, N, \mathbf{M}) &= \left[\frac{\partial \boldsymbol{\Gamma}}{\partial \mathbf{d}_2}(\bar{\mathbf{x}}, \mathbf{d}_1, \mathbf{d}_3) \right]^T \cdot \mathbf{N} \\ &\quad + \left[\frac{\partial \boldsymbol{\Omega}}{\partial \mathbf{d}_2}(\mathbf{d}_1, \mathbf{d}_3) \right]^T \cdot \mathbf{M}, \\ \mathbf{f}^{3,\text{int}}(\bar{\mathbf{x}}, \mathbf{d}_1, \mathbf{d}_2, N, \mathbf{M}) &= \left[\frac{\partial \boldsymbol{\Gamma}}{\partial \mathbf{d}_3}(\bar{\mathbf{x}}, \mathbf{d}_1, \mathbf{d}_2) \right]^T \cdot \mathbf{N} \\ &\quad + \left[\frac{\partial \boldsymbol{\Omega}}{\partial \mathbf{d}_3}(\mathbf{d}_1, \mathbf{d}_2) \right]^T \cdot \mathbf{M}. \end{aligned} \tag{14}$$

The geometrically exact beam model presented is able to take into account coupling terms not only at the level of the stiffness, but also at the level of the mass/inertia. This feature is of high interest in wind energy or aeronautic applications, specially to evaluate static and dynamic critical behavior of slender blades made of multilayer composite materials like divergence or flutter.

2.2.2 Spatial discretization

To spatially discretize the geometrically exact beam into two-node finite elements, we approximate the generalized displacement fields $\bar{\mathbf{x}}$ and \mathbf{d}_i as well as the generalized velocity fields $\bar{\mathbf{v}}$ and \mathbf{w}_i and their admissible variations as follows: $\bar{\mathbf{x}}(\theta^3; t) \approx N^I(\theta^3)\bar{\mathbf{x}}_I(t)$, $\mathbf{d}_i(\theta^3; t) \approx N^I(\theta^3)\mathbf{d}_{i,I}(t)$, $\bar{\mathbf{v}}(\theta^3; t) \approx N^I(\theta^3)\bar{\mathbf{v}}_I(t)$, $\mathbf{w}_i(\theta^3; t) \approx N^I(\theta^3)\mathbf{w}_{i,I}(t)$, $\delta \bar{\mathbf{x}}(\theta^3) \approx N^I(\theta^3)\delta \bar{\mathbf{x}}_I$, $\delta \mathbf{d}_i(\theta^3) \approx N^I(\theta^3)\delta \mathbf{d}_{i,I}$, $\delta \bar{\mathbf{v}}(\theta^3) \approx N^I(\theta^3)\delta \bar{\mathbf{v}}_I$ and $\delta \mathbf{w}_i(\theta^3) \approx N^I(\theta^3)\delta \mathbf{w}_{i,I}$ for I from 1 to 2, and $N^I(\theta)$ denotes linear Lagrange-type functions of $\theta^3 \in [-1, +1]$. In addition, the mutual orthogonality condition among the directors is also imposed discretely at the nodes. Finally, the semi-discrete version of the weak form of the governing equations for a single finite element becomes

$$\begin{aligned}
& \left\langle \delta \hat{\mathbf{v}}, \int_{-1}^{+1} \mathbf{N}^T \cdot [I^0(\bar{\mathbf{v}}, \mathbf{w}_1, \mathbf{w}_2) - I^0(\bar{\mathbf{x}}, \mathbf{d}_1, \mathbf{d}_2)] \frac{\partial \mathcal{L}_0}{\partial \theta^3} d\theta^3 \right\rangle \\
& + \left\langle \delta \hat{\mathbf{w}}_1, \int_{-1}^{+1} \mathbf{N}^T \cdot [I^1(\bar{\mathbf{v}}, \mathbf{w}_1, \mathbf{w}_2) - I^1(\bar{\mathbf{x}}, \mathbf{d}_1, \mathbf{d}_2)] \frac{\partial \mathcal{L}_0}{\partial \theta^3} d\theta^3 \right\rangle \\
& + \left\langle \delta \hat{\mathbf{w}}_2, \int_{-1}^{+1} \mathbf{N}^T \cdot [I^2(\bar{\mathbf{v}}, \mathbf{w}_1, \mathbf{w}_2) - I^2(\bar{\mathbf{x}}, \mathbf{d}_1, \mathbf{d}_2)] \frac{\partial \mathcal{L}_0}{\partial \theta^3} d\theta^3 \right\rangle \\
& + \left\langle \delta \hat{\mathbf{x}}, \int_{-1}^{+1} \mathbf{N}^T \cdot [f^{0,\text{int}}(\mathbf{d}_1, \mathbf{d}_2, \mathbf{d}_3, N) \right. \\
& \left. + I^0(\bar{\mathbf{v}}, \mathbf{w}_1, \mathbf{w}_2) - f^{0,\text{ext}}] + \mathbf{H}_0^T \cdot \mathbf{N}_\lambda \cdot \boldsymbol{\lambda} \right\} \frac{\partial \mathcal{L}_0}{\partial \theta^3} d\theta^3 \\
& + \left\langle \delta \hat{\mathbf{d}}_1, \int_{-1}^{+1} \mathbf{N}^T \cdot [f^{1,\text{int}}(\bar{\mathbf{x}}, \mathbf{d}_2, \mathbf{d}_3, N, \mathbf{M}) \right. \\
& \left. + I^1(\bar{\mathbf{v}}, \mathbf{w}_1, \mathbf{w}_2) - f^{1,\text{ext}}] + \mathbf{H}_1^T \cdot \mathbf{N}_\lambda \cdot \boldsymbol{\lambda} \right\} \frac{\partial \mathcal{L}_0}{\partial \theta^3} d\theta^3 \\
& + \left\langle \delta \hat{\mathbf{d}}_2, \int_{-1}^{+1} \mathbf{N}^T \cdot [f^{2,\text{int}}(\bar{\mathbf{x}}, \mathbf{d}_1, \mathbf{d}_3, N, \mathbf{M}) \right. \\
& \left. + I^2(\bar{\mathbf{v}}, \mathbf{w}_1, \mathbf{w}_2) - f^{2,\text{ext}}] + \mathbf{H}_2^T \cdot \mathbf{N}_\lambda \cdot \boldsymbol{\lambda} \right\} \frac{\partial \mathcal{L}_0}{\partial \theta^3} d\theta^3 \\
& + \left\langle \delta \hat{\mathbf{d}}_3, \int_{-1}^{+1} \mathbf{N}^T \cdot [f^{3,\text{int}}(\bar{\mathbf{x}}, \mathbf{d}_1, \mathbf{d}_2, N, \mathbf{M}) - f^{3,\text{ext}}] \right. \\
& \left. + \mathbf{H}_3^T \cdot \mathbf{N}_\lambda \cdot \boldsymbol{\lambda} \right\} \frac{\partial \mathcal{L}_0}{\partial \theta^3} d\theta^3 \\
& + \left\langle \delta \hat{\boldsymbol{\lambda}}, \int_{-1}^{+1} \mathbf{N}_\lambda^T \cdot \mathbf{h} \frac{\partial \mathcal{L}_0}{\partial \theta^3} d\theta^3 \right\rangle = 0,
\end{aligned} \tag{15}$$

where $\hat{(\cdot)}$ denotes nodal variables, \mathbf{N} is the matrix containing the shape functions and \mathbf{N}_λ is a collocation matrix to set discretely the constraints at the nodes.

As a consequence of the adopted discrete imposition of the internal constraints, the approximation of the rotation tensor is given by

$$\begin{aligned}
\mathbf{R}(\theta^3; t) & \approx N^1(\theta^3) \mathbf{d}_{i,1}(t) \otimes \mathbf{i}^i + N^2(\theta^3) \mathbf{d}_{i,2}(t) \otimes \mathbf{i}^i \\
& = N^1(\theta^3) \mathbf{R}_1(t) + N^2(\theta^3) \mathbf{R}_2(t),
\end{aligned} \tag{16}$$

which does not belong in general to $\text{SO}(3)$, except at θ^3 equal to -1 or $+1$, and for the case \mathbf{R}_1 equal to \mathbf{R}_2 . This lack of orthonormality of the directors, i.e. the unit length is not preserved and the orthogonality is lost, requires finer discretizations than standard beam elements equipped with angle-based parametrizations, but at the same time, it does possess a very important feature, since this discrete setting preserves the objectivity, invariance of the discrete strain measures under rigid body motions. Furthermore, the path independence is guaranteed, e.g. for conservative actions the work produced through any arbitrary closed path is identically zero, see for instance [5] and [9]. The second property is destroyed when updated-Lagrangian approaches are adopted, and the first one is destroyed when the spatial descriptions of the rotation tensor based on the Cartesian rotation vector are employed. Contrarily, the material description

of the rotation tensor based on the Cartesian rotation vector does not destroy the objectivity of the formulation, see for example [4] und [11]. Pimenta et al. [13] and Gay Neto [50] developed formulations for geometrically exact beams by using the Rodrigues rotation parameters, with which the authors achieved the objectivity at the discrete level. Alternatively, Ghosh and Roy [51] developed a frame-invariant scheme using the rotation vector parametrization in the context of an Eulerian formulation. Since we want to analyze slender structures with variable properties along their length, the demand for finer meshes does not represent a problem. To capture the nonlinear dynamics of such a kind of structures accurately finer meshes are necessary anyway. For an exhaustive review and classification in regard to the interpolation of rotations in the context of geometrically exact beams, the reader is referred to [52].

2.3 Solid-degenerate shell

2.3.1 Kinematic description and weak form of the governing equations

The position at time t of any given point belonging to the shell shown in Fig. 3 can be written as

$$\mathbf{x}(\boldsymbol{\theta}; t) = \bar{\mathbf{x}}(\theta^1, \theta^2; t) + \theta^3 \frac{\vartheta}{2} \mathbf{d}(\theta^1, \theta^2; t), \tag{17}$$

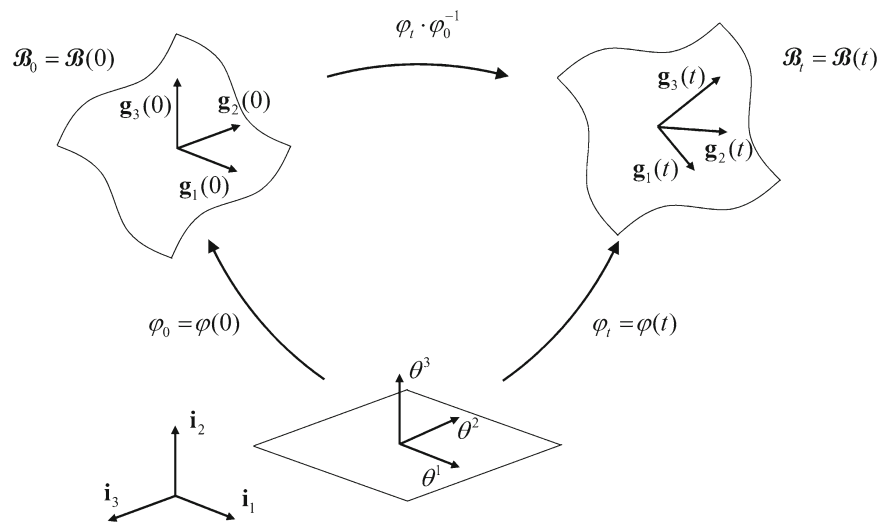
in which $\bar{\mathbf{x}} \in \bar{\mathcal{X}} \subseteq \mathbb{R}^3$ is the position vector of the middle surface, ϑ represents the thickness of the shell and $\mathbf{d} \in \mathcal{D} \subseteq \mathbb{R}^3$ is an extensible director, which admits multiplicative decomposition, i.e. $\mathbf{d} = d \hat{\mathbf{d}}$ with $d \in \mathbb{R}^+$ and $\hat{\mathbf{d}} \in \mathbb{S}_1^2$. $\boldsymbol{\theta} = (\theta^1, \theta^2, \theta^3)$ is a set of parameters chosen in the way that $\bar{\boldsymbol{\theta}} = (\theta^1, \theta^2, 0)$ describes the middle surface. For instance, we can choose $\boldsymbol{\theta}$ to span the domain \mathbb{D} , such as $\mathbb{D} := \{[-1, 1] \times [-1, 1] \times [-1, 1]\}$. The spatial metric structure induced by this construction agrees with Eq. (8). Analogously, the velocity can be written as

$$\mathbf{v}(\boldsymbol{\theta}; t) = \bar{\mathbf{v}}(\theta^1, \theta^2; t) + \theta^3 \frac{\vartheta}{2} \mathbf{w}(\theta^1, \theta^2; t), \tag{18}$$

in which $\bar{\mathbf{v}} \in \bar{\mathcal{V}} \subseteq \mathbb{R}^3$ is the translational velocity of the middle surface and $\mathbf{w} \in \mathcal{W} \subseteq \mathbb{R}^3$ is the director velocity. By employing the same idea applied already for the rigid body and the geometrically exact beam, the governing equation for the solid-degenerate shell, in its weak form, becomes

$$\begin{aligned}
& \int_{\mathbb{D}} \{ \langle \delta \mathbf{v}, \mathbf{l}(\mathbf{v}) - \mathbf{l}(\mathbf{x}) \rangle + \langle \delta \mathbf{x}, \mathbf{f}^{\text{int}}(\mathbf{x}, \mathbf{S}^\sharp) + \dot{\mathbf{l}}(\mathbf{v}) - \mathbf{f}^{\text{ext}} \\
& \left. + \mathbf{H}^T \cdot \boldsymbol{\lambda} \right\} + \langle \delta \boldsymbol{\lambda}, \mathbf{h} \rangle + \langle \delta \tilde{\mathbf{E}}_b, \mathbf{S}^\sharp \rangle \sqrt{\det[\mathbf{G}(\boldsymbol{\theta}; 0)]} d^3 \boldsymbol{\theta},
\end{aligned} \tag{19}$$

Fig. 3 The solid-degenerate shell concept—time evolution among configurations through the regular motion $\varphi_t \circ \varphi_0^{-1}$



where $\langle\langle \cdot, \cdot \rangle\rangle : V \times V \times V^* \times V^* \rightarrow \mathbb{R}$ represents the double dual pairing, $\delta \tilde{\mathbf{E}}_b$ is an admissible variation of the enhanced part of the Green–Lagrange strain tensor, $\tilde{\mathbf{E}}_b : T_{\mathbf{x}(0)}\mathcal{X}_0 \times T_{\mathbf{x}(0)}\mathcal{X}_0 \rightarrow \mathbb{R}$, and $\sqrt{\det[\mathbf{G}(\boldsymbol{\theta}; 0)]}d^3\theta$ is the volume element.

The velocity-based and displacement-based linear momentum densities, and the internal force density are defined as $\mathbf{l}(\mathbf{v}) = \rho_0 \mathbf{v}$, $\mathbf{l}(\mathbf{x}) = \rho_0 \dot{\mathbf{x}}$ and $\mathbf{f}^{\text{int}}(\mathbf{x}, \mathbf{S}^\sharp) = [\bar{\mathbf{B}}^T(\mathbf{x})](\mathbf{S}^\sharp)$, respectively. The continuous operator $[\bar{\mathbf{B}}(\mathbf{x})](\cdot)$ relates the variation of the displacement field to the variation of the strain field.

2.3.2 Spatial discretization

To spatially discretized the solid-degenerate shell into four-node finite elements, we approximate the displacement as well as the velocity fields, and their admissible variations as follows: $\mathbf{x}(\boldsymbol{\theta}; t) \approx \mathbf{N}(\boldsymbol{\theta}, \vartheta) \cdot \hat{\mathbf{x}}(t)$, $\mathbf{v}(\boldsymbol{\theta}; t) \approx \mathbf{N}(\boldsymbol{\theta}, \vartheta) \cdot \hat{\mathbf{v}}(t)$, $\delta \mathbf{x}(\boldsymbol{\theta}) \approx \mathbf{N}(\boldsymbol{\theta}, \vartheta) \cdot \delta \hat{\mathbf{x}}$ and $\delta \mathbf{v}(\boldsymbol{\theta}) \approx \mathbf{N}(\boldsymbol{\theta}, \vartheta) \cdot \delta \hat{\mathbf{v}}$. $\mathbf{N}(\boldsymbol{\theta}, \vartheta)$ is the interpolation matrix, whose rows are dual vectors constructed as

$$\mathbf{N}^i(\boldsymbol{\theta}, \vartheta) = [N^1(\bar{\boldsymbol{\theta}})i^i, \theta^3 \frac{\vartheta}{2} N^1(\bar{\boldsymbol{\theta}})i^i, N^2(\bar{\boldsymbol{\theta}})i^i, \theta^3 \frac{\vartheta}{2} N^2(\bar{\boldsymbol{\theta}})i^i, N^3(\bar{\boldsymbol{\theta}})i^i, \theta^3 \frac{\vartheta}{2} N^3(\bar{\boldsymbol{\theta}})i^i, N^4(\bar{\boldsymbol{\theta}})i^i, \theta^3 \frac{\vartheta}{2} N^4(\bar{\boldsymbol{\theta}})i^i]. \quad (20)$$

The functions $N^A(\bar{\boldsymbol{\theta}})$, with A taking values from 1 to 4, are the bilinear Lagrange-type shape functions. In this context, it means that $\hat{\mathbf{x}}(t) \in \hat{\mathcal{X}}_t \subseteq \mathbb{R}^{24}$, $\hat{\mathbf{v}}(t) \in \hat{\mathcal{V}}_t \subseteq \mathbb{R}^{24}$, $\delta \hat{\mathbf{x}} \in T_{\hat{\mathcal{X}}(t)}\hat{\mathcal{X}}_t$ and $\delta \hat{\mathbf{v}} \in T_{\hat{\mathcal{V}}(t)}\hat{\mathcal{V}}_t$. Given that $\mathbf{N}(\boldsymbol{\theta}, \vartheta)\hat{\mathbf{x}}(t) = N_A^i(\boldsymbol{\theta}, \vartheta)\hat{x}^A(t)i_i$, the displacement-based strain can be simply approximated as

$$\begin{aligned} \bar{E}_{ab}[\mathbf{x}(\boldsymbol{\theta}; t)] &\approx \bar{E}_{ab}[\boldsymbol{\theta}, \hat{\mathbf{x}}(t), \hat{\mathbf{x}}(0)] \\ &= \frac{\delta_{ij}}{2} \frac{\partial N_A^i(\boldsymbol{\theta}, \vartheta)}{\partial \theta^a} \frac{\partial N_B^j(\boldsymbol{\theta}, \vartheta)}{\partial \theta^b} [\hat{x}^A(t)\hat{x}^B(t) - \hat{x}^A(0)\hat{x}^B(0)]. \end{aligned} \quad (21)$$

Having already introduced the spatial approximation, the discrete version of $\bar{\mathbf{B}}(\mathbf{x})$ becomes

$$\begin{aligned} [\bar{\mathbf{B}}(\hat{\mathbf{x}})](\cdot) &= [\bar{\mathbf{B}} \cdot \mathbf{N}](\hat{\mathbf{x}})(\cdot) \\ &= \begin{bmatrix} \delta_{ij} \frac{\partial N_A^i}{\partial \theta^1} \hat{x}^A \frac{\partial N^j}{\partial \theta^1}(\cdot) \\ \delta_{ij} \frac{\partial N_A^i}{\partial \theta^2} \hat{x}^A \frac{\partial N^j}{\partial \theta^2}(\cdot) \\ \delta_{ij} \frac{\partial N_A^i}{\partial \theta^3} \hat{x}^A \frac{\partial N^j}{\partial \theta^3}(\cdot) \\ \delta_{ij} \frac{\partial N_A^i}{\partial \theta^2} \hat{x}^A \frac{\partial N^j}{\partial \theta^3}(\cdot) + \delta_{ij} \frac{\partial N_A^i}{\partial \theta^3} \hat{x}^A \frac{\partial N^j}{\partial \theta^2}(\cdot) \\ \delta_{ij} \frac{\partial N_A^i}{\partial \theta^1} \hat{x}^A \frac{\partial N^j}{\partial \theta^3}(\cdot) + \delta_{ij} \frac{\partial N_A^i}{\partial \theta^3} \hat{x}^A \frac{\partial N^j}{\partial \theta^1}(\cdot) \\ \delta_{ij} \frac{\partial N_A^i}{\partial \theta^1} \hat{x}^A \frac{\partial N^j}{\partial \theta^2}(\cdot) + \delta_{ij} \frac{\partial N_A^i}{\partial \theta^2} \hat{x}^A \frac{\partial N^j}{\partial \theta^1}(\cdot) \end{bmatrix}. \end{aligned} \quad (22)$$

It is well-known that purely displacement-based formulations suffer from some pathologies, e.g. shear locking, artificial thickness strains and membrane locking. These deficiencies are caused by the adopted simplified kinematics and the chosen discretization, leading to a poor representation of the involved quantities that are necessary to set the finite-dimensional version of the equilibrium properly. To cure the shear locking and the artificial thickness strains, we use the assumed natural strain method. To complete the strain field in the thickness direction and to cure the membrane locking, we employ the enhanced assumed strain method. The assumed natural strain method is a mean to cure some locking issues without introducing additional degrees of freedom. It

Table 1 Tying points for the assumed natural strain method (isoparametric coordinates)

	A	B	C	D	1	2	3	4
(θ^1, θ^2)	(0, +1)	(−1, 0)	(0, −1)	(+1, 0)	(+1, +1)	(−1, +1)	(−1, −1)	(+1, −1)

involves only redefinition of some terms based on those originally computed from the displacement-based ones. Here, we use the assumed natural strain formulation developed in [19] to eliminate the shear-locking issue. To eliminate the artificial thickness strain issue, we also employ the assumed natural strain formulation, which is a further development of the ideas presented in [23] and [25]. For this purpose, we assume tying points lying in the middle surface of the shell, which are summarized in Table 1.

The tying points $\bar{\theta}_A, \bar{\theta}_B, \bar{\theta}_C$ and $\bar{\theta}_D$ are employed to cure the shear locking. We redefine $\bar{E}_{23}(\bar{\theta})$ and $\bar{E}_{13}(\bar{\theta})$ as

$$\begin{aligned}\bar{E}_{23}(\bar{\theta}) &= \frac{1}{2}(1 - \theta^1)\bar{E}_{23}(\theta_B) + \frac{1}{2}(1 + \theta^1)\bar{E}_{23}(\theta_D) \quad \text{and} \\ \bar{E}_{13}(\bar{\theta}) &= \frac{1}{2}(1 - \theta^2)\bar{E}_{13}(\theta_C) + \frac{1}{2}(1 + \theta^2)\bar{E}_{13}(\theta_A).\end{aligned}\quad (23)$$

The tying points $\bar{\theta}_1, \bar{\theta}_2, \bar{\theta}_3$ and $\bar{\theta}_4$ are employed to cure the artificial thickness strain. We redefine $\bar{E}_{33}(\bar{\theta})$ as

$$\begin{aligned}\bar{E}_{33}(\bar{\theta}) &= N^1(\bar{\theta})\bar{E}_{33}(\theta_1) + N^2(\bar{\theta})\bar{E}_{33}(\theta_2) \\ &\quad + N^3(\bar{\theta})\bar{E}_{33}(\theta_3) + N^4(\bar{\theta})\bar{E}_{33}(\theta_4).\end{aligned}\quad (24)$$

The enhanced assumed strain method allows the improvement of the strain field and the curing of some locking issues as well, but the introduction of additional elemental degrees of freedom is necessary. The method proposed in [53] enables the definition of enhanced strains spanned by outer products of the elements of the dual basis at $\theta = \mathbf{0}$, i.e.

$$\begin{aligned}\bar{E}_{ab}(\theta; t)g^a(\theta; 0) \otimes g^b(\theta; 0) &= \\ \sqrt{\frac{\det[\mathbf{G}(\mathbf{0}; 0)]}{\det[\mathbf{G}(\theta; 0)]}} \bar{E}_{ab}[\theta; \tilde{e}(t)]g^a(\mathbf{0}; 0) \otimes g^b(\mathbf{0}; 0),\end{aligned}\quad (25)$$

in which \bar{E}_{ab} are the enhancements, where “by design” $\bar{E}_{ab}(\mathbf{0}, 0)$ is set equal to zero, and $\tilde{e}(t) \subseteq \mathbb{R}^8$ contains the elemental degrees of freedom. For the membrane strain state, the inclusion of some terms proportional to θ^1 and to θ^2 in the strain components \bar{E}_{11} , \bar{E}_{22} and \bar{E}_{12} is necessary. For improving the strain component \bar{E}_{33} the inclusion of terms proportional to θ^3 , $\theta^1\theta^3$, $\theta^2\theta^3$ and $\theta^1\theta^2\theta^3$ is necessary as well. Notice that the condition $\left\langle \int_{\mathcal{B}_0} \bar{E}_b \cdot \mathbf{S}^\# d\mathcal{B}_0 = 0 \right\rangle$ was implicitly replaced by $\left\langle \int_{\mathcal{B}_0} \bar{E}_b d\mathcal{B}_0, \mathbf{S}_{\text{const}}^\# = 0 \right\rangle$, which is a more restrictive condition and in which $\mathbf{S}_{\text{const}}^\#$ represents a constant nominal stress state. This constant nominal stress

state condition is closely related to the satisfaction of the patch test in its nonlinear form [24]. By design, the adopted enhancements fulfill the constant nominal stress state condition. Now, we can define the discrete operator related to the enhanced strain as $\bar{\mathbf{B}}_d = \bar{\mathbf{B}}_l \circ \bar{\mathbf{B}}_r$, where the matrix representation of $\bar{\mathbf{B}}_l$ is merely a transformation rule for the enhanced strains in its Voigt form, which is based on Eq. (25), and the matrix representation of $\bar{\mathbf{B}}_r$ is merely

$$\bar{\mathbf{B}}_r(\theta) = \begin{bmatrix} \theta^1 & 0 & 0 & 0 & 0 & 0 & 0 & 0 & 0 \\ 0 & \theta^2 & 0 & 0 & 0 & 0 & 0 & 0 & 0 \\ 0 & 0 & 0 & 0 & \theta^3 & \theta^1\theta^3 & \theta^2\theta^3 & \theta^1\theta^2\theta^3 & 0 \\ 0 & 0 & 0 & 0 & 0 & 0 & 0 & 0 & 0 \\ 0 & 0 & 0 & 0 & 0 & 0 & 0 & 0 & 0 \\ 0 & 0 & \theta^1 & \theta^2 & 0 & 0 & 0 & 0 & 0 \end{bmatrix}.\quad (26)$$

The inclusion of additional terms is possible just by adding new columns. It becomes apparent that particular considerations are required to justify the new enhancements. For more details see [41]. Finally, the semi-discrete version of the weak form of the governing equations for a single finite element becomes

$$\begin{aligned}\left\langle \delta \hat{\mathbf{v}}, \int_{\mathcal{D}} \mathbf{N}^T \cdot [\mathbf{l}(\mathbf{v}) - \mathbf{l}(\mathbf{x})] \sqrt{\det[\mathbf{G}(\theta; 0)]} d^3\theta \right\rangle \\ + \left\langle \delta \hat{\mathbf{x}}, \int_{\mathcal{D}} \{ \mathbf{N}^T \cdot [\mathbf{f}^{\text{int}}(\mathbf{x}, \mathbf{S}^\#) + \dot{\mathbf{l}}(\mathbf{v}) - \mathbf{f}^{\text{ext}}] \right. \\ \left. + \mathbf{H}^T \cdot \mathbf{N}_\lambda \cdot \boldsymbol{\lambda} \} \sqrt{\det[\mathbf{G}(\theta; 0)]} d^3\theta \right\rangle \\ + \left\langle \left\langle \delta \bar{\mathbf{E}}_b, \int_{\mathcal{D}} \bar{\mathbf{S}}^\# \sqrt{\det[\mathbf{G}(\theta; 0)]} d^3\theta \right\rangle \right\rangle \\ + \left\langle \delta \hat{\boldsymbol{\lambda}}, \int_{\mathcal{D}} \mathbf{N}_\lambda^T \cdot \mathbf{h} \sqrt{\det[\mathbf{G}(\theta; 0)]} d^3\theta \right\rangle = 0,\end{aligned}\quad (27)$$

where $\bar{\mathbf{S}}^\#$ represents the stress consistently accommodated in the basis at $\theta = \mathbf{0}$. The resulting finite element in combination with the robust integration can be regarded as a new evolution of the work developed by Gebhardt and Rolfes [41], which belongs to a similar element family to the MITC4 developed by Dvorkin and Bathe [19] and Bathe and Dvorkin [20]. The current extended version is a very effective alternative to recent developments [54].

The improvement of the current element with respect to Gebhardt and Rolfes [41] is two-fold because the concepts presented here are firstly, valid for every material law derived from a potential function, while equally preserving the objec-

tivity of the discrete strain measure and path independence. And secondly, also for structures made of composite multilayer materials, which is accomplished by means of the single equivalent-layer theory. The corresponding integration is performed layerwise within a single element with two Gaussian integration points per layer. For a similar recent development in the static context see [38]. Moreover, the proposed shell element is in fact a fully-integrated degenerated solid, which relies on an extensible director kinematics. In contrast to some reduced-integrated elements available in the literature, that are based upon standard shell kinematics, our element is free of spurious modes and drilling issues. Therefore, no stabilization technique is necessary. Adding drilling degrees of freedom may result very interesting to capture the change of in-plane direction for materials with preferenceable orientations.

3 Temporal discretization and robust integration

A fundamental aspect to produce acceptable numerical results in the context of conservative systems is the preservation of mechanical invariants like the linear momentum, the angular momentum, the total energy (basically first integrals of motion) or even the symplectic form. These conservation properties ensure that beyond the approximation errors, the computed solution remains consistent with respect to the underlying physical essence. The construction of numerical schemes showing the preservation of one or several of these properties consists in finding discrete versions of the continuous terms, which after their corresponding evaluation at the time-quadrature points and in combination with appropriate admissible variations of the position and velocity vectors yield to the desired preservation rules. These preservation rules are typically materialized in terms of the continuous invariant quantities evaluated only at the boundaries of the time interval. For nonlinear systems, this is not directly achieved just by evaluating the continuous terms at the temporal collocation points, because consistency and directionality of the discrete partial derivatives are not *per se* satisfied. Therefore, the discrete setting ought to parallel the continuous framework. Moreover, not all mechanical invariants can be discretely preserved for a fixed time step h . The preservation of linear momentum and angular momentum in combination with the preservation of the total energy and the symplectic form is only achieved by adaptation of the time step, whose size is obtained by solving an optimization problem subjected to inequality time constraints, see for example Kane et al. [55].

In this work, we chose the family of integration methods that is derived by direct discretization of the equations of motion, which are obtained from the continuous variational

principle. Thus, the properties to be preserved are the linear momentum, the angular momentum and the total energy without the necessity for imposing additional algebraic constraints, see [56]. Moreover, to achieve the preservation of total energy for the conservative case, the discrete derivative of the elastic potential function is computed by employing the second-order “average vector field” proposed by Harten et al. [57] and later by McLachlan et al. [58] instead of the nonstandard quadrature proposed by Gonzalez [59], which leads to a unsymmetric Hessian matrix even for the conservative case. As far as we know, no publication is available, in which the “average vector field” is employed in the context of slender structures. As follows, we introduce a definition of a discrete derivative due to Gonzalez [59], an example of a discrete derivative based on the “average vector field”, and proofs that the proposed discrete derivative fulfills the introduced requirements.

Definition 1 For \mathbf{x} and $\mathbf{y} \in \mathbb{R}^n$, $DV : \mathbb{R}^n \times \mathbb{R}^n \rightarrow \mathbb{R}^n$ is a discrete derivative of $V : \mathbb{R}^n \rightarrow \mathbb{R}$ that satisfies:

i) directionality:

$$DV(\mathbf{x}, \mathbf{y}) \cdot (\mathbf{y} - \mathbf{x}) = V(\mathbf{y}) - V(\mathbf{x}). \quad (28)$$

ii) consistency:

$$DV(\mathbf{x}, \mathbf{x}) = \frac{\partial V(\mathbf{x})}{\partial \mathbf{x}}. \quad (29)$$

Proposition 1 The discrete derivative of $V : \mathbb{R}^n \rightarrow \mathbb{R}$ is given by

$$DV(\mathbf{x}, \mathbf{y}) = \frac{1}{2} \int_{-1}^{+1} \left. \frac{\partial V(\mathbf{z})}{\partial \mathbf{z}} \right|_{\mathbf{z}(\xi)} d\xi, \quad (30)$$

where $\mathbf{z}(\xi)$ is defined as $\frac{1}{2}(1 - \xi)\mathbf{x} + \frac{1}{2}(1 + \xi)\mathbf{y}$ for $\xi \in [-1, +1]$.

Proof The directionality property is verified as follows:

$$\begin{aligned} DV(\mathbf{x}, \mathbf{y}) \cdot (\mathbf{y} - \mathbf{x}) &= \frac{1}{2} \int_{-1}^{+1} \left. \frac{\partial V(\mathbf{z})}{\partial \mathbf{z}} \right|_{\mathbf{z}(\xi)} d\xi \cdot (\mathbf{y} - \mathbf{x}) \\ &= \int_{-1}^{+1} \left. \frac{\partial V(\mathbf{z})}{\partial \mathbf{z}} \right|_{\mathbf{z}(\xi)} \cdot \frac{(\mathbf{y} - \mathbf{x})}{2} d\xi \\ &= \int_{-1}^{+1} \left. \frac{\partial V(\mathbf{z})}{\partial \mathbf{z}} \right|_{\mathbf{z}(\xi)} \cdot \frac{\partial \mathbf{z}(\xi)}{\partial \xi} d\xi \\ &= \int_{\mathbf{x}}^{\mathbf{y}} \frac{\partial V(\mathbf{z})}{\partial \mathbf{z}} d\mathbf{z} \\ &= \boxed{V(\mathbf{y}) - V(\mathbf{x})} \end{aligned}$$

□

Proof The consistency property is verified as follows:

$$\begin{aligned}
 DV(\mathbf{x}, \mathbf{x}) &= \frac{1}{2} \int_{-1}^{+1} \left. \frac{\partial V(\mathbf{z})}{\partial \mathbf{z}} \right|_{\mathbf{z}=\mathbf{x}} d\xi \\
 &= \frac{\partial V(\mathbf{x})}{\partial \mathbf{x}} \frac{1}{2} \int_{-1}^{+1} d\xi \\
 &= \boxed{\frac{\partial V(\mathbf{x})}{\partial \mathbf{x}}}
 \end{aligned}$$

□

This concept of directional derivative is necessary not only to compute the algorithmic internal forces, but also may result necessary to compute the discrete version of the Jacobian matrix associated to the constraints. However, Romero [60] proved that there is an infinite number of second-order approximations for the algorithmic stress formula. For the finite elasticity problem, objective strain measures ought to be employed to warrant the invariance of the potential function under rigid space transformations. Finally, by combining the mid-point rule, i.e. $(\cdot)_{n+\frac{1}{2}} \approx [(\cdot)_{n+1} + (\cdot)_n]/2$ and $(\dot{\cdot})_{n+\frac{1}{2}} \approx [(\dot{\cdot})_{n+1} - (\dot{\cdot})_n]/h$, for the inertial internal terms and the discrete derivative, i.e. the “average vector field”, for the elastic internal terms and for the Jacobian matrix of the constraints, it is possible for the conservative case to preserve linear momentum and angular momentum in combination with the total energy.

The adopted integration approach is an alternative to variational integration schemes that preserve typically the linear momentum, the angular momentum and the symplectic form of the underlying Hamiltonian system [61,62]. In contrast with our choice, that second family of integration methods is derived by direct discretization of the action integral followed by the discrete minimization of the discrete action. The variational integration in its standard form is less robust toward highly stiff problems that typically arise in the context of beams and shells. Therefore, this is not an effective alternative for our investigations.

The preservation of linear momentum and the angular momentum in combination with the conservation of the total energy does not warrant the robustness of the integration scheme. It means that the presence of unresolved high frequencies could trigger the failure of the Newton–Raphson algorithm. One remedy to alleviate this problem is to add some artificial dissipation to the system. However, the dissipation proportional to discrete rate of strain *per se* not able to damp the unresolved high-frequency content; therefore, the addition of some damping related to the discrete rate of velocity module is necessary. Following the ideas presented in [6–8,29], the velocity-based discrete linear momentum and the discrete internal loads are modified to achieve the desired dissipation properties preserving at the same time the objectivity of the formulation. To the best of our knowledge, there is no work available in the literature, in where the robust

integration method with controlled energy dissipation, the “average vector field” for the discrete derivative, and a unified director-based formulation for rigid bodies, geometrically exact beams and solid-degenerate shells with the simplest additive actualization have been consistently combined and implemented in a highly-extensible object-oriented framework as the one proposed in the current manuscript and specially towards real-world applications.

It is also worth mentioning that in [63–65], the null space projection and the nodal reparametrization were introduced in the context of structure-preserving integration (see for a very clear exposure of the basic ideas [66]) with the aim of reducing the number of unknowns by eliminating the Lagrange multipliers. The multipliers are then easily recovered by post-processing the solution for the solved reduced problem. On the one hand, analytical constructions of null-space projectors are not possible in general, and then linear algebra libraries are necessary to compute the basis for the null space. As the reformulated problem requires the computation of directional derivatives for the projectors, and as they are not available in an analytical form generally, numerical computation with finite differences is required, which is very expensive. On the other hand, introducing nodal reparametrization is equivalent to formulations based upon minimal representations of the rotation group and updated Lagrangian descriptions. In contrast to these major drawbacks, the aforementioned authors showed that the null-space method improves substantially the condition number of the iteration matrix, since director-based formulations are more prone to conditioning problems than formulations based on a minimal representation of the rotation group. However, for all the cases considered along this work, the solution of the nonlinear equations system took in average 3–4 iterations, even for the cases showing the snap-through phenomenon. One alternative to alleviate the condition number issue could be achieved by employing scaling techniques as those proposed in [67].

3.1 Rigid body

Next, we describe the particularization of the momentum-preserving, energy-preserving integration scheme for the “rigid body” case. For this purpose, the following nomenclature is necessary:

$$\begin{aligned}
 \mathbf{q} &= \begin{Bmatrix} \bar{\mathbf{x}} \\ d_1 \\ d_2 \\ d_3 \end{Bmatrix}, \quad \mathbf{s} = \begin{Bmatrix} \bar{\mathbf{v}} \\ \mathbf{w}_1 \\ \mathbf{w}_2 \\ \mathbf{w}_3 \end{Bmatrix}, \quad \mathbf{p} = \begin{Bmatrix} l^0 \\ l^1 \\ l^2 \\ l^3 \end{Bmatrix} \quad \text{and} \\
 \mathbf{Q}^{\text{ext}} &= \begin{Bmatrix} \mathbf{f}^{0,\text{ext}} \\ \mathbf{f}^{1,\text{ext}} \\ \mathbf{f}^{2,\text{ext}} \\ \mathbf{f}^{3,\text{ext}} \end{Bmatrix}.
 \end{aligned} \tag{31}$$

While \mathbf{q} is the vector of generalized coordinates, \mathbf{s} stands for the vector of generalized velocities, \mathbf{p} collects the generalized momenta and \mathbf{Q}^{ext} contains the generalized external loads. The discrete version of Eq. (4) can be expressed at time $n + \frac{1}{2}$ as

$$\begin{aligned} & \langle \delta \mathbf{s}_{n+\frac{1}{2}}, \mathbf{p}_d(\mathbf{s}_n, \mathbf{s}_{n+1}) - \mathbf{p}_d(\mathbf{q}_n, \mathbf{q}_{n+1}) \rangle \\ & + \langle \delta \mathbf{q}_{n+\frac{1}{2}}, \dot{\mathbf{p}}_d(\mathbf{s}_n, \mathbf{s}_{n+1}) - \mathbf{Q}_{n+\frac{1}{2}}^{\text{ext}} \rangle \\ & + \mathbf{H}_d^T(\mathbf{q}_n, \mathbf{q}_{n+1}) \cdot \boldsymbol{\lambda}_{n+\frac{1}{2}} \rangle \\ & + \langle \delta \boldsymbol{\lambda}_{n+1}, \mathbf{h}(\mathbf{q}_{n+1}) \rangle = 0. \end{aligned} \tag{32}$$

A key point to achieve the desired preservation properties, is to define the momentum terms by using the mid-point rule, i.e.

$$\begin{aligned} \mathbf{p}_d(\mathbf{s}_n, \mathbf{s}_{n+1}) &= \frac{\mathbf{M}}{2} \cdot (\mathbf{s}_{n+1} + \mathbf{s}_n), \quad \mathbf{p}_d(\mathbf{q}_n, \mathbf{q}_{n+1}) \\ &= \frac{\mathbf{M}}{h} \cdot (\mathbf{q}_{n+1} - \mathbf{q}_n), \quad \text{and} \quad \dot{\mathbf{p}}_d(\mathbf{s}_n, \mathbf{s}_{n+1}) \\ &= \frac{\mathbf{M}}{h} \cdot (\mathbf{s}_{n+1} - \mathbf{s}_n), \end{aligned} \tag{33}$$

in which the mass matrix takes the form

$$\mathbf{M} = \begin{bmatrix} \mathcal{E}_{00} \mathbf{I}_{3 \times 3} & \mathcal{E}_{01} \mathbf{I}_{3 \times 3} & \mathcal{E}_{02} \mathbf{I}_{3 \times 3} & \mathcal{E}_{03} \mathbf{I}_{3 \times 3} \\ \mathcal{E}_{01} \mathbf{I}_{3 \times 3} & \mathcal{E}_{11} \mathbf{I}_{3 \times 3} & \mathcal{E}_{12} \mathbf{I}_{3 \times 3} & \mathcal{E}_{13} \mathbf{I}_{3 \times 3} \\ \mathcal{E}_{02} \mathbf{I}_{3 \times 3} & \mathcal{E}_{12} \mathbf{I}_{3 \times 3} & \mathcal{E}_{22} \mathbf{I}_{3 \times 3} & \mathcal{E}_{23} \mathbf{I}_{3 \times 3} \\ \mathcal{E}_{03} \mathbf{I}_{3 \times 3} & \mathcal{E}_{13} \mathbf{I}_{3 \times 3} & \mathcal{E}_{23} \mathbf{I}_{3 \times 3} & \mathcal{E}_{33} \mathbf{I}_{3 \times 3} \end{bmatrix} \tag{34}$$

and \mathcal{E}_{ij} for i and j running from 0 to 3 being defined as in Sect. 2.1. This very simple construction satisfies, only for the rigid body case, the preservation of linear and angular momenta in combination with the total energy in absence of external loads. For further clarifications the reader is referred to [68].

The discrete version of the Jacobian matrix of the constraints is given by

$$\mathbf{H}_d(\mathbf{q}_n, \mathbf{q}_{n+1}) = \frac{1}{2} \int_{-1}^{+1} \left. \frac{\partial \mathbf{h}}{\partial \mathbf{q}} \right|_{\mathbf{q}(\xi)} d\xi, \tag{35}$$

where $\mathbf{q}(\xi)$ is defined as $\frac{1}{2}(1 - \xi)\mathbf{q}_n + \frac{1}{2}(1 + \xi)\mathbf{q}_{n+1}$ for $\xi \in [-1, +1]$. The algorithmic Jacobian matrix defined in this way satisfies for any admissible solution the discrete version of the hidden constraints, i.e. $\mathbf{H}_d(\mathbf{q}_n, \mathbf{q}_{n+1}) \cdot (\mathbf{q}_{n+1} - \mathbf{q}_n) = \mathbf{0}$.

3.2 Geometrically exact beam

Next, we describe the particularization of the momentum-preserving, energy-preserving/dissipative integration scheme for the “geometrically exact beam” case. For this purpose, the following nomenclature is necessary:

$$\begin{aligned} \mathbf{Q}^{\text{int}} &= \begin{Bmatrix} \mathbf{f}^{0,\text{int}} \\ \mathbf{f}^{1,\text{int}} \\ \mathbf{f}^{2,\text{int}} \\ \mathbf{f}^{3,\text{int}} \end{Bmatrix}, \quad \boldsymbol{\pi} = \begin{Bmatrix} \boldsymbol{\Gamma} \\ \boldsymbol{\Omega} \end{Bmatrix}, \quad \boldsymbol{\sigma} = \begin{Bmatrix} \mathbf{N} \\ \mathbf{M} \end{Bmatrix} \quad \text{and} \\ \mathbf{e}^{\text{beam}} &= \begin{bmatrix} \mathbf{e}_{\Gamma\Gamma} & \mathbf{e}_{\Gamma\Omega} \\ \mathbf{e}_{\Omega\Gamma} & \mathbf{e}_{\Omega\Omega} \end{bmatrix}. \end{aligned} \tag{36}$$

\mathbf{Q}^{int} contains the generalized internal loads, $\boldsymbol{\pi}$ and $\boldsymbol{\sigma}$ contains the objective strain measures and internal loads, respectively, and $\mathbf{e}_n^{\text{beam}}$ stands for the tangent constitutive matrix at time t_n . The discrete version of Eq. (15) can be expressed at time $n + \frac{1}{2}$ as

$$\begin{aligned} & \left\langle \delta \mathbf{s}_{n+\frac{1}{2}}, \int_{-1}^{+1} \mathbf{N}^T \cdot [\mathbf{p}_d(\mathbf{s}_n, \boldsymbol{\pi}_n, \mathbf{s}_{n+1}, \boldsymbol{\pi}_{n+1}) \right. \\ & \quad \left. - \mathbf{p}_d(\mathbf{q}_n, \mathbf{q}_{n+1})] \frac{\partial \mathcal{L}_0}{\partial \theta^3} d\theta^3 \right\rangle \\ & + \left\langle \delta \mathbf{q}_{n+\frac{1}{2}}, \int_{-1}^{+1} \left\{ \mathbf{N}^T \cdot [\dot{\mathbf{p}}_d(\mathbf{s}_n, \mathbf{s}_{n+1}) \right. \right. \\ & \quad \left. \left. + \mathbf{Q}_d^{\text{int}}(\mathbf{q}_n, \mathbf{s}_n, \mathbf{q}_{n+1}, \mathbf{s}_{n+1}) - \mathbf{Q}_{n+\frac{1}{2}}^{\text{ext}} \right] \right. \\ & \quad \left. + \mathbf{H}_d^T(\mathbf{q}_n, \mathbf{q}_{n+1}) \cdot \mathbf{N}_\lambda \cdot \boldsymbol{\lambda}_{n+\frac{1}{2}} \right\} \frac{\partial \mathcal{L}_0}{\partial \theta^3} d\theta^3 \right\rangle \\ & + \left\langle \delta \boldsymbol{\lambda}_{n+1}, \int_{-1}^{+1} \mathbf{N}_\lambda^T \cdot \mathbf{h}(\mathbf{q}_{n+1}) \frac{\partial \mathcal{L}_0}{\partial \theta^3} d\theta^3 \right\rangle = 0, \end{aligned} \tag{37}$$

where the admissible variations correspond to the nodal variables and therefore, further distinction are unnecessary and from now, \mathbf{N} gathers all nodal contributions.

On the one hand, the momentum term computed from generalized velocities can be redefined as the additive combination of a conservative part and a dissipative part, i.e.

$$\begin{aligned} \mathbf{p}_d(\mathbf{s}_n, \boldsymbol{\pi}_n, \mathbf{s}_{n+1}, \boldsymbol{\pi}_{n+1}) &= \mathbf{p}_d^{\text{cons}}(\mathbf{s}_n, \mathbf{s}_{n+1}) \\ & + \mathbf{p}_d^{\text{diss}}(\|\mathbf{s}_n\|_{\mathbf{M}}, \boldsymbol{\pi}_n, \|\mathbf{s}_{n+1}\|_{\mathbf{M}}, \boldsymbol{\pi}_{n+1}), \end{aligned} \tag{38}$$

where \mathbf{M} is the consistent mass matrix and the conservative part is

$$\mathbf{p}_d^{\text{cons}}(\mathbf{s}_n, \mathbf{s}_{n+1}) = \frac{\tilde{\mathbf{M}}}{2} \cdot (\mathbf{s}_{n+1} + \mathbf{s}_n), \tag{39}$$

in which the augmented mass matrix per unit length takes the form

$$\tilde{\mathbf{M}} = \begin{bmatrix} \mathcal{E}_{00} \mathbf{I}_{3 \times 3} & \mathcal{E}_{01} \mathbf{I}_{3 \times 3} & \mathcal{E}_{02} \mathbf{I}_{3 \times 3} & \mathbf{0}_{3 \times 3} \\ \mathcal{E}_{01} \mathbf{I}_{3 \times 3} & \mathcal{E}_{11} \mathbf{I}_{3 \times 3} & \mathcal{E}_{12} \mathbf{I}_{3 \times 3} & \mathbf{0}_{3 \times 3} \\ \mathcal{E}_{02} \mathbf{I}_{3 \times 3} & \mathcal{E}_{12} \mathbf{I}_{3 \times 3} & \mathcal{E}_{22} \mathbf{I}_{3 \times 3} & \mathbf{0}_{3 \times 3} \\ \mathbf{0}_{3 \times 3} & \mathbf{0}_{3 \times 3} & \mathbf{0}_{3 \times 3} & \mathbf{I}_{3 \times 3} \end{bmatrix} \tag{40}$$

and \mathcal{E}_{ij} for i and j running from 0 to 2 being defined as in Sect. 2.2. $\tilde{\mathbf{M}}$ differs from \mathbf{M} only in the block placed in the

lower right corner, $\mathbf{I}_{3 \times 3}$ instead of $\mathbf{0}_{3 \times 3}$, which includes the condition $\mathbf{w}_3 = \dot{\mathbf{d}}_3$ without adding further constraints. The dissipative part that supports cross definition involving $\|\mathbf{s}\|_M$ and $\boldsymbol{\pi}$ is given by

$$\begin{aligned} \mathcal{P}_d^{\text{diss}}(\|\mathbf{s}_n\|_M, \boldsymbol{\pi}_n, \|\mathbf{s}_{n+1}\|_M, \boldsymbol{\pi}_{n+1}) \\ = \frac{2\mathcal{D}_P(\|\mathbf{s}_n\|_M, \boldsymbol{\pi}_n, \|\mathbf{s}_{n+1}\|_M, \boldsymbol{\pi}_{n+1})}{\|\mathbf{s}_{n+1}\|_M^2 - \|\mathbf{s}_n\|_M^2} \cdot \mathbf{M} \cdot \mathbf{s}_{n+\frac{1}{2}}, \end{aligned} \quad (41)$$

in which the associated dissipation function \mathcal{D}_P is positive semidefinite.

On the other hand, the discrete generalized load due to internal terms can be also redefined as the additive combination of a conservative part and a dissipative part, i.e.

$$\begin{aligned} \mathcal{Q}_d^{\text{int}}(\mathbf{q}_n, \mathbf{s}_n, \mathbf{q}_{n+1}, \mathbf{s}_{n+1}) = \mathcal{Q}_d^{\text{int, cons}}(\mathbf{q}_n, \mathbf{q}_{n+1}) \\ + \mathcal{Q}_d^{\text{int, diss}}(\mathbf{q}_n, \|\mathbf{s}_n\|_M, \mathbf{q}_{n+1}, \|\mathbf{s}_{n+1}\|_M). \end{aligned} \quad (42)$$

The conservative part is

$$\mathcal{Q}_d^{\text{int, cons}}(\mathbf{q}_n, \mathbf{q}_{n+1}) = \left[\frac{\partial \boldsymbol{\pi}}{\partial \mathbf{q}} \right]_{n+\frac{1}{2}}^T \cdot \boldsymbol{\sigma}_d^{\text{cons}}(\boldsymbol{\pi}_n, \boldsymbol{\pi}_{n+1}) \quad (43)$$

for the conservative algorithmic internal loads given by

$$\boldsymbol{\sigma}_d^{\text{cons}}(\boldsymbol{\pi}_n, \boldsymbol{\pi}_{n+1}) = \frac{1}{2} \int_{-1}^{+1} \left. \frac{\partial V^{\text{beam}}}{\partial \boldsymbol{\pi}} \right|_{\boldsymbol{\pi}(\xi)} d\xi, \quad (44)$$

where $\boldsymbol{\pi}(\xi)$ is defined as $\frac{1}{2}(1 - \xi)\boldsymbol{\pi}_n + \frac{1}{2}(1 + \xi)\boldsymbol{\pi}_{n+1}$ for $\xi \in [-1, +1]$.

The dissipative part that also supports cross definition involving $\|\mathbf{s}\|_M$ and $\boldsymbol{\pi}$ is given by

$$\begin{aligned} \mathcal{Q}_d^{\text{int, diss}}(\mathbf{q}_n, \|\mathbf{s}_n\|_M, \mathbf{q}_{n+1}, \|\mathbf{s}_{n+1}\|_M) \\ = \left[\frac{\partial \boldsymbol{\pi}}{\partial \mathbf{q}} \right]_{n+\frac{1}{2}}^T \cdot \boldsymbol{\sigma}_d^{\text{diss}}(\|\mathbf{s}_n\|_M, \boldsymbol{\pi}_n, \|\mathbf{s}_{n+1}\|_M, \boldsymbol{\pi}_{n+1}) \end{aligned} \quad (45)$$

for the dissipative algorithmic loads

$$\begin{aligned} \boldsymbol{\sigma}_d^{\text{diss}}(\|\mathbf{s}_n\|_M, \boldsymbol{\pi}_n, \|\mathbf{s}_{n+1}\|_M, \boldsymbol{\pi}_{n+1}) \\ = \frac{\mathcal{D}_Q(\|\mathbf{s}_n\|_M, \boldsymbol{\pi}_n, \|\mathbf{s}_{n+1}\|_M, \boldsymbol{\pi}_{n+1})}{\|\boldsymbol{\pi}_{n+1} - \boldsymbol{\pi}_n\|_{\mathbf{c}_n^{\text{beam}}}^2} \\ \cdot \mathbf{c}_n^{\text{beam}} \cdot (\boldsymbol{\pi}_{n+1} - \boldsymbol{\pi}_n), \end{aligned} \quad (46)$$

in which the dissipation function \mathcal{D}_S is positive semidefinite as well. Finally, the following condition

$$\mathcal{H}_{n+1}^{\text{beam}} + \mathcal{D}_P + \mathcal{D}_Q = \mathcal{H}_n^{\text{beam}} \quad \text{for } \mathcal{D}_P + \mathcal{D}_Q \geq 0, \quad (47)$$

is warranted “by design”, being the corresponding Hamiltonian function $\mathcal{H}^{\text{beam}}$.

3.3 Solid-degenerate shell

Next, we describe the particularization of the momentum-preserving, energy-preserving/dissipative integration scheme for the “solid-degenerate shell” case. For this purpose, the following nomenclature is necessary:

$$\mathbf{q} = \begin{Bmatrix} \bar{\mathbf{x}} \\ \mathbf{d} \end{Bmatrix} \quad \text{and} \quad \mathbf{s} = \begin{Bmatrix} \bar{\mathbf{v}} \\ \mathbf{w} \end{Bmatrix}. \quad (48)$$

While \mathbf{q} is the vector of generalized coordinates, \mathbf{s} stands for the vector of generalized velocities.

The discrete version of Eq. (27) can be expressed at the time $n + \frac{1}{2}$ as

$$\begin{aligned} \left\langle \delta \mathbf{s}_{n+\frac{1}{2}}, \int_{\mathbb{D}} \mathbf{N}^T \cdot [I_d(\mathbf{v}_n, \mathbf{E}_n, \mathbf{v}_{n+1}, \mathbf{E}_{n+1}) \right. \\ \left. - I_d(\mathbf{x}_n, \mathbf{x}_{n+1})] \sqrt{\det[\mathbf{G}(\boldsymbol{\theta}; 0)]} d^3\boldsymbol{\theta} \right\rangle \\ + \left\langle \delta \mathbf{q}_{n+\frac{1}{2}}, \int_{\mathbb{D}} \mathbf{N}^T \cdot [I_d(\mathbf{v}_n, \mathbf{v}_{n+1}) \right. \\ \left. + \mathbf{f}_d^{\text{int}}(\mathbf{x}_n, \mathbf{v}_n, \tilde{\mathbf{E}}_n, \mathbf{x}_{n+1}, \mathbf{v}_{n+1}, \tilde{\mathbf{E}}_{n+1}) - \mathbf{f}_{n+\frac{1}{2}}^{\text{ext}}] \right. \\ \left. + \mathbf{H}_d^T(\mathbf{q}_n, \mathbf{q}_{n+1}) \cdot \mathbf{N}_\lambda \cdot \boldsymbol{\lambda}_{n+\frac{1}{2}} \right\rangle \sqrt{\det[\mathbf{G}(\boldsymbol{\theta}; 0)]} d^3\boldsymbol{\theta} \\ + \left\langle \delta \tilde{\mathbf{e}}_{n+\frac{1}{2}}, \int_{\mathbb{D}} \tilde{\mathbf{B}}^T [S_d(\mathbf{v}_n, \mathbf{E}_n, \mathbf{v}_{n+1}, \mathbf{E}_{n+1})] \sqrt{\det[\mathbf{G}(\boldsymbol{\theta}; 0)]} d^3\boldsymbol{\theta} \right\rangle \\ + \left\langle \delta \boldsymbol{\lambda}_{n+1}, \int_{\mathbb{D}} \mathbf{N}_\lambda^T \cdot \mathbf{h}(\mathbf{x}_{n+1}) \sqrt{\det[\mathbf{G}(\boldsymbol{\theta}; 0)]} d^3\boldsymbol{\theta} \right\rangle = 0. \end{aligned} \quad (49)$$

On the one hand, the discrete linear momentum density computed from velocities can be redefined as the additive combination of a conservative part and a dissipative part, i.e.

$$\begin{aligned} I_d(\mathbf{v}_n, \mathbf{E}_n, \mathbf{v}_{n+1}, \mathbf{E}_{n+1}) = I_d^{\text{cons}}(\mathbf{v}_n, \mathbf{v}_{n+1}) \\ + I_d^{\text{diss}}(\|\mathbf{v}_n\|, \mathbf{E}_n, \|\mathbf{v}_{n+1}\|, \mathbf{E}_{n+1}), \end{aligned} \quad (50)$$

where the conservative part is

$$I_d^{\text{cons}}(\mathbf{v}_n, \mathbf{v}_{n+1}) = \frac{\varrho_0}{2} (\mathbf{v}_{n+1} + \mathbf{v}_n). \quad (51)$$

The dissipative part that supports cross definition involving $\|\mathbf{v}\|$ and \mathbf{E} is given by

$$\begin{aligned} I_d^{\text{diss}}(\|\mathbf{v}_n\|, \mathbf{E}_n, \|\mathbf{v}_{n+1}\|, \mathbf{E}_{n+1}) \\ = \frac{2\mathcal{D}_L(\|\mathbf{v}_n\|, \mathbf{E}_n, \|\mathbf{v}_{n+1}\|, \mathbf{E}_{n+1})}{\|\mathbf{v}_{n+1}\|^2 - \|\mathbf{v}_n\|^2} \mathbf{v}_{n+\frac{1}{2}}, \end{aligned} \quad (52)$$

in which the associated dissipation function \mathcal{D}_L is positive semidefinite.

On the other hand, the discrete internal load term can be also redefined as the additive combination of a conservative part and a dissipative part, i.e.

$$\begin{aligned} & f_d^{\text{int}}(\mathbf{x}_n, \mathbf{v}_n, \tilde{\mathbf{E}}_n, \mathbf{x}_{n+1}, \mathbf{v}_{n+1}, \tilde{\mathbf{E}}_{n+1}) \\ &= f_d^{\text{int, cons}}(\mathbf{x}_n, \tilde{\mathbf{E}}_n, \mathbf{x}_{n+1}, \tilde{\mathbf{E}}_{n+1}) \\ &+ f_d^{\text{int, diss}}(\mathbf{x}_n, \|\mathbf{v}_n\|, \tilde{\mathbf{E}}_n, \mathbf{x}_{n+1}, \|\mathbf{v}_{n+1}\|, \tilde{\mathbf{E}}_{n+1}) \end{aligned} \quad (53)$$

Being consistent with the ideas already employed for the beam, the conservative part is

$$f_d^{\text{int, cons}}(\mathbf{x}_n, \tilde{\mathbf{E}}_n, \mathbf{x}_{n+1}, \tilde{\mathbf{E}}_{n+1}) = [\mathbf{B}_d]_{n+\frac{1}{2}}^T \cdot \mathbf{S}_d^{\text{cons}}(\mathbf{E}_n, \mathbf{E}_{n+1}), \quad (54)$$

for the conservative algorithmic stress given by

$$\mathbf{S}_d^{\text{cons}}(\mathbf{E}_n, \mathbf{E}_{n+1}) = \frac{1}{2} \int_{-1}^{+1} \left. \frac{\partial V^{\text{shell}}}{\partial \mathbf{E}} \right|_{\mathbf{E}(\xi)} d\xi, \quad (55)$$

where $\mathbf{E}(\xi)$ is defined as $\frac{1}{2}(1 - \xi)\mathbf{E}_n + \frac{1}{2}(1 + \xi)\mathbf{E}_{n+1}$ for $\xi \in [-1, +1]$.

The dissipative part that also supports cross definition involving $\|\mathbf{v}\|$ and \mathbf{E} is given by

$$\begin{aligned} & f_d^{\text{int, diss}}(\mathbf{x}_n, \|\mathbf{v}_n\|, \tilde{\mathbf{E}}_n, \mathbf{x}_{n+1}, \|\mathbf{v}_{n+1}\|, \tilde{\mathbf{E}}_{n+1}) \\ &= [\mathbf{B}_d]_{n+\frac{1}{2}}^T \cdot \mathbf{S}_d^{\text{diss}}(\|\mathbf{v}_n\|, \mathbf{E}_n, \|\mathbf{v}_{n+1}\|, \mathbf{E}_{n+1}), \end{aligned} \quad (56)$$

for the dissipative algorithmic stress

$$\begin{aligned} & \mathbf{S}_d^{\text{diss}}(\|\mathbf{v}_n\|, \mathbf{E}_n, \|\mathbf{v}_{n+1}\|, \mathbf{E}_{n+1}) \\ &= \frac{\mathcal{D}_F(\|\mathbf{v}_n\|, \mathbf{E}_n, \|\mathbf{v}_{n+1}\|, \mathbf{E}_{n+1})}{\|\mathbf{E}_{n+1} - \mathbf{E}_n\|_{\mathcal{C}_n}^2} \\ &\cdot \mathcal{C}_n \cdot (\mathbf{E}_{n+1} - \mathbf{E}_n), \end{aligned} \quad (57)$$

in which the dissipation function \mathcal{D}_S is positive semidefinite as well. Finally, the following condition

$$\mathcal{H}_{n+1}^{\text{shell}} + \mathcal{D}_L + \mathcal{D}_F = \mathcal{H}_n^{\text{shell}} \quad \text{for } \mathcal{D}_L + \mathcal{D}_F \geq 0, \quad (58)$$

is warranted “by design”, being the corresponding Hamiltonian function $\mathcal{H}^{\text{shell}}$.

4 Kinematic constraints

The introduction of kinematic constraints is a very effective manner to render, for example, very complex structures that arise from the combination of simpler structural components. This methodology requires the solution of differential-algebraic equations, which are originated from the combination of differential equations that describe the motion of the modeled rigid or flexible bodies and algebraic equations that describe the enforced conditions.

These restrictions can be either internal, which come on the scene in the case of parameterizing the configuration manifold of a system with a number of parameters larger than its intrinsic dimension, e.g. by employing three directors to describe the Lie group $\text{SO}(3)$ (basically for rigid bodies and beams) or by employing a single unit director to describe the two-dimensional sphere with unit radius embedded in the three-dimensional Euclidean space, i.e. \mathbb{S}_1^2 , (basically for inextensible shells, in which the E_{33} component of the Green–Lagrange strain tensor is set to be zero at every time), or external ones, which come on the scene in the case of constraining bodies by means of joints, connections or supports. Next, we present briefly some selected kinematic constraints that allow: (i) the combination of nodes equipped with twelve coordinates (one position and three mutually orthogonal directors), the so-called “Nodes 12”; (ii) the combination of nodes equipped with six coordinates (one position and one extensible director), the so-called “Nodes 6”; and, (iii) the hybrid combination of both.

Realize that we consider some constraints called supports, with which we can set a reference to a given single node irrespective of its type, and some other constraints called joints, connections or transitions, with which we can combine two or more nodes of the same or of a different type. For example, to study the dynamic behavior of a given structure under seismic action, we can impose displacements, velocities or even accelerations at the level of the anchoring of the structure. The support also can be used as a “transfer node” if the current code is hooked with another numerical tool, for example to study soil-structure interactions. Here, we consider the support as a specific kind of constraint and not as a particularization derived from another kind of constraint like joints. In few words, the main contribution of this section relies on the reformulation of existing kinematic constraints with the kinematic descriptions adopted and the formulation of new ones in the context of shells and their combination with geometrically exact beams and rigid bodies. For recent developments in the context of nonlinear beams and continua see Romero [69].

4.1 “Node 12” constraints

– *Spherical support* It allows the fixing of the position of a point related to the node whose relative position is described by the offset vector $\boldsymbol{\phi}$, with components $\{\phi^1, \phi^2, \phi^3\}$, but leaving free the change of orientation of the associated frame. This is $\mathbf{h} = \mathbf{0} \in \mathbb{R}^3$,

$$\mathbf{h} = [\bar{\mathbf{x}}(t) + \boldsymbol{\phi}(t)] - [\bar{\mathbf{x}}(0) + \boldsymbol{\phi}(0)]. \quad (59)$$

– *Revolute support* It allows the fixing the position of a point related to the node whose relative position is described by the offset vector $\boldsymbol{\phi}$, and at the same time, the

change of orientation of the associated frame about the unit vector \mathbf{v} , with components $\{v^1, v^2, v^3\}$ is permitted. This is $\mathbf{h} = \mathbf{0} \in \mathbb{R}^5$ for i and j different,

$$\mathbf{h} = \begin{Bmatrix} [\bar{\mathbf{x}}(t) + \boldsymbol{\phi}(t)] - [\bar{\mathbf{x}}(0) + \boldsymbol{\phi}(0)] \\ \mathbf{v}(t) \cdot \mathbf{d}_i(t) - \mathbf{v}(0) \cdot \mathbf{d}_i(0) \\ \mathbf{v}(t) \cdot \mathbf{d}_j(t) - \mathbf{v}(0) \cdot \mathbf{d}_j(0) \end{Bmatrix}. \quad (60)$$

- *Rigid support* It allows the fixing of the position of a point related to the node whose relative position is described by the offset vector $\boldsymbol{\phi}$, and at the same time, the orientation of the associated frame is fixed with respect to its initial configuration. This is $\mathbf{h} = \mathbf{0} \in \mathbb{R}^{12}$,

$$\mathbf{h} = \begin{Bmatrix} [\bar{\mathbf{x}}(t) + \boldsymbol{\phi}(t)] - [\bar{\mathbf{x}}(0) + \boldsymbol{\phi}(0)] \\ \mathbf{d}_1(t) - \mathbf{d}_1(0) \\ \mathbf{d}_2(t) - \mathbf{d}_2(0) \\ \mathbf{d}_3(t) - \mathbf{d}_3(0) \end{Bmatrix}. \quad (61)$$

- *Spherical joint* It allows the connection of two points, indicated with A and B , respectively, and each one has a relative position $\boldsymbol{\phi}$ with respect to its reference node. The positions of both points are set to be equal and the change of relative orientation of the associated frames is set to be free. This is $\mathbf{h} = \mathbf{0} \in \mathbb{R}^3$,

$$\mathbf{h} = \{[{}^A\bar{\mathbf{x}}(t) + {}^A\boldsymbol{\phi}(t)] - [{}^B\bar{\mathbf{x}}(t) + {}^B\boldsymbol{\phi}(t)]\}. \quad (62)$$

- *Revolute joint* It allows the connection of two points, indicated with A and B , respectively, and each one has a relative position $\boldsymbol{\phi}$ with respect to its reference node. The positions of both points are set to be equal, but this time, the change of relative orientation between the associated frames is permitted to take place only about the unit vector \mathbf{v} . This is $\mathbf{h} = \mathbf{0} \in \mathbb{R}^5$ for i and j different,

$$\mathbf{h} = \begin{Bmatrix} [{}^A\bar{\mathbf{x}}(t) + {}^A\boldsymbol{\phi}(t)] - [{}^B\bar{\mathbf{x}}(t) + {}^B\boldsymbol{\phi}(t)] \\ {}^A\mathbf{v}(t) \cdot {}^B\mathbf{d}_i(t) - {}^A\mathbf{v}(0) \cdot {}^B\mathbf{d}_i(0) \\ {}^A\mathbf{v}(t) \cdot {}^B\mathbf{d}_j(t) - {}^A\mathbf{v}(0) \cdot {}^B\mathbf{d}_j(0) \end{Bmatrix}. \quad (63)$$

- *Rigid connection* It allows the connection of two points, indicated with A and B , respectively. The relative position $\boldsymbol{\phi}$ of the node B with respect to the node A is expressed in terms of the directors associated to the node A . The positions of both points are set to be equal and the change of relative orientation between the associated frames is not permitted. The current relative orientation is set to be fixed with respect to that one at the initial configuration, i.e. ${}^A\mathbf{R}^B(t) = {}^A\mathbf{R}^B(0)$. This is $\mathbf{h} = \mathbf{0} \in \mathbb{R}^{12}$,

$$\mathbf{h} = \begin{Bmatrix} [{}^B\bar{\mathbf{x}}(t) - {}^A\bar{\mathbf{x}}(t)] - \boldsymbol{\phi}(t) \\ {}^A\mathbf{d}_1(t) \cdot {}^B\mathbf{d}_1(t) - {}^A\mathbf{d}_1(0) \cdot {}^B\mathbf{d}_1(0) \\ {}^A\mathbf{d}_1(t) \cdot {}^B\mathbf{d}_2(t) - {}^A\mathbf{d}_1(0) \cdot {}^B\mathbf{d}_2(0) \\ {}^A\mathbf{d}_1(t) \cdot {}^B\mathbf{d}_3(t) - {}^A\mathbf{d}_1(0) \cdot {}^B\mathbf{d}_3(0) \\ {}^A\mathbf{d}_2(t) \cdot {}^B\mathbf{d}_1(t) - {}^A\mathbf{d}_2(0) \cdot {}^B\mathbf{d}_1(0) \\ {}^A\mathbf{d}_2(t) \cdot {}^B\mathbf{d}_2(t) - {}^A\mathbf{d}_2(0) \cdot {}^B\mathbf{d}_2(0) \\ {}^A\mathbf{d}_2(t) \cdot {}^B\mathbf{d}_3(t) - {}^A\mathbf{d}_2(0) \cdot {}^B\mathbf{d}_3(0) \\ {}^A\mathbf{d}_3(t) \cdot {}^B\mathbf{d}_1(t) - {}^A\mathbf{d}_3(0) \cdot {}^B\mathbf{d}_1(0) \\ {}^A\mathbf{d}_3(t) \cdot {}^B\mathbf{d}_2(t) - {}^A\mathbf{d}_3(0) \cdot {}^B\mathbf{d}_2(0) \\ {}^A\mathbf{d}_3(t) \cdot {}^B\mathbf{d}_3(t) - {}^A\mathbf{d}_3(0) \cdot {}^B\mathbf{d}_3(0) \end{Bmatrix}, \quad (64)$$

with the component ϕ^i defined as $[{}^B\bar{\mathbf{x}}(0) - {}^A\bar{\mathbf{x}}(0)] \cdot {}^A\mathbf{d}_i(0)$.

4.2 “Node 6” constraints

- *Spherical support* It allows the fixing of the position of a point related to the node whose relative position is described by the offset vector $\boldsymbol{\phi}$, but leaving free the change of orientation of the associated director. This is $\mathbf{h} = \mathbf{0} \in \mathbb{R}^3$,

$$\mathbf{h} = \{[\bar{\mathbf{x}}(t) + \boldsymbol{\phi}(t)] - [\bar{\mathbf{x}}(0) + \boldsymbol{\phi}(0)]\}. \quad (65)$$

- *Semi-rigid support* It allows the fixing of the position of a point related to the node whose relative position is described by the offset vector $\boldsymbol{\phi}$ and the associated director is fixed with respect its initial configuration. However, the change of orientation about the director is permitted. This is $\mathbf{h} = \mathbf{0} \in \mathbb{R}^6$,

$$\mathbf{h} = \begin{Bmatrix} [\bar{\mathbf{x}}(t) + \boldsymbol{\phi}(t)] - [\bar{\mathbf{x}}(0) + \boldsymbol{\phi}(0)] \\ \mathbf{d}(t) - \mathbf{d}(0) \end{Bmatrix}. \quad (66)$$

- *Spherical connection* It allows the connection of two adjacent shells by introducing constraints at the interfacing edges, indicated with A and B , respectively. The positions of each pair of nodes are set to be equal and the change of relative orientation is set to be free. This is $\mathbf{h} = \mathbf{0} \in \mathbb{R}^3$,

$$\mathbf{h} = \{{}^A\bar{\mathbf{x}}(t) - {}^B\bar{\mathbf{x}}(t)\}. \quad (67)$$

- *Continuous connection* It allows the joining of two adjacent shells, see Fig. 4a, by introducing constraints at their interfacing edges, indicated with A and B , respectively. The positions and extensible directors at the edge are set to be equal, but no restriction over the magnitude of the extensible directors is considered. Therefore, the E_{33} component of the Green–Lagrange strain tensor can take values different from zero. This is $\mathbf{h} = \mathbf{0} \in \mathbb{R}^6$,

$$\mathbf{h} = \begin{Bmatrix} {}^A\bar{\mathbf{x}}(t) - {}^B\bar{\mathbf{x}}(t) \\ {}^A\mathbf{d}(t) - {}^B\mathbf{d}(t) \end{Bmatrix}. \quad (68)$$

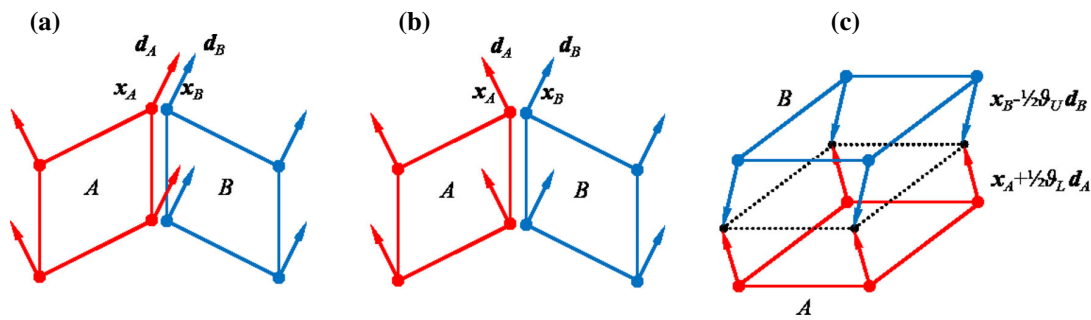


Fig. 4 “Node 6” constraints: three special connections. **a** Continuous connection. **b** Discontinuous connection. **c** Layer connection

– *Discontinuous connection* It allows the dealing with folded shells, see Fig. 4b, by introducing constraints at the junction, indicated with A and B , respectively. Then the positions are set to be equal, the directors are set to be inextensible and the projection between directors is set to be constant. In this case, the E_{33} component of the Green–Lagrange strain tensor is identically zero at every time step, which is required to avoid discontinuities in the change of thickness across the junction. This is $\mathbf{h} = \mathbf{0} \in \mathbb{R}^6$,

$$\mathbf{h} = \left\{ \begin{array}{l} {}^A \bar{\mathbf{x}}(t) - {}^B \bar{\mathbf{x}}(t) \\ {}^A \mathbf{d}(t) \cdot {}^A \mathbf{d}(t) - {}^A \mathbf{d}(0) \cdot {}^A \mathbf{d}(0) \\ {}^B \mathbf{d}(t) \cdot {}^B \mathbf{d}(t) - {}^B \mathbf{d}(0) \cdot {}^B \mathbf{d}(0) \\ {}^A \mathbf{d}(t) \cdot {}^B \mathbf{d}(t) - {}^A \mathbf{d}(0) \cdot {}^B \mathbf{d}(0) \end{array} \right\}. \quad (69)$$

– *Layer connection* It allows stacking two single shells, see Fig. 4c, by introducing constraints at a single fictitious interfacing surface, which lies at a relative position equal to half the thickness of the lower layer $\frac{\vartheta_L}{2}$, indicated as surface A , times its extensible director, which is seen from the middle surface of the lower shell, and at a relative position equal to minus half the thickness of the upper layer $\frac{\vartheta_U}{2}$, indicated as surface B , times its extensible director, which is seen from the middle surface of the upper shell. Then the positions at the interfacing surface from both sides are set to be equal. This constraint enables the consideration of situations in which the displacement field across two adjacent layers is C^0 . This is $\mathbf{h} = \mathbf{0} \in \mathbb{R}^3$,

$$\mathbf{h} = \left\{ {}^A \bar{\mathbf{x}}(t) + \frac{\vartheta_L}{2} {}^A \mathbf{d}(t) - {}^B \bar{\mathbf{x}}(t) + \frac{\vartheta_U}{2} {}^B \mathbf{d}(t) \right\}. \quad (70)$$

4.3 “Node 6” to “Node 12” constraints

This family of constraints allows dealing with combinations of beams and shells that typically arises in the geometric multi-scale analysis, for the combination of beams and solids see for instance [69]. Some regions of a complex structure

are modeled with shells and the remaining ones are modeled with beams. This strategy allows correct determination of strain and stress states on the regions discretized with shell elements, but at the same time, the essential nonlinear dynamics of the remaining parts discretized with beam elements is properly represented.

According to [70], the following assumptions are necessary: (i) a rigid plane cross section in accordance with the geometrically exact beam theory does exist with normal \mathbf{d}_3 . It means that warping effects are not allowed and therefore, this assumption could be very restrictive; and, (ii) those nodes belonging to the shell and the node belonging to the beam node, which is taken as a master node for the transition, are contained in this plane, see Fig. 5.

– *Soft transition* It allows the relative motion of all “Nodes 6” along a straight line whose origin is located at “Node 12” and whose direction remains constant with respect to the moving frame attached to the master node. The direction of this line is defined as

$$\mathbf{v}(t) = v^1 \mathbf{d}_1(t) + v^2 \mathbf{d}_2(t) + v^3 \mathbf{d}_3(t), \quad (71)$$

in which the components are computed at the initial configuration by means of the formula

$$v^i := \frac{[\mathbf{x}_6(0) - \mathbf{x}_{12}(0)] \cdot \mathbf{d}_i(0)}{\|\mathbf{x}_6(0) - \mathbf{x}_{12}(0)\|_2}. \quad (72)$$

The definition of a bi-normal direction is obtained as

$$\boldsymbol{\tau}(t) = \mathbf{v}(t) \times \mathbf{d}_3(t) = v^2 \mathbf{d}_1(t) - v^1 \mathbf{d}_2(t), \quad (73)$$

and the soft transition for each “Node 6” with respect to the master “Node 12” is $\mathbf{h} = \mathbf{0} \in \mathbb{R}^2$,

$$\mathbf{h} = \left\{ \begin{array}{l} [\mathbf{x}_6(t) - \mathbf{x}_{12}(t)] \cdot \boldsymbol{\tau}(t) \\ [\mathbf{x}_6(t) - \mathbf{x}_{12}(t)] \cdot \mathbf{d}_3(t) - [\mathbf{x}_6(0) - \mathbf{x}_{12}(0)] \cdot \mathbf{d}_3(0) \end{array} \right\}. \quad (74)$$

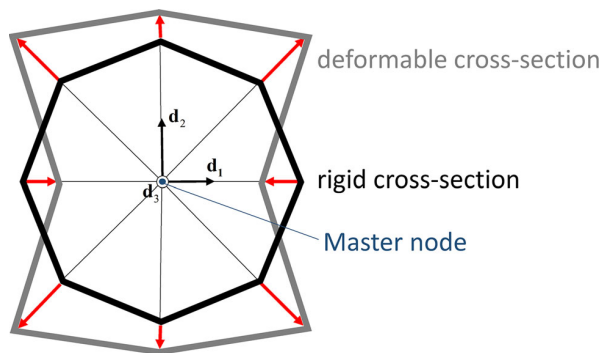


Fig. 5 “Node 6” to “Node 12” constraints: the rigid and soft transitions

- *Rigid transition* The relative motion along the in-plane straight line is not longer permitted. The rigid transition for each “Node 6” with respect to the master “Node 12” is $\mathbf{h} = \mathbf{0} \in \mathbb{R}^3$, in which

$$\mathbf{h} = \begin{Bmatrix} [\mathbf{x}_6(t) - \mathbf{x}_{12}(t)] \cdot \boldsymbol{\tau}(t) \\ [\mathbf{x}_6(t) - \mathbf{x}_{12}(t)] \cdot \mathbf{d}_3(t) - [\mathbf{x}_6(0) - \mathbf{x}_{12}(0)] \cdot \mathbf{d}_3(0) \\ [\mathbf{x}_6(t) - \mathbf{x}_{12}(t)] \cdot \mathbf{v}(t) - [\mathbf{x}_6(0) - \mathbf{x}_{12}(0)] \cdot \mathbf{v}(0) \end{Bmatrix}. \quad (75)$$

This rigid transition represents a more restrictive condition than the soft one and therefore, additional strains are introduced due to the obstruction of transversal deformations. Wagner and Gruttmann [70] showed that for a hybrid beam-shell thin-walled H-beam under axial load, the magnitude of the transversal stress component is higher than the one obtained with the soft transition.

5 Results

In this section, we present some numerical examples to illustrate the potential of the proposed object-oriented framework. All examples were calculated with the self-developed object-oriented finite element method, multibody system software DeSiO, which is entirely coded in Fortran 2008. To validate the presented effort, some of our results are contrasted with those results obtained with conventional finite element software, i.e. ANSYS 17.0 and Abaqus FEA “3DEXPERIENCE R2016x HotFix 3”.

In the first two examples, we set the focus on the adopted director-based geometrically exact beam formulation. Example 1 examines the dynamic snap-through of a shallow arc beam structure and Example 2 considers the dynamic behavior of a swinging rubber rod under gravity. In Examples 3 and 4, we concentrate on the solid-degenerate shell formulation and examine the dynamic behavior of a layered composite cantilever plate under bending and shear loading, and the

dynamic snap-through of a layered composite cylindrical panel. The last two examples focus on hybrid representations, such as the combination of rigid bodies and beams and the combination of beams and shells with guaranteed total energy preservation. Hence, no comparison with results computed with commercial software is provided. Therefore, Example 5 includes a simplified dynamic analysis of a large-scale horizontal-axis wind turbine, in which rigid bodies and geometrically exact beams elements are combined, and Example 6 shows a tumbling slender structure, in which one part of the structure is discretized with solid-degenerate shell elements and the other part is discretized with geometrically exact beam elements.

For the Examples 1 and 4, we consider additional dissipation. The dissipation functions that we employ are those proposed by [5–7], which were calibrated to achieve similar results to those obtained with Abaqus FEA and ANSYS. For both softwares, there are options to automatically stabilize the dynamic solutions by means of introducing of dissipation, but this works like a black box and the extraction of dissipation parameters is not possible. Therefore, we regard these two examples not as benchmarks, but as plausibility studies.

5.1 Example 1: dynamic snap-through of a shallow arc beam structure

The geometry of the shallow arc beam structure is depicted in Fig. 6. The applied cross section properties are $A = 8.45 \times 10^{-3} \text{ m}^2$, $I_{xx} = 2.31 \times 10^{-4} \text{ m}^4$, $I_{yy} = 1.32 \times 10^{-5} \text{ m}^4$, $I_{zz} = 5.11 \times 10^{-7} \text{ m}^4$, and the used material parameters are $E = 2.1 \times 10^{11} \text{ N/m}^2$, $\nu = 0.3$, $G = 8.0 \times 10^{10} \text{ N/m}^2$ and $\rho = 7.85 \times 10^3 \text{ kg/m}^3$. The structure is subdivided into 20 beam elements. The end nodes are simply supported and a concentrated force is applied to point P_1 , which is located at half the arc length of the structure. The corresponding time history of the force is given in Fig. 6 as well. The performed simulation time is 0.4 s with a constant time step of $1.0 \times 10^{-3} \text{ s}$.

Figure 7 presents the vertical displacement u_3 , evaluated at point P_1 , calculated with DeSiO and compared with the results from ANSYS, with the beam element BEAM188 (a two-node element based on Timoshenko theory), and Abaqus FEA, with the beam element B31 (a two-node element based on Timoshenko theory). The diagram at the top shows the solution for the undamped case, whereas the diagram at the bottom contains the solution for the damped case. In both diagrams, it can be seen that the results show a very good agreement for the sub critical responses before snap-through and critical responses during snap-through. For the undamped case, the super critical responses after snap-through, show similar amplitude and mean values. The differences among the three results are attributed to the ele-

Fig. 6 Shallow arc beam structure

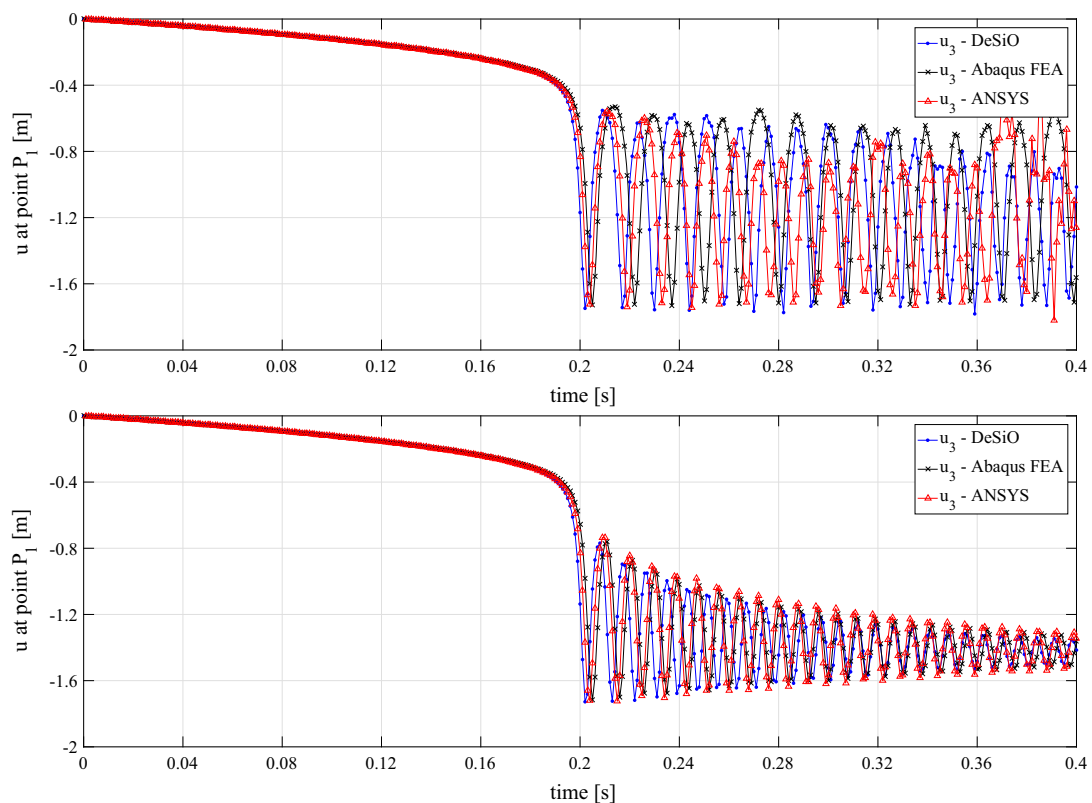
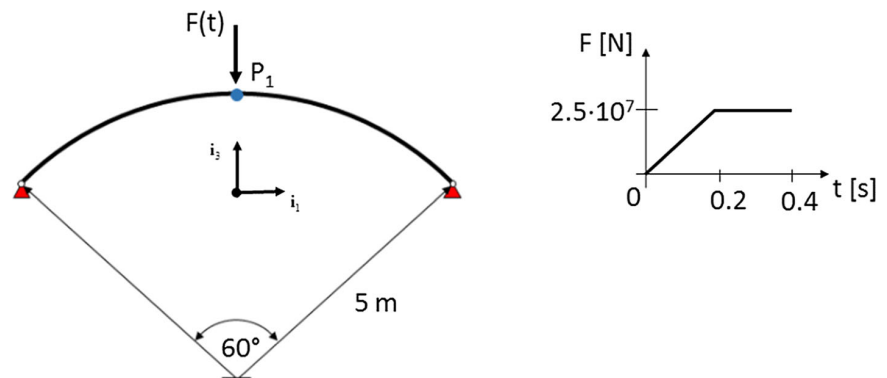


Fig. 7 Shallow arc beam structure—vertical displacement at point P_1 : undamped (top) and damped (bottom)

ment technology and to the integration approaches. The commercial codes employ non conservative integration algorithms, e.g. Newmark's method in ANSYS and HHT method in Abaqus FEA, which in the best case scenario could reach warranted stability only in the linear setting providing a suitable set of integration parameters. In contrast, the robust integration approach we adopted is unconditionally stable even in the nonlinear regime. For the damped case, we consider dissipating loads proportional to the temporal rate of the objective strain measures. The reduction of energy resulting

from the damping is dominant over additional numerical dissipation, if present for non conservative approaches. Due to this, the integration scheme employed by commercial software, meaning that the three approaches perform well under the considered conditions. As a consequence, the agreement during the post critical behavior among all solutions is indeed very good. For this case, the remaining differences are mainly attributed to the element technology, but a detailed analysis of that topic is far away from the scope of the current work.

Fig. 8 Swinging rubber rod—deformed shape at different times computed with DeSiO

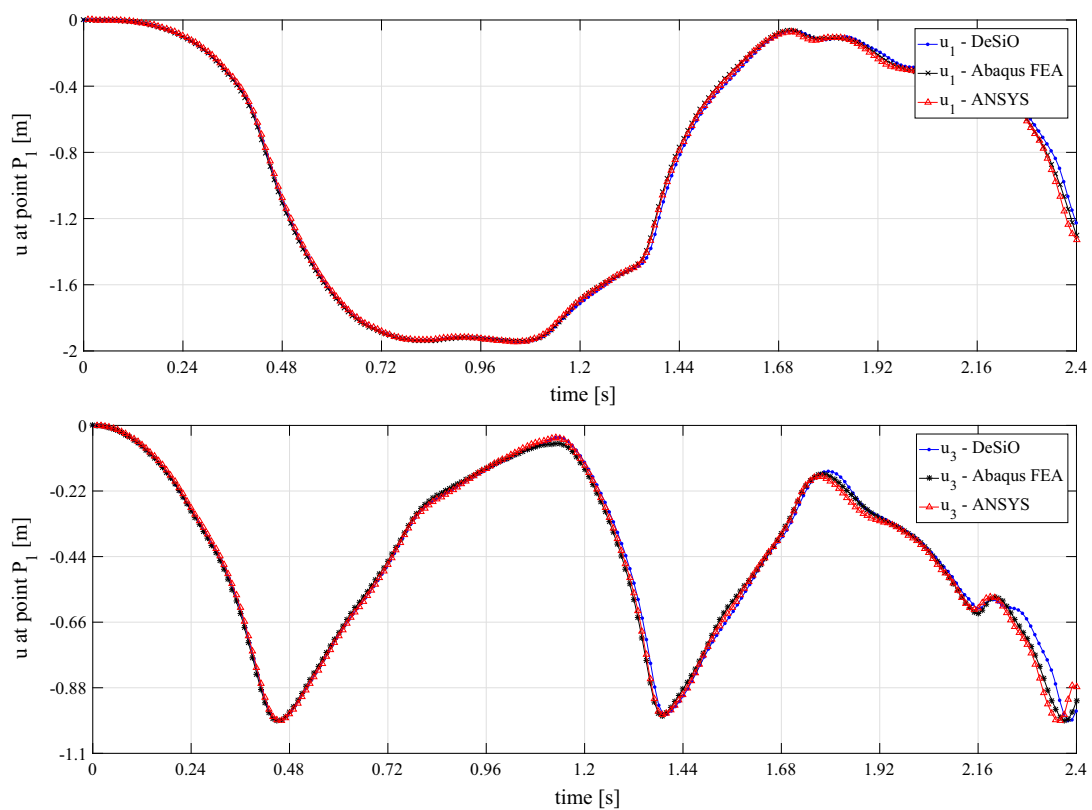
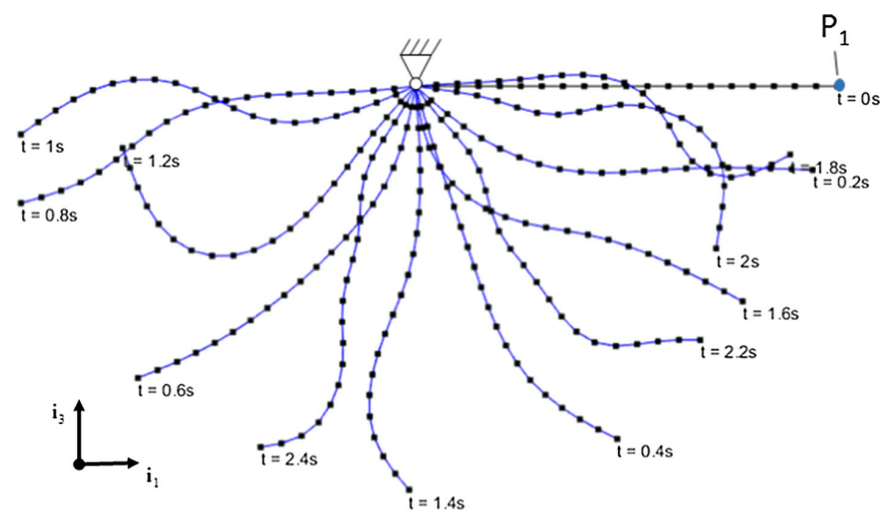


Fig. 9 Swinging rubber rod—displacements (u_1 and u_3) at point P_1

5.2 Example 2: dynamic behavior of a swinging rubber rod under gravity

The dynamic behavior of a swinging rubber rod under the action of gravity was largely studied, see for instance [71]. The rod has a length of 1.0 m and a circular cross section with a radius of 5.0×10^{-3} m. The elastic rod is only loaded by its

self-weight due to the gravity acceleration $g = 9.81 \text{ m/s}^2$. In addition, the rod is simply supported at one end. The rubber material parameters used are $E = 5.0 \times 10^6 \text{ N/m}^2$, $\nu = 0.5$, $G = E/2(1+\nu)$ and $\rho = 1.1 \times 10^3 \text{ kg/m}^3$. No dissipation is considered and discretization comprises 20 beam elements. The performed simulation time is 2.4 s with a constant time step of 1.0×10^{-2} s.

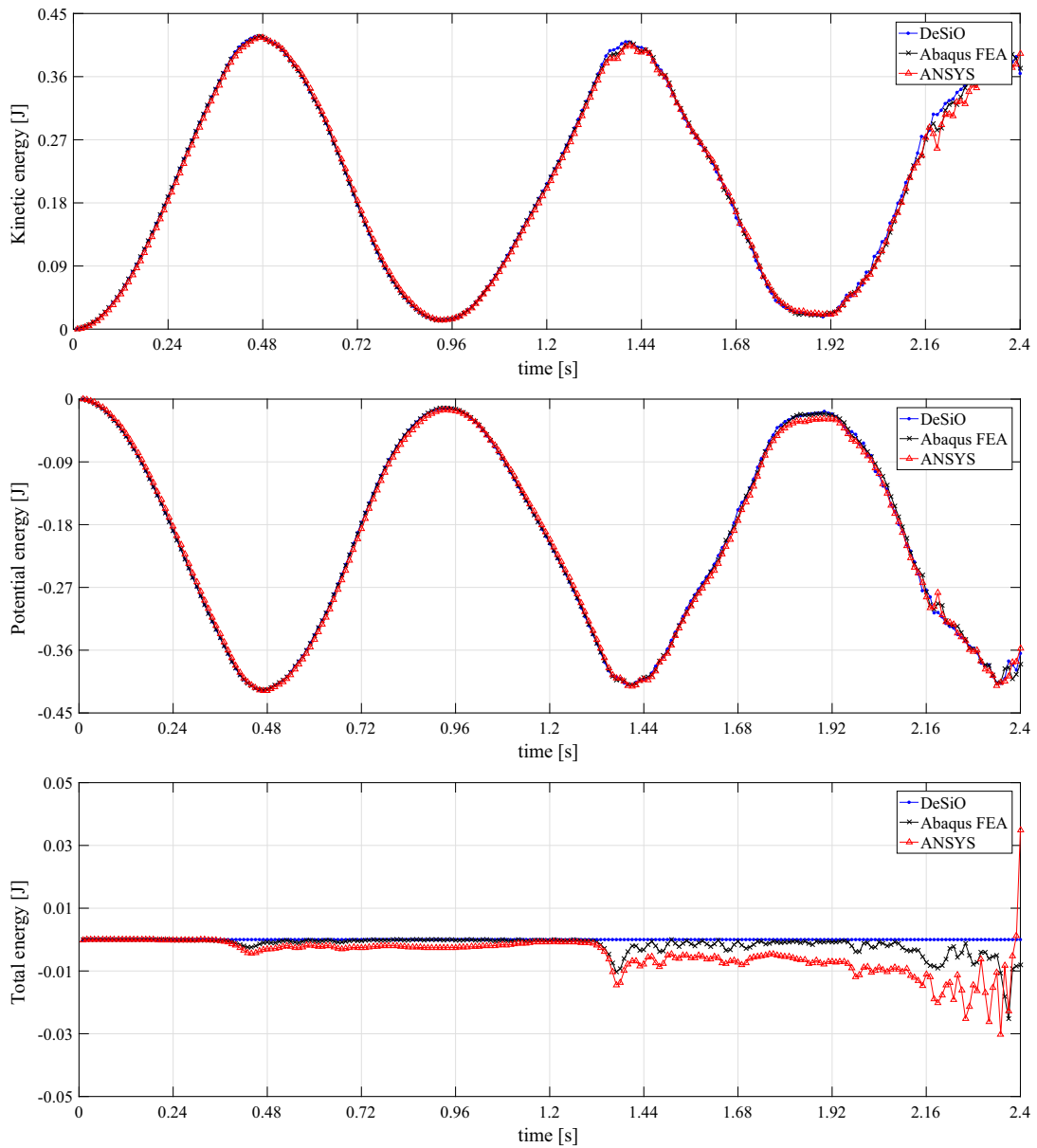


Fig. 10 Swinging rubber rod—energy conservation

Fig. 11 Layered composite cantilever plate—finite element representation and problem setting

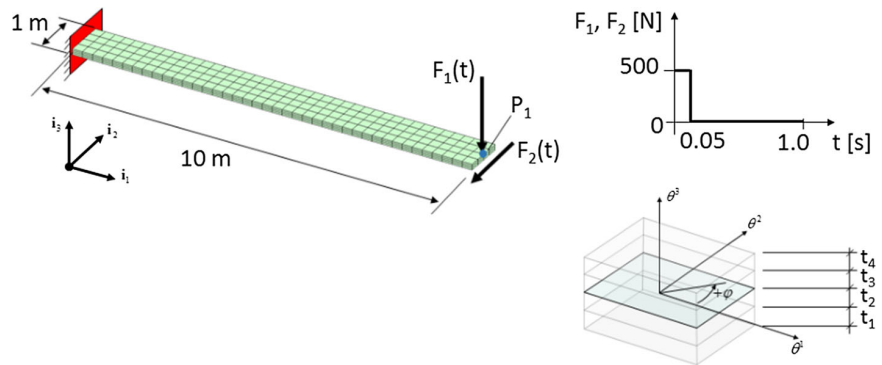


Figure 8 shows the resulting motion sequence within the time interval between $t = 0$ s and $t = 2.4$ s. Large displacements and large rotations become apparent. Figure 9 presents the time history of displacement components u_1 (top), horizontal displacement, and u_3 (bottom), vertical displacements, at point P_1 located at the free end. It can be observed that DeSiO provides a very good consistency regarding the solutions obtained with the commercial software.

Figure 10 shows the time history of the resulting energy for the simulation performed with the current approach and also with Abaqus FEA and ANSYS. For the current formulation, the kinetic and potential energies are equal and with opposite signs and, as required in the adopted conservative time integration scheme, the total energy is identically preserved during the whole simulation. For the commercial software, it is observed that the total energy is not preserved showing sharp rates that are sometimes positives and sometimes negatives. This fact shows that those integration schemes are not stable in the nonlinear sense.

5.3 Example 3: dynamic behavior of a layered composite cantilever plate

The layered composite plate was proposed in Masud et al. [72] in the context of static nonlinear analysis with shell finite elements. The cantilever plate has a length of 10.0 m, a width of 1.0 m and its overall thickness across the four layers is 0.1479 m. Thus, each layer has a thickness of 0.036975 m. The material parameters are $E_1 = 1.379 \times 10^8$ N/m², $E_2 = E_3 = 1.448 \times 10^7$ N/m², $G_{12} = G_{13} = G_{23} = 5.86 \times 10^6$ N/m², $\nu = 0.21$ and $\rho = 5.0$ kg/m³. As shown in Fig. 11, the structure is fixed at its left short edge and loaded at the middle node of the right short edge with concentrated forces in normal direction F_1 , bending force, and in traversal direction F_2 , shear force. The performed simulation time is 1.0 s with a constant time step of 1.0×10^{-2} s.

The time history of the forces used is given in Fig. 11 as well. Here, we analyzed the dynamic response for two layouts with different layer orientation angles in combination with each of the given forces, making a total of four cases. The settings of all the four cases are listed in Table 2.

Figure 12 shows the time history of the displacement in some selected directions at point P_1 for all the four cases. Additionally, the solutions obtained with Abaqus FEA with the shell element S4 (a fully integrated four-node element based on the thick shell theory) and ANSYS with the element SHELL181 (a fully/reduced integrated four-node element for shell finite strain that includes thickness change) are available for comparison. We observe that the solutions obtained with DeSiO, Abaqus FEA and ANSYS are very close to each other showing an excellent agreement. The solution obtained with

Table 2 Layered composite cantilever plate—analyzed cases

Case	F_1 [N]	F_2 [N]	θ_1 [°]	θ_2 [°]	θ_3 [°]	θ_4 [°]
1	−500	0	45	−45	−45	45
2	0	500	45	−45	−45	45
3	−500	0	45	−45	45	−45
4	0	500	45	−45	45	−45

Abaqus FEA shows for case 2 and 4 a vibration frequency that is barely higher. However, the agreement between the solutions obtained with DeSiO and ANSYS and the solution obtained with Abaqus FEA is still very good and acceptable. The differences are mainly attributed to the element technology. At any rate, this discussion is beyond the scope of this work.

Figure 13 shows a motion sequence for case 1, where the initial configuration is located at the upper left corner, and some deformed configurations are sequentially shown from left to right and from top to bottom. The cantilever plate exhibits large displacements and large rotations, therefore the nonlinear kinematic behavior becomes apparent. Figure 14 shows the time evolution of the total energy for the same case computed with the current approach and also with Abaqus FEA and ANSYS. For the current formulation, it can be observed that total energy varies during the time where load is active, i.e. the first 0.05 s. After the disappearance of the external load, the total energy is identically preserved through the time. This particular case shows no unresolved high-frequency content, therefore no dissipation is necessary to compute a convergent long-term response of the system. As already showed for rubber rod example, it is observed that Abaqus FEA and ANSYS fail to preserve the total energy. This fact shows also that those employed integration schemes are dissipative.

5.4 Example 4: dynamic snap-through of a layered composite cylindrical panel

The snap-through of an isotropic cylindrical panel was proposed by Kuhl and Ramm [73] in the context of solid-degenerate shell elements, and later studied by Romero and Armero [29] in the context of geometrically exact shells. Here, we take the same example, but this time the cylindrical panel is a composite multilayer structure made from a single transversal isotropic material, i.e. carbon fiber reinforced plastic. As depicted in Fig. 15, the structure has a constant curvature along the transverse direction. Further geometrical properties are defined by: radius 5.0 m, angle of the arc 60° and length of the longitudinal direction 5.0 m.

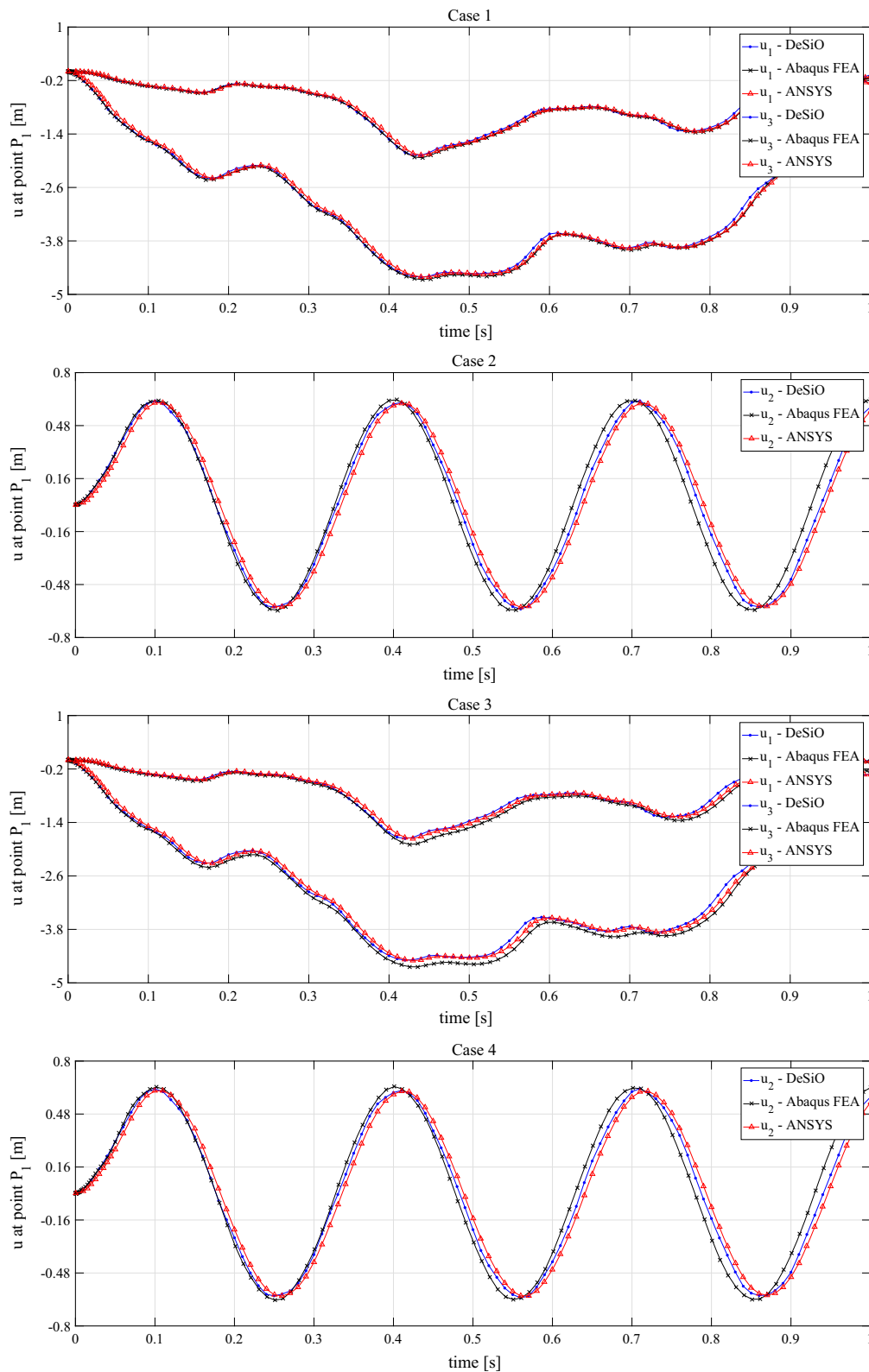


Fig. 12 Layered composite cantilever plate—displacement at point P_1

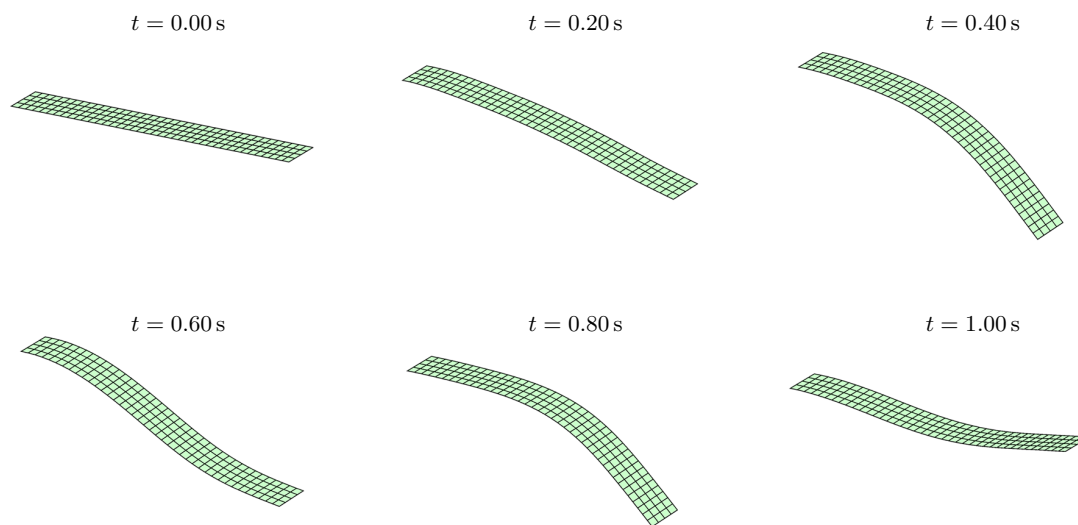


Fig. 13 Layered composite cantilever plate—motion sequence for case 1 computed with DeSiO

The cylindrical panel consists of four layers and each layer has a constant thickness. Layer one is located at the bottom and the following layers are arranged in ascending order to the top, see Fig. 15. The corresponding orientation angles are given by $\theta_1 = \theta_3 = 15^\circ$ and $\theta_2 = \theta_4 = -45^\circ$. The material properties of the carbon fiber reinforced plastic are $E_1 = 1.4 \times 10^{11} \text{ N/m}^2$, $E_2 = E_3 = 1.2 \times 10^{10} \text{ N/m}^2$, $G_{12} = 5.8 \times 10^9 \text{ N/m}^2$, $G_{13} = G_{23} = 5.4 \times 10^9 \text{ N/m}^2$, $G_{23} = 5.4 \times 10^9 \text{ N/m}^2$, $\nu_{12} = \nu_{13} = \nu_{23} = 0.26$ and $\rho = 1.5 \times 10^3 \text{ kg/m}^3$. The structure is discretized into 256 elements, from which 16 elements are located along the longitudinal direction and 16 elements along the transverse direction. The total number of nodes is 289. Both straight edges are simply supported and the panel is subjected to a concentrated force that is applied to the point, which is located at half the arc length in both principal directions of the structure. The corresponding time history of the force is depicted in Fig. 15 as well. The performed simulation time is 0.3 s with a constant time step of $1.0 \times 10^{-3} \text{ s}$.

Figure 16 shows the vertical displacement at point P_1 as a function of time without considering numerical dissipation (top) and with numerical dissipation (bottom). For this example, the dissipation does play an important role. Whilst ANSYS and Abaqus FEA employ dissipation proportional to the velocity, DeSiO employs the complex dissipation explained in the second section of this manuscript. For the case without dissipation, only DeSiO was able to reach the convergent solution for a time interval of 0.3 s. The simulation with ANSYS abruptly stopped a few time steps after the snap-through and the simulation with Abaqus FEA abruptly stopped a few time steps before reaching 0.3 s. The unconditional stability of the method adopted in DeSiO is guaranteed

even in the nonlinear cases provided that the initial guess belongs to the basin of attraction of the Newton–Raphson method. For the damped case, all the solutions performed very well over the whole time interval. The solution obtained with the present approach shows after the snap-through a replica with a slightly higher amplitude than those obtained with commercial software. Since our element is a mixed solid-degenerate shell element, it possesses an enhanced kinematics in terms of displacement and strains. It could play a role regarding the dynamic behavior after snap-through. A corresponding experimental test and the validation of the current numerical models should provide more information about this behavior.

5.5 Example 5: simplified dynamic analysis of a wind turbine

In this example, we present a model for the reference wind turbine defined in [74], see Fig. 17. It consists of one beam component for the tower and three beam components for the individual rotor blades. Hub and nacelle are modeled as rigid bodies. The geometric and material properties for this example are also taken from [74]. Blade pre-cone and shaft tilt are also taken into account. The tower root is rigidly clamped. The rigid connection is used to connect the topmost tower node to the nacelle. The three blades are rigidly connected to the hub, and rotation of the hub about the rotor axis is permitted.

The structure is loaded with a spatial force (initially tangent to the rotation plane) at the ten outermost nodes of the reference blade. The load is applied using a triangle function with a peak force of $1.0 \times 10^5 \text{ N}$ per node during the

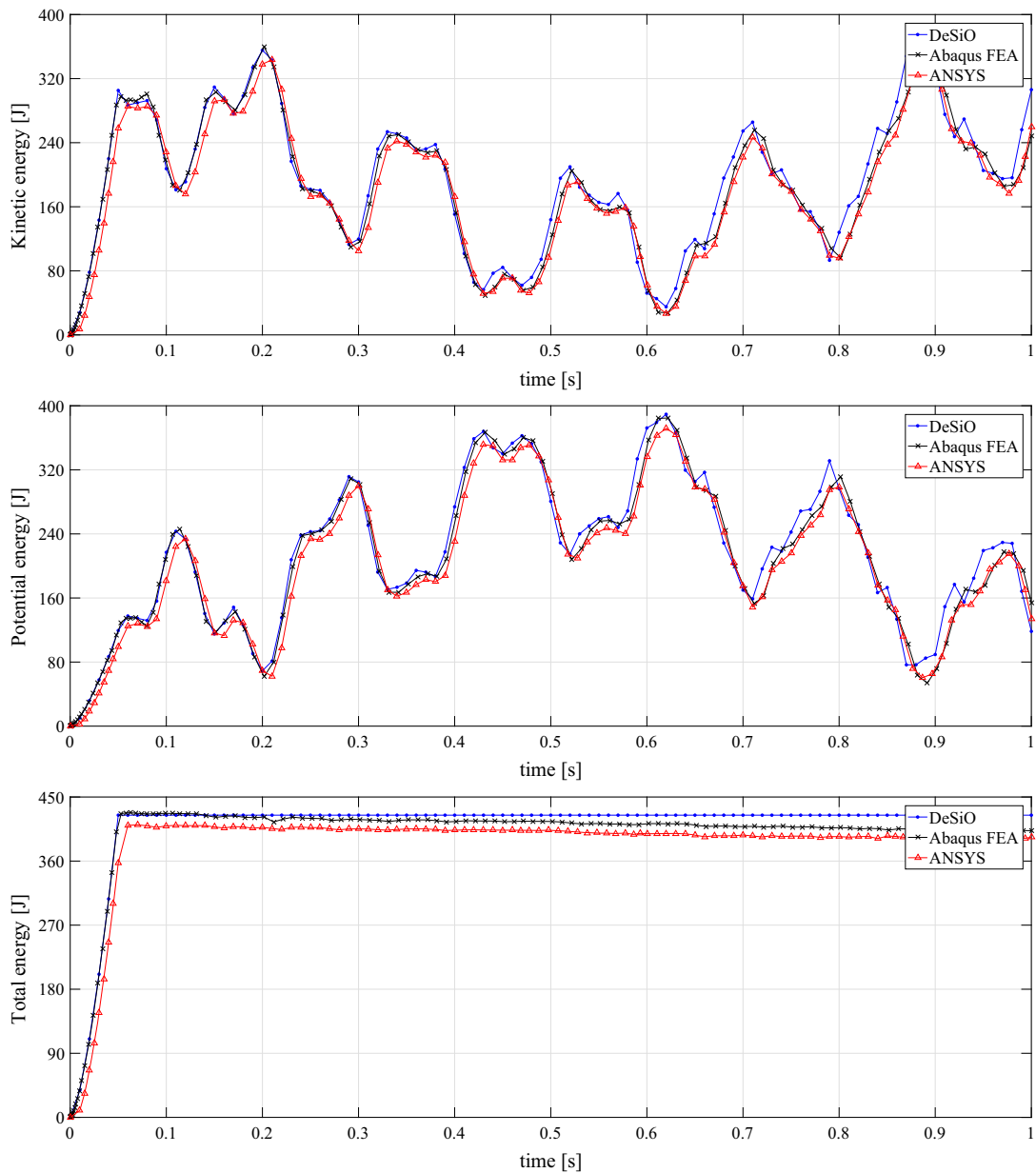


Fig. 14 Layered composite cantilever plate—energy conservation for case 1

first 1.5 s of the simulation. After this time period, the forces vanish. Gravity is available during the whole simulation, and is accounted for the conservation of energy during the force free interval, see Fig. 18. The total simulation time is 10.0 s with a time step of 5.0×10^{-2} s. In Fig. 19, we present the reaction forces at the tower base and at the blade root. It is possible to observe that the time step is very coarse with respect to the vibrations observed, however the method is very robust since total energy is exactly preserved. Under these conditions, the real-time feature is achieved and war-

ranted, since the simulation performs several times faster than the elapsed actual time. Although there is more place for further efficiency improvements, this is already a very promising indicator. Figure 20 shows a motion sequence for the whole wind turbine within the time interval $[0, 2.5]$ s. It is also clear that for a more realistic analysis, it is necessary to account for: (i) unsteady aerodynamic loads and fluid-structure interactions [75–77]; (ii) soil-structure interactions [78,79]; and, (iii) and scattering conditions and their probabilistic treatment in a consistent framework [80–82].

Fig. 15 Layered composite cylindrical panel—finite element representation and problem setting

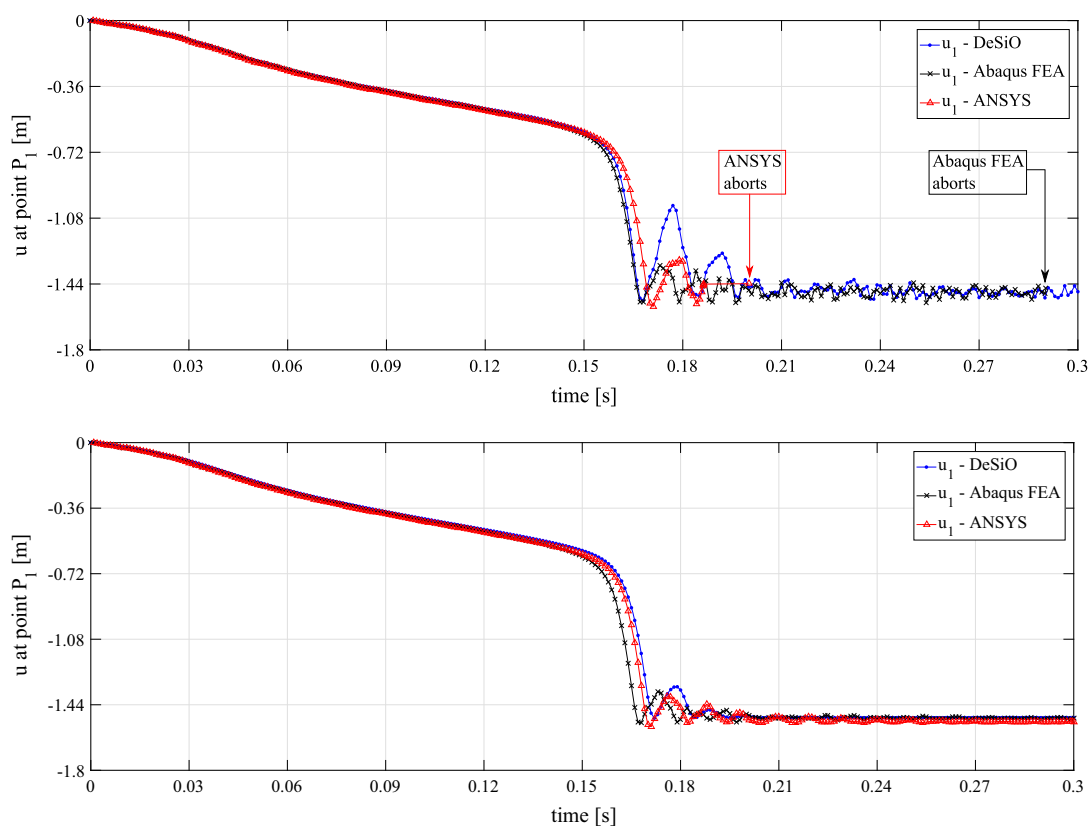
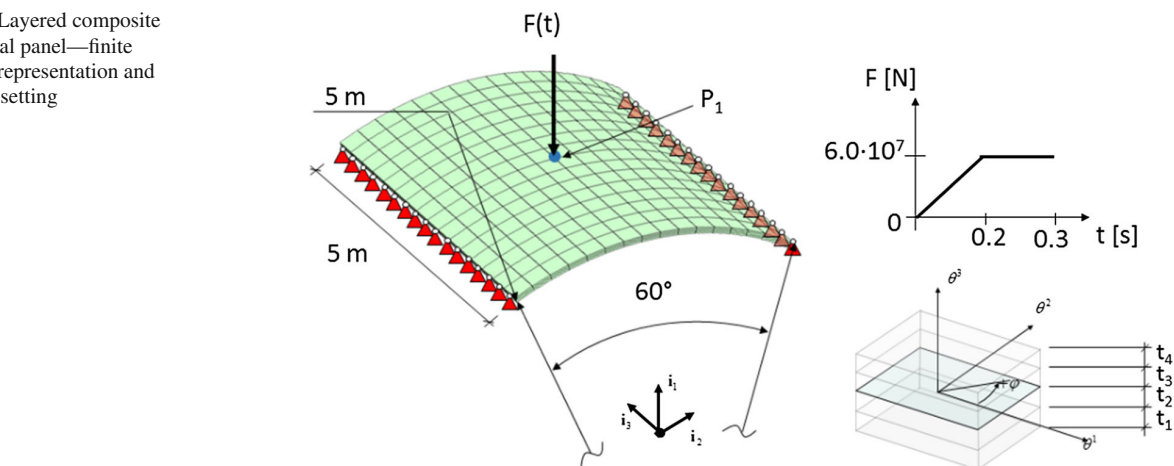


Fig. 16 Layered composite cylindrical panel—vertical displacement at point P_1 : undamped (top) and damped (bottom)

5.6 Example 6: slender cylindrical structure

In the last example, we consider a tumbling slender cylindrical structure, in which one part of the structure is discretized with solid-degenerate shell elements and the other part is discretized with geometrically exact beam elements. The total length of the cylindrical slender structure is 4.0 m. At the half, the connection of the different element types, degenerate-

solid shells and geometrically exact beams, is realized using the soft transition connection previously described. The geometrical and material properties are the following: outer diameter 0.20 m, wall thickness 0.02 m, total length 4.0 m (2.0 m for the shell part and 2.0 m for the beam part), elastic modulus $E = 1 \times 10^8 \text{ N/m}^2$, shear modulus $G = 4 \times 10^7 \text{ N/m}^2$, mass per volume unit $\rho = 1 \times 10^3 \text{ kg/m}^3$. The cylinder is discretized with 360 shell elements (16 ele-

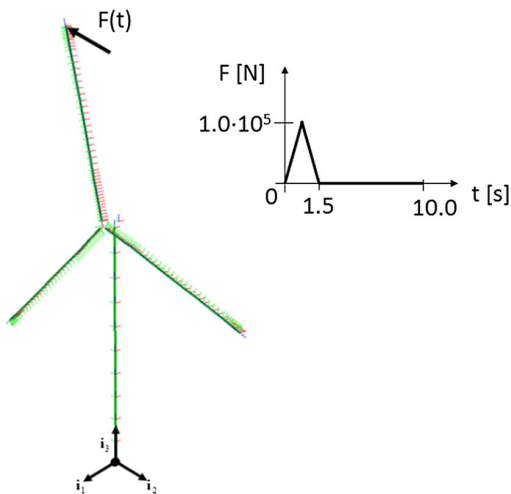


Fig. 17 Wind turbine—finite element representation showing the location of nodes by directors

ments are located along the circumference and 30 elements along the longitudinal direction) and 20 beam elements. The total number of nodes is 393. No further kinematic boundary condition is enforced and no dissipation is considered. Figure 21 shows the geometry and finite element representation. Moreover, the structure is loaded with forces, whose maximal values are $F_1 = F_2 = 1 \times 10^3$ N acting at the free end of the beam part. The simulation time is 2.0 s with a constant time step of 5.0×10^{-3} s. Figure 22 presents a sequence of motion, where the original configuration is located at the upper left corner of the plot, and some deformed configurations are sequentially shown from left to right and from top to bottom. As it can be observed, the slender cylindrical structure exhibits large displacements and large rotations,

therefore the nonlinear kinematic behavior becomes apparent. Figure 23 shows the time history for linear momentum and angular momenta as well as the total energy. The mechanical quantities vary during the time interval, when the load is active. After that, all the invariant quantities are identically preserved through the time. For this case, no unresolved frequency response was observed, therefore no damping is necessary to obtain a long-term response convergent solution. For the rigid transition, linear and angular momenta as well as the total energy are almost identical to the ones obtained with the soft transition and thus, these are not here presented. As the evaluation of local behavior is beyond the scope of this work, the comparison of strains and stresses obtained with both transitions is also left out.

6 Concluding remarks, limitations and future work

We presented a new object-oriented framework to study the nonlinear dynamics of slender structures made of composite multilayer materials, which combines finite element method and multibody system formalism with a robust integration scheme. The approach, which can deal with rigid bodies, geometrically exact beams and solid-degenerate shells, was successfully verified and tested with results computed with standard and well-established commercial tools. In the proposed framework, all advantages of all involved basic ingredients are inherited, e.g. objectivity, unconditional stability, robustness, etc. Moreover, the proposed methodology was fully implemented using the object-oriented programming philosophy, which ensures an easy maintenance and the reusability of existing classes. In summary, we can claim

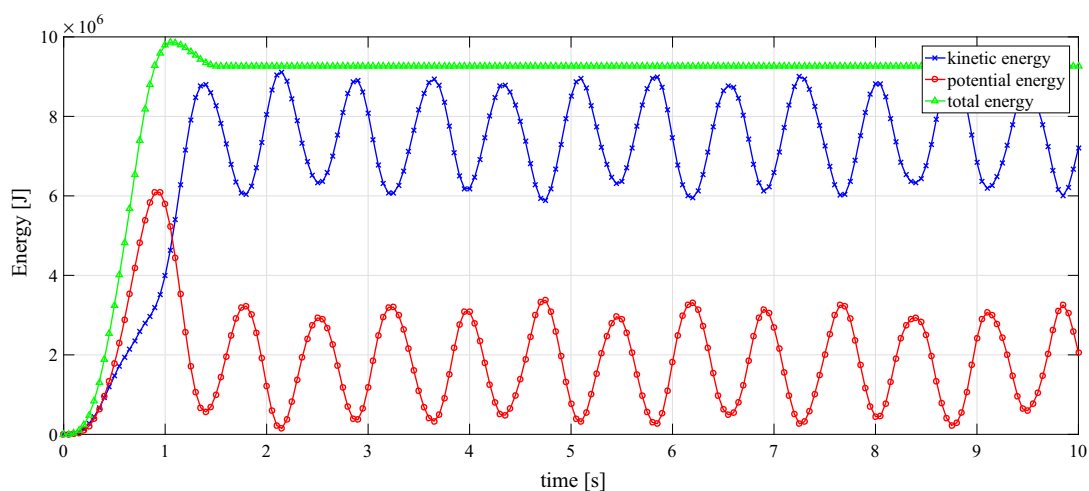


Fig. 18 Wind turbine—energy conservation

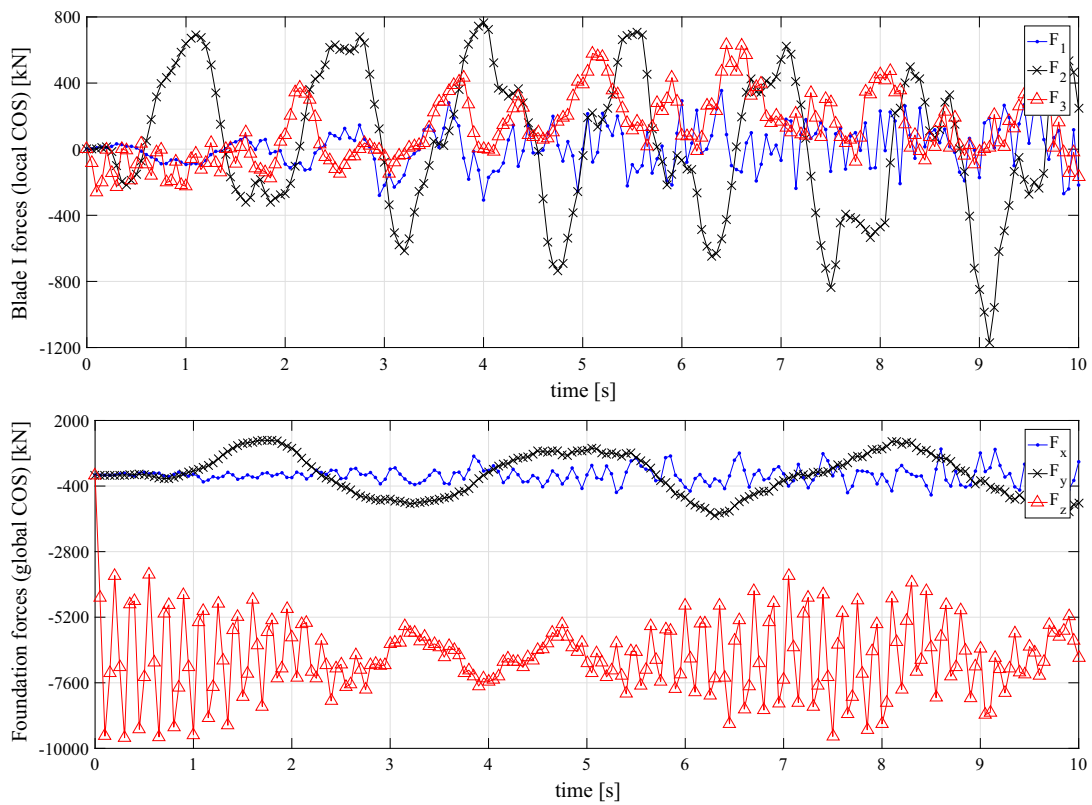


Fig. 19 Wind turbine—forces at tower base and the blade root (reference blade)

Fig. 20 Wind turbine—motion sequence

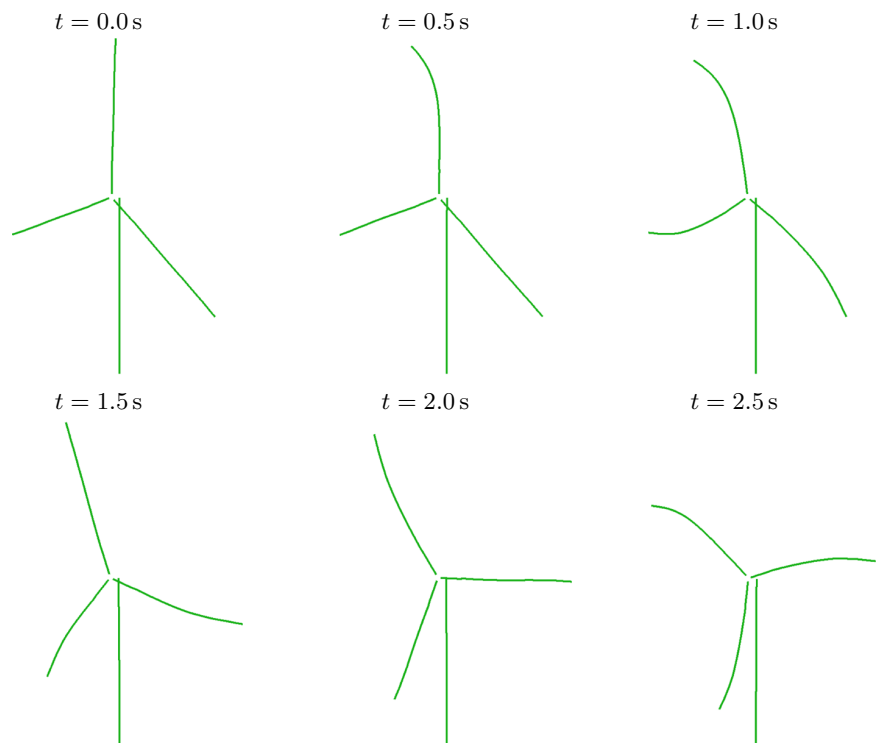


Fig. 21 Slender cylindrical structure—finite element representation

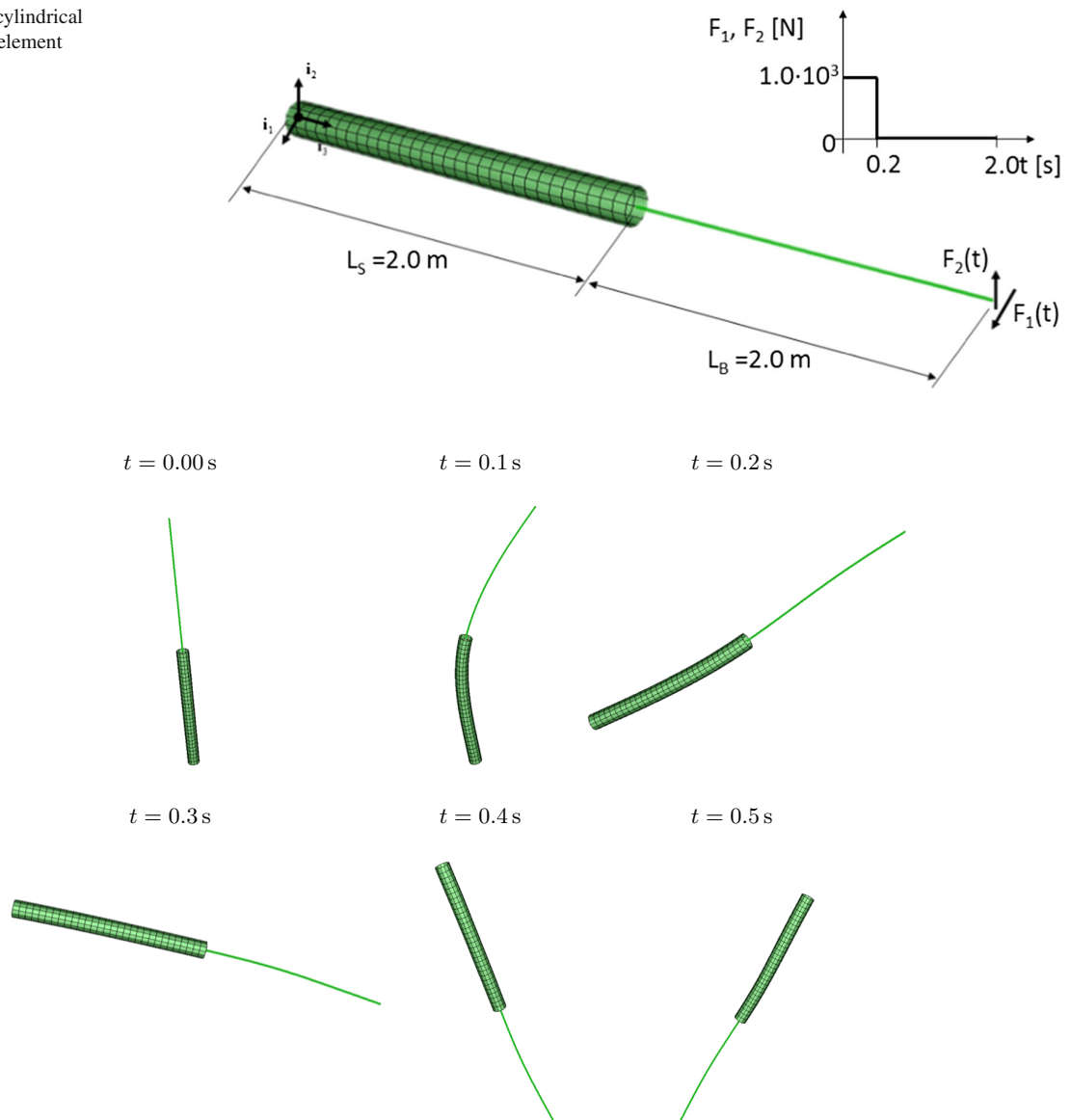


Fig. 22 Slender cylindrical structure—motion sequence

that the approach is able to handle very complicated nonlinear cases, in which rigid bodies, geometrically exact beams and solid-degenerate shells are combined, and the robustness-precision relation is well-balanced. However, the proposed methodology possesses also some limitations. The number of available element formulations is reduced, the material models are restricted to be hyperelastic, and no consideration of contact is possible for now. In addition, the current

approach ought to be enhanced and enriched, for example, by implementing hyper-reduction techniques, off-line pre-computation of coefficients that remain constant during the simulation and enrichment of the kinematics to account for warping in the case of beams or zig-zag functions in the case of shells.

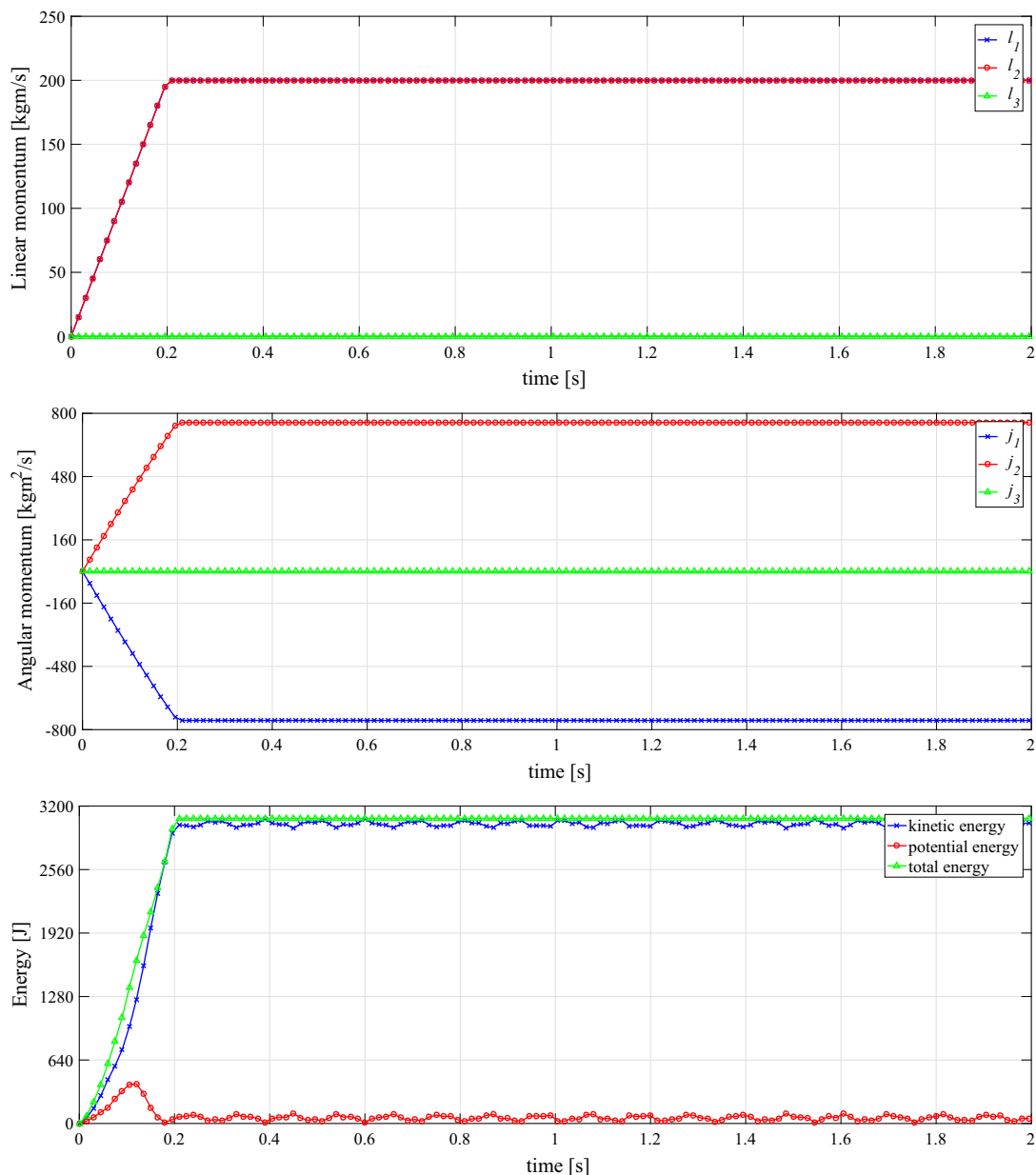


Fig. 23 Slender cylindrical structure—linear momentum, angular momentum and energy

Acknowledgements We greatly acknowledge the financial support of the Lower Saxony Ministry of Science and Culture (research Project *ventus efficiens*, FKZ ZN3024) and the German Federal Ministry for Economic Affairs and Energy (research Project *Deutsche Forschungsplattform für Windenergie*, FKZ 0325936E) that enabled this work. We also thank the reviewers for their valuable comments.

Appendix: Summary: numerical implementation

To achieve very competitive numerical performance, the adopted formulations ought to be generalized in regard to the implementation aspects, for example avoiding redundant code, storing the information to facilitate an optimized handling of data, minimize the amount of required operations, taking advantage of sparse structures, among others. At the same time reusability and extensibility of the produced code must be warranted. Satisfying several criteria at the same time

can result very complicated. Therefore, we think that presenting our scheme for efficient numerical implementation to that kind of problems is as important as the formulation aspects already presented. In the scope of this section, we describe how our self-developed object-oriented finite element method, multibody system software, dubbed DeSiO (**D**esign and **S**imulation Framework for **O**ffshore Support Structures) was conceived.

A.1 Object-oriented programming

The presented ideas are implemented in object-oriented Fortran 2008 by following the design rules of object-oriented programming. Data belonging to the entities modeled in the program like structures and finite elements are confined to the respective Fortran modules. The control flow is designed in such a way that the solver module drives the time integration scheme. The “model” object is called to update force, stiffness and constraint data for every increment.

In Fig. 24, the object hierarchy and information about data and functionality is shown in brief. The following subsections give a detailed description of these entities.

A.1.1 Class “solver”

The “solver” class is responsible for step control, assembling and solving the system of equations for every iteration. After assembly of the iteration matrix and the residual vector, the linear system of equations is solved. According to the Newton–Raphson iteration scheme, the nodal positions and velocities, elemental strains and Lagrange’s multipliers are updated. This also encompasses check of convergence by a numerical tolerance criterion and code to abort the simulation in case of divergence.

Since the structure of the iteration matrix is invariant to the geometrical configuration and loading, reordering and memory organization can be done once before the actual finite element calculation. Nonzero elements are identified by running the iteration matrix assembly using specially conditioned input data for all variables of the formulation that numerically change the iteration matrix:

- Node positions at the beginning of the time step
- Node positions at the current time
- Material loads
- Lagrange multipliers

Parameter coefficients of the employed material law like density and moduli are invariant during the simulation, so zero entries in the iteration matrix arising for example from material symmetries are not considered for the solution.

Considering the “three intersecting plates” problem [56], for a finite element mesh containing 7896 degrees of freedom,

the iteration matrix has a fraction of 99.54% zero elements. Figure 25 displays the structure of the iteration matrix in this case.

Generally, the fraction of zero elements increases with degrees of freedom, which means that the speed advantage gained by employing a sparse solver is pronounced in problems with large numbers of elements. The present code solves the system of equations using the PARDISO [83] parallel sparse solver code.

A.1.2 Class “model”

The “model” class contains every entity in the mechanical system considered in the simulation. When the code starts, it calls the constructor of the “model” class which will in turn open simulation input files. The input files are parsed and instances of structure modules are created according to the information provided. Also constraint input is processed and constraint objects are created accordingly.

During the simulation, the model class is called to assemble the iteration matrix by passing the respective row and column coordinates of the iteration matrix to the simulation entities.

A.1.3 Class “structure”

The “structure” class is a master class to provide an external force calculation routine and assembly handling for entities in the mechanical system considered in the simulation. The external force calculation is placed outside of the element formulation to prevent redundant code which would arise, if this was done in the actual beam and shell classes. Since this simulation framework is intended to be mostly used in context of fluid-structure interactions with non-matching grids (flow field computed with boundary elements), information is transferred using an extended version of the approach exposed in [77], which warrants the primary consistency condition (equivalency at the level of the virtual work) during the data transferring for loads located at fixed isoparametric coordinates and therefore, the calculation can be performed outside the elemental scope. This assumption could result very restrictive for other situations, in which requirements on invariant preservation along the data transefernce from one field to another field are not required. However, a broad exposure of this topic is outside the reach of this manuscript.

A.1.4 Class “rigid body”, “beam”, and “shell”

The “rigid body” class provides a means to simulate concentrated masses and inertias. During the simulation, stiffness matrices corresponding to the inertia of the rigid body are provided for assembly into the iteration matrix.

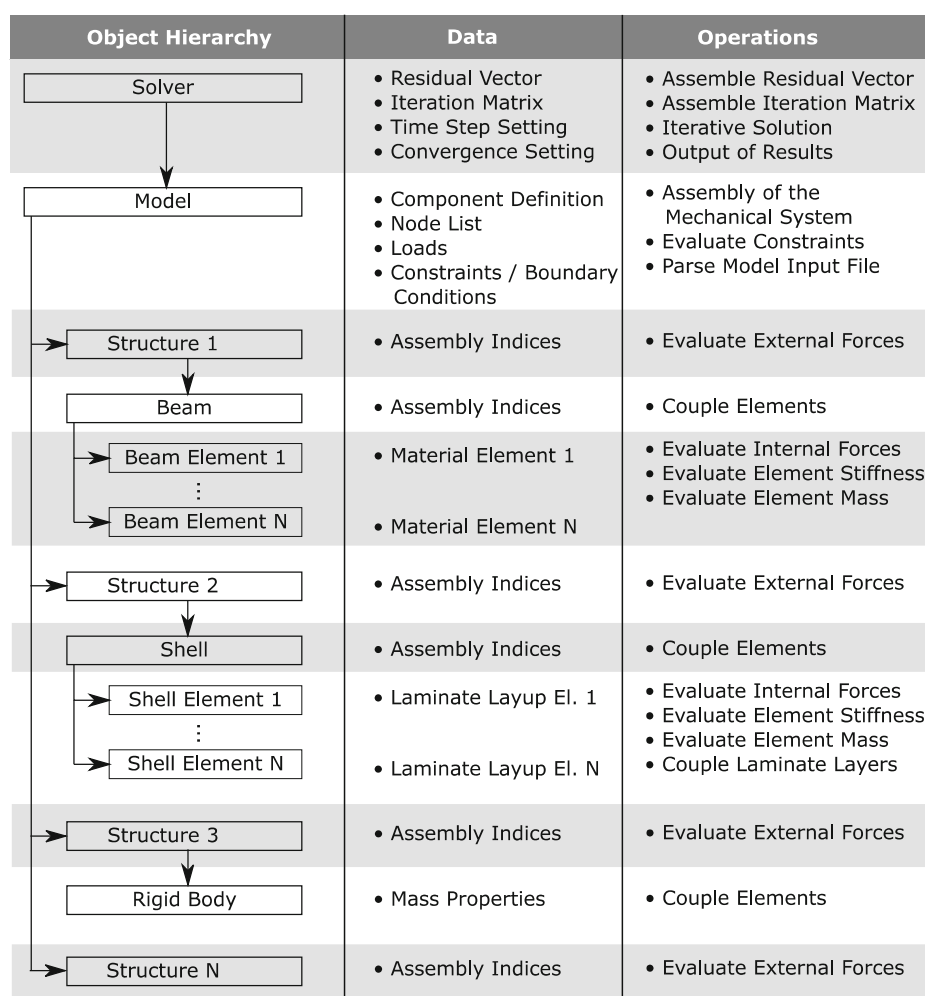


Fig. 24 Object hierarchy and functionality

The “beam” class contains the actual finite elements and element connectivity. During the update for every iteration, the update function for stiffness and internal forces for each element is called. Updated element stiffness and internal forces are then assembled according to the element connectivity stored in the “beam” class.

The “shell” class has the same functionality as the “beam” class. Additional complexity arises from the fact that for quadrilateral elements more connected neighboring elements have to be considered during assembly than during beam assembly and the existence of elemental degree of freedom due to the enhanced assumed strains (these are not condensed).

A.1.5 Class “beam element” and “shell element”

The “element” classes provide the actual mathematical implementation of the finite element as proposed in sections

2.2 and 2.3. Due to the object-oriented implementation, each finite element is an instance of the corresponding Fortran module. This makes passing stiffness and mass information easy by making member variables of the class accessible from the outside. After an update to the internal terms of the element and hence the update of the member variables, all subsequent data queries to the element will provide internal terms for the latest time step.

In every iteration the stiffness and internal forces are updated using the current configuration in generalized coordinates and velocities.

A.1.6 Class “constraint”

The “constraint” class is a master class which is inherited to create a specific kinematic constraint of the type described in Sect. 4. It provides the block vector \mathbf{h} and block matrix \mathbf{H} for the coupling terms between Lagrange’s multipliers

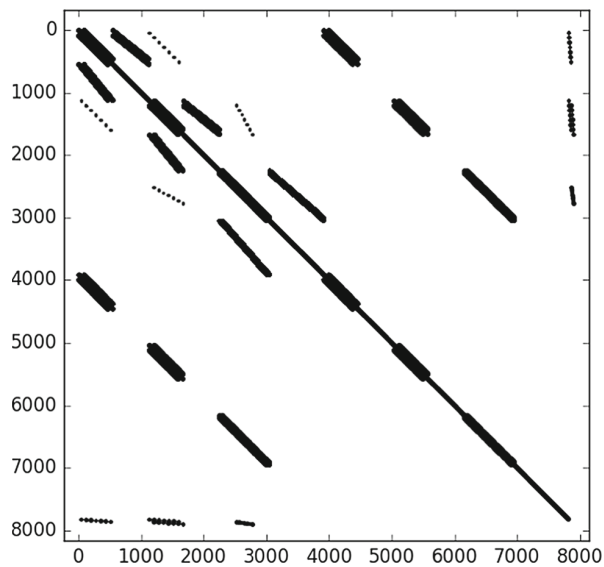


Fig. 25 Skyline plot of the iteration matrix for the “three intersecting plates” problem [41,56]

and generalized coordinates. A method is provided for the Lagrange multiplier update based on the configuration at the current iteration. To enable internal constraints and certain types of joint connections, optionally a stiffness block matrix contribution can be provided.

As discussed in Sect. 4, there are three classes of constraint to couple the “Node 6” and “Node 12” node types: “constraint6”, “constraint12” and “constraint6to12”.

A.1.7 Class “node”

For both “Node 6” and “Node 12”, a separate class exists in the code. These classes are derived from the “node” class and provide the routine to calculate external nodal loads. Loads which should follow the structure, also called material loads, further provide a stiffness block matrix contribution.

A.2 Pre- and post-processing

A.2.1 Pre-processing

Since geometry definition and meshing routines are outside the scope of the finite element kernel, pre-processing is done in external software. Import routines are written in the language Python to read node and element list formats from various commercial finite element solvers and convert geometry and material definitions into the simple format used by the present finite element code. Import of constraints, forces and boundary conditions is semi-automated, since in some cases, the present formulation needs extra information regarding the director-based approach.

A.2.2 Post-processing

For graphical post-processing, a script was developed which enables interactive video display of the transient simulation results. Since commercially available finite element solvers do not implement the concept of directors in the formulation, there is no simple way to convert analysis output to formats used by established post-processors. The in-house visualization tool thus enables a quick check for model sanity by making directors and mesh visible.

References

1. Reissner E (1972) On one-dimensional finite-strain beam theory: the plane problem. *J Appl Math Phys* 23:795–804
2. Bathe K-J, Bolourchi S (1979) Large displacement analysis of three-dimensional beam structures. *Int J Numer Methods Eng* 14:961–986
3. Simo JC (1985) A finite strain beam formulation. The three-dimensional dynamic problem. Part I. *Comput Methods Appl Mech Eng* 49:55–70
4. Cardona A, Géradin M (1988) A beam finite element non-linear theory with finite rotations. *Int J Numer Methods Eng* 26:2403–2438
5. Romero I, Armero F (2002) An objective finite element approximation of the kinematics of geometrically exact rods and its use in the formulation of an energy-momentum conserving scheme in dynamics. *Int J Numer Methods Eng* 54:1683–1716
6. Armero F, Romero I (2001) On the formulation of high-frequency dissipative time-stepping algorithms for nonlinear dynamics. Part I: low-order methods for two model problems and nonlinear elastodynamics. *Comput Methods Appl Mech Eng* 190:2603–2649
7. Armero F, Romero I (2001) On the formulation of high-frequency dissipative time-stepping algorithms for nonlinear dynamics. Part II: second-order methods. *Comput Methods Appl Mech Eng* 190:6783–6824
8. Armero F, Romero I (2003) Energy-dissipative momentum-conserving time-stepping algorithms for the dynamics of nonlinear Cosserat rods. *Comput Mech* 31:3–26
9. Betsch P, Steinmann P (2003) Constrained dynamics of geometrically exact beams. *Comput Mech* 31:49–59
10. Yu W, Liao L, Hodges DH, Volovoi VV (2005) Theory of initially twisted, composite, thin-walled beams. *Thin-Walled Struct* 43:1296–1311
11. Mäkinen J (2007) Total lagrangian Reissner’s geometrically exact beam element without singularities. *Int J Numer Methods Eng* 70:1009–1048
12. Auricchio F, Carotenuto P, Reali A (2008) On the geometrically exact beam model: a consistent, effective and simple derivation from three-dimensional finite-elasticity. *Int J Solids Struct* 45:4766–4781
13. Pimenta PM, Campello EM, Wriggers P (2008) An exact conserving algorithm for nonlinear dynamics with rotational dofs and general hyperelasticity. Part 1: rods. *Comput Mech* 42:715–732
14. Romero I (2008) A comparison of finite elements for nonlinear beams: the absolute nodal coordinate and geometrically exact formulations. *Multibody Syst Dyn* 20:51–68
15. Pai PF (2014) Problems in geometrically exact modeling of highly flexible beams. *Thin-Walled Struct* 76:65–76

16. de Miranda S, Gutierrez A, Melchionda D, Patruño L (2015) Linearly elastic constitutive relations and consistency for GBT-based thin-walled beams. *Thin-Walled Struct* 92:55–64
17. Sprague MA, Jonkman JM, Jonkman B (2015) FAST modular framework for wind turbine simulation: new algorithms and numerical examples. In: 33rd Wind energy symposium, AIAA SciTech Forum, American Institute of Aeronautics and Astronautics
18. Wang Q, Sprague MA, Jonkman J, Johnson N, Jonkman B (2017) Beamdyn: a high-fidelity wind turbine blade solver in the fast modular framework. *Wind Energy* 20:1439–1462
19. Dvorkin EN, Bathe K-J (1984) A continuum mechanics based four-node shell element for general non-linear analysis. *Eng Comput* 1:77–88
20. Bathe K-J, Dvorkin EN (1986) A formulation of general shell elements—the use of mixed interpolation of tensorial components. *Int J Numer Methods Eng* 22:697–722
21. Choi CK, Paik JG (1996) An effective four node degenerated shell element for geometrically nonlinear analysis. *Thin-Walled Struct* 24:261–283
22. Betsch P, Stein E (1995) An assumed strain approach avoiding artificial thickness straining for a non-linear 4-node shell element. *Commun Numer Methods Eng* 11:899–909
23. Betsch P, Stein E (1996) A nonlinear extensible 4-node shell element based on continuum theory and assumed strain interpolations. *J Nonlinear Sci* 6:169–199
24. Simo JC, Armero F (1992) Geometrically non-linear enhanced strain mixed methods and the method of incompatible modes. *Int J Numer Methods Eng* 33:1413–1449
25. Bischoff M, Ramm E (1997) Shear deformable shell elements for large strains and rotations. *Int J Numer Methods Eng* 40:4427–4449
26. Sansour C, Wriggers P, Sansour J (1997) Nonlinear dynamics of shells: theory, finite element formulation, and integration schemes. *Nonlinear Dyn* 13:279–305
27. Betsch P, Menzel A, Stein E (1998) On the parametrization of finite rotations in computational mechanics: a classification of concepts with application to smooth shells. *Comput Methods Appl Mech Eng* 155:273–305
28. Sansour C, Wagner W, Wriggers P, Sansour J (2002) An energy-momentum integration scheme and enhanced strain finite elements for the non-linear dynamics of shells. *Int J Non-Linear Mech* 37:951–966
29. Romero I, Armero F (2002) Numerical integration of the stiff dynamics of geometrically exact shells: an energy-dissipative momentum-conserving scheme. *Int J Numer Meth Eng* 54:1043–1086
30. Bauchau OA, Choi J-Y, Bottasso CL (2002) On the modeling of shells in multibody dynamics. *Multibody Syst Dyn* 8:459–489
31. Aksu Ozkul T (2004) A finite element formulation for dynamic analysis of shells of general shape by using the Wilson- θ method. *Thin-Walled Struct* 42:497–513
32. Betsch P, Sanger N (2009) On the use of geometrically exact shells in a conserving framework for flexible multibody dynamics. *Comput Methods Appl Mech Eng* 198:1609–1630
33. Vaziri A (2009) Mechanics of highly deformed elastic shells. *Thin-Walled Struct* 47:692–700
34. Campello EM, Pimenta PM, Wriggers P (2011) An exact conserving algorithm for nonlinear dynamics with rotational dofs and general hyperelasticity. Part 2: shells. *Comput Mech* 48:195–211
35. Wu T-Y (2013) Dynamic nonlinear analysis of shell structures using a vector form intrinsic finite element. *Eng Struct* 56:2028–2040
36. Ahmed A, Sluys LJ (2015) Implicit/explicit elastodynamics of isotropic and anisotropic plates and shells using a solid-like shell element. *Eur J Mech A Solids* 43:118–132
37. Pietraszkiewicz W, Konopińska V (2015) Junctions in shell structures: a review. *Thin-Walled Struct* 95:310–334
38. Reinoso J, Blázquez A (2016) Application and finite element implementation of 7-parameter shell element for geometrically nonlinear analysis of layered CFRP composites. *Compos Struct* 139:263–276
39. Caliri MF Jr, Ferreira AJM, Tita V (2016) A review on plate and shell theories for laminated and sandwich structures highlighting the finite element method. *Compos Struct* 156:63–77
40. Ota NSN, Wilson L, Gay Neto A, Pellegrino S, Pimenta PM (2016) Nonlinear dynamic analysis of creased shells. *Finite Elem Anal Des* 121:64–74
41. Gebhardt CG, Rolfes R (2017) On the nonlinear dynamics of shell structures: combining a mixed finite element formulation and a robust integration scheme. *Thin-Walled Struct* 118:56–72
42. Bucleam ML, Bathe K-J (2011) *The mechanics of solids and structures—hierarchical modeling and the finite element solution*. Springer, Berlin
43. Eisenberg M, Guy R (1979) A proof of the hairy ball theorem. *Am Math Monthly* 86:571–574
44. Arnold VI (1989) *Mathematical methods of classical mechanics*. Springer, Berlin
45. Hearsh WB (2006) *Rigid body mechanics: mathematics, physics and applications*. Wiley, Hoboken
46. Romero I (2001) *Formulation and analysis of dissipative algorithms for nonlinear elastodynamics*. Ph.D. thesis, University of California, Berkeley
47. Gebhardt CG (2012) *Desarrollo de simulaciones numéricas del comportamiento aeroelástico de grandes turbinas eólicas de eje horizontal*. Ph.D. thesis, Universidad Nacional de Córdoba
48. Betsch P, Steinmann P (2001) Frame-indifferent beam finite elements based upon the geometrically exact beam theory. *Int J Numer Methods Eng* 54:1775–1788
49. Gebhardt CG, Matusevich AE, Inaudi JA (2018) Coupled transverse and axial vibrations including warping effect in asymmetric short beams. *J Eng Mech* 144(6):04018043
50. Gay Neto A (2017) *Simulation of mechanisms modeled by geometrically-exact beams using rodrigues rotation parameters*. *Comput Mech* 59:459–481
51. Ghosh S, Roy D (2009) A frame-invariant scheme for the geometrically exact beam using rotation vector parametrization. *Comput Mech* 44:103–118
52. Romero I (2004) The interpolation of rotations and its application to finite element models of geometrically exact rods. *Comput Mech* 34:121–133
53. Simo JC, Rifai MS (1990) A class of mixed assumed strain methods and the method of incompatible modes. *Int J Numer Methods Eng* 29:1595–1638
54. Ko Y, Lee P-S, Bathe K-J (2017) A new mitc4+ shell element. *Comput Struct* 182:404–418
55. Kane C, Marsden JE, Ortiz M (1999) Symplectic-energy-momentum preserving variational integrators. *J Math Phys* 40:3353–3371
56. Simo JC, Tarnow N (1994) A new energy and momentum conserving algorithm for the non-linear dynamics of shells. *Int J Numer Methods Eng* 37:2527–2549
57. Harten A, Lax B, Leer P (1983) On upstream differencing and Godunov-type schemes for hyperbolic conservation laws. *SIAM Rev* 25:35–61
58. McLachlan RI, Quispel GRW, Robideux N (1999) Geometric integration using discrete gradients. *Philos Trans Math Phys Eng Sci* 357:1021–1045
59. Gonzalez O (1996) Time integration and discrete Hamiltonian systems. *J Nonlinear Sci* 6:449–467
60. Romero I (2012) An analysis of the stress formula for energy-momentum methods in nonlinear elastodynamics. *Comput Mech* 50:603–610
61. Romero I (2008) Formulation and performance of variational integrators for rotating bodies. *Comput Mech* 42:825–836

62. Leyendecker S, Marsden J, Ortiz M (2008) Variational integrators for constrained dynamical systems. *Zeitschrift für Angewandte Mathematik und Mechanik* 88:677–708
63. Betsch P (2005) The discrete null space method for the energy consistent integration of constrained mechanical systems. Part i: holonomic constraints. *Comput Methods Appl Mech Eng* 194:5159–5190
64. Betsch P, Leyendecker S (2006) The discrete null space method for the energy consistent integration of constrained mechanical systems. Part ii: multibody dynamics. *Int J Numer Methods Eng* 67:499–552
65. Leyendecker S, Betsch P, Steinmann P (2008) The discrete null space method for the energy-consistent integration of constrained mechanical systems. Part iii: flexible multibody dynamics. *Multibody Syst Dyn* 19:45–72
66. Betsch P (2016) *Structure-preserving integrators in nonlinear structural dynamics and flexible multibody dynamics*. Springer, Berlin
67. Klöppel T, Gee MW, Wall WA (2011) A scaled thickness conditioning for solid- and solid-shell discretizations of thin-walled structures. *Comput Methods Appl Mech Eng* 200:1301–1310
68. Simo JC, Tarnow N (1992) The discrete energy-momentum method. Conserving algorithms for nonlinear elastodynamics. *Zeitschrift für Angewandte Mathematik und Physik* 43:757–792
69. Romero I (2018) Coupling nonlinear beams and continua: Variational principles and finite element approximations. *Int J Numer Methods Eng* (in press)
70. Wagner W, Gruttmann F (2002) Modeling of shell-beam transitions in the presence of finite rotations. *Comput Assist Mech Eng Sci* 9:4005–4018
71. Lang H, Linn J, Arnold M (2011) Multi-body dynamics simulation of geometrically exact Cosserat rods. *Multibody Syst Dyn* 25:285–312
72. Masud A, Tham CL, Liu WK (2000) A stabilized 3-D co-rotational formulation for geometrically nonlinear analysis of multi-layered composite shells. *Comput Mech* 26:1–12
73. Kuhl D, Crisfield M (1999) Energy-conserving and decaying algorithms in non-linear structural dynamics. *Int J Numer Methods Eng* 45:569–599
74. Jonkman J, Butterfield S, Musial W, Scott G (2009) Definition of a 5-MW reference wind turbine for offshore system development. Technical report, National Renewable Energy Laboratory (NREL) Golden, CO
75. Gebhardt CG, Preidikman S, Massa JC (2010) Numerical simulations of the aerodynamic behavior of large horizontal-axis wind turbines. *Int J Hydrog Energy* 35:6005–6011
76. Gebhardt CG, Preidikman S, Jørgensen MH, Massa JC (2012) Non-linear aeroelastic behavior of large horizontal-axis wind turbines: a multibody system approach. *Int J Hydrog Energy* 37:14719–14724
77. Gebhardt CG, Rocca BA (2014) Non-linear aeroelasticity: an approach to compute the response of three-blade large-scale horizontal-axis wind turbines. *Renew Energy* 66:495–514
78. Häfele J, Hübler C, Gebhardt CG, Rolfes R (2016) An improved two-step soil-structure interaction modeling method for dynamical analyses of offshore wind turbines. *Appl Ocean Res* 55:141–150
79. Hübler C, Häfele J, Gebhardt CG, Rolfes R (2018) Experimentally supported consideration of operating point dependent soil properties in coupled dynamics of offshore wind turbines. *Mar Struct* 57:18–37
80. Hübler C, Gebhardt CG, Rolfes R (2017) Hierarchical four-step global sensitivity analysis of offshore wind turbines based on aeroelastic time domain simulations. *Renew Energy* 111:878–891
81. Hübler C, Gebhardt CG, Rolfes R (2017) Development of a comprehensive data basis of scattering environmental conditions and simulation constraints for offshore wind turbines. *Wind Energy Sci* 2:491–505
82. Häfele J, Hübler C, Gebhardt CG, Rolfes R (2018) A comprehensive fatigue load set reduction study for offshore wind turbines with jacket substructures. *Renew Energy* 118:99–112
83. Intel Corporation (2015) Intel® Math Kernel Library 11.3 Developer Reference. <https://software.intel.com/en-us/mkl>. Accessed Oct 2017

Publisher's Note Springer Nature remains neutral with regard to jurisdictional claims in published maps and institutional affiliations.

4. Article C: Understanding the nonlinear dynamics of beam structures: a principal geodesic analysis approach

This article presents a comprehensive framework to analyze the nonlinear dynamics of beam structures that goes beyond classical procedures that assume linearity on the configuration space, *e.g.*, modal analysis and principal component analysis. The proposed approach relies on: *i*) a frame-invariant path-independent finite-element formulation for geometrically exact beams; *ii*) a multibody formalism to deal with general boundary conditions and to render more complicated structures through connections and junctions; *iii*) a momentum-preserving energy-preserving/dissipative scheme to integrate the governing equations in the time domain; and, *iv*) a *principal geodesic analysis* to directly identify the main kinematic features from the solution. The proposed approach is very powerful to identify motion patterns/modes in a fully nonlinear setting, which is the main innovation of the present research. Such motion patterns could be used very effectively to generate models of reduced order for design purposes or to investigate changes of the mechanical features of a given structure, which is highly relevant in the context of model-based Structural-Health-Monitoring for damage identification, localization and quantification. Along this work, the theoretical and numerical foundations are addressed, since they are necessary to identify motion patterns. This provides a very robust procedure to improve the understanding of the matter with respect to classical approaches available in the literature. The proposed approach may be used very effectively to build reduced-order models or to evaluate changes of the mechanical features of a given structure.

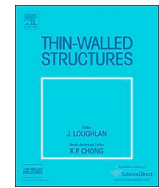
This article is published in *Thin-Walled Structures* 140 (2019), 357–372. The work was conducted in cooperation with a partner from the **Institute of Applied Mathematics** at **Leibniz Universität Hannover**. The main work was done by the author of this *Habilitationsschrift*. Marc Steinbach contributed with the numerical implementation of the *principal geodesic analysis* and its subsequent application. Raimund Rolfes contributed with technical suggestions and supporting work.

Permanent link: <https://doi.org/10.1016/j.tws.2019.03.009>



Contents lists available at ScienceDirect

Thin-Walled Structures

journal homepage: www.elsevier.com/locate/tws

Full length article

Understanding the nonlinear dynamics of beam structures: A principal geodesic analysis approach

Cristian Guillermo Gebhardt^{a,*}, Marc Christian Steinbach^b, Raimund Rolfes^a^a Leibniz Universität Hannover, Institute of Structural Analysis and ForWind Hannover, Appelstraße 9A, 30167 Hannover, Germany^b Leibniz Universität Hannover, Institute of Applied Mathematics, Welfengarten 1, 30167 Hannover, Germany

ARTICLE INFO

Keywords:

Nonlinear dynamics
 Beam structures
 Finite-element method
 Robust integration
 Principal geodesic analysis

ABSTRACT

We present a framework to identify the main kinematic features that arise when considering the nonlinear dynamics of beam structures that takes advantage of the mathematical structure provided by the configuration space. This relies on: *i*) a finite-element formulation for geometrically exact beams; *ii*) a multibody formalism to deal with boundary conditions and to render complex structures; *iii*) a robust integration scheme; and, *iv*) a principal geodesic analysis to directly identify the main kinematic features. Our framework contributes to improve the understanding of the very complex nonlinear dynamics, and at the same time, provides some hints regarding the further model order reduction, but in a fully nonlinear setting. The proposed ideas are tested and their capabilities are illustrated with four examples: a swinging rod under gravity, a free oscillating clamped-free straight beam with pre-stress, a triple pendulum under gravity and a complete wind turbine.

1. Introduction

The fully nonlinear analysis of current and modern beam structures is becoming more and more popular in different applications like wind energy, aeronautics, offshore oil and gas industry, among others. In this context, the nonlinear dynamics of such slender structures is very rich, but also very complex. The configuration space of any given point along the beam is completely described by its position, which can be described by a vector $\bar{\mathbf{x}}$ that belongs to the three-dimensional Euclidean space, and its orientation, which can be described by a matrix \mathbf{R} that belongs to the group of rotations. This group is a very special one because beyond satisfying the group axioms (*e.g.*, for the case of rotation matrices, we have that: *i*) the product of two rotations is also a rotation; *ii*) there is a neutral element, namely the identity; and, *iii*) there is an inverse element, namely for each rotation matrix there is another rotation matrix such as their product is equal to the identity) also possesses a manifold structure (*i.e.*, a curved space that is smoothly defined everywhere and can be locally described as a linear space). These features are already evidenced when describing the kinematic/kinetic quantities like the curvature $\mathbf{\Omega}$ and the angular velocity \mathbf{W} , that can not be derived from an orientation vector, but as the axial representations of skew-symmetric matrices that are computed as $\hat{\mathbf{\Omega}} = \mathbf{R}^T \mathbf{R}'$, where $(\cdot)'$ stands for the derivative along the arc-length, and $\hat{\mathbf{W}} = \mathbf{R}^T \dot{\mathbf{R}}$, where (\cdot) stands for the time derivative, respectively. This fact shows that the complex nonlinear motion of beam structures can not be described as a

linear combination of time-invariant patterns at the level of the configuration space, *i.e.*, modal decomposition and proper orthogonal decomposition are no longer possible without destroying intrinsic features of the motion.

Reissner [1] formulated a one-dimensional large-strain beam theory for plane deformations of plane beams. Bathe and Boloruchi [2] discussed fundamental aspects regarding the formulation of three-dimensional geometrically nonlinear beam elements. Simó [3] extended the concepts considered by Reissner in [1] to the three-dimensional case, from which resulted the so-called geometrically exact beam theory. Cardona and Géradin [4] developed an objective beam finite element based on the geometrically exact beam theory and a material description of the rotation group. Romero and Armero [5] presented a finite element formulation for geometrically exact beams, which is frame-indifferent. Relying on the straightforward interpolation of the directors, the authors provided a detailed derivation of the spatial and temporal discretizations. The proposed framework allowed the development of an unconditionally stable time-stepping algorithm that preserves some first integrals of motion. Armero and Romero [6,7] developed a family of schemes for nonlinear three-dimensional elastodynamics that exhibits controllable numerical dissipation in the high-frequency range. Armero and Romero [8] particularized that integration approach to the Cosserat rod case. In the energy-preserving context, Betsch and Steinmann [9] presented a brief overview of the constrained dynamics of

* Corresponding author.

E-mail address: c.gebhardt@isd.uni-hannover.de (C.G. Gebhardt).

nonlinear beams. In contrast to the standard formulations based on rotational degrees of freedom, the authors proposed the interpolation of a triad consisting of three orthonormal directors, where the mutual orthonormality is achieved by imposing holonomic constraints. For an exhaustive review and classification in regard to the interpolation of rotations in the context of geometrically exact beams, the reader is referred to Romero [10]. Fletcher et al. [11] developed the principal geodesic analysis, a generalization of the principal component analysis to the manifold setting, and demonstrated its use in describing the variability of medially-defined anatomical objects. Yu et al. [12] considered geometrically exact beams with initially large twisting and large curvature in the context of thin-walled structures. Mäkinen [13] derived an improved version of the formulation proposed by Cardona and Gérardin in [4], which, beyond being objective like in its original version, is also path independent. Auricchio et al. [14] emphasized some intrinsic features of the three-dimensional beam model proposed by Simó in [3]. The formulation was also re-derived in a consistent and compact form. Pimenta et al. [15] developed a fully conservative algorithm for the integration of the equations of motion in nonlinear rod dynamics, with which the authors achieved the objectivity at the discrete level. Romero [16] compared the absolute nodal coordinate and geometrically exact formulations. Ghosh and Roy [17] developed a frame-invariant scheme using the rotation vector parametrization in the context of an Eulerian formulation. Pai [18] discussed occurrent problems for different beam theories under large deformations. Huckemann et al. [19] developed a general framework, which is laid out for principal component analysis on quotient spaces that result from an isometric Lie group action on a complete Riemannian manifold. Machado and Piován [20] investigated the nonlinear dynamics of rotating planar beams using nonlinear modes. The model is based on a one-dimensional Euler-Bernoulli formulation where the geometric cubic nonlinear terms are included in the equation of motion. Pai [21] considered an energy-consistent formulation and order deficiency of linear and nonlinear shear-deformable beam theories, including Timoshenko's theory and Cosserat rod theory. Special attention is paid to the order deficiency, shear correction factors, shear locking and nonlinearities. Pai [18] considered an advanced total-Lagrangian geometrically exact displacement-based beam theory without singularities. Such a model was used to compare with and reveal, by in-depth derivations and reasoning, theoretical and numerical problems of other nonlinear beam theories that intend to be geometrically exact in the literature. De Miranda et al. [22] discussed briefly the constitutive assumptions normally done for linear elastic isotropic and orthotropic materials in the framework of thin-walled beams. Wu and Tiso [23] investigated the model order reduction for planar geometrically nonlinear beams by means of the “modal-derivative” concept in combination with the Craig-Bampton technique. Hauberg [24] considered extensions of the principal component analysis to Riemannian manifolds by means of employing the concept of principal curves. Gebhardt and Rolfe [25] considered the nonlinear dynamics of shell structures, where a mixed finite element formulation and a robust integration scheme are combined. The formulation proposed by Pimenta et al. [15] was enhanced by Gay Neto [26] in the context of mechanism with contact. Sonnevile et al. [27] considered the interpolation of the kinematic fields describing the configuration of geometrically exact beams, *i.e.*, the position and rotation fields. Two kinematic representations were investigated: the classical approach that treats the displacement and rotation fields separately and the motion approach that treats those two fields as a unit. Brüls et al. [28] investigated the application of the proper orthogonal decomposition method to dynamic systems including the construction of the snapshot matrix and the definition of the projection operation on the Lie group. An alternative approach to investigate the nonlinear dynamics of beams is provided by the co-rotational technique that relies on the separation of primary motions, due to large rotations and displacements in the space of the structure or a part of the structure as a whole, and secondary motions, due to small/

moderate rotations and displacements originating from elastic deformations. Special attention ought to be paid to the fact that the nonlinear internal force vectors and stiffness matrices differ from applying transformation to the linear internal force vectors and stiffness matrices. Such vector and matrix quantities should be derived from the adopted deformation measures consistently. This is crucial for capturing properly softening/stiffening effects among others. In contrast to that approach, our formulation relies on the geometrically exact beam concept, and therefore the only possibility of separating motions requires the polar decomposition of the tangent map $F := d(\varphi_t \circ \varphi_0^{-1}): T_{X(\theta,0)}\mathcal{X}_0 \rightarrow T_{X(\theta,t)}\mathcal{X}_t$, the so-called deformation gradient. Next, few works dealing with co-rotational beam formulations are quoted for the sake of completeness. Crisfield [29] derived a co-rotational formulation for three-dimensional beams in which the “strains” relate to conventional small-deflection beam theory but are embedded in a continuously rotating frame. In contrast to many previous formulations, internal force vectors and tangent stiffness matrices were consistently computed from those “strains”. Galvanetto and Crisfield [30] presented an energy conserving procedure for the implicit nonlinear dynamic analysis of planar beam structures, where the method is based on a form of co-rotational technique that is external to the element. Following the same approach, Crisfield et al. [31] investigated different types of implicit time integration algorithms for the dynamics of spatial beams. In the thin-walled beam context, Alsafadie et al. [32] proposed a co-rotational formulation of a three-dimensional elastoplastic mixed beam element that can undergo large displacements and rotations. Le et al. [33] realized a comparative study of established and new formulations for the nonlinear dynamics of three-dimensional beams in a co-rotational context. Gebhardt [34], Gebhardt et al. [35] and Gebhardt and Rocca [36] employed a co-rotational formulation for three dimensional beams to investigate the nonlinear aeroelastic behavior of large-scale horizontal-axis wind turbines. Foti et al. [37] dealt with the numerical simulation of the dynamic response of frame structures undergoing large displacements and three-dimensional rotations. In that work, the co-rotational and the geometrically exact approaches were combined in the formulation of a single three-dimensional beam element. Meanwhile, Mathisen et al. [38] investigated and compared the two families of beam formulations, *i.e.*, co-rotational technique *versus* geometrically exact approach, by means of several examples. The authors concluded that for low order interpolations the superiority of one formulation over the other one cannot be claimed. Banerjee et al. [39] presented a generalization of the principal geodesic analysis that can cope with manifold-valued input data and respect the intrinsic geometry of the underlying manifold. Additionally, it takes advantage of the sparsity not only for easy interpretability, but for also computational efficiency. Gebhardt et al. [40] derived a displacement-field based beam formulation with five components. The proposed formulation extends Timoshenko's beam theory to asymmetric cases and adds two displacement components to estimate in-plane warping. Gebhardt et al. [41] presented a new object-oriented framework to investigate the nonlinear dynamics of slender structures made of composite multilayer and hyperelastic materials, which includes rigid bodies, geometrically exact beams, solid-degenerate shells, supports and joints. That framework was successfully verified and tested with results computed with standard and well-established commercial tools, *i.e.*, ANSYS and Abaqus FEA, see also [42,43]. Relying on that previous work, we extend the proposed formulation for the geometrically exact beam to identify the main kinematic features that arise from the nonlinear dynamics, but this time taking full advantage of the configuration space. Zwölfer and Gerstmayr [44] considered the generalized mode component analysis in the context of model reduction for industrial applications. And very recently, Wu et al. [45] investigated the model order reduction for geometrically nonlinear multibody systems by means of the “modal-derivative” concept in combination with the Rubin method. However in none of the seminal works cited before, the complex nonlinear dynamics was revealed in a fully nonlinear setting.

Here, we present a comprehensive framework to analyze the nonlinear dynamics of beam structures that goes beyond classical procedures that assume linearity on the configuration space, e.g., modal analysis and principal component analysis. The proposed approach relies on: *i*) a frame-invariant path-independent finite-element formulation for geometrically exact beams¹; *ii*) a multibody formalism to deal with general boundary conditions and to render more complicated structures through connections and junctions; *iii*) a momentum-preserving energy-preserving/dissipative scheme to integrate the governing equations in the time domain; and, *iv*) a principal geodesic analysis to directly identify the main kinematic features from the solution. The proposed approach is very powerful to identify motion patterns in a fully nonlinear setting, which is the main innovation of the present research. Such motion patterns could be used very effectively to generate models of reduced order for design purposes or to investigate changes of the mechanical features of a given structure, which is highly relevant in the context of model-based Structural-Health-Monitoring for damage identification, localization and quantification. Along this work, we address the theoretical and numerical foundations that are necessary to identify motion patterns. This provides a very robust procedure to improve the understanding of the matter with respect to classical approaches available in the literature. The further application of the approach to build reduced-order models or to evaluate changes of the mechanical features of a given structure are beyond the scope of the current manuscript and are addressed in sequels.

The remainder of this article is organized as follows. Section 2 presents the approach adopted to analyze the nonlinear dynamics of beam structures. It comprises a general description of a three-director formulation for geometrically exact beams. The resulting continuous equations are discretized spatially with low-order effective finite elements. The semi-discrete equations are then solved by means of a momentum-preserving energy-preserving/decaying integration scheme. Section 3 describes the principal geodesic analysis on $SE(3)$, the special Euclidean group (a Riemannian manifold that naturally describes the configuration space of rigid bodies and geometrically exact beams). It starts with a brief description of the principal component analysis on E^3 , the three-dimensional Euclidean space. This method clearly assumes the linear structure of the configuration space, which is true for the translational motion. Then it follows the description of the principal geodesic analysis on $SO(3)$, the group of rotations. This can be understood as a nonlinear extension of the principal component analysis. Finally, it concludes with the combination of the principal component analysis on E^3 and the principal geodesic analysis on $SO(3)$ to render the principal geodesic analysis on $SE(3)$. Section 4 presents four examples that are solved and analyzed with the formulation described. Finally, Section 5 is dedicated to concluding remarks, limitations and future work.

2. Numerical modeling of the nonlinear dynamics of beam structures

2.1. Kinematics and equilibrium

The position at time t , for $t \in [t_1, t_2] \subset \mathbb{R}_{\geq 0}$ of any given point belonging to the beam shown in Fig. 1, namely $\mathbf{x}(\theta; t) \in \mathcal{X}_t \subseteq \mathbb{R}^3$, can be written as

$$\mathbf{x}(\theta; t) = \bar{\mathbf{x}}(\theta^3; t) + \theta^1 \mathbf{d}_1(\theta^3; t) + \theta^2 \mathbf{d}_2(\theta^3; t), \quad (1)$$

¹ Here, we employ a non-orthogonal interpolation for the rotations as proposed by Romero and Armero [5] and Betsch and Steinmann [46], and recently used by Gebhardt et al. [41]. This formulation based on this kinematics and deformation measures is objective and does not require additional storage. Moreover, Romero [10] carried out simulations that confirm that finite element solutions with fine meshes are almost identical to the ones computed by means of several well-established interpolations.

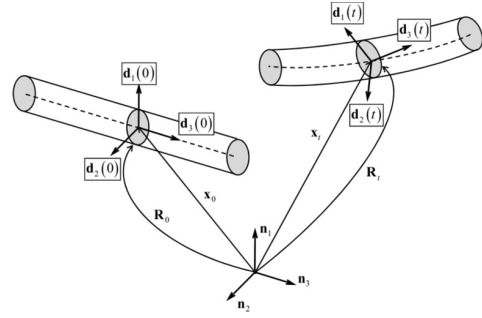


Fig. 1. The geometrically exact beam concept: time evolution among configurations through the regular motion $\varphi_t \circ \varphi_0^{-1}$.

in which $\bar{\mathbf{x}} \in \bar{\mathcal{X}} \subseteq \mathbb{R}^3$ is the position vector of the beam axis and \mathbf{d}_1 and \mathbf{d}_2 together with \mathbf{d}_3 are three mutually orthonormal directors. On that basis, the rotation tensor can be simply obtained as $\mathbf{R} = \mathbf{d}_i \otimes \mathbf{i}^i \in SO(3)$, in which \mathbf{i}^i for i from 1 to 3 stands for the elements of the dual basis of E^3 (\mathbb{R}^3 with the standard Euclidean structure), i.e., the space of row vectors. $\theta = (\theta^1, \theta^2, \theta^3)$ is a set of parameters chosen in the way that $\bar{\theta} = \theta^1 \mathbf{d}_1 + \theta^2 \mathbf{d}_2$ describes the cross section at $\mathcal{L}(\theta^3)$, which intersects the beam axis and $\mathbf{x} = \mathbf{x}(\theta; t)$ is the given parametrization rule in time and space. The spatial metric structure induced by this construction is

$$\mathbf{G} = \delta_{ij} \frac{\partial x^i}{\partial \theta^a} \frac{\partial x^j}{\partial \theta^b} \mathbf{g}^a \otimes \mathbf{g}^b, \quad (2)$$

where δ_{ij} are the components of the Euclidean metric tensor, $\mathbf{g}_a \in T_\theta \mathcal{X}$ defined as $\mathbf{g}_a = \frac{\partial x^i}{\partial \theta^a} \mathbf{i}_i$ with \mathbf{i}_i for i from 1 to 3 standing for the elements of the standard orthonormal basis in E^3 , i.e., the space of column vectors, and the elements of the covariant basis $\mathbf{g}^a \in T_\theta^* \mathcal{X}$ defined in the usual form, that is, $\langle \mathbf{g}^b, \mathbf{g}_a \rangle = \delta_a^b$, the elements of the contravariant basis. $\langle \cdot, \cdot \rangle: V \times V^* \rightarrow \mathbb{R}$ is the dual pairing, in which V is a given vector space (whose elements are called vectors) and V^* is its algebraic dual space (whose elements are called co-vectors or linear forms). δ_{ij} and δ_a^b are simply Kronecker deltas. At this point, it is clear that $\mathbf{G}: T_\theta \mathcal{X} \times T_\theta \mathcal{X} \rightarrow \mathbb{R}_{\geq 0}$.

Then the doubly-covariant Green-Lagrange strain tensor is

$$\bar{\mathbf{E}}_b(\theta; t) = \frac{1}{2} \{ (\varphi_t \circ \varphi_0^{-1})^* \mathbf{G}[\mathbf{x}(\theta; t)] - \mathbf{G}[\mathbf{x}(\theta; 0)] \}, \quad (3)$$

where $(\varphi_t \circ \varphi_0^{-1})^*(\cdot)$ denotes the pullback from the current configuration to the original one through the regular motion $\varphi_t \circ \varphi_0^{-1}$, and the symbols \flat and \sharp indicate that a rank- n tensor is n times covariant and n times contravariant, respectively. In the context of geometrically exact beams, the Green-Lagrange strain tensor can be simplified by eliminating quadratic strain. Thus, the components are approximated as

$$\bar{\mathbf{E}}_{ij}(\theta; t) \approx \text{symm} \{ \delta_{ij} \delta_{jk} [\Gamma^k(\theta^3; t) - \varepsilon_{im}^k \bar{\theta}^m \Omega^m(\theta^3; t)] \}, \quad (4)$$

where $\text{symm}(\cdot)$ is the symmetric part of the tensor considered, $\Gamma^i(\theta^3; t)$ defined as $\mathbf{d}_i(\theta^3; t) \cdot \bar{\mathbf{x}}'(\theta^3; t) - \mathbf{d}_i(\theta^3; 0) \cdot \bar{\mathbf{x}}'(\theta^3; 0)$ is a first vector strain measure (for shear refer to first and second components and for elongation refer to the third one), $\Omega^i(\theta^3; t)$ defined as $\frac{1}{2} \varepsilon_{ijk}^i [\mathbf{d}_k(\theta^3; t) \cdot \mathbf{d}'_j(\theta^3; t) - \mathbf{d}_k(\theta^3; 0) \cdot \mathbf{d}'_j(\theta^3; 0)]$ is a second vector strain measure (for bending refer to first and second components and for torsion refer to the third one) and ε_{ijk}^i is the alternating symbol that appears in the computation of the cross product in three-dimensional Euclidean space. Analogously, the velocity, namely $\mathbf{v}(\theta; t) \in \mathcal{V}_t \subseteq \mathbb{R}^3$, can be written as

$$\mathbf{v}(\theta; t) = \bar{\mathbf{v}}(\theta^3; t) + \theta^1 \mathbf{w}_1(\theta^3; t) + \theta^2 \mathbf{w}_2(\theta^3; t), \quad (5)$$

in which $\bar{\mathbf{v}} \in \bar{\mathcal{V}} \subseteq \mathbb{R}^3$ is the translational velocity of the beam axis and \mathbf{w}_1 , \mathbf{w}_2 together with \mathbf{w}_3 are three director velocity vectors. The dynamic behavior of the geometrically exact beam can be formulated as

$$\int_{\mathcal{L}_0} \int_{\mathcal{A}_0} \{ \langle \delta \mathbf{v}, \mathbf{I}(\mathbf{v}) - \mathbf{I}(\mathbf{x}) \rangle + \langle \delta \mathbf{x}, \mathbf{f}^{\text{int}}(\mathbf{x}, \mathbf{S}^\sharp) + \dot{\mathbf{I}}(\mathbf{v}) - \mathbf{f}^{\text{ext}} + \mathbf{H}^\top \lambda \rangle + \langle \delta \lambda, \mathbf{h} \rangle \} d\mathcal{A}_0 d\mathcal{L}_0 = 0, \quad (6)$$

where \mathcal{A}_0 represents the cross-sectional area and \mathcal{L}_0 stands for the arc length in the original configuration. $\delta \mathbf{v} \in T_v^* \mathcal{V}$ and $\delta \mathbf{x} \in T_x^* \mathcal{X}$ are admissible variations of the position and the velocity vectors, respectively. $\mathbf{I}(\mathbf{v})$ and $\mathbf{I}(\mathbf{x})$, both in $T_v^* \mathcal{V}$, are densities for the velocity-based momentum and the displacement-based momentum, correspondingly. $\mathbf{f}^{\text{int}}(\mathbf{x}, \mathbf{S}^\sharp)$, $\dot{\mathbf{I}}(\mathbf{v})$ and $\mathbf{f}^{\text{ext}}(\mathbf{x})$, all three in $T_x^* \mathcal{X}$ are densities for the internal force, the time rate of the velocity-based momentum and the external force, respectively. $\mathbf{S}^\sharp \in T_{x(0)} \mathcal{X}_0 \times T_{x(0)} \mathcal{X}_0$ is an appropriate stress definition, here the second Piola-Kirchhoff stress tensor. $\mathbf{H}: \mathbb{R}^n \times T_x \mathcal{X} \rightarrow \mathbb{R}$ is the Jacobian matrix of $\mathbf{h} = \mathbf{0} \in \mathbb{R}^n$, a finite-dimensional set of holonomic restrictions and $\delta \lambda$ is an admissible variation of the corresponding Lagrange multipliers $\lambda: [t_1, t_2] \rightarrow \mathbb{R}^n$. The equality (6) shall hold for every combination of admissible variations, namely $(\delta \mathbf{v}, \delta \mathbf{x}, \delta \lambda)$, otherwise it would not be an equilibrium statement. At this point, it should be clear that a state-space description is adopted instead of a phase-state description. This setting (in contrast to approaches based only on generalized coordinates) is necessary to include in a natural way the dissipation of energy at the level of the generalized velocities for the flexible bodies that are described along the next subsection.

Moreover, given two mutually orthonormal directors \mathbf{d}_1 and \mathbf{d}_2 , a third director \mathbf{d}_3 could be simply computed as $\mathbf{d}_1 \times \mathbf{d}_2$. This description would lead to a two-director formulation. An alternative to this formulation results from the additional consideration of \mathbf{d}_3 in combination with the mutual orthonormality condition for the three directors as already introduced by (8). The resulting representation is a so-called three-director formulation, which we adopt to facilitate the combination among beams and rigid bodies and evenly to avoid special treatment of the third director, i.e., \mathbf{d}_3 , during the discretization procedure. The cost associated to this choice is that the mass matrix becomes singular, but this singularity is removed when the additional information coming from internal kinematic restrictions is accounted for. After introducing explicitly \mathbf{d}_3 in the variational principle and performing the integration over the cross section, the governing equation for the geometrically exact beam, in its weak form, becomes

$$\begin{aligned} & \int_{\mathcal{L}_0} \{ \langle \delta \bar{\mathbf{v}}, \mathbf{I}^0(\bar{\mathbf{v}}, \mathbf{w}_1, \mathbf{w}_2) - \mathbf{I}^0(\bar{\mathbf{x}}, \mathbf{d}_1, \mathbf{d}_2) \rangle \\ & + \langle \delta \mathbf{w}_1, \mathbf{I}^1(\bar{\mathbf{v}}, \mathbf{w}_1, \mathbf{w}_2) - \mathbf{I}^1(\bar{\mathbf{x}}, \mathbf{d}_1, \mathbf{d}_2) \rangle \\ & + \langle \delta \mathbf{w}_2, \mathbf{I}^2(\bar{\mathbf{v}}, \mathbf{w}_1, \mathbf{w}_2) - \mathbf{I}^2(\bar{\mathbf{x}}, \mathbf{d}_1, \mathbf{d}_2) \rangle \\ & + \langle \delta \bar{\mathbf{x}}, \mathbf{f}^{0,\text{int}}(\mathbf{d}_1, \mathbf{d}_2, \mathbf{d}_3, \mathbf{n}) - \mathbf{f}^{0,\text{ext}} + \dot{\mathbf{I}}^0(\bar{\mathbf{v}}, \mathbf{w}_1, \mathbf{w}_2) + \mathbf{H}_0^\top \lambda \rangle \\ & + \langle \delta \mathbf{d}_1, \mathbf{f}^{1,\text{int}}(\bar{\mathbf{x}}, \mathbf{d}_2, \mathbf{d}_3, \mathbf{n}, \mathbf{m}) - \mathbf{f}^{1,\text{ext}} + \dot{\mathbf{I}}^1(\bar{\mathbf{v}}, \mathbf{w}_1, \mathbf{w}_2) + \mathbf{H}_1^\top \lambda \rangle \\ & + \langle \delta \mathbf{d}_2, \mathbf{f}^{2,\text{int}}(\bar{\mathbf{x}}, \mathbf{d}_1, \mathbf{d}_3, \mathbf{n}, \mathbf{m}) - \mathbf{f}^{2,\text{ext}} + \dot{\mathbf{I}}^2(\bar{\mathbf{v}}, \mathbf{w}_1, \mathbf{w}_2) + \mathbf{H}_2^\top \lambda \rangle \\ & + \langle \delta \mathbf{d}_3, \mathbf{f}^{3,\text{int}}(\bar{\mathbf{x}}, \mathbf{d}_1, \mathbf{d}_2, \mathbf{n}, \mathbf{m}) - \mathbf{f}^{3,\text{ext}} + \mathbf{H}_3^\top \rangle + \langle \delta \lambda, \mathbf{h} \rangle \} d\mathcal{L}_0 = 0. \quad (7) \end{aligned}$$

The equality (7) shall hold for every combination of admissible variations, i.e., $(\delta \bar{\mathbf{v}}, \delta \mathbf{w}_1, \delta \mathbf{w}_2, \delta \bar{\mathbf{x}}, \delta \mathbf{d}_1, \delta \mathbf{d}_2, \delta \mathbf{d}_3, \delta \lambda)$ under observation of $\mathbf{w}_3 = \mathbf{d}_3$. The generalized velocity-based momentum $\mathbf{I}^i(\bar{\mathbf{v}}, \mathbf{w}_1, \mathbf{w}_2)$ is defined as $\mathcal{E}_{i0} \bar{\mathbf{v}} + \mathcal{E}_{i1} \mathbf{w}_1 + \mathcal{E}_{i2} \mathbf{w}_2$ and the generalized displacement-based momentum $\mathbf{I}^i(\bar{\mathbf{x}}, \mathbf{d}_1, \mathbf{d}_2)$ as $\mathcal{E}_{i0} \bar{\mathbf{x}} + \mathcal{E}_{i1} \mathbf{d}_1 + \mathcal{E}_{i2} \mathbf{d}_2$, where \mathcal{E}_{ij} is computed by means of $\int_{\mathcal{A}_0} \varrho_0 \theta^i \theta^j d\mathcal{A}_0$ for i and j from 0 to 2. This consideration allows the handling of cross sections with arbitrary shape and material properties, which exactly applies to the case of modern beam structures made of composite multilayer materials. \mathbf{H}_0 and \mathbf{H}_i (for $i = 1, 2, 3$) stand for $\frac{\partial \mathbf{h}}{\partial \bar{\mathbf{x}}}$ and $\frac{\partial \mathbf{h}}{\partial \mathbf{d}_i}$, respectively. Finally, the mutual orthogonality condition among the directors is simply included by considering

$$\mathbf{h}^{\text{int}}(\mathbf{t}) = \begin{pmatrix} \mathbf{d}_1(\mathbf{t}) \cdot \mathbf{d}_1(\mathbf{t}) - \mathbf{d}_1(0) \cdot \mathbf{d}_1(0) \\ \mathbf{d}_2(\mathbf{t}) \cdot \mathbf{d}_2(\mathbf{t}) - \mathbf{d}_2(0) \cdot \mathbf{d}_2(0) \\ \mathbf{d}_3(\mathbf{t}) \cdot \mathbf{d}_3(\mathbf{t}) - \mathbf{d}_3(0) \cdot \mathbf{d}_3(0) \\ \mathbf{d}_2(\mathbf{t}) \cdot \mathbf{d}_3(\mathbf{t}) - \mathbf{d}_2(0) \cdot \mathbf{d}_3(0) \\ \mathbf{d}_1(\mathbf{t}) \cdot \mathbf{d}_3(\mathbf{t}) - \mathbf{d}_1(0) \cdot \mathbf{d}_3(0) \\ \mathbf{d}_1(\mathbf{t}) \cdot \mathbf{d}_2(\mathbf{t}) - \mathbf{d}_1(0) \cdot \mathbf{d}_2(0) \end{pmatrix} = \mathbf{0}. \quad (8)$$

This completes the dynamic description; for more details on the handling of internal constraints see [46]. Given the beam potential energy density per unit length V^{beam} , the internal force and moment densities per unit length are $\mathbf{n} = \frac{\partial V^{\text{beam}}}{\partial \Gamma}$ and $\mathbf{m} = \frac{\partial V^{\text{beam}}}{\partial \Omega}$, respectively. The components of the cross-sectional tangent constitutive matrices are in principle computed as

$$\begin{aligned} (\mathcal{C}_{\Gamma\Gamma})_{ij} &= \int_{\mathcal{A}_0} \mathcal{C}^{\text{IJKL}} \frac{\partial \bar{E}_{ij}}{\partial \Gamma^i} \frac{\partial \bar{E}_{KL}}{\partial \Gamma^j} d\mathcal{A}_0, & (\mathcal{C}_{\Gamma\Omega})_{ij} &= \int_{\mathcal{A}_0} (\mathcal{C})^{\text{IJKL}} \frac{\partial \bar{E}_{ij}}{\partial \Gamma^i} \frac{\partial \bar{E}_{KL}}{\partial \Omega^j} d\mathcal{A}_0, \\ (\mathcal{C}_{\Omega\Gamma})_{ij} &= \int_{\mathcal{A}_0} \mathcal{C}^{\text{IJKL}} \frac{\partial \bar{E}_{ij}}{\partial \Omega^i} \frac{\partial \bar{E}_{KL}}{\partial \Gamma^j} d\mathcal{A}_0, & (\mathcal{C}_{\Omega\Omega})_{ij} &= \int_{\mathcal{A}_0} (\mathcal{C})^{\text{IJKL}} \frac{\partial \bar{E}_{ij}}{\partial \Omega^i} \frac{\partial \bar{E}_{KL}}{\partial \Omega^j} d\mathcal{A}_0. \end{aligned} \quad (9)$$

Here $\mathcal{C}^{\text{IJKL}}$ represents the components of the tangent elasticity tensor and \bar{E}_{ij} stands for the components of the strain tensor presented by (4). For thin-walled structures, additional assumptions about the strain and stress states may be necessary [22]. At this point, warping effects are completely neglected. In the case of the blade of a wind turbine, which is in some regions far away from the thin-walled structure hypothesis and also non-negligible variations of the cross section may take place, the primary warping due to torsion ought to be combined with the consideration of secondary warping due to shear. This would require to include additional displacements fields, see for example [40]. Therefore, standard assumptions regarding warping effects may be inadequate in this context. However, a detailed discussion and treatment of a this aspect is beyond the scope of the current work. The acting internal load densities are indicated as follows:

$$\begin{aligned} \mathbf{f}^{0,\text{int}}(\mathbf{d}_1, \mathbf{d}_2, \mathbf{d}_3, \mathbf{n}) &= \left[\frac{\partial \Gamma}{\partial \bar{\mathbf{x}}}(\mathbf{d}_1, \mathbf{d}_2, \mathbf{d}_3) \right]^\top \mathbf{n}, \\ \mathbf{f}^{1,\text{int}}(\bar{\mathbf{x}}, \mathbf{d}_2, \mathbf{d}_3, \mathbf{n}, \mathbf{m}) &= \left[\frac{\partial \Gamma}{\partial \mathbf{d}_1}(\bar{\mathbf{x}}, \mathbf{d}_2, \mathbf{d}_3) \right]^\top \mathbf{n} + \left[\frac{\partial \Omega}{\partial \mathbf{d}_1}(\mathbf{d}_2, \mathbf{d}_3) \right]^\top \mathbf{m}, \\ \mathbf{f}^{2,\text{int}}(\bar{\mathbf{x}}, \mathbf{d}_1, \mathbf{d}_3, \mathbf{n}, \mathbf{m}) &= \left[\frac{\partial \Gamma}{\partial \mathbf{d}_2}(\bar{\mathbf{x}}, \mathbf{d}_1, \mathbf{d}_3) \right]^\top \mathbf{n} + \left[\frac{\partial \Omega}{\partial \mathbf{d}_2}(\mathbf{d}_1, \mathbf{d}_3) \right]^\top \mathbf{m}, \\ \mathbf{f}^{3,\text{int}}(\bar{\mathbf{x}}, \mathbf{d}_1, \mathbf{d}_2, \mathbf{n}, \mathbf{m}) &= \left[\frac{\partial \Gamma}{\partial \mathbf{d}_3}(\bar{\mathbf{x}}, \mathbf{d}_1, \mathbf{d}_2) \right]^\top \mathbf{n} + \left[\frac{\partial \Omega}{\partial \mathbf{d}_3}(\mathbf{d}_1, \mathbf{d}_2) \right]^\top \mathbf{m}. \end{aligned} \quad (10)$$

The geometrically exact beam model presented is capable of taking into account coupling terms not only at the level of the stiffness, but also at the level of the mass/inertia. This feature is of high interest in wind energy or aeronautic applications, especially to evaluate static and dynamic critical behavior of slender blades made of multilayer composite materials like divergence or flutter.

2.2. Discretization in space via the finite element method

To spatially discretize the geometrically exact beam into two-node finite elements, we approximate the generalized displacement fields $\bar{\mathbf{x}}$ and \mathbf{d}_i as well as the generalized velocity fields $\bar{\mathbf{v}}$ and \mathbf{w}_i and their admissible variations as follows: $\bar{\mathbf{x}}(\theta^3; t) \approx N^l(\theta^3) \bar{\mathbf{x}}_l(t)$, $\mathbf{d}_i(\theta^3; t) \approx N^l(\theta^3) \mathbf{d}_{i,l}(t)$, $\bar{\mathbf{v}}(\theta^3; t) \approx N^l(\theta^3) \bar{\mathbf{v}}_l(t)$, $\mathbf{w}_i(\theta^3; t) \approx N^l(\theta^3) \mathbf{w}_{i,l}(t)$, $\delta \mathbf{d}_i(\theta^3) \approx N^l(\theta^3) \delta \mathbf{d}_{i,l}$, $\delta \bar{\mathbf{v}}(\theta^3) \approx N^l(\theta^3) \delta \bar{\mathbf{v}}_l$ and $\delta \mathbf{w}_i(\theta^3) \approx N^l(\theta^3) \delta \mathbf{w}_{i,l}$ for l from 1 to 2, and $N^l(\theta)$ denotes linear Lagrange-type functions of $\theta^3 \in [-1, +1]$. In addition, the mutual orthogonality condition among the directors is also imposed discretely at the nodes. Finally, the semi-discrete version of the weak form of the governing equations for a single finite element becomes

$$\begin{aligned}
& \left\langle \delta \hat{\mathbf{v}}_1, \int_{-1}^{+1} \mathbf{N}^T [\mathbf{l}^0(\bar{\mathbf{v}}, \mathbf{w}_1, \mathbf{w}_2) - \mathbf{l}^0(\bar{\mathbf{x}}, \mathbf{d}_1, \mathbf{d}_2)] \frac{\partial \mathcal{L}_0}{\partial \theta^3} d\theta^3 \right\rangle + \\
& \left\langle \delta \hat{\mathbf{w}}_1, \int_{-1}^{+1} \mathbf{N}^T [\mathbf{l}^1(\bar{\mathbf{v}}, \mathbf{w}_1, \mathbf{w}_2) - \mathbf{l}^1(\bar{\mathbf{x}}, \mathbf{d}_1, \mathbf{d}_2)] \frac{\partial \mathcal{L}_0}{\partial \theta^3} d\theta^3 \right\rangle + \\
& \left\langle \delta \hat{\mathbf{w}}_2, \int_{-1}^{+1} \mathbf{N}^T [\mathbf{l}^2(\bar{\mathbf{v}}, \mathbf{w}_1, \mathbf{w}_2) - \mathbf{l}^2(\bar{\mathbf{x}}, \mathbf{d}_1, \mathbf{d}_2)] \frac{\partial \mathcal{L}_0}{\partial \theta^3} d\theta^3 \right\rangle + \\
& \left\langle \delta \hat{\mathbf{x}}, \int_{-1}^{+1} \{ \mathbf{N}^T [\mathbf{f}^{0,int}(\bar{\mathbf{x}}, \mathbf{d}_2, \mathbf{d}_3, \mathbf{n}) - \mathbf{f}^{0,ext} + \mathbf{l}^0(\bar{\mathbf{v}}, \mathbf{w}_1, \mathbf{w}_2)] + \mathbf{H}_1^T \mathbf{N}_i \lambda_i \} \frac{\partial \mathcal{L}_0}{\partial \theta^3} d\theta^3 \right\rangle + \\
& \left\langle \delta \hat{\mathbf{d}}_1, \int_{-1}^{+1} \{ \mathbf{N}^T [\mathbf{f}^{1,int}(\bar{\mathbf{x}}, \mathbf{d}_2, \mathbf{d}_3, \mathbf{n}, \mathbf{m}) - \mathbf{f}^{1,ext} + \mathbf{l}^1(\bar{\mathbf{v}}, \mathbf{w}_1, \mathbf{w}_2)] + \mathbf{H}_2^T \mathbf{N}_i \lambda_i \} \frac{\partial \mathcal{L}_0}{\partial \theta^3} d\theta^3 \right\rangle + \\
& \left\langle \delta \hat{\mathbf{d}}_2, \int_{-1}^{+1} \{ \mathbf{N}^T [\mathbf{f}^{2,int}(\bar{\mathbf{x}}, \mathbf{d}_1, \mathbf{d}_3, \mathbf{n}, \mathbf{m}) - \mathbf{f}^{2,ext} + \mathbf{l}^2(\bar{\mathbf{v}}, \mathbf{w}_1, \mathbf{w}_2)] + \mathbf{H}_2^T \mathbf{N}_i \lambda_i \} \frac{\partial \mathcal{L}_0}{\partial \theta^3} d\theta^3 \right\rangle + \\
& \left\langle \delta \hat{\mathbf{d}}_3, \int_{-1}^{+1} \{ \mathbf{N}^T [\mathbf{f}^{3,int}(\bar{\mathbf{x}}, \mathbf{d}_1, \mathbf{d}_3, \mathbf{n}, \mathbf{m}) - \mathbf{f}^{3,ext}] + \mathbf{H}_3^T \mathbf{N}_i \lambda_i \} \frac{\partial \mathcal{L}_0}{\partial \theta^3} d\theta^3 \right\rangle + \\
& \left\langle \delta \hat{\lambda}, \int_{-1}^{+1} \mathbf{N}_i^T \mathbf{h} \frac{\partial \mathcal{L}_0}{\partial \theta^3} d\theta^3 \right\rangle = 0, \tag{11}
\end{aligned}$$

where $\hat{(\cdot)}$ denotes nodal variables, \mathbf{N} is the matrix containing the shape functions and \mathbf{N}_i is a collocation matrix to set discretely the constraints at the nodes. The equality (11) shall hold for every combination of admissible variations, *i.e.*, $(\delta \hat{\mathbf{v}}, \delta \hat{\mathbf{w}}_1, \delta \hat{\mathbf{w}}_2, \delta \hat{\mathbf{x}}, \delta \hat{\mathbf{d}}_1, \delta \hat{\mathbf{d}}_2, \delta \hat{\mathbf{d}}_3, \delta \hat{\lambda})$ under observation of $\hat{\mathbf{w}}_3 = \hat{\mathbf{d}}_3$.

As a consequence of the adopted discrete imposition of the internal constraints, the approximation of the rotation tensor is given by

$$\begin{aligned}
\mathbf{R}(\theta^3; t) & \approx \mathbf{N}^l(\theta^3) \mathbf{d}_{i,1}(t) \otimes \mathbf{i}^i + \mathbf{N}^2(\theta^3) \mathbf{d}_{i,2}(t) \otimes \mathbf{i}^i \\
& = \mathbf{N}^l(\theta^3) \mathbf{R}_1(t) + \mathbf{N}^2(\theta^3) \mathbf{R}_2(t), \tag{12}
\end{aligned}$$

which does not belong in general to $\text{SO}(3)$, except at θ^3 equal to -1 or $+1$, and for the case \mathbf{R}_1 equal to \mathbf{R}_2 . This lack of orthonormality of the directors, *i.e.*, the unit length is not preserved and the orthogonality is lost, requires finer discretizations than standard beam elements equipped with angle-based parametrizations, but at the same time, it does possess a very important feature, since this discrete setting preserves the objectivity, invariance of the discrete strain measures under rigid body motions. Furthermore, the path independence is guaranteed, *i.e.*, for conservative actions the work produced through any arbitrary closed path is identically zero. Regarding finer discretization requirements and convergence properties for beam models relying on a non-orthogonal interpolation, Romero [10] showed that the static performance of beam structures with linear constitutive laws, the three-director-based kinematics and deformation measures behave properly as required. This claim is also in very good agreement with our observations of the dynamic performance of beam structures.

2.3. Discretization in time via a robust integration scheme

Next, we describe the specialization of the momentum-preserving, energy-preserving/dissipative integration scheme for the “geometrically exact beam” case. For this purpose, the following nomenclature is used:

$$\mathbf{q} = \begin{pmatrix} \bar{\mathbf{x}} \\ \mathbf{d}_1 \\ \mathbf{d}_2 \\ \mathbf{d}_3 \end{pmatrix}, \quad \mathbf{s} = \begin{pmatrix} \bar{\mathbf{v}} \\ \mathbf{w}_1 \\ \mathbf{w}_2 \\ \mathbf{w}_3 \end{pmatrix}, \quad \mathbf{p} = \begin{pmatrix} \mathbf{l}^0 \\ \mathbf{l}^1 \\ \mathbf{l}^2 \\ \mathbf{l}^3 \end{pmatrix}, \quad \mathbf{Q}^{\text{int}} = \begin{pmatrix} \mathbf{f}^{0,int} \\ \mathbf{f}^{1,int} \\ \mathbf{f}^{2,int} \\ \mathbf{f}^{3,int} \end{pmatrix}, \quad \mathbf{Q}^{\text{ext}} = \begin{pmatrix} \mathbf{f}^{0,ext} \\ \mathbf{f}^{1,ext} \\ \mathbf{f}^{2,ext} \\ \mathbf{f}^{3,ext} \end{pmatrix}. \tag{13}$$

While \mathbf{q} is the vector of generalized coordinates, \mathbf{s} stands for the vector of generalized velocities, \mathbf{p} collects the generalized momenta, \mathbf{Q}^{int} and \mathbf{Q}^{ext} contain the generalized internal and external loads, correspondingly. Additionally, we have

$$\boldsymbol{\pi} = \begin{pmatrix} \boldsymbol{\Gamma} \\ \boldsymbol{\Omega} \end{pmatrix}, \quad \boldsymbol{\sigma} = \begin{pmatrix} \mathbf{n} \\ \mathbf{m} \end{pmatrix}, \quad \boldsymbol{\epsilon}^{\text{beam}} = \begin{bmatrix} \boldsymbol{\epsilon}_{\Gamma} & \boldsymbol{\epsilon}_{\Omega} \\ \boldsymbol{\epsilon}_{\Omega} & \boldsymbol{\epsilon}_{\Omega} \end{bmatrix}. \tag{14}$$

While $\boldsymbol{\pi}$ and $\boldsymbol{\sigma}$ contain the objective strain measures and internal resultant loads, respectively, $\boldsymbol{\epsilon}^{\text{beam}}$ stands for the tangent constitutive

matrix.

The discrete version of (11) can be expressed at time $n + \frac{1}{2}$ as

$$\begin{aligned}
& \left\langle \delta \mathbf{s}_{n+\frac{1}{2}}, \int_{-1}^{+1} \mathbf{N}^T [\mathbf{p}_d(\mathbf{s}_n, \boldsymbol{\pi}_n, \mathbf{s}_{n+1}, \boldsymbol{\pi}_{n+1}) - \mathbf{p}_d(\mathbf{q}_n, \mathbf{q}_{n+1})] \frac{\partial \mathcal{L}_0}{\partial \theta^3} d\theta^3 \right\rangle \\
& + \left\langle \delta \mathbf{q}_{n+\frac{1}{2}}, \int_{-1}^{+1} \{ \mathbf{N}^T [\dot{\mathbf{p}}_d(\mathbf{s}_n, \mathbf{s}_{n+1}) + \mathbf{Q}_d^{\text{int}}(\mathbf{q}_n, \mathbf{s}_n, \mathbf{q}_{n+1}, \mathbf{s}_{n+1}) - \mathbf{Q}_{n+\frac{1}{2}}^{\text{ext}}] \right. \\
& + \mathbf{H}_d(\mathbf{q}_n, \mathbf{q}_{n+1})^T \mathbf{N}_i \lambda_{n+\frac{1}{2}} \} \frac{\partial \mathcal{L}_0}{\partial \theta^3} d\theta^3 \right\rangle + \left\langle \delta \lambda_{n+1}, \int_{-1}^{+1} \mathbf{N}_i^T \mathbf{h}(\mathbf{q}_{n+1}) \frac{\partial \mathcal{L}_0}{\partial \theta^3} d\theta^3 \right\rangle \\
& = 0, \tag{15}
\end{aligned}$$

where the admissible variations correspond to the nodal variables and therefore, further distinctions are unnecessary and from now, \mathbf{N} gathers all nodal contributions. The equality (15) shall hold for every combination of admissible discrete variations, namely $(\delta \mathbf{s}_{n+\frac{1}{2}}, \delta \mathbf{q}_{n+\frac{1}{2}}, \delta \lambda_{n+1})$, otherwise it would not be a discrete equilibrium statement. On the one hand, the momentum term computed from generalized velocities can be redefined as the additive combination of a conservative part and a dissipative part, *i.e.*,

$$\begin{aligned}
\mathbf{p}_d(\mathbf{s}_n, \boldsymbol{\pi}_n, \mathbf{s}_{n+1}, \boldsymbol{\pi}_{n+1}) & = \mathbf{p}_d^{\text{cons}}(\mathbf{s}_n, \mathbf{s}_{n+1}) \\
& + \mathbf{p}_d^{\text{diss}}(\|\mathbf{s}_n\|_m, \boldsymbol{\pi}_n, \|\mathbf{s}_{n+1}\|_m, \boldsymbol{\pi}_{n+1}), \tag{16}
\end{aligned}$$

where \mathfrak{M} is the consistent mass matrix per unit of length

$$\mathfrak{M} = \begin{bmatrix} \mathcal{E}_{00} \mathbf{I}_{3 \times 3} & \mathcal{E}_{01} \mathbf{I}_{3 \times 3} & \mathcal{E}_{02} \mathbf{I}_{3 \times 3} & \mathbf{0}_{3 \times 3} \\ \mathcal{E}_{01} \mathbf{I}_{3 \times 3} & \mathcal{E}_{11} \mathbf{I}_{3 \times 3} & \mathcal{E}_{12} \mathbf{I}_{3 \times 3} & \mathbf{0}_{3 \times 3} \\ \mathcal{E}_{02} \mathbf{I}_{3 \times 3} & \mathcal{E}_{12} \mathbf{I}_{3 \times 3} & \mathcal{E}_{22} \mathbf{I}_{3 \times 3} & \mathbf{0}_{3 \times 3} \\ \mathbf{0}_{3 \times 3} & \mathbf{0}_{3 \times 3} & \mathbf{0}_{3 \times 3} & \mathbf{0}_{3 \times 3} \end{bmatrix}, \tag{17}$$

that is singular, and the conservative part is

$$\mathbf{p}_d^{\text{cons}}(\mathbf{s}_n, \mathbf{s}_{n+1}) = \frac{\tilde{\mathfrak{M}}}{2} (\mathbf{s}_{n+1} + \mathbf{s}_n), \tag{18}$$

in which the augmented mass matrix per unit length takes the form

$$\tilde{\mathfrak{M}} = \begin{bmatrix} \mathcal{E}_{00} \mathbf{I}_{3 \times 3} & \mathcal{E}_{01} \mathbf{I}_{3 \times 3} & \mathcal{E}_{02} \mathbf{I}_{3 \times 3} & \mathbf{0}_{3 \times 3} \\ \mathcal{E}_{01} \mathbf{I}_{3 \times 3} & \mathcal{E}_{11} \mathbf{I}_{3 \times 3} & \mathcal{E}_{12} \mathbf{I}_{3 \times 3} & \mathbf{0}_{3 \times 3} \\ \mathcal{E}_{02} \mathbf{I}_{3 \times 3} & \mathcal{E}_{12} \mathbf{I}_{3 \times 3} & \mathcal{E}_{22} \mathbf{I}_{3 \times 3} & \mathbf{0}_{3 \times 3} \\ \mathbf{0}_{3 \times 3} & \mathbf{0}_{3 \times 3} & \mathbf{0}_{3 \times 3} & \mathbf{I}_{3 \times 3} \end{bmatrix} \tag{19}$$

and \mathcal{E}_{ij} for i and j running from 0 to 2 being defined above. $\tilde{\mathfrak{M}}$ differs from \mathfrak{M} only in the block placed in the lower right corner, $\mathbf{I}_{3 \times 3}$ instead of $\mathbf{0}_{3 \times 3}$, which includes the condition $\mathbf{w}_3 = \mathbf{d}_3$ without adding further constraints. The dissipative part that supports cross definition involving $\|\mathbf{s}\|_m$ and $\boldsymbol{\pi}$ is given by

$$\begin{aligned}
\mathbf{p}_d^{\text{diss}}(\|\mathbf{s}_n\|_m, \boldsymbol{\pi}_n, \|\mathbf{s}_{n+1}\|_m, \boldsymbol{\pi}_{n+1}) \\
= \frac{2 \mathcal{D}_p(\|\mathbf{s}_n\|_m, \boldsymbol{\pi}_n, \|\mathbf{s}_{n+1}\|_m, \boldsymbol{\pi}_{n+1})}{\|\mathbf{s}_{n+1}\|_m^2 - \|\mathbf{s}_n\|_m^2} \mathfrak{M} \mathbf{s}_{n+\frac{1}{2}}, \tag{20}
\end{aligned}$$

in which the associated dissipation function \mathcal{D}_p is positive semidefinite.

On the other hand, the discrete generalized load due to internal terms can be also redefined as the additive combination of a conservative part and a dissipative part, *i.e.*,

$$\begin{aligned}
\mathbf{Q}_d^{\text{int}}(\mathbf{q}_n, \mathbf{s}_n, \mathbf{q}_{n+1}, \mathbf{s}_{n+1}) & = \mathbf{Q}_d^{\text{int,cons}}(\mathbf{q}_n, \mathbf{q}_{n+1}) \\
& + \mathbf{Q}_d^{\text{int,diss}}(\mathbf{q}_n, \|\mathbf{s}_n\|_m, \mathbf{q}_{n+1}, \|\mathbf{s}_{n+1}\|_m). \tag{21}
\end{aligned}$$

The conservative part is

$$\mathbf{Q}_d^{\text{int,cons}}(\mathbf{q}_n, \mathbf{q}_{n+1}) = \left[\frac{\partial \pi}{\partial \mathbf{q}} \right]_{n+\frac{1}{2}}^T \boldsymbol{\sigma}_d^{\text{cons}}(\boldsymbol{\pi}_n, \boldsymbol{\pi}_{n+1}), \tag{22}$$

with the conservative algorithmic internal loads given by

$$\sigma_d^{\text{cons}}(\pi_n, \pi_{n+1}) = \frac{1}{2} \int_{-1}^{+1} \left. \frac{\partial V^{\text{beam}}}{\partial \pi} \right|_{\pi(\xi)} d\xi, \quad (23)$$

where $\pi(\xi)$ is defined as $\frac{1}{2}(1 - \xi)\pi_n + \frac{1}{2}(1 + \xi)\pi_{n+1}$ for $\xi \in [-1, +1]$.

The dissipative part that also supports cross definition involving $\|\mathbf{s}\|_m$ and π is given by

$$\begin{aligned} \mathbf{Q}_d^{\text{int,diss}}(\mathbf{q}_n, \|\mathbf{s}_n\|_m, \mathbf{q}_{n+1}, \|\mathbf{s}_{n+1}\|_m) \\ = \left[\frac{\partial \pi}{\partial \mathbf{q}} \right]_{\mathbf{q}_{n+\frac{1}{2}}}^T \sigma_d^{\text{diss}}(\|\mathbf{s}_n\|_m, \pi_n, \|\mathbf{s}_{n+1}\|_m, \pi_{n+1}), \end{aligned} \quad (24)$$

with the dissipative algorithmic loads

$$\begin{aligned} \sigma_d^{\text{diss}}(\|\mathbf{s}_n\|_m, \pi_n, \|\mathbf{s}_{n+1}\|_m, \pi_{n+1}) \\ = \frac{\mathcal{D}_Q(\|\mathbf{s}_n\|_m, \pi_n, \|\mathbf{s}_{n+1}\|_m, \pi_{n+1})}{\|\pi_{n+1} - \pi_n\|_{\mathcal{L}_{\text{beam}}} \pi_{n+1} - \pi_n^2} \mathbf{c}_n^{\text{beam}}(\pi_{n+1} - \pi_n), \end{aligned} \quad (25)$$

in which the dissipation function \mathcal{D}_Q is positive semidefinite as well. Finally, the following condition

$$\mathcal{H}_{n+1}^{\text{beam}} + \mathcal{D}_P + \mathcal{D}_Q = \mathcal{H}_n^{\text{beam}}, \quad (26)$$

for $\mathcal{D}_P + \mathcal{D}_Q \geq 0$, is automatically warranted, being the corresponding Hamiltonian function $\mathcal{H}^{\text{beam}}$.

The discrete version of the Jacobian matrix of the constraints is given by

$$\mathbf{H}_d(\mathbf{q}_n, \mathbf{q}_{n+1}) = \frac{1}{2} \int_{-1}^{+1} \left. \frac{\partial \mathbf{h}}{\partial \mathbf{q}} \right|_{\mathbf{q}(\xi)} d\xi, \quad (27)$$

where $\mathbf{q}(\xi)$ is defined as $\frac{1}{2}(1 - \xi)\mathbf{q}_n + \frac{1}{2}(1 + \xi)\mathbf{q}_{n+1}$ for $\xi \in [-1, +1]$. The algorithmic Jacobian matrix defined in this way satisfies for any admissible solution the discrete version of the hidden constraints, i.e., $\mathbf{H}_d(\mathbf{q}_n, \mathbf{q}_{n+1})(\mathbf{q}_{n+1} - \mathbf{q}_n) = \mathbf{0}$ (this is a second-order discrete approximation of $\mathbf{h}(\mathbf{q}) = \mathbf{0}$).

Notice that (23) and (27) are defined employing the second-order “average vector field” proposed in [47,48]. This concept satisfies the definition of discrete derivative proposed in [49]. By means of the discrete derivative it is possible to design integration methods that are second-order accurate, and momentum and energy preserving, which are the basis for the robust integration method that completes the numerical representation for beam structures and their nonlinear dynamics.

2.4. Further technical aspects of the current formulation

The three-director-based kinematic description as well as the deformation measures employed in the current work are exactly the same as proposed by Romero and Armero [5] and Betsch and Steinmann [46], but our dynamical formulation differs and is presented in a more general setting. Meanwhile, Romero and Armero [5] employed a nodal procedure based on Cayley’s transform for the multiplicative updating of the directors, Betsch and Steinmann [9] employed Lagrange’s multipliers method for enforcing directors’ orthonormality at the nodes, where the resulting update procedure is the simplest additive one. As previously indicated, we adopted the second approach as proposed in [46,9] due to its simplicity and robustness.

Regarding the formulation of the dynamic problem, Betsch and Steinmann [9] presented a Hamiltonian formulation for the geometrically exact beam that relies on a description in the “phase space”, i.e., the variables are generalized coordinates and generalized momenta. After temporal discretization of the derived Hamilton equations by means of the mixed Galerkin method, the resulting approach is capable of satisfying the discrete conservation of some first integral of motion, i.e., linear and angular momenta as well as total energy. Therefore, that formulation can be labeled as a purely conservative one.

The current formulation is intended for general non-conservative

systems that may arise in the presence of dissipation functions and/or non-integrable constraints, which are highly relevant for industrial applications. Therefore, we adopted a description in the “state space”, i.e., the variables are generalized coordinates and generalized velocities (such a kind of representations were introduced by Poincaré, see for instance Heard [50]). This description allows to introduce dissipation functions as well as non-holonomic constraints in a very natural way (both can be easily stated in terms of velocities, but not in terms of momenta). For the general non-conservative case, the resulting governing equations can be reverted to the Lagrange-D’Alembert equations, which are non-variational. For the conservative case, the resulting governing equations can be reverted to the Euler-Lagrange equations, which are variational. A comprehensive treatment of this topic can be found in Bloch [51]. After the temporal discretization by means of a combination of the midpoint rule and the “average vector field” method, our approach preserves identically the linear and angular momenta as well as the total energy in absence of external loads. Thus, it can be understood as a “complementary” formulation with respect to the one based on the Hamiltonian setting.

The adopted numerical quadrature for the integration of elemental contributions in time and space is the standard Gauss-Legendre quadrature rule. The spatial integrals involving inertial terms are computed by means of a two-point integration scheme. Meanwhile, those spatial integrals involving internal terms are computed by means of a one-point integration scheme that avoids shear locking issues. Moreover, even for coarse meshes, no additional residual stress corrections are necessary. All time integrals for the computation of the average vector field are calculated by means of a two-point integration scheme.

3. Principal geodesic analysis

3.1. Principal component analysis in \mathbb{R}^m (standard approach)

Given a set of n data vectors in \mathbb{R}^m , one naturally obtains a matrix in $\mathbb{R}^{m \times n}$ with the vectors as columns. Intuitively, *principal component analysis* (PCA) uses this data matrix to determine a representation of the linear subspace of minimal dimension that contains the given vectors. This is done in a way that extracts information on the behavior of the data vectors as a finite sequence, and also in a way that allows for the direct construction of optimal approximate representations of the data vectors in spaces of even lower dimension. The technique has many applications in data analysis and various related areas. It is known under several different names in those areas; in particular, *proper orthogonal decomposition* (POD) is often used in applications to dynamic systems.

In our case the data vectors are discrete-time snapshots, such as time steps in a numerical simulation, of continuous-time trajectories of the elastic beam structures under consideration. Here the PCA will determine dominating patterns/modes of the system’s motion, such as the natural oscillations that actually appear in the particular data set. In addition, the PCA will automatically detect and exploit special cases such as planar motion. Thus one may obtain a better understanding of the dynamics, which is the main purpose of our investigation. Moreover, the approach is often used for model order reduction (MOR), i.e., the construction of lower-dimensional approximate dynamic models with the intent to save computational cost.

Mathematically, PCA is based on the *singular value decomposition* (SVD) of the data matrix $\mathbf{D} \in \mathbb{R}^{m \times n}$, which determines a rectangular diagonal matrix $\mathbf{\Sigma} \in \mathbb{R}^{m \times n}$ with orthogonal matrices $\mathbf{U} \in O(m) \subset \mathbb{R}^{m \times m}$ and $\mathbf{V} \in O(n) \subset \mathbb{R}^{n \times n}$ such that

$$\mathbf{D} = \mathbf{U}\mathbf{\Sigma}\mathbf{V}^T = \sum_{i=1}^r \sigma_i \mathbf{u}_i \mathbf{v}_i^T, \quad \mathbf{\Sigma} = \text{Diag}(\sigma_1, \dots, \sigma_r, 0), \quad \sigma_1 \geq \dots \geq \sigma_r > 0. \quad (28)$$

The diagonal elements σ_i of $\mathbf{\Sigma}$ are called the *singular values* of the matrix

\mathbf{D} , and the columns \mathbf{u}_i of \mathbf{U} and \mathbf{v}_i of \mathbf{V} are called its left and right singular vectors, respectively. The number of nonzero singular values, $r \leq \min(m, n)$, is the rank of \mathbf{D} . The matrix Σ is uniquely determined whereas \mathbf{U}, \mathbf{V} are only unique up to sign switches of the singular vectors and the choice of singular vectors associated with identical singular values. The space containing the data vectors is spanned by $\mathbf{u}_1, \dots, \mathbf{u}_r \in \mathbb{R}^m$ while $\mathbf{v}_1, \dots, \mathbf{v}_r \in \mathbb{R}^n$ represent the sequential behavior.

Best rank- p approximations of \mathbf{D} (in terms of the spectral or Frobenius matrix norms, $\|\cdot\|_2$ and $\|\cdot\|_F$) are naturally obtained by the truncated SVD (TSVD), i.e., by dropping all but the p largest singular values in Σ ,

$$\mathbf{D}_p = \mathbf{U}\Sigma_p\mathbf{V}^T = \sum_{i=1}^p \sigma_i \mathbf{u}_i \mathbf{v}_i^T, \quad \Sigma_p = \text{Diag}(\sigma_1, \dots, \sigma_p, 0) \in \mathbb{R}^{m \times n}, \quad p \leq r. \tag{29}$$

In practice, a suitable rank p is usually determined by some application-specific accuracy requirement.

3.2. Principal geodesic analysis in SO(3)

When considering motion in a Riemannian manifold rather than in a linear space, such as motion along geodesics, principal component analysis can be generalized to *principal geodesic analysis* [11,19,24,39]. Manifolds are curved in general, but every point possesses a (linear) tangent space which is smoothly mapped onto the manifold by the so-called exponential map. Rather than a global inverse, which does not exist in general, the exponential map has infinitely many local inverses, called logarithm maps, each of which maps some subset of the manifold into the tangent space. The basic idea of principal geodesic analysis (PGA) consists in lifting trajectories from the manifold to trajectories in a suitable tangent space and performing a principal component analysis on the lifted trajectory. Results are then mapped back to the manifold by means of the exponential map. The initial lifting requires one or more local inverses of the exponential map.

For the purpose of the current paper we are concerned with the matrix manifold of rotations in \mathbb{R}^3 , i.e., the special orthogonal group $\text{SO}(3) \subset \mathbb{R}^{3 \times 3}$. This three-dimensional manifold, though quite complicated, has favorable mathematical properties that allow for an efficient implementation of PGA via simple analytic representations of the exponential and logarithm maps. The main properties can be illustrated by planar rotations, $\text{SO}(2) \subset \mathbb{R}^{2 \times 2}$, which are a one-dimensional submanifold of $\text{SO}(3)$ (parameterized by the rotation angle θ) when considered as rotations in the xy -plane about the z axis,

$$\text{SO}(2) = \left\{ \mathbf{R}(\theta) = \begin{bmatrix} \cos \theta & \sin \theta \\ -\sin \theta & \cos \theta \end{bmatrix}; \theta \in \mathbb{R} \right\} \rightarrow \left\{ \begin{bmatrix} \cos \theta & \sin \theta & 0 \\ -\sin \theta & \cos \theta & 0 \\ 0 & 0 & 1 \end{bmatrix} \right. \\ \left. : \theta \in \mathbb{R} \right\} \subset \text{SO}(3).$$

Clearly, $\text{SO}(2)$ is equivalently represented by the set of first rows of $\mathbf{R}(\theta)$, the unit circle S^1 , see Fig. 2. Its tangent space at $\theta = 0$ is the line $T_{(1,0)}S^1 = \{(1, \theta): \theta \in \mathbb{R}\} \cong \mathbb{R}$, and the exponential map simply wraps this line around the circle, yielding the first row of $\mathbf{R}(\theta)$. Using the second row of $\mathbf{R}(\theta)$ gives the same picture, except that the tangent space is rotated by $\frac{\pi}{2}$, $T_{(0,1)}S^1 = \{(-\theta, 1): \theta \in \mathbb{R}\}$.

Finally, the full rotation matrix $\mathbf{R}(\theta)$ is given by the standard matrix exponential as

$$\exp(\theta \mathbf{J}) = \sum_{k=0}^{\infty} \frac{(\theta \mathbf{J})^k}{k!} = \sum_{k=0}^{\infty} \frac{(-1)^k \theta^{2k}}{(2k)!} \mathbf{I}_{2 \times 2} + \sum_{k=0}^{\infty} \frac{(-1)^k \theta^{2k+1}}{(2k+1)!} \mathbf{J} \\ = \cos(\theta) \mathbf{I}_{2 \times 2} + \sin(\theta) \mathbf{J} \quad \text{with} \quad \mathbf{J} = \begin{bmatrix} 0 & 1 \\ -1 & 0 \end{bmatrix}.$$

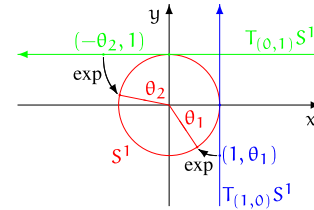


Fig. 2. Planar rotations $\text{SO}(2)$ represented by the unit circle S^1 , with two tangent spaces and associated exponential maps.

This maps the space of skew-symmetric matrices, $\mathbf{A}(2) \cong \mathbb{R}$, parameterized by θ , to $\text{SO}(2)$, satisfying $\exp(0\mathbf{J}) = \mathbf{I}_{2 \times 2}$ and $\exp(\theta_1 \mathbf{J} + \theta_2 \mathbf{J}) = \mathbf{R}(\theta_1 + \theta_2) = \mathbf{R}(\theta_1) \mathbf{R}(\theta_2) = \exp(\theta_1 \mathbf{J}) \exp(\theta_2 \mathbf{J})$. Again \exp wraps around $\text{SO}(2)$ infinitely often, and a local inverse exists for the restriction of \exp to every open ball with radius π , $B_{\theta} = (\theta - \pi, \theta + \pi) \mathbf{J} \subset \mathbf{A}(2)$.

The corresponding properties of $\text{SO}(3)$ are mathematically expressed as follows. $\text{SO}(3)$ is a compact multiplicative Lie group. Its associated Lie algebra, the tangent space $T_{\mathbf{I}}\text{SO}(3)$, is canonically isomorphic to $\mathbf{A}(3) \subset \mathbb{R}^{3 \times 3}$, the linear space of skew-symmetric matrices. (Here we write \mathbf{I} for $\mathbf{I}_{3 \times 3}$ and similarly $\mathbf{0}$ for $\mathbf{0}_{3 \times 3}$.) The exponential map and its inverses are only needed for the specific tangent space $T_{\mathbf{I}}\text{SO}(3) \cong \mathbf{A}(3) \cong \mathbb{R}^3$, and again these mappings reduce to the standard matrix exponential and its inverses. We will compare PGA with PCA of embedded rotations $\text{SO}(3) \subset \mathbb{R}^{3 \times 3} \cong \mathbb{R}^9$.

For the exponential map $\exp: \mathbf{A}(3) \cong T_{\mathbf{I}}\text{SO}(3) \rightarrow \text{SO}(3)$ we have the numerical representation

$$\exp(\mathbf{A}) = \begin{cases} \mathbf{I}, & \theta \in [0, \varepsilon_M], \\ \mathbf{I} + \frac{\sin \theta}{\theta} \mathbf{A} + \frac{1 - \cos \theta}{\theta^2} \mathbf{A}^2, & \theta \in (\varepsilon_M, 2\pi), \end{cases} \tag{30}$$

where ε_M is the machine precision and $\theta \in [0, 2\pi)$ is the normalized rotation angle,

$$\theta = \theta_0 - 2\pi \left\lfloor \frac{\theta_0}{2\pi} \right\rfloor, \quad \theta_0 = \sqrt{\frac{1}{2} \text{tr}(\mathbf{A}^T \mathbf{A})} = \frac{\|\mathbf{A}\|_F}{\sqrt{2}} =: \|\mathbf{A}\|_{\mathbf{A}(3)}. \tag{31}$$

With vector \mathbf{a} and matrix \mathbf{A} in standard notation (no covariant and contravariant index conventions),

$$\mathbf{a} = \begin{pmatrix} a_1 \\ a_2 \\ a_3 \end{pmatrix} \quad \text{and} \quad \mathbf{A} = \text{skew}(\mathbf{a}) = \begin{bmatrix} 0 & -a_3 & a_2 \\ a_3 & 0 & -a_1 \\ -a_2 & a_1 & 0 \end{bmatrix}, \tag{32}$$

the full rotation angle above is $\theta_0 = \|\mathbf{a}\|_2 = \|\mathbf{A}\|_{\mathbf{A}(3)}$. The exponential map is surjective: with $B_{\mathbf{A}} \subset \mathbf{A}(3)$ denoting the open ball of radius π centered at \mathbf{A} , the image of every closed ball $\bar{B}_{\mathbf{A}}$ covers all of $\text{SO}(3)$ such that $\exp|_{B_{\mathbf{A}}}$ is injective while every pair of antipodal surface points on $\bar{B}_{\mathbf{A}}$ has the same image point. Hence the exponential map has infinitely many local inverses: the branches of the logarithm map. Every matrix $\mathbf{A} \in \mathbf{A}(3)$ defines a branch $\log_{\mathbf{A}}$ that satisfies $\log_{\mathbf{A}}(\exp(\mathbf{A})) = \mathbf{0}$ and that maps a maximal (relatively) open subset $\text{SO}(3)/\exp(\partial B_{\mathbf{A}})$ to $B_{\mathbf{A}}$. (Here $S_1 \setminus S_2$ denotes the set-theoretic difference.) The principal branch, $\log = \log_{\mathbf{0}}: \text{SO}(3)/\exp(\partial B_{\mathbf{0}}) \rightarrow \mathbf{A}(3)$, has the numerical representation

$$\log(\mathbf{R}) = \begin{cases} \mathbf{0}, & \theta \in [0, \varepsilon_M], \\ \frac{\theta}{\sin \theta} \frac{\mathbf{R} - \mathbf{R}^T}{2}, & \theta \in (\varepsilon_M, \pi), \end{cases}$$

$$\text{where } \theta = \arccos \frac{\text{tr}(\mathbf{R}) - 1}{2} \in (0, \pi). \tag{33}$$

Every other branch is then obtained as

$$\log_{\mathbf{A}}: \text{SO}(3)/\exp(\partial B_{\mathbf{A}}) \rightarrow \mathbf{A}(3), \quad \log_{\mathbf{A}}(\mathbf{R}) = \log(\mathbf{R} \exp(\mathbf{A})^T). \tag{34}$$

Finally, we use $\log_{\mathbf{A}}$ to define the lift of $\mathbf{R} \in \text{SO}(3)$ with respect to $\mathbf{A} \in \mathbf{A}(3)$ as

$$\text{lift}_{\mathbf{A}}(\mathbf{R}) = \mathbf{A} + \log_{\mathbf{A}}(\mathbf{R}) = \mathbf{A} + \log(\mathbf{R} \exp(\mathbf{A})^T). \tag{35}$$

This allows to lift snapshots $(\mathbf{R}(t_n))_{n=0}^N \subset \text{SO}(3)$ of a continuous trajectory to $(\mathbf{A}(t_n))_{n=0}^N \subset \text{A}(3)$ by setting

$$\mathbf{A}(t_0) = \log(\mathbf{R}(t_0)), \quad (36)$$

$$\mathbf{A}(t_n) = \text{lift}_{\mathbf{A}(t_{n-1})}(\mathbf{R}(t_n)) = \mathbf{A}(t_{n-1}) + \log(\mathbf{R}(t_n)\mathbf{R}(t_{n-1})^T), \quad n = 1, \dots, N, \quad (37)$$

provided that each relative rotation of successive snapshots, $\mathbf{R}(t_n)\mathbf{R}(t_{n-1})^T$, has a rotation angle less than π .

3.3. Principal geodesic analysis in SE(3)

We also consider the direct extension to the special Euclidian group of combined translations and rotations, $\text{SE}(3) = \mathbb{R}^3 \times \text{SO}(3)$. The Lie algebra $\text{T}_{(0,1)}\text{SE}(3)$ of that Lie group is canonically isomorphic to $\mathbb{R}^3 \times \text{A}(3) \cong \mathbb{R}^3 \times \mathbb{R}^3$. Since the translation part \mathbb{R}^3 of $\text{SE}(3)$ is a linear space and an additive Lie group, its exponential map $\exp \mathbb{R}^3 \cong \text{T}_0\mathbb{R}^3 \rightarrow \mathbb{R}^3$ is the identity map. Thus, one may simply combine PCA in \mathbb{R}^3 with PGA in $\text{SO}(3)$ to perform PGA in $\text{SE}(3)$.

3.4. A brief comment on the use of principal geodesic analysis for model order reduction

The *principal geodesic analysis* plays a very important role regarding the further model order reduction of beam structures. Therefore, we present in this subsection the main idea behind a nonlinear technique to derive reduced representations. For sake of brevity and without loss of generality, let us consider the fully conservative unconstrained problem emanating from (15) that can be described as

$$\left\langle \delta \mathbf{q}_{n+\frac{1}{2}}, \int_{-1}^{+1} \mathbf{N}^T [\dot{\mathbf{p}}_d(\mathbf{q}_n, \mathbf{q}_{n+1}) + \mathbf{Q}_d^{\text{int}}(\mathbf{q}_n, \mathbf{q}_{n+1}) - \mathbf{Q}_{n+\frac{1}{2}}^{\text{ext}}] \frac{\partial \mathcal{L}_0}{\partial \theta^3} d\theta^3 \right\rangle = 0, \quad (38)$$

in which \mathbf{q} collects all nodal contributions. An admissible local re-parameterization for the i -th node is given by

$$\mathbf{q}_{n+1}^i = \begin{bmatrix} \mathbf{I} & \mathbf{0} & \mathbf{0} & \mathbf{0} \\ \mathbf{0} & \mathbf{0} & \mathbf{0} & \mathbf{0} \\ \mathbf{0} & \mathbf{0} & \mathbf{0} & \mathbf{0} \\ \mathbf{0} & \mathbf{0} & \mathbf{0} & \mathbf{0} \end{bmatrix} \begin{pmatrix} \bar{\mathbf{x}} \\ \mathbf{d}_1 \\ \mathbf{d}_2 \\ \mathbf{d}_3 \end{pmatrix}_{n+1} + \begin{bmatrix} \mathbf{0} & \mathbf{0} & \mathbf{0} & \mathbf{0} \\ \mathbf{0} & \exp(\mathbf{A}_{n+1}^i) & \mathbf{0} & \mathbf{0} \\ \mathbf{0} & \mathbf{0} & \exp(\mathbf{A}_{n+1}^i) & \mathbf{0} \\ \mathbf{0} & \mathbf{0} & \mathbf{0} & \exp(\mathbf{A}_{n+1}^i) \end{bmatrix} \begin{pmatrix} \bar{\mathbf{x}} \\ \mathbf{d}_1 \\ \mathbf{d}_2 \\ \mathbf{d}_3 \end{pmatrix}_n, \quad (39)$$

where the skew-symmetric matrix \mathbf{A}_{n+1}^i is computed as $\text{skew}(\mathbf{a}_{n+1}^i)$ with $\text{skew}: \mathbb{R}^3 \rightarrow \text{A}(3)$. Be aware that this re-parameterization avoids the necessity of imposing internal constraints on the three mutually orthonormal directors, since \mathbf{a}_{n+1}^i can be regarded as the incremental Cartesian rotation vector. Additionally, we have that

$$\delta \mathbf{q}_{n+\frac{1}{2}}^i = \frac{1}{2} \begin{bmatrix} \frac{\partial \mathbf{q}_{n+1}^i}{\partial \bar{\mathbf{q}}_{n+1}^i} \end{bmatrix} \delta \bar{\mathbf{q}}_{n+1}^i, \quad \begin{bmatrix} \frac{\partial \mathbf{q}_{n+1}^i}{\partial \bar{\mathbf{q}}_{n+1}^i} \end{bmatrix} = \begin{bmatrix} \mathbf{I} & \mathbf{0} \\ \mathbf{0} & -\text{skew}(\mathbf{d}_{1,n}^i) \\ \mathbf{0} & -\text{skew}(\mathbf{d}_{2,n}^i) \\ \mathbf{0} & -\text{skew}(\mathbf{d}_{3,n}^i) \end{bmatrix} \quad \text{and} \quad \bar{\mathbf{q}}_{n+1}^i = \begin{pmatrix} \bar{\mathbf{x}} \\ \mathbf{a} \end{pmatrix}_{n+1}, \quad (40)$$

where $\bar{\mathbf{q}}$ denotes the vector containing the generalized coordinates that allows the local reparameterization of the original vector of generalized coordinates \mathbf{q} . The main idea of the model reduction relies on adopting an approximation of the form

$$\begin{pmatrix} \bar{\mathbf{x}} \\ \mathbf{a} \end{pmatrix}_{n+1}^i \approx \begin{pmatrix} \bar{\mathbf{x}}_{\text{ref}} \\ \mathbf{a}_{\text{ref}} \end{pmatrix}_{n+1}^i + \begin{bmatrix} \frac{\partial \bar{\mathbf{q}}_{n+1}^i}{\partial \xi} \end{bmatrix} \xi \quad \text{and} \quad \begin{bmatrix} \frac{\partial \bar{\mathbf{q}}_{n+1}^i}{\partial \xi} \end{bmatrix} = \begin{bmatrix} \frac{\partial \bar{\mathbf{x}}}{\partial \xi} \\ \frac{\partial \mathbf{a}}{\partial \xi} \end{bmatrix}, \quad (41)$$

in which $\bar{\mathbf{x}}_{\text{ref}}$ and \mathbf{a}_{ref} are reference or offset values, $\frac{\partial \bar{\mathbf{x}}}{\partial \xi}$ and $\frac{\partial \mathbf{a}}{\partial \xi}$ are rectangular matrices (the number of columns is considerably smaller than the number of rows) containing a reduced basis obtained from the *principal geodesic analysis*. They correspond to those patterns associated with the higher singular values and thus, the chosen reduced basis will span the subspace where the reduced dynamics will take place. $\xi \in \mathbb{R}^m$ for $m \ll \dim(\bar{\mathbf{q}}) < \dim(\mathbf{q})$ is the vector of reduced coordinates that will evolve in time on the reduced subspace. By considering (39), (40) and (41), the weak form (38) can be rewritten as

$$\left\langle \delta \xi, \frac{1}{2} \left[\frac{\partial \bar{\mathbf{q}}_{n+1}^i}{\partial \xi} \right]^T \left[\frac{\partial \mathbf{q}_{n+1}^i}{\partial \bar{\mathbf{q}}_{n+1}^i} \right]^T \int_{-1}^{+1} \mathbf{N}^T [\dot{\mathbf{p}}_d(\mathbf{q}_n, \xi) + \mathbf{Q}_d^{\text{int}}(\mathbf{q}_n, \xi) - \mathbf{Q}_{n+\frac{1}{2}}^{\text{ext}}] \frac{\partial \mathcal{L}_0}{\partial \theta^3} d\theta^3 \right\rangle = \langle \delta \xi, \mathbf{r}_{n+1}(\xi) \rangle = 0. \quad (42)$$

Finally, the residual vector $\mathbf{r}_{n+1}(\xi)$ is minimized by solving a sequence of quadratic programs, namely

$$\Delta \xi^* = \arg \min_{\Delta \xi \in \mathbb{R}^m} \frac{1}{2} \left\| \mathbf{r}_{n+1}(\xi) + \frac{\partial \mathbf{r}_{n+1}}{\partial \xi}(\xi) \cdot \Delta \xi \right\|_{\mathcal{O}}^2, \quad (43)$$

for \mathcal{O} being a symmetric non-singular square matrix with adequate dimensions, in combination with the actualization rule given by $\xi \mapsto \xi + \Delta \xi^*$ until $\Delta \xi^*$ is smaller than a tolerance. The reader should be aware that firstly, many details are omitted due to the scope of the work, and secondly, for sake of clarity, the ideas are not presented in their optimal form regarding the computational implementation. For model-order reduction techniques based on a minimal parameterization of the three-dimensional rotation group with orthonormal interpolation and the generalized- α method, a very different philosophy than the one adopted here, see [52,53].

4. Results

In this section, we present four examples to show the potential of the principal geodesic analysis applied to beam structures (described as a special class of Cosserat continua) that are developing very complex motions. The four cases were computed using DeSiO (Design and Simulation Framework for Offshore Support Structures), an in-house object-oriented finite element method, multibody system software that is under development at Institute of Structural Analysis [25,41].

The first example considers a swinging rubber rod under the action of gravity. The second example comprises a straight beam that is statically loaded and then being pre-stressed and further on, we remove the load and the beam deforms dynamically. The third example is a triple pendulum under the action of gravity, which comprises three flexible links. The fourth and last example considers the simplified dynamic analysis of a large-scale onshore wind turbine, where in addition to flexible beam components, we also consider stiff components like the nacelle and the cube that are modeled as rigid bodies, whose configuration space is also described by SE(3).

For the four examples, the boundary conditions and the combination of several structural components are achieved by means of the introduction of kinematic constraints. With this approach, we can model very complex structures that can be built from simpler structural members. This approach requires solving differential-algebraic equations that come on the scene when combining differential equations that describe the motion and algebraic equations that describe the enforced conditions, further details on the constraints can be found in [41].

4.1. Swinging rubber rod

The dynamic behavior of a swinging rubber rod under the action of gravity was largely studied, see for instance [54]. The rod has a length of 1.0 m and a circular cross section with a radius of 0.005 m. The elastic rod is only loaded by its self-weight due to the gravity acceleration $g = 9.81 \text{ m/s}^2$. In addition, the rod is simply supported at one end. The rubber material parameters used are $E = 5.0 \times 10^6 \text{ N/m}^2$, $\nu = 0.5$, $G = E/2(1 + \nu)$ and $\rho = 1.1 \times 10^3 \text{ kg/m}^3$. No dissipation is considered and the discretization comprises 20 beam elements, *i.e.*, 21 nodes. The performed simulation time is 2.48 s with a constant time step of 0.01 s, *i.e.*, including the initial condition, we have 249 solution sets. The reader must be warned that this example is very delicate. For the adopted discretization setting, simulations based on well-established and validated commercial software like ANSYS and Abaqus FEA blow up after 2.0 s, see [40], where the solutions after 1.5 s show severe unstable behavior. With our approach, we are able to compute a high-quality solution up to 2.5 s approximately. After that the mesh becomes severely distorted at one single element located at one quarter of the length from the simply supported end, and even if convergent, the rest of the solution is considered as invalid. A preliminary study indicates that this is somehow related with the relatively poor condition of the iteration matrix in combination with the chaotic behavior of the rod in itself. However, a detailed analysis of this instability is not part of the current work and would require further investigations.

Fig. 3 presents a motion sequence where the original configuration and some deformed configurations at given time instants are shown. As it can be observed, the rubber rod exhibits large displacements and rotations, therefore the nonlinear kinematic behavior is apparent. Since in this case we deal with a purely conservative system, the total energy of the system must be identically preserved. Table 1 presents energy values at different time instants. These results numerically demonstrate that the adopted formulation preserves the total energy, which is a first integral of motion. Moreover, for this particular case, we observed no unresolved high-frequency content along the simulated time. Therefore, no dissipation is necessary to compute a convergent long-term response.

The discretization above yields a discrete trajectory with 249 snapshots in the space

$$\text{SE}(3)^{21} = (\mathbb{R}^3 \times \text{SO}(3))^{21} \subset (\mathbb{R}^3 \times \mathbb{R}^{3 \times 3})^{21} \cong \mathbb{R}^{252}. \quad (44)$$

We compute singular value decompositions (SVD) and associated truncated singular value decompositions (TSVD) for the following discrete trajectories (see Table 2):

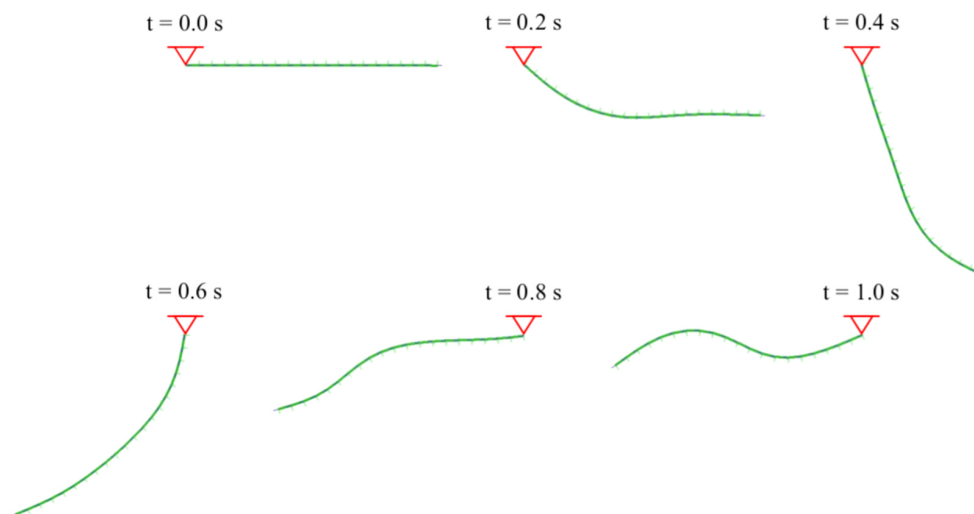


Fig. 3. Swinging rubber rod: motion sequence.

Table 1

Swinging rubber rod: energy values for $t \in [T_1, T_2]$ ($T_1 = 0 \text{ s}$, $T_2 = 2 \text{ s}$).

Time (s)	Kinetic energy (J)	Potential energy (J)	Total energy (J)
0.0	0.000000	0.000000	0.000000
0.5	0.410061	-0.410061	0.000000
1.0	0.027473	-0.027473	0.000000
1.5	0.358499	-0.358499	0.000000
2.0	0.063050	-0.063050	0.000000

Table 2

Swinging rubber rod: computing times, rank and accuracy.

	CPU times (s)				Rank p	$\ \mathbf{D} - \mathbf{D}_p\ _{\max}$
	Lift	SVD	TSVD	Total		
Pos + Rot	-	0.033	0.004	0.037	83	1.67×10^{-14}
Pos - Rot	-	0.022	0.003	0.025	40 + 43: 83	4.31×10^{-14}
Pos + Lift	0.003	0.010	0.002	0.015	61	2.83×10^{-14}
Pos - Lift	0.003	0.004	0.000	0.007	40 + 21: 61	4.31×10^{-14}

(Pos + Rot) positions and embedded rotations combined in $\mathbb{R}^{252 \times 249}$;
 (Pos - Rot) positions and embedded rotations separately in $\mathbb{R}^{63 \times 249}$
 and $\mathbb{R}^{189 \times 249}$;

(Pos + Lift) positions and lifted rotations combined in $\mathbb{R}^{126 \times 249}$;
 (Pos - Lift) positions and lifted rotations separately in $\mathbb{R}^{63 \times 249}$ each.

Table 2 gives the CPU times for computing the lifted trajectory of rotations, the SVD and truncated SVD, and the total CPU time. It also gives the rank of the truncated SVD (the sum in case of separate SVDs) and its accuracy, where the rank is determined as the smallest integer p such that

- $\sigma_{p+1} < \sqrt{\epsilon_M} \sigma_p$ or else
- $\sigma_{p+1} < \sqrt{\epsilon_M} \sigma_1$,

and the accuracy is the maximal absolute difference between corresponding elements of the original matrix and its approximation, $\|\mathbf{D} - \mathbf{D}_p\|_{\max}$. The machine precision and its square root are $\epsilon_M \approx 2.22 \times 10^{-16}$ and $\sqrt{\epsilon_M} \approx 1.49 \times 10^{-8}$. The plots in Figs. 4 and 5 show all numerically computed singular values for the combined SVD (left) and separate SVD (right, position blue, rotation red).

In all four cases the computational effort is clearly dominated by

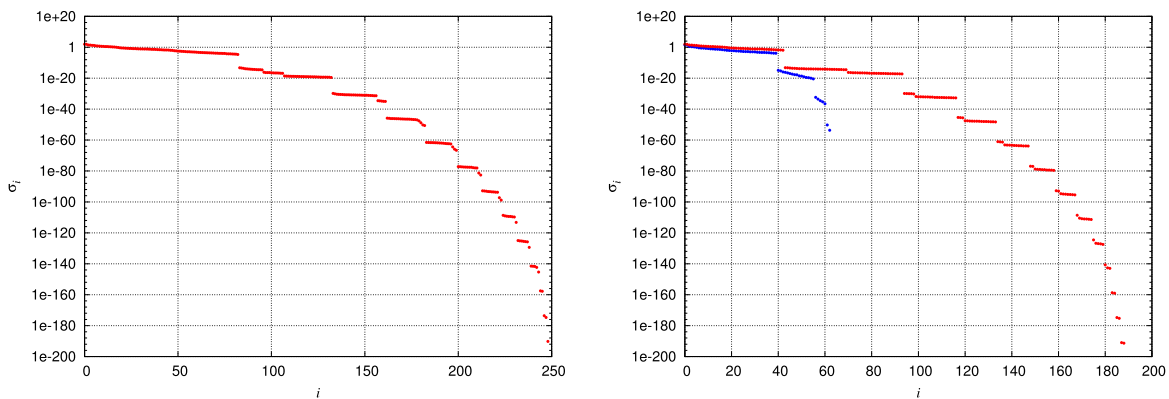


Fig. 4. PCA of swinging rubber rod: singular values of position and embedded rotation combined (left) and separate (right, position blue, rotation right). (For interpretation of the references to color in this figure legend, the reader is referred to the web version of this article).

performing the SVD. Since two SVDs on small matrices are much cheaper than one SVD on the combined matrix, separating positions and rotations reduces the total time substantially. Moreover, lifting the rotations to $A(3)$ is comparatively inexpensive and reduces the matrix dimensions even further. Thus, in addition to capturing the nonlinear structure of $SO(3)$, it has by far the lowest total effort: PGA in $SE(3)$ is about 5 times as fast as PCA in $\mathbb{R}^3 \times \mathbb{R}^{3 \times 3}$.

The rod's motion is actually planar, which leads to “gaps” in the singular value distributions. As it turns out, the rank p is always determined by the first gap here, and we obtain approximations of moderate rank and near-perfect accuracy. Thus, the truncated SVD nicely exploits the inherent structure.

4.2. Free oscillating clamped-free straight beam

In a first static simulation, a clamped-free straight beam is statically loaded with a concentrated moment at the free end. The concentrated moment is normal to the longitudinal axis of the beam and is applied in ten load steps. As result of this static simulation, the clamped-free straight beam adopts a deformed configuration that is identically semi circular, which is perfectly consistent with the analytic solution. In a second dynamic simulation, the moment is eliminated totally and then, the beam starts to oscillate freely. The clamped-free straight beam has a length of 1.0 m and a circular cross section with a radius of 0.005 m. The material parameters used are $E = 1.273 \times 10^9 \text{ N/m}^2$, $G = 6.366 \times 10^8 \text{ N/m}^2$ and $\rho = 3.183 \times 10^3 \text{ kg/m}^3$. The discretization comprises 200 beam elements, *i.e.*, 201 nodes. The performed simulation time is 10.0 s with a constant time step of 0.001 s both for the first

seconds (static simulation) and for the remaining time (dynamic simulation).

Fig. 6 presents a motion sequence of the free oscillating straight beam, where the pre-stressed configuration and some subsequent deformed configurations at given time instants are shown. As it can be observed, the straight beam exhibits large displacements and rotations, therefore the nonlinear kinematic behavior is apparent. After the complete elimination of the moment applied, we deal with a purely conservative system, the total energy of the system must be identically preserved. Table 3 presents some energy values at different time instants. Once again, these results numerically demonstrate that the adopted formulation preserves the total energy. As in the previous example, this particular case shows no unresolved high-frequency content along the simulated time. Therefore, no dissipation is necessary for computing a convergent long-term response.

Here we have 201 nodes and 9012 solution sets (see results in Table 4 and Figs. 7 and 8):

- (Pos + Rot) positions and embedded rotations combined in $\mathbb{R}^{2412 \times 9012}$;
- (Pos – Rot) positions and embedded rotations separately in $\mathbb{R}^{603 \times 9012}$ and $\mathbb{R}^{1809 \times 9012}$;
- (Pos + Lift) positions and lifted rotations combined in $\mathbb{R}^{1206 \times 9012}$;
- (Pos – Lift) positions and lifted rotations separately in $\mathbb{R}^{603 \times 9012}$ each.

Due to much higher dimensions, the SVD dominates the computational effort even more than before, and the differences between the four cases are more pronounced. In particular, separating positions and rotations yields drastic time reductions even though the total

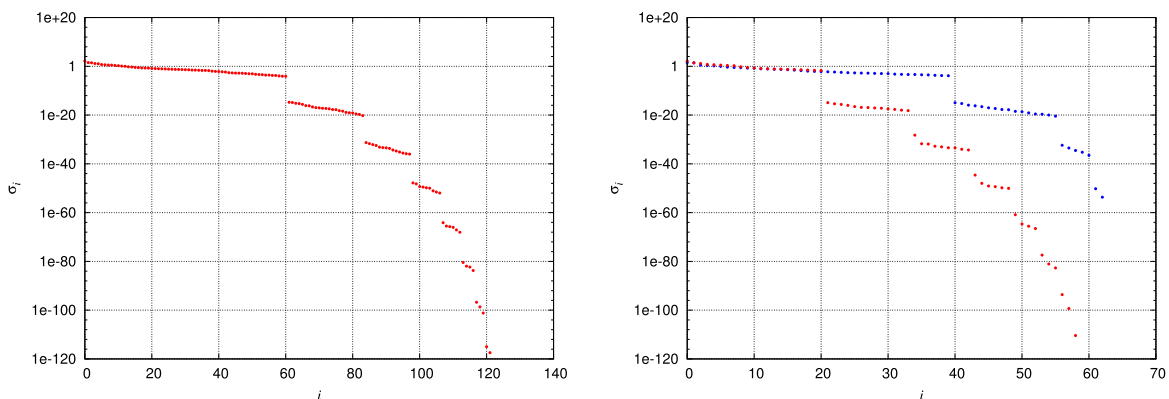


Fig. 5. PGA of swinging rubber rod: singular values of position and lifted rotation combined (left) and separate (right, position blue, rotation right). (For interpretation of the references to color in this figure legend, the reader is referred to the web version of this article).

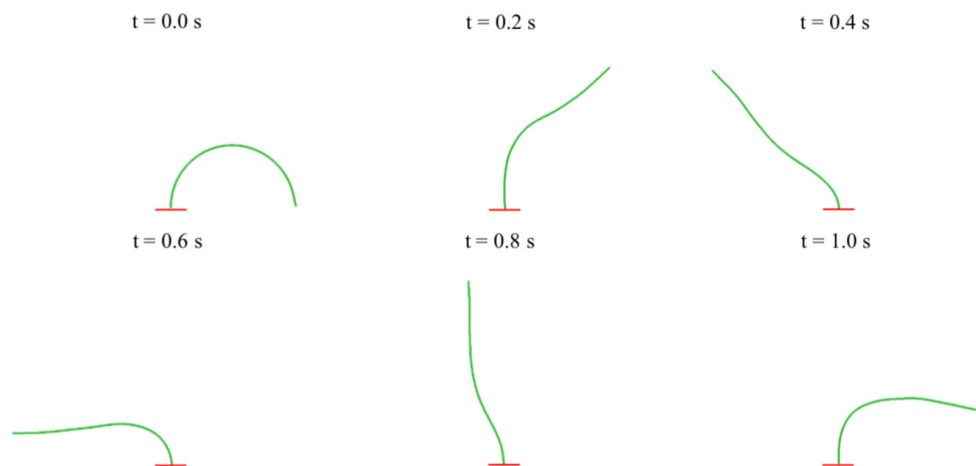


Fig. 6. Free oscillating straight beam: motion sequence.

Table 3

Free oscillating straight beam: energy values for $t \in [T_1, T_2]$ ($T_1 = 1$ s, $T_2 = 3$ s).

Time (s)	Kinetic energy (J)	Potential energy (J)	Total energy (J)
1.0	3.042741	0.000000	3.042741
1.5	2.381333	0.661408	3.042741
2.0	1.994711	1.048030	3.042741
2.5	1.201059	1.841682	3.042741
3.0	0.990583	2.052158	3.042741

approximation rank p is larger than in the combined cases, both with and without lifting. Here PGA in SE(3) is about 11 times as fast as PCA in $\mathbb{R}^3 \times \mathbb{R}^{3 \times 3}$.

As with the rod, the beam's motion is planar, which again creates gaps in the singular value distributions. However, here the rank p is always smaller than the position of the first gap. We obtain approximations of moderate rank and high accuracy. Again, the truncated SVD nicely detects the inherent structure.

4.3. Triple pendulum

Next, we consider a triple pendulum under the action of gravity. This example, which can be considered as a sort of extension of the first example, comprises three identical flexible links joined by spherical joints and thus, this is the first one of the two multibody systems considered along this work. Each link is modeled as a beam and has a length of 1.0 m. The triple pendulum is only loaded by its self-weight due to the gravity acceleration $g = 9.81$ m/s². In addition, the triple pendulum is simply supported at one end. The cross-sectional properties are $GA_1 = GA_2 = 5.0 \times 10^4$ N/m, $EA_3 = 1.0 \times 10^5$ N/m, $EI_1 = EI_2 = 6.2510^{-1}$ Nm², $GJ_3 = 6.239 \times 10^{-1}$ Nm², $\varrho A = 2.5 \times 10^{-1}$ kg/m and $\varrho I_1 = \varrho I_2 = 1.562 \times 10^{-6}$ kgm. No dissipation is

Table 4

Oscillating beam: computing times, rank and accuracy.

	Lift	SVD	TSVD	Total	Rank p	$\ D - D_p\ _{\max}$
Pos + Rot	–	109.828	6.790	116.618	473	6.72×10^{-07}
Pos – Rot	–	65.606	3.986	69.592	252 + 323: 575	5.73×10^{-07}
Pos + Lift	0.947	20.949	2.320	23.269	365	3.75×10^{-07}
Pos – Lift	0.947	9.239	1.387	10.626	252 + 155: 407	1.67×10^{-07}

considered and the discretization comprises 20 beam elements per link, i.e., a total of 63 nodes. The performed simulation time is 10.0 s and the fixed time step is 0.001 s, i.e., we have 10001 solution sets.

Fig. 9 presents a motion sequence, where the original configuration and some deformed configurations at given time instants are shown. Large displacements and rotations are evident. Also the discontinuities in the slope take place at the revolute joints as expected. Since this case is purely conservative the energy is exactly preserved, see Table 5.

The discretization considered produces a discrete trajectory with 63 nodes and 10001 solution sets (see results in Table 6 and Figs. 10 and 11):

- (Pos + Rot) positions and embedded rotations combined in $\mathbb{R}^{756 \times 10001}$;
- (Pos – Rot) positions and embedded rotations separately in $\mathbb{R}^{189 \times 10001}$ and $\mathbb{R}^{567 \times 10001}$;
- (Pos + Lift) positions and lifted rotations combined in $\mathbb{R}^{378 \times 10001}$;
- (Pos – Lift) positions and lifted rotations separately in $\mathbb{R}^{189 \times 10001}$ each.

Here the computation times of the four different cases behave similar to the straight beam, except that the differences are less pronounced with PGA in SE(3) being roughly 6 times as fast as PCA in $\mathbb{R}^3 \times \mathbb{R}^{3 \times 3}$.

As with the rod, the triple pendulum's motion is planar, which again creates gaps in the singular value distributions, and the rank p is always determined by the first gap. We obtain approximations of moderate rank and very high accuracy. Again, the truncated SVD nicely detects the inherent structure.

4.4. Wind turbine

In this example, we present a model for the reference wind turbine defined in [55]. It consists of one beam component for the tower and three beam components for the individual rotor blades. Hub and nacelle

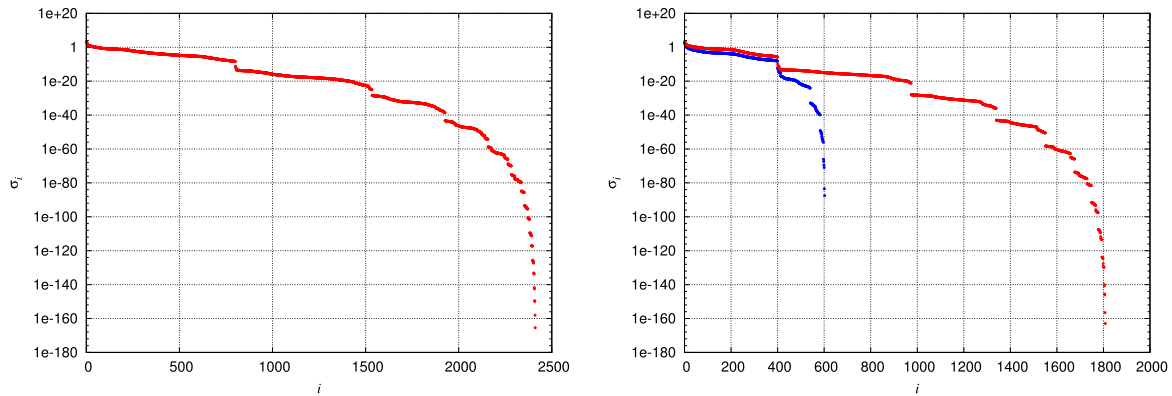


Fig. 7. PCA of oscillating beam: singular values of position and embedded rotation combined (left) and separate (right, position blue, rotation right). (For interpretation of the references to color in this figure legend, the reader is referred to the web version of this article).

are modeled as rigid bodies. The geometric and material properties for this example are also taken from [55]. Blade pre-cone and shaft tilt are also taken into account. The tower root is rigidly clamped. A rigid connection is used to connect the topmost tower node to the nacelle. The three blades are rigidly connected to the hub, and rotation of the hub about the rotor axis is permitted. The tower is discretized into 10 finite elements, each blade into 48. A conservative load set is applied at the ten outermost nodes of one of the three blades. The load set follows a triangular law with maximum of 1.0×10^5 N at each node and remains active during the first 1.5 s. The finite element representation and the applied loads are illustrated in Fig. 12.

Fig. 13 presents a motion sequence where the original configuration and some deformed configurations at given time instants are shown. As it can be observed, the nonlinear kinematic behavior is apparent. Table 7 presents energy values at different time instants. Once again, the total energy is identically preserved and no unresolved high-frequency content along the simulated time is observed.

Here we have 160 nodes and 4001 time steps (see results in Table 8 and Figs. 14 and 15):

- (Pos + Rot) positions and embedded rotations combined in $\mathbb{R}^{1920 \times 4001}$;
- (Pos - Rot) positions and embedded rotations separately in $\mathbb{R}^{480 \times 4001}$ and $\mathbb{R}^{1440 \times 4001}$;
- (Pos + Lift) positions and lifted rotations combined in $\mathbb{R}^{960 \times 4001}$;
- (Pos - Lift) positions and lifted rotations separately in $\mathbb{R}^{480 \times 4001}$ each.

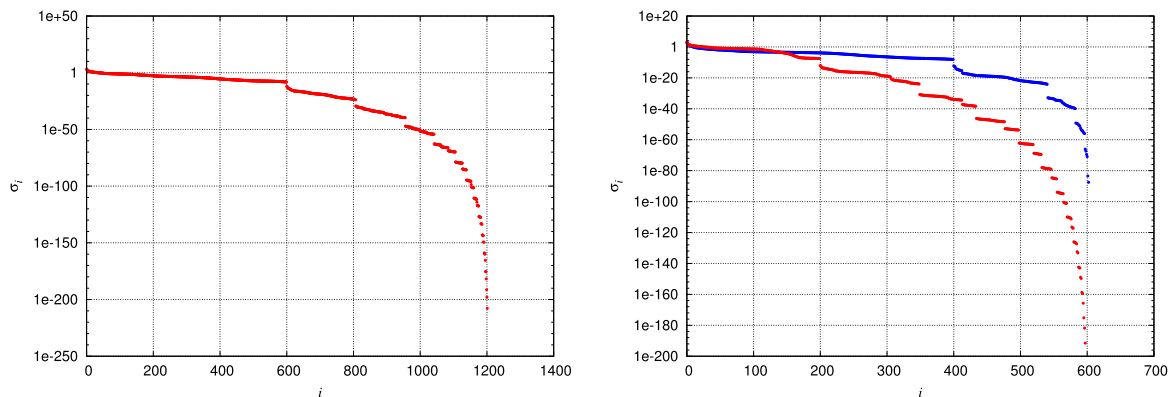


Fig. 8. PGA of oscillating beam: singular values of position and lifted rotation combined (left) and separate (right, position blue, rotation right). (For interpretation of the references to color in this figure legend, the reader is referred to the web version of this article).

Again we observe substantial reductions of the computational effort due to both separation and lifting, although the total rank p with separation is now much larger than without, and the truncated SVD in case 2 is much more expensive than in case 1. PGA in $SE(3)$ is about 10 times as fast as PCA in $\mathbb{R}^3 \times \mathbb{R}^{3 \times 3}$.

The overall motion of the wind turbine (tower and blades) is genuinely 3-dimensional. The singular value distributions look rather smooth here, with gaps occurring only at very small singular values. Here the rank p is always determined by the second truncation criterion (ratio of current and first singular values). We obtain approximations of moderate rank and moderate accuracy. There is no special structure here. The truncated SVD shows the usual behavior that is to be expected in the general case.

5. Concluding remarks, limitation and future works

In this work, we presented a comprehensive framework intended to investigate the nonlinear dynamics of beam structures. The proposed approach that relies on geometrically exact beam finite-elements, a multibody system formalism, a robust time integration scheme and a principal geodesic analysis, takes full advantage of the underlying mathematical structure provided by the configuration space $SE(3)$ (the three-dimensional special Euclidean group). By applying the principal geodesic analysis, it was possible to show that motion patterns/modes are identifiable, but this time in the fully nonlinear setting. Even,

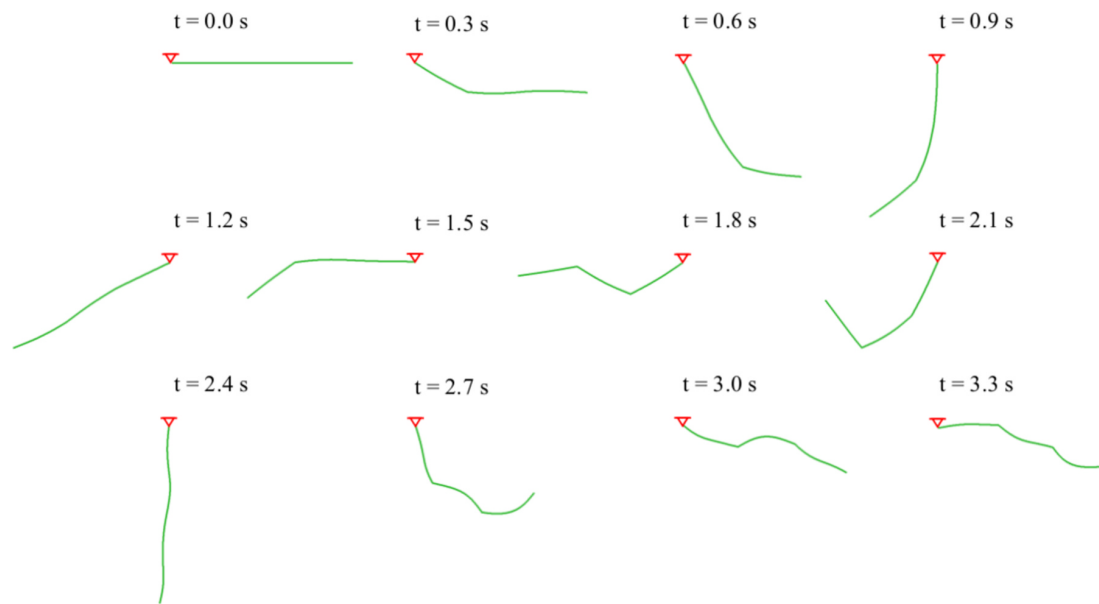


Fig. 9. Triple pendulum: motion sequence.

Table 5

Triple pendulum: energy values for $t \in [T_1, T_2]$ ($T_1 = [s]0, T_2 = [s]8$).

Time (s)	Kinetic energy (J)	Potential energy (J)	Total energy (J)
0.0	0.000000	0.000000	0.000000
2.0	4.439267	- 4.439267	0.000000
4.0	10.187456	- 10.187456	0.000000
6.0	4.771004	- 4.771004	0.000000
8.0	0.928892	- 0.928892	0.000000

Table 6

Triple pendulum: computing times, rank and accuracy.

	Lift	SVD	TSVD	Total	Rank p	$\ D - D_p\ _{\max}$
Pos + Rot	-	8.526	0.973	9.499	247	1.16×10^{-12}
Pos - Rot	-	5.330	0.528	5.858	120 + 127:247	1.32×10^{-11}
Pos + Lift	0.336	2.117	0.388	2.841	378	1.35×10^{-12}
Pos - Lift	0.336	1.089	0.203	1.628	120 + 63:183	2.15×10^{-12}

provided that we adopted a non-orthogonal interpolation for the rotations over each element, the principal geodesic analysis was safely applied to the nodes, where the orthogonality is warranted in a strong sense and therefore, no re-orthonormalization strategy is necessary. Moreover, the dynamics of some beam structures could be satisfactorily reconstructed by employing a reduced set of patterns/modes. The accuracy of the reconstructed solutions is very good and interesting speed ups of the computations were observed, which is of high importance especially when solving for engineering applications. This result is very encouraging especially when structure-preserving reduction techniques are required, where we do understand the term structure-preserving as the capability of a formulation to preserve the underlying mathematical structure, in this context the Lie group structure. Before deriving a generalized method for order reduction, further investigations with respect to the solvability and the robustness are still necessary. Additionally, the current approach is in principle restricted to nonlinearities due to the kinematic description. In future works further extensions regarding, first, nonlinearities due to complex material constitutive laws, and second, nonlinearities due to contact will be considered.

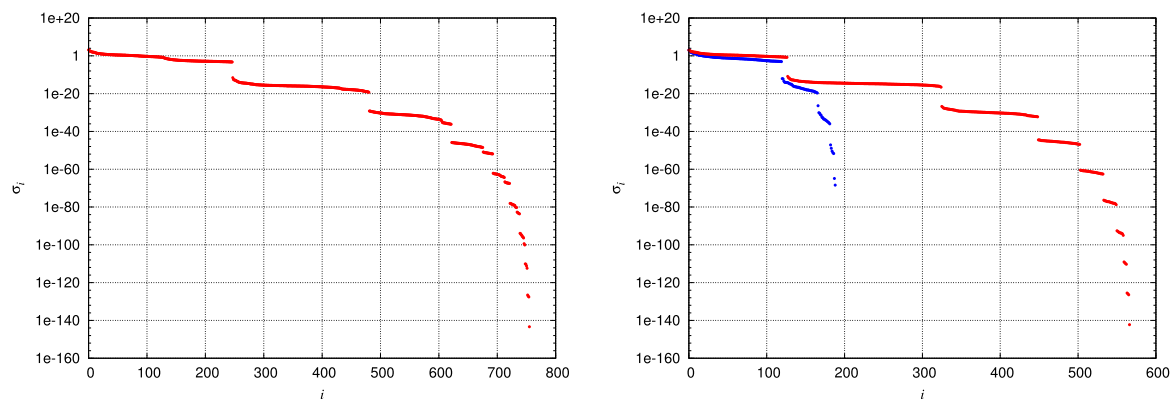


Fig. 10. PCA of triple pendulum: singular values of position and embedded rotation combined (left) and separate (right, position blue, rotation right). (For interpretation of the references to color in this figure legend, the reader is referred to the web version of this article).

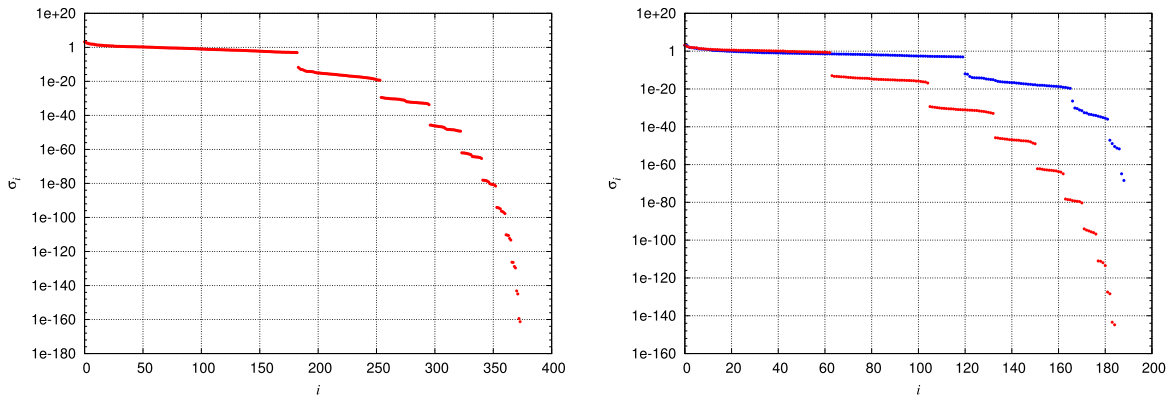


Fig. 11. PGA of triple pendulum: singular values of position and lifted rotation combined (left) and separate (right, position blue, rotation right). (For interpretation of the references to color in this figure legend, the reader is referred to the web version of this article).

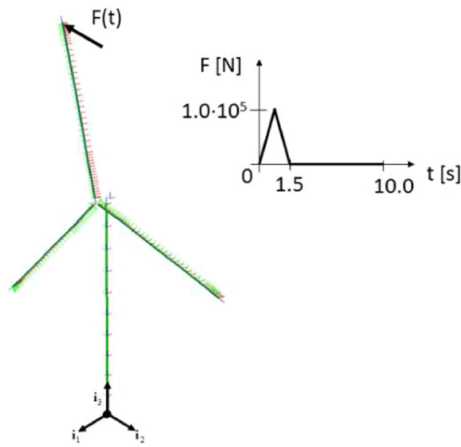


Fig. 12. Wind turbine: finite element representation and applied loads.

Table 7

Wind turbine: energy values for $t \in [T_1, T_2]$ ($T_1 = 4$ s, $T_2 = 8$ s).

Time (s)	Kinetic energy (J)	Potential energy (J)	Total energy (J)
4.0	6.437354×10^6	3.010235×10^6	9.447589×10^6
5.0	8.839348×10^6	0.608241×10^6	9.447589×10^6
6.0	7.325392×10^6	2.122197×10^6	9.447589×10^6
7.0	7.071510×10^6	2.376079×10^6	9.447589×10^6
8.0	8.892539×10^6	0.555050×10^6	9.447589×10^6

Table 8

Wind turbine: computing times, rank and accuracy.

	Lift	SVD	TSVD	Total	Rank p	$\ D - D_p\ _{\max}$
Pos + Rot	-	49.050	1.387	50.437	323	3.16×10^{-5}
Pos - Rot	-	26.162	2.354	28.516	159 + 670: 829	3.92×10^{-5}
Pos + Lift	0.332	9.488	0.856	10.344	408	2.61×10^{-4}
Pos - Lift	0.332	4.167	0.609	5.108	159 + 401: 560	3.92×10^{-5}

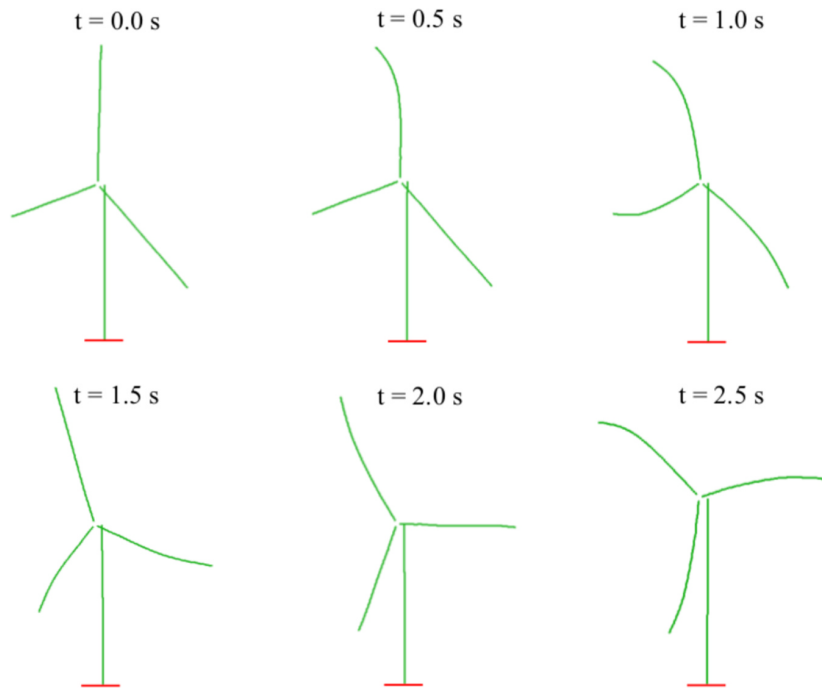


Fig. 13. Wind turbine: motion sequence.

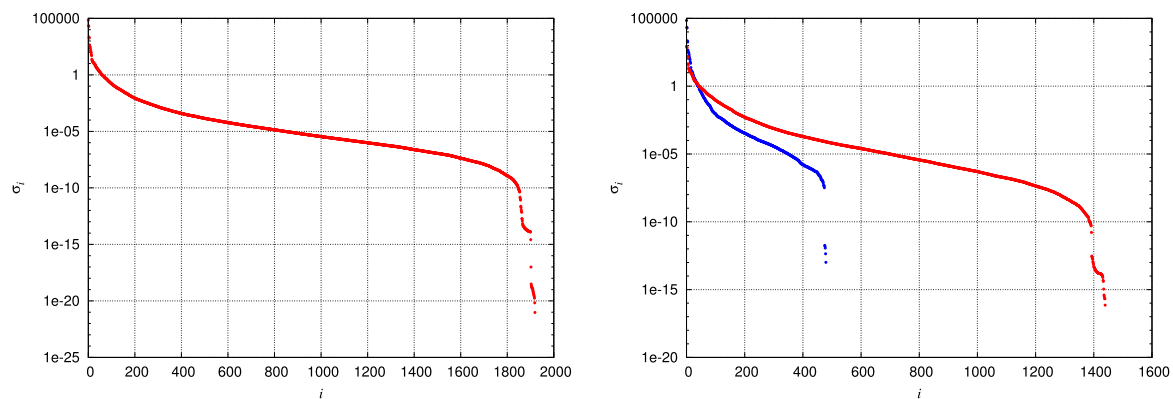


Fig. 14. PCA of wind turbine: singular values of position and embedded rotation combined (left) and separate (right, position blue, rotation right). (For interpretation of the references to color in this figure legend, the reader is referred to the web version of this article).

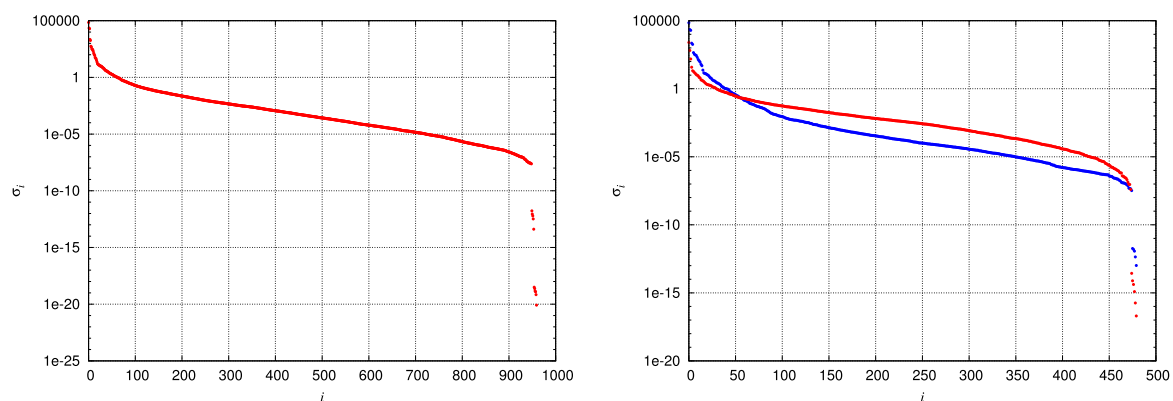


Fig. 15. PGA of Wind turbine: singular values of position and lifted rotation combined (left) and separate (right, position blue, rotation right). (For interpretation of the references to color in this figure legend, the reader is referred to the web version of this article).

Acknowledgments

We gratefully acknowledge the financial support of the Lower Saxony Ministry of Science and Culture (research project *ventus efficiens*, FKZ ZN3024) and of the German Federal Ministry for Economic Affairs and Energy (research project *Deutsche Forschungsplattform für Windenergie*, FKZ 0325936E) that enabled this work.

We also thank the reviewers for their valuable comments.

References

- [1] E. Reissner, On one-dimensional finite-strain beam theory: the plane problem, *J. Appl. Math. Phys.* 23 (1972) 795–804, <https://doi.org/10.1007/BF01602645>.
- [2] K.-J. Bathe, S. Bolourchi, Large displacement analysis of three-dimensional beam structures, *Int. J. Numer. Methods Eng.* 14 (1979) 961–986, <https://doi.org/10.1002/nme.1620140703>.
- [3] J.C. Simó, A finite strain beam formulation. The three-dimensional dynamic problem, Part I, *Comput. Methods Appl. Mech. Eng.* 49 (1985) 55–70, [https://doi.org/10.1016/0045-7825\(85\)90050-7](https://doi.org/10.1016/0045-7825(85)90050-7).
- [4] A. Cardona, M. Géradin, A beam finite element non-linear theory with finite rotations, *Int. J. Numer. Methods Eng.* 26 (1988) 2403–2438, <https://doi.org/10.1002/nme.1620261105>.
- [5] I. Romero, F. Armero, An objective finite element approximation of the kinematics of geometrically exact rods and its use in the formulation of an energy-momentum conserving scheme in dynamics, *Int. J. Numer. Methods Eng.* 54 (2002) 1683–1716, <https://doi.org/10.1002/nme.486>.
- [6] F. Armero, I. Romero, On the formulation of high-frequency dissipative time-stepping algorithms for nonlinear dynamics. Part I: low-order methods for two model problems and nonlinear elastodynamics, *Comput. Methods Appl. Mech. Eng.* 190 (2001) 2603–2649, [https://doi.org/10.1016/S0045-7825\(00\)00256-5](https://doi.org/10.1016/S0045-7825(00)00256-5).
- [7] F. Armero, I. Romero, On the formulation of high-frequency dissipative time-stepping algorithms for nonlinear dynamics. Part II: second-order methods, *Comput. Methods Appl. Mech. Eng.* 190 (2001) 6783–6824, [https://doi.org/10.1016/S0045-7825\(01\)00233-x](https://doi.org/10.1016/S0045-7825(01)00233-x).
- [8] F. Armero, I. Romero, Energy-dissipative momentum-conserving time-stepping algorithms for the dynamics of nonlinear Cosserat rods, *Comput. Mech.* 31 (2003) 3–26, <https://doi.org/10.1007/s00466-002-0389-9>.
- [9] P. Betsch, P. Steinmann, Constrained dynamics of geometrically exact beams, *Comput. Mech.* 31 (2003) 49–59, <https://doi.org/10.1007/s00466-002-0392-1>.
- [10] I. Romero, The interpolation of rotations and its application to finite element models of geometrically exact rods, *Comput. Mech.* 34 (2004) 121–133, <https://doi.org/10.1007/s00466-004-0559-z>.
- [11] P. Fletcher, C. Lu, S.M. Pizer, S. Joshi, Principal geodesic analysis for the study of nonlinear statistics of shape, *IEEE Trans. Med. Imaging* 23 (2004) 995–1005, <https://doi.org/10.1109/TMI.2004.831793>.
- [12] W. Yu, L. Liao, D.H. Hodges, V.V. Volovoi, Theory of initially twisted, composite, thin-walled beams, *Thin-Walled Struct.* 43 (2005) 1296–1311, <https://doi.org/10.1016/j.tws.2005.02.001>.
- [13] J. Mäkinen, Total lagrangian Reissner's geometrically exact beam element without singularities, *Int. J. Numer. Methods Eng.* 70 (2007) 1009–1048, <https://doi.org/10.1002/nme.1892>.
- [14] F. Auricchio, P. Carotenuto, A. Reali, On the geometrically exact beam model: a consistent, effective and simple derivation from three-dimensional finite-elasticity, *Int. J. Solids Struct.* 45 (2008) 4766–4781, <https://doi.org/10.1016/j.ijsolstr.2008.04.015>.
- [15] P.M. Pimenta, E.M. Campello, P. Wriggers, An exact conserving algorithm for nonlinear dynamics with rotational dofs and general hyperelasticity. Part 1: rods, *Comput. Mech.* 42 (2008) 715–732, <https://doi.org/10.1007/s00466-008-0271-5>.
- [16] I. Romero, A comparison of finite elements for nonlinear beams: the absolute nodal coordinate and geometrically exact formulations, *Multibody Syst. Dyn.* 20 (2008) 51–68, <https://doi.org/10.1007/s11044-008-9105-7>.
- [17] S. Ghosh, D. Roy, A frame-invariant scheme for the geometrically exact beam using rotation vector parametrization, *Comput. Mech.* 44 (2009) 103–118, <https://doi.org/10.1007/s00466-008-0358-z>.
- [18] P.F. Pai, Problems in geometrically exact modeling of highly flexible beams, *Thin-Walled Struct.* 76 (2014) 65–76, <https://doi.org/10.1016/j.tws.2013.11.008>.
- [19] S. Huckemann, T. Hotz, A. Munk, Intrinsic shape analysis: geodesic pca for riemannian manifolds modulo isometric lie group actions, *Stat. Sin.* 20 (2010) 1–58.
- [20] S. Machado, M. Pivov, Nonlinear dynamics of rotating box gfm beams using nonlinear normal modes, *Thin-Walled Struct.* 62 (2013) 158–168, <https://doi.org/10.1016/j.tws.2012.09.005>.

- [21] F. Pai, Energy-consistent formulation and order deficiency of linear and nonlinear shear-deformable beam theories, *Thin-Walled Struct.* 65 (2013) 7–13, <https://doi.org/10.1016/j.tws.2013.01.001>.
- [22] S. de Miranda, A. Gutierrez, D. Melchionda, L. Patruno, Linearly elastic constitutive relations and consistency for GBT-based thin-walled beams, *Thin-Walled Struct.* 92 (2015) 55–64, <https://doi.org/10.1016/j.tws.2015.02.022>.
- [23] L. Wu, P. Tiso, Nonlinear model order reduction for flexible multibody dynamics: a modal derivatives approach, *Multibody Syst. Dyn.* 36 (2016) 405–425, <https://doi.org/10.1007/s11044-015-9476-5>.
- [24] S. Hauberg, Principal curves on riemannian manifolds, *IEEE Trans. Pattern Anal. Mach. Intell.* 38 (2016) 1915–1921, <https://doi.org/10.1109/TPAMI.2015.2496166>.
- [25] C.G. Gebhardt, R. Rolfes, On the nonlinear dynamics of shell structures: combining a mixed finite element formulation and a robust integration scheme, *Thin-Walled Struct.* 118 (2017) 56–72, <https://doi.org/10.1016/j.tws.2017.05.001>.
- [26] A. Gay Neto, Simulation of mechanisms modeled by geometrically-exact beams using rodrigues rotation parameters, *Comput. Mech.* 59 (2017) 459–481, <https://doi.org/10.1007/s00466-016-1355-2>.
- [27] V. Sonneville, O. Brüls, O. Bauchau, Interpolation schemes for geometrically exact beams: a motion approach, *Int. J. Numer. Methods Eng.* 112 (2017) 1129–1153, <https://doi.org/10.1002/nme.5548>.
- [28] O. Brüls, V. Martinusi, V. Sonneville, On the proper orthogonal decomposition for the reduced-order modelling of geometrically nonlinear elastic bodies, *ECCOMAS Themat. Conf. Multibody Dyn.* (2017) 1–2.
- [29] M.A. Crisfield, A consistent co-rotational formulation for non-linear, three-dimensional, beam-elements, *Comput. Methods Appl. Mech. Eng.* 81 (1990) 131–150, [https://doi.org/10.1016/0045-7825\(90\)90106-V](https://doi.org/10.1016/0045-7825(90)90106-V).
- [30] U. Galvanetto, M.A. Crisfield, An energy-conserving co-rotational procedure for the dynamics of planar beam structures, *Int. J. Numer. Methods Eng.* 39 (1996) 2265–2282, [https://doi.org/10.1002/\(SICI\)1097-0207\(19960715\)39:133.O.CO;2-O](https://doi.org/10.1002/(SICI)1097-0207(19960715)39:133.O.CO;2-O).
- [31] M.A. Crisfield, U. Galvanetto, G. Jelenić, Dynamics of 3-d co-rotational beams, *Comput. Mech.* 20 (1997) 507–519, <https://doi.org/10.1007/s004660050271>.
- [32] R. Alsafadie, H. M., J.-M. Battini, Three-dimensional formulation of a mixed corotational thin-walled beam element incorporating shear and warping deformation, *Thin-Walled Struct.* 49 (2011) 523–533, <https://doi.org/10.1016/j.tws.2010.12.002>.
- [33] T.-P. Le, J.-M. Battini, M. Hjjaj, Dynamics of 3d beam elements in a corotational context: a comparative study of established and new formulations, *Finite Elem. Anal. Des.* 61 (2012) 97–111, <https://doi.org/10.1016/j.finel.2012.06.007>.
- [34] C.G. Gebhardt, Desarrollo de Simulaciones Numéricas del Comportamiento Aeroelástico de Grandes Turbinas Eólicas de Eje Horizontal (Ph.D. Thesis), Universidad Nacional de Córdoba, 2012.
- [35] C.G. Gebhardt, S. Preidikman, M.H. Jørgensen, J.C. Massa, Non-linear aeroelastic behavior of large horizontal-axis wind turbines: a multibody system approach, *Int. J. Hydrog. Energy* 37 (2012) 14719–14724, <https://doi.org/10.1016/j.ijhydene.2011.12.090>.
- [36] C.G. Gebhardt, B.A. Roccia, Non-linear aeroelasticity: an approach to compute the response of three-blade large-scale horizontal-axis wind turbines, *Renew. Energy* 66 (2014) 495–514, <https://doi.org/10.1016/j.renene.2013.12.040>.
- [37] F. Foti, L. Martinelli, F. Perotti, Numerical integration of the equations of motion of structural systems undergoing large 3d rotations: dynamics of corotational slender beam elements, *Meccanica* 50 (2015) 751–765, <https://doi.org/10.1007/s11012-014-0013-z>.
- [38] K.M. Mathisen, Y. Bazilevs, B. Haugen, T.A. Helgedagsrud, T. Kvamsdal, K.M. Okstad, S.B. Raknes, A comparative study of beam element formulations for nonlinear analysis: corotational vs. geometrically exact formulations, *MekIT'17 - Ninth Natl. Conf. Comput. Mech.* (2017) 245–272.
- [39] M. Banerjee, R. Chakraborty, B.C. Vemuri, Sparse exact pga on riemannian manifolds, in: *Proceedings of IEEE International Conference on Computer Vision, 2017*, pp. 5020–5028. <http://dx.doi.org/10.1109/ICCV.2017.536>.
- [40] C.G. Gebhardt, A.E. Matusевич, J.A. Inaudi, Coupled transverse and axial vibrations including warping effect in asymmetric short beams, *J. Eng. Mech.* 144 (2018), [https://doi.org/10.1061/\(ASCE\)EM.1943-7889.0001471\(04018043-1-12\)](https://doi.org/10.1061/(ASCE)EM.1943-7889.0001471(04018043-1-12)).
- [41] C.G. Gebhardt, B. Hofmeister, C. Hente, R. Rolfes, Nonlinear dynamics of slender structures: a new object-oriented framework, *Comput. Mech.* (2018) 1–34, <https://doi.org/10.1007/s00466-018-1592-7>.
- [42] C. Hente, C.G. Gebhardt, B. Hofmeister, R. Rolfes, On the modal analysis of flexible multibody systems with singular mass and stiffness matrices, *Proc. Appl. Math. Mech.* 18 (2018) e201800115, <https://doi.org/10.1002/pamm.201800115>.
- [43] B. Hofmeister, C.G. Gebhardt, C. Hente, R. Rolfes, Sparsity pattern extraction for assembly of kkt-like matrices in multibody dynamics, *Proc. Appl. Math. Mech.* 18 (2018) e201800105, <https://doi.org/10.1002/pamm.201800105>.
- [44] A. Zwölfer, J. Gerstmayr, Selection of generalized component modes for modally reduced flexible multibody systems, in: *Proceedings of the 5th Joint International Conference on Multibody System Dynamics*, 2018, pp. 1–19.
- [45] L. Wu, K. Tassis, E. Chatzi, F. Van Keulen, P. Tiso, A modal derivatives enhanced rubin substructuring method for geometrically nonlinear multibody systems, *Multibody Syst. Dyn.* 45 (2019) 57–85, <https://doi.org/10.1007/s11044-018-09644-2>.
- [46] P. Betsch, P. Steinmann, Frame-indifferent beam finite elements based upon the geometrically exact beam theory, *Int. J. Numer. Methods Eng.* 54 (2001) 1775–1788, <https://doi.org/10.1002/nme.487>.
- [47] A. Harten, B. Lax, P. Leer, On upstream differencing and Godunov-type schemes for hyperbolic conservation laws, *SIAM Rev.* 25 (1983) 35–61, <https://doi.org/10.1137/1025002>.
- [48] R.I. McLachlan, G.R.W. Quispel, N. Robideux, Geometric integration using discrete gradients, *Philosophical Transactions: mathematical, Phys. Eng. Sci.* 357 (1999) 1021–1045, <https://doi.org/10.1098/rsta.1999.0363>.
- [49] O. Gonzalez, Time integration and discrete Hamiltonian systems, *J. Nonlinear Sci.* 6 (1996) 449–467, <https://doi.org/10.1007/BF02440162>.
- [50] W.B. Heard, *Rigid Body Mechanics: Mathematics, Physics and Applications*, Wiley, 2006.
- [51] A.M. Bloch, *Nonholonomic Mechanics and Control*, Springer-Verlag, 2003, <https://doi.org/10.1007/978-0-387-21644-7>.
- [52] C. Farhat, F. Avery, T. Chapman, J. Cortial, Dimensional reduction of nonlinear finite element dynamic models with finite rotations and energy-based mesh sampling and weighting for computational efficiency, *Int. J. Numer. Methods Eng.* 98 (2014) 625–662, <https://doi.org/10.1002/nme.4668>.
- [53] C. Farhat, T. Chapman, F. Avery, Structure-preserving, stability, and accuracy properties of the energy-conserving sampling and weighting method for the hyper reduction of nonlinear finite element dynamic models, *Int. J. Numer. Methods Eng.* 102 (2015) 1077–1110, <https://doi.org/10.1002/nme.4820>.
- [54] H. Lang, J. Linn, M. Arnold, Multi-body dynamics simulation of geometrically exact Cosserat rods, *Multibody Syst. Dyn.* 25 (2011) 285–312, <https://doi.org/10.1007/s11044-010-9223-x>.
- [55] J. Jonkman, S. Butterfield, W. Musial, G. Scott, Definition of a 5-MW reference wind turbine for offshore system development, *Tech. Rep.*, National Renewable Energy Laboratory (NREL), Golden, CO, 2009.

5. Article D: A new conservative/dissipative time integration scheme for nonlinear mechanical systems

This article considers the conservative/dissipative time integration of the equations of motion that typically arise during the analysis of nonlinear mechanical systems. More specifically, the novel approach renders, by construction, methods with the desired conservation or dissipation properties. These discretize the equations of motion and add some perturbations related to the main field variables through a collection of ancillary linearly constrained quadratic programs that guarantee the conservation/dissipation properties. This kind of programs are analytically solvable and therefore, very attractive from the computational point of view. One possible interpretation of the contributions in this article is that it results in conservative/dissipative methods where the geometric arguments typically employed for their design have been replaced by optimality conditions. The perturbations proposed in the new methods are designed to correct some of the unwanted effects coming from the discretization of the governing equations. From a geometric point of view, the idea is to redesign the problem in such a way that the behavior of the system on the discrete constrained submanifold remains unaltered, but acts as an attractor for trajectories outside of it. Since the constrained programs can be solved in closed form, corrected formulas for the algorithmic internal forces and generalized velocities can be provided, and thus easily incorporated in existing simulation codes based on reduced-order models, finite-elements models and multibody systems. Additionally, the similarities and differences of the newly proposed approach with respect to existing ones are pointed out and critically discussed.

This article is published in *Computational Mechanics* 65 (2020), 405–427. The work was conducted in cooperation with a partner from the **IMDEA Materials Institute** and the **Universidad Politécnica de Madrid**, Spain. The main work was done by the author of this *Habilitationschrift*. Ignacio Romero contributed with the revision of the formulation, technical suggestions and supporting work. Raimund Rolfes contributed with technical suggestions and supporting work.

Permanent link: <https://doi.org/10.1007/s00466-019-01775-3>



A new conservative/dissipative time integration scheme for nonlinear mechanical systems

Cristian Guillermo Gebhardt¹ · Ignacio Romero^{2,3} · Raimund Rolfes¹

Received: 14 March 2019 / Accepted: 4 October 2019 / Published online: 12 October 2019
 © Springer-Verlag GmbH Germany, part of Springer Nature 2019

Abstract

We present a conservative/dissipative time integration scheme for nonlinear mechanical systems. Starting from a weak form, we derive algorithmic forces and velocities that guarantee the desired conservation/dissipation properties. Our approach relies on a collection of linearly constrained quadratic programs defining high order correction terms that modify, in the minimum possible way, the classical midpoint rule so as to guarantee the strict energy conservation/dissipation properties. The solution of these programs provides explicit formulas for the algorithmic forces and velocities which can be easily incorporated into existing implementations. Similarities and differences between our approach and well-established methods are discussed as well. The approach, suitable for reduced-order models, finite element models, or multibody systems, is tested and its capabilities are illustrated by means of several examples.

Keywords Conservative/dissipative time integration scheme · Nonlinear mechanical systems · Linearly constrained quadratic programs · Optimality conditions · Unconditional energy stability

1 Introduction

A key feature in the numerical approximations of conservative mechanical systems is their ability to exactly preserve the first integrals of their motion (energy, momenta, symplecticity, ...), replicating the properties of the continuous counterparts (see, e.g., [1,2]). This interest in *structure preserving integrators* is hence justified by the qualitative similarity between the dynamical behaviour of a mechanical system and the *discrete dynamics* generated by the time integration scheme [3]. In addition, a wealth of evidence supports the fact that this kind of time-stepping methods behaves extremely well for long-term simulations [4–9].

It is not easy to formulate numerical schemes that unconditionally preserve one or more invariants of the discrete

motion. Generally speaking, this goal is accomplished by ensuring that some of the (abstract) geometric structures that appear in the continuous picture are replicated in the discrete dynamics. Since it is well-known that, in general, all invariants cannot be preserved for a fixed time step size scheme, different families of methods strive for the preservation of specific subsets of the various symmetries of the continuous system. For example, some numerical methods resemble discrete Hamiltonian systems [6], based on discrete gradient operators, and unconditionally preserve the energy and the (at most quadratic) momenta. Other methods emanate from discrete variational principles [10] and obtain the update formula from the stationarity conditions of these principles. In fact, it is possible to formulate methods that preserve energy, momenta, and the symplectic form of the system, if the time step size is added as an unknown to the method's equations [7].

In the context of nonlinear elastodynamics, the first energy and momentum conserving algorithms were developed by Simo and co-workers [4]. This pioneering work showed that for Saint Venant–Kirchhoff materials, such structure preserving methods can be easily obtained by a simple modification of the midpoint rule in which the stress, instead of being evaluated at the midpoint instant, should be taken as the average of the stresses at the endpoints of the time interval. Since

Cristian Guillermo Gebhardt
 c.gebhardt@isd.uni-hannover.de

- ¹ Institute of Structural Analysis and ForWind Hannover, Leibniz Universität Hannover, Appelstraße 9A, 30167 Hannover, Germany
- ² IMDEA Materials Institute, C/ Eric Kandel 2, Tecnogetafe, 28906 Madrid, Spain
- ³ Escuela Técnica Superior de Ingenieros Industriales, Universidad Politécnica de Madrid, José Gutiérrez Abascal 2, 28006 Madrid, Spain

the constitutive law is linear in the strain, this turns to be equivalent to compute the algorithmic stress with the average of the strains at the endpoints of the time interval. This simple idea was later applied to the conserving integration of shells [5], rods [11,12], contact mechanics [13], multibody systems [14,15], etc., and generalized to elastic materials of arbitrary type [16,17]. The key idea for such generalization is the definition of a *discrete gradient* operator, a consistent approximation of the gradient that guarantees the strict conservation of energy in Hamiltonian systems [16,18–20]. Alternatively, one might derive conserving methods by defining an *average vector field* [8,21]. In the context of the continuous Galerkin method, an optimization approach was employed to systematically develop high-order energy conserving schemes [22,23]. Very recently, a new mixed variational framework that takes advantage of the structure of polyconvex stored energy functions was proposed [24], and the properties of several formulas for the *discrete gradient* that are available in the literature were carefully analyzed in the context of multibody systems [25].

Many Hamiltonian problems are modeled with stiff differential equations for which conserving integration schemes might not be the most robust. For these problems, numerical methods with controllable numerical dissipation in the high-frequency range provide often a practical solution [26–30]. Based on a modification of the discrete gradient operator, Armero and Romero [9,31] developed a family of schemes for nonlinear three-dimensional elastodynamics that exhibits this kind of algorithmic dissipation, while preserving the momenta and providing a strict control of the energy, applicable to elastodynamics, as well as to rods and shells [32,33]. Following an alternative path based on the *average vector field*, Gebhardt and co-workers have proposed similar conserving/dissipative methods for general solid and structural problems [34,35].

This work considers the conservative/dissipative time integration of the equations of motion that typically arise during the analysis of nonlinear mechanical systems. More specifically, we present a novel approach that renders, by construction, methods with the desired conservation or dissipation properties. These methods discretize the equations of motion and add some perturbations related to the main field variables through a collection of ancillary linearly constrained quadratic programs that guarantee the conservation/dissipation properties. This kind of programs are analytically solvable and therefore, very attractive from the computational point of view. One possible interpretation of the contributions in this article is that it results in conservative/dissipative methods where the geometric arguments typically employed for their design have been replaced by optimality conditions.

The perturbations proposed in the new methods are designed to correct some of the unwanted effects coming

from the discretization of the governing equations. From a geometric point of view, the idea is to redesign the problem in such a way that the behavior of the system on the discrete constrained sub-manifold remains unaltered, but acts as an attractor for trajectories outside of it. Since the constrained programs can be solved in closed form, corrected formulas for the algorithmic internal forces and generalized velocities can be provided, and thus easily incorporated in existing simulation codes. The similarities and differences of the newly proposed method with respect to existing ones are pointed out and discussed critically.

The remaining of the article is organized as follows: In Sect. 2, we present the basic framework for nonlinear mechanical systems. In Sect. 3, we address in a comprehensive manner the new time discretization. In Sect. 4, we present several examples of increasing complexity for the verification of the method. Finally, conclusions, limitations and future work are presented in Sect. 5. Additionally, the “Appendix” introduces the precision quotient, with which the correctness of an implementation can be tested.

2 Mechanical framework

2.1 Statement

In this work we consider mechanical systems whose configuration is completely defined by a vector $\mathbf{q} \in Q$, where $Q \subseteq \mathbb{R}^n$. Denoting by t the time, the state of the system at any instant is given by the pair $(\mathbf{q}, \mathbf{s}) \in W \equiv TQ$, where $\mathbf{s} = \dot{\mathbf{q}}$ is the velocity, and in which we have employed the notation $\dot{(\cdot)} = \frac{d(\cdot)}{dt}$. The dynamical behavior of this system, for $t \in [t_a, t_b]$ is governed by the variational equation:

$$\int_{t_a}^{t_b} \left[\langle \delta \mathbf{s}, \mathbf{p}(\dot{\mathbf{q}}) - \boldsymbol{\pi}(\mathbf{s}) \rangle - \langle \delta \mathbf{q}, \dot{\boldsymbol{\pi}}(\mathbf{s}) + \mathbf{f}^{\text{int}}(\mathbf{q}) - \mathbf{f}^{\text{ext}}(\mathbf{q}) \rangle \right] dt = 0, \quad (1)$$

where $(\delta \mathbf{q}, \delta \mathbf{s}) \in TW$ are admissible variations of the generalized coordinates and velocities, $\mathbf{p}(\dot{\mathbf{q}}) \in T_s^*S$ and $\boldsymbol{\pi}(\mathbf{s}) \in T_s^*S$ stand for the generalized-coordinate-based and generalized-velocity-based momenta, respectively, $\mathbf{f}^{\text{int}} \in T_q^*Q$ is the vector of internal forces, $\mathbf{f}^{\text{ext}} \in T_q^*Q$ is the vector of external loads that can be of conservative or non-conservative nature, and finally, $\langle \cdot, \cdot \rangle$ represents a suitable pairing. Additionally, we assume the following two conditions: (i) the system possesses a positive-definite symmetric mass matrix \mathbf{M} such that

$$\boldsymbol{\pi}(\mathbf{s}) = \mathbf{M}\mathbf{s}, \quad \mathbf{p}(\dot{\mathbf{q}}) = \mathbf{M}\dot{\mathbf{q}} \quad (2)$$

and, (ii) both the internal and the external forces derive from potential functions depending only on the configuration \mathbf{q} , i.e.,

$$\mathbf{f}^{\text{int}} = -\frac{\partial V^{\text{int}}}{\partial \mathbf{q}}, \quad \mathbf{f}^{\text{ext}} = -\frac{\partial V^{\text{ext}}}{\partial \mathbf{q}}, \quad (3)$$

and we define the total potential energy of the system as $V = V^{\text{int}} + V^{\text{ext}}$.

We would like to analyze next the implications that symmetry has on the form of the internal forces and the appropriate notions of linear and angular momentum in the abstract space Q . For that, the relation between the configuration space Q and the ambient space \mathbb{R}^3 has to be carefully considered. We start by defining $\Phi : \mathbb{R}^3 \times Q \rightarrow Q$ to be a smooth action of \mathbb{R}^3 on the configuration space such that $\Phi(\mathbf{a}, \mathbf{q})$ is the configuration of the system after all its points have been translated in space by constant vector \mathbf{a} . The infinitesimal generator of this translation at \mathbf{q} is the vector $\boldsymbol{\tau}_a(\mathbf{q}) \in T_{\mathbf{q}}Q$ defined as

$$\boldsymbol{\tau}_a(\mathbf{q}) = \left. \frac{\partial}{\partial \epsilon} \right|_{\epsilon=0} \Phi(\epsilon \mathbf{a}, \mathbf{q}), \quad (4)$$

with $\epsilon \in \mathbb{R}$. Let us now assume internal potential energy is invariant under translations, i.e.,

$$V^{\text{int}} = V^{\text{int}} \circ \Phi. \quad (5)$$

Then, choosing a one parameter curve of translations $\Phi(\epsilon \mathbf{a}, \cdot)$ in Eq. (5) and differentiating with respect to ϵ , it follows that a translation invariant potential implies that the internal forces satisfy

$$\begin{aligned} 0 &= \left. \frac{\partial}{\partial \epsilon} \right|_{\epsilon=0} V^{\text{int}}(\Phi(\epsilon \mathbf{a}, \mathbf{q})) = \left\langle \frac{\partial}{\partial \mathbf{q}} V^{\text{int}}(\mathbf{q}), \boldsymbol{\tau}_a(\mathbf{q}) \right\rangle \\ &= -\langle \mathbf{f}^{\text{int}}(\mathbf{q}), \boldsymbol{\tau}_a(\mathbf{q}) \rangle. \end{aligned} \quad (6)$$

To study the conservation of angular momentum, we must repeat the same argument but considering now a second smooth action $\Psi : \mathbb{R}^3 \times Q \rightarrow Q$ such that $\Psi(\boldsymbol{\theta}, \mathbf{q})$ is the configuration of the system after all its points have rotated in ambient space by the application of a rotation $\exp[\hat{\boldsymbol{\theta}}]$. Defining, as before, the infinitesimal generator of this action to be the vector $\boldsymbol{\rho}_\theta(\mathbf{q}) \in T_{\mathbf{q}}Q$ calculated as

$$\boldsymbol{\rho}_\theta(\mathbf{q}) = \left. \frac{\partial}{\partial \epsilon} \right|_{\epsilon=0} \Psi(\epsilon \boldsymbol{\theta}, \mathbf{q}), \quad (7)$$

again with $\epsilon \in \mathbb{R}$. If the potential energy is now rotation invariant, i.e.,

$$V^{\text{int}} = V^{\text{int}} \circ \Psi. \quad (8)$$

Then the internal force must satisfy

$$0 = \left. \frac{\partial}{\partial \epsilon} \right|_{\epsilon=0} V^{\text{int}}(\Psi(\epsilon \boldsymbol{\theta}, \mathbf{q})) = \left\langle \frac{\partial}{\partial \mathbf{q}} V^{\text{int}}(\mathbf{q}), \boldsymbol{\rho}_\theta(\mathbf{q}) \right\rangle$$

$$= -\langle \mathbf{f}^{\text{int}}(\mathbf{q}), \boldsymbol{\rho}_\theta(\mathbf{q}) \rangle. \quad (9)$$

The precise notion of linear and angular momentum for the system defined in this section is provided by the following result:

Theorem 1 Consider a mechanical system with configuration space $Q \subseteq \mathbb{R}^n$ and vanishing external forces. Let $\Phi(\mathbf{a}, \cdot), \Psi(\boldsymbol{\theta}, \cdot)$ be the translation and rotation actions on the configuration space with infinitesimal generators $\boldsymbol{\tau}_a$ and $\boldsymbol{\rho}_\theta$, respectively, and define the linear momentum $\mathbf{l} \in \mathbb{R}^3$ and the angular momentum $\mathbf{j} \in \mathbb{R}^3$ as the two quantities that verify

$$\langle \mathbf{l}, \mathbf{a} \rangle = \langle \boldsymbol{\tau}_a(\mathbf{q}), \boldsymbol{\pi} \rangle, \quad \langle \mathbf{j}, \boldsymbol{\theta} \rangle = \langle \boldsymbol{\rho}_\theta(\mathbf{q}), \boldsymbol{\pi} \rangle. \quad (10)$$

Then, the linear momentum is conserved if the potential energy is invariant with respect to translations. Similarly, if the potential energy is invariant under rotations, the angular momentum is a constant of the motion. Moreover, the total energy

$$E = \frac{1}{2} \langle \mathbf{s}, \mathbf{M} \mathbf{s} \rangle + V(\mathbf{q}) \quad (11)$$

is preserved by the motion, due to its time invariance.

Proof The proof of momenta conservation follows from taking the derivative of these quantities and using (1) with admissible variations $(\delta \mathbf{q}, \delta \mathbf{s}) = (\boldsymbol{\tau}_a(\mathbf{q}), \mathbf{0})$ and $(\boldsymbol{\rho}_\theta(\mathbf{q}), \mathbf{0})$, respectively. The conservation of energy property follows similarly by choosing $(\delta \mathbf{q}, \delta \mathbf{s}) = (\mathbf{s}, \mathbf{0})$. \square

3 Time discretization

The interest in the current work is in algorithms to approximate the solution of Eq. (1). To define them, let us start by considering a partition of the interval $[t_a, t_b]$ into disjoint subintervals $(t_n, t_{n+1}]$ with $t_a = t_0 < t_1 < \dots < t_N = t_b$, and $\Delta t_n = t_{n+1} - t_n$. Then, the integration algorithms that we consider are based on the midpoint approximation of Eq. (1) and of the form:

$$\begin{aligned} 0 &= \left\langle \delta \mathbf{s}, \mathbf{M} \frac{\mathbf{q}_{n+1} - \mathbf{q}_n}{\Delta t_n} - \mathbf{M} \mathbf{s}_{n+1/2} \right\rangle - \left\langle \delta \mathbf{q}, \frac{\boldsymbol{\pi}_{n+1} - \boldsymbol{\pi}_n}{\Delta t_n} \right. \\ &\quad \left. + \mathbf{f}^{\text{int}}(\mathbf{q}_n, \mathbf{q}_{n+1}) - \mathbf{f}^{\text{ext}}(\mathbf{q}_{n+1/2}) \right\rangle \end{aligned} \quad (12)$$

where the configuration and rate, respectively, at time t_n are approximated by $\mathbf{q}_n, \mathbf{s}_n$, we have defined $\boldsymbol{\pi}_n = \mathbf{M} \mathbf{s}_n$, and we have used the notation $(\cdot)_{n+1/2} = \frac{1}{2}(\cdot)_n + \frac{1}{2}(\cdot)_{n+1}$. The update depends on the definition of an approximation to the internal force at the midpoint $t_{n+1/2}$ that we have denoted as \mathbf{f}^{int} .

Equation (12) provides an implicit or explicit update $(\mathbf{q}_n, \mathbf{s}_n) \mapsto (\mathbf{q}_{n+1}, \mathbf{s}_{n+1})$ that, together with the initial conditions of the configuration and velocity, suffices to generate discrete trajectories. We note that the approximation to the internal force in Eq. (12) is a function of two arguments that, by consistency, must satisfy

$$\mathbf{f}^{\text{int}}(\mathbf{q}, \mathbf{q}) = \mathbf{f}^{\text{int}}(\mathbf{q}), \tag{13}$$

for all configurations $\mathbf{q} \in Q$.

We are interested, in particular, in formulating time integration schemes of the form (12) that preserve (some of) the invariants in the motion of the system (1), while controlling the value of the energy at all times. Let us first consider the update Eq. (12) with variations of the form $(\delta \mathbf{q}, \delta \mathbf{s}) = (\mathbf{0}, \mathbf{c})$, where \mathbf{c} is an arbitrary but constant vector in TQ . Then, trivially, it follows that

$$\frac{\mathbf{q}_{n+1} - \mathbf{q}_n}{\Delta t_n} = \mathbf{s}_{n+1/2}. \tag{14}$$

Next, we would like to explore whether the proposed class of integration schemes preserves momenta for mechanical systems defined in the configuration space Q . The result, for every configuration space, is given next.

Theorem 2 Consider the time discretization (12) of a mechanical system with configuration space $Q \subseteq \mathbb{R}^n$. Let Φ and Ψ denote, as above, the actions of \mathbb{R}^3 on Q representing, respectively, translations and rotations. The integration scheme preserves linear momentum if

$$0 = \langle \boldsymbol{\tau}_a(\mathbf{q}_{n+1/2}), \mathbf{f}^{\text{int}}(\mathbf{q}_n, \mathbf{q}_{n+1}) \rangle \tag{15a}$$

$$\langle \boldsymbol{\tau}_a(\mathbf{q}_{n+1/2}), \boldsymbol{\pi}_{n+1} - \boldsymbol{\pi}_n \rangle = \langle \mathbf{l}_{n+1} - \mathbf{l}_n, \mathbf{a} \rangle, \tag{15b}$$

for every $\mathbf{a} \in \mathbb{R}^3$. Likewise, the integration algorithm preserves angular momentum if for every $\boldsymbol{\theta} \in \mathbb{R}^3$

$$0 = \langle \boldsymbol{\rho}_\theta(\mathbf{q}_{n+1/2}), \mathbf{f}^{\text{int}}(\mathbf{q}_n, \mathbf{q}_{n+1}) \rangle \tag{16a}$$

$$\langle \boldsymbol{\rho}_\theta(\mathbf{q}_{n+1/2}), \boldsymbol{\pi}_{n+1} - \boldsymbol{\pi}_n \rangle = \langle \mathbf{j}_{n+1} - \mathbf{j}_n, \boldsymbol{\theta} \rangle. \tag{16b}$$

The verification of conditions (15)–(16) depends, first, on the structure of Q . For example, if we consider $Q \equiv \mathbb{R}^{3n}$, the configuration space of n particles in three-dimensional Euclidean space, conditions (15b)–(16b) are easily verified. Conditions (15a)–(16a) depend not only on Q but also on the form of \mathbf{f}^{int} which has been, up to this point, left unspecified. For example, the canonical midpoint rule employs $\mathbf{f}^{\text{int}}(\mathbf{x}, \mathbf{y}) = \mathbf{f}^{\text{int}}((\mathbf{x} + \mathbf{y})/2)$, and preserves both linear and angular momenta, but not energy. In turn, the Energy-Momentum method [4,5] provides an expression for this force that guarantees strict energy conservation in the discrete update map, without upsetting the preservation of

momenta. Expanding on this idea, the Energy-Dissipative-Momentum-Conserving method [9,31] adds controllable energy dissipation to the solution, so small that does not upset the accuracy of the solution, yet large enough that can damp out some of the spurious oscillations in the high-frequency part of the solution.

3.1 Discrete derivative

As already mentioned, the direct evaluation of the internal forces at the midpoint configuration does not guarantee, in general, the preservation of energy. There exist however, consistent approximations of these forces that strictly enforce this property of conservative equations.

To introduce the form of this “conservative” approximation of the internal energy let us assume as in Sect. 2 that the internal forces derive from a smooth potential $V : Q \rightarrow \mathbb{R}$. Be aware that from now on, we remove the superindex *int*, since no external force is longer considered along the derivation presented next. The type of approximations we search for are referred in the literature as “discrete derivatives” [6] and are functions $\mathbf{f} : Q \times Q \rightarrow \mathbb{R}$ that satisfy, for every $\mathbf{x}, \mathbf{y} \in Q$, two properties, namely:

- i. Directionality:

$$\langle \mathbf{f}(\mathbf{x}, \mathbf{y}), \mathbf{y} - \mathbf{x} \rangle = V(\mathbf{y}) - V(\mathbf{x}). \tag{17}$$

- ii. Consistency:

$$\mathbf{f}(\mathbf{x}, \mathbf{x}) = -DV(\mathbf{x}) = \mathbf{f}(\mathbf{x}), \tag{18}$$

where D denotes the standard derivative operator.

When $Q \subset \mathbb{R}$, there only exists one discrete derivative [8] and its closed form expression is given by

$$\mathbf{f}(x, y) = \frac{V(y) - V(x)}{|y - x|}, \tag{19}$$

with the well-defined limit

$$\lim_{y \rightarrow x} \mathbf{f}(x, y) = -DV(x) = \mathbf{f}(x). \tag{20}$$

In higher dimensions, there are actually an infinite number of discrete derivatives [8,20] since only the component of \mathbf{f} along the direction of $\mathbf{y} - \mathbf{x}$ needs to have a precise value in order to guarantee energy conservation, and its orthogonal complement is free to vary, as long as consistency of the approximation is preserved. This statement is formalized next:

Theorem 3 Any discrete derivative can be rewritten as

$$\mathbf{f}(\mathbf{x}, \mathbf{y}) = \frac{V(\mathbf{y}) - V(\mathbf{x})}{\|\mathbf{y} - \mathbf{x}\|^2}(\mathbf{y} - \mathbf{x}) + \mathbf{g}(\mathbf{x}, \mathbf{y}), \quad (21)$$

with $\mathbf{g}(\mathbf{x}, \mathbf{y})$ a vector-valued function such that

$$\langle \mathbf{g}(\mathbf{x}, \mathbf{y}), \mathbf{y} - \mathbf{x} \rangle = 0, \quad (\mathbf{y} \neq \mathbf{x}), \quad (22)$$

and

$$\lim_{\mathbf{y} \rightarrow \mathbf{x}} \left(\mathbf{g}(\mathbf{x}, \mathbf{y}) - \mathfrak{P}_{(\mathbf{y}-\mathbf{x})}^\perp \mathbf{f}(\mathbf{x}) \right) = \mathbf{0}, \quad (23)$$

where $\mathfrak{P}_{(\mathbf{y}-\mathbf{x})}^\perp$ is the projection on the component perpendicular to $\mathbf{y} - \mathbf{x}$.

Proof Let $\mathbf{g}(\mathbf{x}, \mathbf{y})$ be defined as

$$\mathbf{g}(\mathbf{x}, \mathbf{y}) = \mathbf{f}(\mathbf{x}, \mathbf{y}) - \frac{V(\mathbf{y}) - V(\mathbf{x})}{\|\mathbf{y} - \mathbf{x}\|^2}(\mathbf{y} - \mathbf{x}), \quad (24)$$

it is apparent that $\mathbf{g}(\mathbf{x}, \mathbf{y})$ is perpendicular to $\mathbf{y} - \mathbf{x}$ because $\langle \mathbf{f}(\mathbf{x}, \mathbf{y}), \mathbf{y} - \mathbf{x} \rangle = V(\mathbf{y}) - V(\mathbf{x})$, and

$$\begin{aligned} \mathbf{g}(\mathbf{x}, \mathbf{y}) - \mathfrak{P}_{(\mathbf{y}-\mathbf{x})}^\perp \mathbf{f}(\mathbf{x}) &= \mathbf{f}(\mathbf{x}, \mathbf{y}) - \frac{V(\mathbf{y}) - V(\mathbf{x})}{\|\mathbf{y} - \mathbf{x}\|^2}(\mathbf{y} - \mathbf{x}) \\ &\quad - \mathbf{f}(\mathbf{x}) + \frac{\langle \mathbf{f}(\mathbf{x}), \mathbf{y} - \mathbf{x} \rangle}{\|\mathbf{y} - \mathbf{x}\|^2}(\mathbf{y} - \mathbf{x}) \\ &= \mathbf{f}(\mathbf{x}, \mathbf{y}) - \mathbf{f}(\mathbf{x}) - \frac{1}{\|\mathbf{y} - \mathbf{x}\|} (V(\mathbf{y}) - V(\mathbf{x})) \\ &\quad - \langle \mathbf{f}(\mathbf{x}), \mathbf{y} - \mathbf{x} \rangle \frac{(\mathbf{y} - \mathbf{x})}{\|\mathbf{y} - \mathbf{x}\|^2}, \end{aligned} \quad (25)$$

which tends to zero as $\mathbf{y} \rightarrow \mathbf{x}$. \square

3.2 Conservative algorithmic force

We explore next a type of discrete derivative that is different to the one usually employed in nonlinear mechanics [4, 16]. For that, we construct first a convex combination of the (exact) derivative at two configurations, i.e.,

$$\mathbf{f}^{\text{cons}} = \frac{1}{2}(1 - \alpha^{\text{cons}})\mathbf{f}(\mathbf{x}) + \frac{1}{2}(1 + \alpha^{\text{cons}})\mathbf{f}(\mathbf{y}) \quad (26)$$

or in a more compact form

$$\mathbf{f}^{\text{cons}} = \mathbf{f}_a + \alpha^{\text{cons}} \tilde{\Delta} \mathbf{f}. \quad (27)$$

In this expression, the scalar α^{cons} has to be determined in order to guarantee directionality, \mathbf{f}_a is the averaged force

$$\mathbf{f}_a = \frac{\mathbf{f}(\mathbf{x}) + \mathbf{f}(\mathbf{y})}{2}, \quad (28)$$

and $\tilde{\Delta} \mathbf{f}$ is one half of the force jump between the configurations at times t_n and t_{n+1} , i.e.,

$$\tilde{\Delta} \mathbf{f} = \frac{\mathbf{f}(\mathbf{y}) - \mathbf{f}(\mathbf{x})}{2}. \quad (29)$$

Notice that this conservative approximation satisfies, by construction, the consistency condition (18). The satisfaction of directionality depends, as advanced, on the choice of the parameter α^{cons} . To enforce it, we select α^{cons} by means of an optimality condition [20], namely, as the scalar that minimizes

$$\frac{1}{2} \|\mathbf{f}^{\text{cons}} - \mathbf{f}_m\|_{\mathfrak{G}}^2 \quad (30)$$

subject to $\langle \mathbf{f}^{\text{cons}}, \mathbf{y} - \mathbf{x} \rangle - V(\mathbf{y}) + V(\mathbf{x}) = 0$.

Assuming $\mathbf{f}(\mathbf{x}) \neq \mathbf{f}(\mathbf{y})$, this optimization problem is a linearly constrained quadratic program that can be solved in closed form. Moreover, the only requirement for the optimization problem to be convex is that $\|\mathbf{f}(\mathbf{y}) - \mathbf{f}(\mathbf{x})\|_{\mathfrak{G}}^2 > 0$. Its solution can be interpreted as the discrete derivative that is closest to \mathbf{f}_m , the continuous force at the midpoint \mathbf{f}_m , namely,

$$\mathbf{f}_m = \mathbf{f} \left(\frac{\mathbf{x} + \mathbf{y}}{2} \right). \quad (31)$$

Here, \mathfrak{G} is a metric tensor. The Lagrangian of the optimization problem is

$$\mathcal{L}(\alpha^{\text{cons}}, \lambda^{\text{cons}}) = \frac{1}{2} \|\mathbf{f}^{\text{cons}} - \mathbf{f}_m\|_{\mathfrak{G}}^2 + \lambda^{\text{cons}} (\langle \mathbf{f}^{\text{cons}}, \mathbf{y} - \mathbf{x} \rangle - V(\mathbf{y}) + V(\mathbf{x})), \quad (32)$$

where λ^{cons} is a Lagrange multiplier that enforces directionality. To find the stationarity condition, the variation of \mathcal{L} is calculated as:

$$\begin{aligned} \delta \mathcal{L}(\alpha^{\text{cons}}, \lambda^{\text{cons}}) &= \langle \delta \mathbf{f}^{\text{cons}}, \mathfrak{G}(\mathbf{f}^{\text{cons}} - \mathbf{f}_m) + \lambda^{\text{cons}}(\mathbf{y} - \mathbf{x}) \rangle \\ &\quad + \delta \lambda^{\text{cons}} (\langle \mathbf{f}^{\text{cons}}, \mathbf{y} - \mathbf{x} \rangle - V(\mathbf{y}) + V(\mathbf{x})). \end{aligned} \quad (33)$$

Now for the sake of brevity, let us introduce a discrete function defined as

$$\tilde{\mathcal{C}}_f(\mathbf{x}, \mathbf{y}) = V(\mathbf{y}) - V(\mathbf{x}) - \langle \mathbf{f}_a, \mathbf{y} - \mathbf{x} \rangle. \quad (34)$$

From now on, we refer to this function as a conservation function, which allows the preservation energy in the discrete setting for a given fixed time step Δt . This conservation function is not unique and depends, in principle, on the shape of the approximated discrete form.

The stationarity condition for the associated Lagrangian function can be reformulated as the linear system that is explicitly given by

$$\begin{pmatrix} A_{11}^f & A_{12}^f \\ A_{12}^f & 0 \end{pmatrix} \begin{bmatrix} \alpha^{\text{cons}} \\ \lambda^{\text{cons}} \end{bmatrix} = \begin{bmatrix} b_1^{f, \text{cons}} \\ b_2^{f, \text{cons}} \end{bmatrix}, \tag{35}$$

with

$$A_{11}^f = \frac{1}{2} \|f(y) - f(x)\|_{\mathfrak{G}}^2, \tag{36}$$

$$A_{12}^f = \langle f(y) - f(x), y - x \rangle, \tag{37}$$

$$b_1^{f, \text{cons}} = \langle f(y) - f(x), \mathfrak{G}(f_m - f_a) \rangle, \tag{38}$$

and

$$b_2^{f, \text{cons}} = 2\tilde{\mathcal{C}}_f(x, y). \tag{39}$$

The solution of this program is

$$\alpha^{\text{cons}} = \frac{2\tilde{\mathcal{C}}_f(x, y)}{\langle f(y) - f(x), y - x \rangle}, \tag{40}$$

and

$$\begin{aligned} \lambda^{\text{cons}} = & -\frac{\langle f(y) - f(x), \mathfrak{G}(f_m - f_a) \rangle}{\langle f(y) - f(x), y - x \rangle} \\ & - \frac{\|f(y) - f(x)\|_{\mathfrak{G}}^2 \tilde{\mathcal{C}}_f(x, y)}{\langle f(y) - f(x), y - x \rangle^2}. \end{aligned} \tag{41}$$

Notice that α^{cons} does not depend on the chosen metric. Then, we can claim that the adopted construction affords a unique definition. This feature represents a main innovation of the current work. However and up to this point, it is not clear to which extent the current formula approaches the commonly used formulas like the one due to Gonzalez [6] or the one due to Harten et al. [21]; a comparison of that second method with the current one is beyond the scope of this work.

In contrast, the Lagrange multiplier λ^{cons} depends on the chosen metric. Finally, the conservative part of the discrete force takes the following explicit form:

$$\begin{aligned} \mathbf{f}^{\text{cons}}(x, y) = & \frac{f(x) + f(y)}{2} \\ & + \frac{\tilde{\mathcal{C}}_f(x, y)}{\langle f(y) - f(x), y - x \rangle} (f(y) - f(x)). \end{aligned} \tag{42}$$

In the context of nonlinear elastodynamics, the first term of the formula is equivalent to the definition proposed by Simo and Tarnow [4] that was derived in the context of Saint Venant–Kirchhoff materials. The second term can be interpreted as a correction for the most general hyperelastic case. The formula proposed by Gonzalez [6] cannot be algebraically reduced to the proposed expression, because the former is basically a correction for f_m and the latter, for f_a .

The conserving force given by Eq. (42) can be rewritten in the form of Eq. (21) and therefore, is a discrete derivative with

$$\mathfrak{P}_{(y-x)}^{\parallel} \mathbf{f}^{\text{cons}}(y - x) = \frac{V(y) - V(x)}{\|y - x\|^2} (y - x), \tag{43}$$

where $\mathfrak{P}_{(y-x)}^{\parallel}$ is the projection parallel to $y - x$, and

$$\mathbf{g}^{\text{cons}}(x, y) := \mathfrak{P}_{(y-x)}^{\perp} \mathbf{f}^{\text{cons}}(x, y). \tag{44}$$

3.3 Dissipative algorithmic force

To account for dissipation, let us assume the existence of a dissipative part of the algorithmic internal force that is proportional to $\tilde{\Delta}f$, this is

$$\mathbf{f}^{\text{diss}} = \alpha^{\text{diss}} \tilde{\Delta}f, \tag{45}$$

where α^{diss} is a scalar whose precise definition is still open. This construction is supported by the analysis done by Romero [20], which showed that other choices may destroy the accuracy of the approximation. We will see later that this expression is very attractive since it provides an unifying treatment of both conservative and dissipative parts of the algorithmic internal force.

To find the value of α^{diss} , we define a discrete dissipation function $\tilde{\mathcal{D}}_f(x, y)$, which must be positive semi-definite, at least second order in $\|y - x\|$ to avoid spoiling the accuracy of the algorithm, and tend to 0 as x tends to y . Then α^{diss} can be obtained as the scalar that minimizes

$$\frac{1}{2} \|\mathbf{f}^{\text{diss}}\|_{\mathfrak{G}}^2 \tag{46}$$

$$\text{subject to } \langle \mathbf{f}^{\text{diss}}, y - x \rangle - \tilde{\mathcal{D}}_f(x, y) = 0.$$

This is also a linearly constrained quadratic program. The solution of this optimization problem can be interpreted as the smallest perturbation force that satisfies the dissipation relation $\langle y - x, \mathbf{f}^{\text{diss}} \rangle = \tilde{\mathcal{D}}_f(x, y)$. Once again, \mathfrak{G} is a given metric tensor and the associated Lagrangian is simply

$$\mathcal{L}(\alpha^{\text{diss}}, \lambda^{\text{diss}}) = \frac{1}{2} \|\mathbf{f}^{\text{diss}}\|_{\mathfrak{G}}^2 + \lambda^{\text{diss}} (\langle \mathbf{f}^{\text{diss}}, y - x \rangle - \tilde{\mathcal{D}}_f(x, y)), \tag{47}$$

where λ^{diss} is a Lagrange multiplier that enforces the dissipation constraint. To formulate the stationarity condition, the variation of the associated Lagrangian has to be computed. This procedure yields

$$\begin{aligned} \delta \mathcal{L}(\alpha^{\text{diss}}, \lambda^{\text{diss}}) = & \langle \delta \mathbf{f}^{\text{diss}}, \mathfrak{G} \mathbf{f}^{\text{diss}} + \lambda^{\text{diss}} (y - x) \rangle \\ & + \delta \lambda^{\text{diss}} (\langle \mathbf{f}^{\text{diss}}, y - x \rangle - \tilde{\mathcal{D}}_f(x, y)). \end{aligned} \tag{48}$$

Noting that $\delta \mathbf{f}^{\text{diss}} = \delta \alpha^{\text{diss}} \tilde{\Delta} \mathbf{f}$, the stationarity condition of the Lagrangian can be written explicitly as

$$\begin{pmatrix} A_{11}^f & A_{12}^f \\ A_{12}^f & 0 \end{pmatrix} \begin{bmatrix} \alpha^{\text{diss}} \\ \lambda^{\text{diss}} \end{bmatrix} = \begin{bmatrix} 0 \\ b_2^{f, \text{diss}} \end{bmatrix}, \quad (49)$$

with

$$b_2^{f, \text{diss}} = 2\tilde{D}_f(\mathbf{x}, \mathbf{y}). \quad (50)$$

The solution of this linearly constrained quadratic program is

$$\alpha^{\text{diss}} = \frac{2\tilde{D}_f(\mathbf{x}, \mathbf{y})}{\langle \mathbf{f}(\mathbf{y}) - \mathbf{f}(\mathbf{x}), \mathbf{y} - \mathbf{x} \rangle}, \quad (51)$$

and

$$\lambda^{\text{diss}} = -\frac{\|\mathbf{f}(\mathbf{y}) - \mathbf{f}(\mathbf{x})\|_{\mathfrak{g}}^2 \tilde{D}_f(\mathbf{x}, \mathbf{y})}{\langle \mathbf{f}(\mathbf{y}) - \mathbf{f}(\mathbf{x}), \mathbf{y} - \mathbf{x} \rangle^2}. \quad (52)$$

As in the case of the conservative part of the algorithmic force, the parameter α^{diss} does not depend on the chosen metric and therefore, it is unique. However and up to this point, it is not clear to which extent the current formula approaches already established formulas, especially the one due to Armero and Romero [9,31]. As in the case of the conservative part of the approximation, the multiplier λ^{diss} depends on the chosen metric. Finally, the formula for the dissipative part of the algorithmic internal force takes the following explicit form:

$$\mathbf{f}^{\text{diss}} = \frac{\tilde{D}_f(\mathbf{x}, \mathbf{y})}{\langle \mathbf{f}(\mathbf{y}) - \mathbf{f}(\mathbf{x}), \mathbf{y} - \mathbf{x} \rangle} (\mathbf{f}(\mathbf{y}) - \mathbf{f}(\mathbf{x})). \quad (53)$$

Notice that this formula has the same structure as the second term of the conservative part of the algorithmic force. However, instead of the conservation function, the dissipation function appears in the numerator. This fact suggests that a unifying formula containing both conservative and dissipative parts is possible, which makes the approach very attractive.

3.4 Generalization and preservation of momenta

Assuming an additive composition of the algorithmic approximation of the force, that is,

$$\mathbf{f} = \mathbf{f}^{\text{cons}} + \mathbf{f}^{\text{diss}}, \quad (54)$$

we can write, using Eqs. (42) and (53),

$$\mathbf{f}(\mathbf{x}, \mathbf{y}) = \frac{\mathbf{f}(\mathbf{x}) + \mathbf{f}(\mathbf{y})}{2} + \frac{\tilde{C}_f(\mathbf{x}, \mathbf{y}) + \tilde{D}_f(\mathbf{x}, \mathbf{y})}{\langle \mathbf{f}(\mathbf{y}) - \mathbf{f}(\mathbf{x}), \mathbf{y} - \mathbf{x} \rangle} (\mathbf{f}(\mathbf{y}) - \mathbf{f}(\mathbf{x})). \quad (55)$$

This formula is very compact and a simple inspection confirms that when the dissipation is zero, the directionality condition is exactly verified.

To accommodate the preservation of linear and angular momenta as discussed in Eqs. (15) and (16), Eq. (55) must be modified as indicated next: Let G be a Lie group with algebra \mathfrak{g} and coalgebra \mathfrak{g}^* , which acts on the configuration space $Q \subseteq \mathbb{R}^{3n}$ by means of the action $\chi : G \times Q \rightarrow Q$. For every $\xi \in \mathfrak{g}$, let $\xi_Q : Q \rightarrow TQ$ denote the infinitesimal generator of the action. Following again Gonzalez [6], we can define G -equivariant derivatives. If $V : Q \rightarrow \mathbb{R}$ is a G -invariant function, its G -invariant discrete derivative is a smooth map $\mathbf{f}^G : Q \times Q \rightarrow \mathbb{R}$ that satisfies the requirements of discrete derivatives and, moreover, the equivariance and orthogonality condition, namely,

$$\mathbf{f}^G(\chi_{\mathfrak{g}}(\mathbf{x}), \chi_{\mathfrak{g}}(\mathbf{y})) = \left(D\chi_{\mathfrak{g}} \left(\frac{\mathbf{x} + \mathbf{y}}{2} \right) \right)^{-T} \mathbf{f}^G(\mathbf{x}, \mathbf{y}), \quad (56)$$

for all $\mathbf{x}, \mathbf{y} \in Q$, $\mathfrak{g} \in G$, and

$$\mathbf{f}^G(\mathbf{x}, \mathbf{y}) \cdot \xi_Q \left(\frac{\mathbf{x} + \mathbf{y}}{2} \right) = 0. \quad (57)$$

To construct a G -equivariant discrete derivative, consider invariant functions under the symmetry action denoted by π_i , $i = 1, 2, \dots, q$ where q is the dimension of the quotient space Q/G . Let $\Pi = (\pi_1, \pi_2, \dots, \pi_q)$. If $V : Q \rightarrow \mathbb{R}$ is G -invariant, a reduced function \tilde{V} can be defined by the relation $V = \tilde{V} \circ \Pi$. If each of the invariants is at most of degree two, then a G -equivariant discrete derivative for V can be constructed as

$$\mathbf{f}^G(\mathbf{x}, \mathbf{y}) = \tilde{\mathbf{f}}(\Pi(\mathbf{x}), \Pi(\mathbf{y})) \circ D\Pi \left(\frac{\mathbf{x} + \mathbf{y}}{2} \right), \quad (58)$$

where, as before $\mathbf{x}, \mathbf{y} \in Q$. In particular, the formulation of a G -equivariant discrete derivative that preserves linear and angular momenta (cf. Eqs. 15 and 16) is straightforward.

The expression of the G -equivariant force in the current context is given by

$$\mathbf{f}(\mathbf{x}, \mathbf{y}) = D\Pi^T(z) \left(\frac{\mathbf{f}(\Pi(\mathbf{y})) + \mathbf{f}(\Pi(\mathbf{x}))}{2} + \alpha(\Pi(\mathbf{x}), \Pi(\mathbf{y})) (\mathbf{f}(\Pi(\mathbf{y})) - \mathbf{f}(\Pi(\mathbf{x}))) \right), \quad (59)$$

with $z = (\mathbf{x} + \mathbf{y})/2$ and

$$\alpha(\Pi(\mathbf{x}), \Pi(\mathbf{y})) = \frac{\tilde{C}_f(\Pi(\mathbf{y}), \Pi(\mathbf{x})) + \tilde{D}_f(\Pi(\mathbf{y}), \Pi(\mathbf{x}))}{\langle \mathbf{f}(\Pi(\mathbf{y})) - \mathbf{f}(\Pi(\mathbf{x})), \Pi(\mathbf{y}) - \Pi(\mathbf{x}) \rangle}. \quad (60)$$

3.5 Interpretation of the conservative algorithmic force

There exist infinite second order accurate approximations of the midpoint force that lead to energy and momentum conserving discretizations [20]. A general expression for the algorithmic force that is in agreement with the definition of the discrete derivative is given by

$$\mathbf{f}_{\mathfrak{G}}(\mathbf{x}, \mathbf{y}) = f\left(\frac{\mathbf{x} + \mathbf{y}}{2}\right) + \frac{\hat{C}_f(\mathbf{x}, \mathbf{y})}{\|\mathbf{y} - \mathbf{x}\|_{\mathfrak{G}^{-1}}^2} \mathfrak{G}^{-1}(\mathbf{y} - \mathbf{x}), \quad (61)$$

where \mathfrak{G} is the matrix representation of a suitable metric tensor and its associated conservation function is

$$\hat{C}_f(\mathbf{x}, \mathbf{y}) = [V(\mathbf{y}) - V(\mathbf{x})] - \langle \mathbf{f}_m, \mathbf{y} - \mathbf{x} \rangle. \quad (62)$$

As shown in [20], the choice of the metric tensor in Eq. (61) is crucial, since a wrong choice can destroy the accuracy of the solution even when the directionality and consistency properties are verified. The general expression can be reduced to the original formula proposed in [6] just by adopting the standard Euclidean metric tensor, i.e.,

$$\mathbf{f}_I(\mathbf{x}, \mathbf{y}) = f\left(\frac{\mathbf{x} + \mathbf{y}}{2}\right) + \frac{\hat{C}_f(\mathbf{x}, \mathbf{y})}{\|\mathbf{y} - \mathbf{x}\|_I^2} (\mathbf{y} - \mathbf{x}). \quad (63)$$

Until now, this original formula has been regarded as the optimal one from the implementation point of view. By visual inspection of Eq. (42), it is also possible to claim that the formula derived in this work is as easy to implement as the original one given in Eq. (63). Moreover, the new formula requires only evaluations at the endpoints of the time interval and not at the midpoint.

Next, we would like to analyze the formula (42) in terms of the general expression provided by Eq. (61). First, defining \mathbf{z} to be the average $\mathbf{z} = (\mathbf{x} + \mathbf{y})/2$, we make use of Taylor’s theorem to compute

$$\begin{aligned} f(\mathbf{x}) &= f(\mathbf{z}) - \frac{1}{2} Df \cdot (\mathbf{y} - \mathbf{x}) + \frac{1}{4} D^2 f \cdot ((\mathbf{y} - \mathbf{x}), (\mathbf{y} - \mathbf{x})) \\ &\quad - \frac{1}{8} D^3 f \cdot ((\mathbf{y} - \mathbf{x}), (\mathbf{y} - \mathbf{x}), (\mathbf{y} - \mathbf{x})) + \mathcal{O}(\|\mathbf{y} - \mathbf{x}\|^4) \end{aligned} \quad (64)$$

and

$$\begin{aligned} f(\mathbf{y}) &= f(\mathbf{z}) + \frac{1}{2} Df \cdot (\mathbf{y} - \mathbf{x}) + \frac{1}{4} D^2 f \cdot ((\mathbf{y} - \mathbf{x}), (\mathbf{y} - \mathbf{x})) \\ &\quad + \frac{1}{8} D^3 f \cdot ((\mathbf{y} - \mathbf{x}), (\mathbf{y} - \mathbf{x}), (\mathbf{y} - \mathbf{x})) + \mathcal{O}(\|\mathbf{y} - \mathbf{x}\|^4). \end{aligned} \quad (65)$$

The averaged force can be expressed as

$$\frac{f(\mathbf{x}) + f(\mathbf{y})}{2} = f(\mathbf{z}) + \mathcal{O}(\|\mathbf{y} - \mathbf{x}\|^2) \quad (66)$$

and

$$\left\langle \frac{f(\mathbf{x}) + f(\mathbf{y})}{2}, \mathbf{y} - \mathbf{x} \right\rangle = \langle f(\mathbf{z}), \mathbf{y} - \mathbf{x} \rangle + \mathcal{O}(\|\mathbf{y} - \mathbf{x}\|^3). \quad (67)$$

The force jump can be written as

$$f(\mathbf{y}) - f(\mathbf{x}) = \langle Df, \mathbf{y} - \mathbf{x} \rangle + \mathcal{O}(\|\mathbf{y} - \mathbf{x}\|^3), \quad (68)$$

and

$$\begin{aligned} \langle f(\mathbf{y}) - f(\mathbf{x}), \mathbf{y} - \mathbf{x} \rangle &= \left\langle \mathbf{y} - \mathbf{x}, D^2 V(\mathbf{z})(\mathbf{y} - \mathbf{x}) \right\rangle + \mathcal{O}(\|\mathbf{y} - \mathbf{x}\|^4) \\ &= \left\langle \mathbf{y} - \mathbf{x}, D^2 V(\mathbf{x})(\mathbf{y} - \mathbf{x}) \right\rangle + \mathcal{O}(\|\mathbf{y} - \mathbf{x}\|^3). \end{aligned} \quad (69)$$

Now putting everything together, we can rewrite Eq.(42) as

$$\begin{aligned} \mathbf{f}^{\text{cons}} &= f(\mathbf{z}) + \frac{V(\mathbf{y}) - V(\mathbf{x}) - \langle f(\mathbf{z}), \mathbf{y} - \mathbf{x} \rangle}{\langle \mathbf{y} - \mathbf{x}, D^2 V(\mathbf{x})(\mathbf{y} - \mathbf{x}) \rangle} D^2 V(\mathbf{x})(\mathbf{y} - \mathbf{x}) \\ &\quad + \mathcal{O}(\|\mathbf{y} - \mathbf{x}\|^2). \end{aligned} \quad (70)$$

Taking a look at this expression, it is apparent that the discrete force (42) is a second order perturbation of the midpoint approximation and that the metric employed for the definition of the conserving correction is just

$$\mathfrak{G} = (D^2 V(\mathbf{x}))^{-1}. \quad (71)$$

We conclude that the an integration scheme based on Eq. (27) would behave locally in a very similar manner to a method based on Eq. (61) with metric (71). Their global behavior can, in general, differ.

3.6 Dissipative algorithmic velocity

As proposed in [9,31], the generalized velocity can also be expressed as the linear combination of a conservative and a dissipative component. If the mass matrix is configuration-independent, the midpoint rule provides precisely the conservative part of the velocity. Following the ideas adopted for the formulation of the dissipative part of the algorithmic force, we find next the smallest perturbation of the midpoint velocity that guarantees dissipation according to a given dissipation function $\tilde{\mathcal{D}}_s(\mathbf{u}, \mathbf{v})$, which must be non-negative, at least second order accurate in $\|\mathbf{v} - \mathbf{u}\|$, and tend to 0 as \mathbf{u} tends to \mathbf{v} .

According to the midpoint rule, the conservative part of the algorithmic velocity can be expressed as

$$\mathbf{s}^{\text{cons}} = \frac{\mathbf{u} + \mathbf{v}}{2} = \mathbf{w}, \quad (72)$$

where the velocity \mathbf{u} corresponds to time instant t_n , the velocity \mathbf{v} corresponds to time instant t_{n+1} and \mathbf{w} is the averaged velocity. This particular choice preserves linear and angular momenta. The preservation of energy is guaranteed when the relation

$$\langle \mathbf{s}^{\text{cons}}, \mathbf{M}(\mathbf{v} - \mathbf{u}) \rangle = T(\mathbf{v}) - T(\mathbf{u}) \quad (73)$$

is satisfied, with T being the kinetic energy. Equivalently, this expression can be obtained from $\langle \delta \mathbf{s}_{n+1/2}, \boldsymbol{\pi}(\mathbf{s}^{\text{cons}}) \rangle = T(\mathbf{v}) - T(\mathbf{u})$ when the variation is of the form $\delta \mathbf{s}_{n+1/2} = \mathbf{v} - \mathbf{u}$. It is apparent that the conservative part of the algorithmic velocity adopted fulfills this condition without need for further corrections.

Now we follow an idea that is slightly different to the one previously used to derive the dissipative part of the algorithmic force. Henceforth, let us assume the existence of a dissipative part of the algorithmic velocity proportional to \mathbf{s}^{cons} , this is

$$\mathbf{s}^{\text{diss}} = \beta^{\text{diss}} \mathbf{s}^{\text{cons}}, \quad (74)$$

where β^{diss} is a scalar to be found that must guaranteed the dissipation of energy according to a given dissipation function $\tilde{\mathcal{D}}_s(\mathbf{u}, \mathbf{v})$. This scalar can be obtained as the minimizer of

$$\frac{1}{2} \|\mathbf{s}^{\text{diss}}\|_{\mathbf{M}}^2 \quad (75)$$

subject to $\langle \mathbf{s}^{\text{diss}}, \mathbf{M}(\mathbf{v} - \mathbf{u}) \rangle - \tilde{\mathcal{D}}_s(\mathbf{u}, \mathbf{v}) = 0$,

where \mathbf{M} is the mass matrix. Equation (75) defines a quadratic program with linear constraints. Its solution can be interpreted as the smallest non-conservative velocity perturbation that satisfies for a discrete variation of the form $\delta \mathbf{s}_{n+1/2} = \mathbf{v} - \mathbf{u}$, an energy dissipation according to the adopted rule. The associated Lagrangian function of the optimization problem is

$$\begin{aligned} \mathcal{L}(\beta^{\text{diss}}, \mu^{\text{diss}}) &= \frac{1}{2} \|\mathbf{s}^{\text{diss}}\|_{\mathbf{M}}^2 + \mu^{\text{diss}} (\langle \mathbf{s}^{\text{diss}}, \mathbf{M}(\mathbf{v} - \mathbf{u}) \rangle - \tilde{\mathcal{D}}_s(\mathbf{u}, \mathbf{v})), \end{aligned} \quad (76)$$

where μ^{diss} is a Lagrange multiplier that enforces the dissipation constraint. To formulate the stationarity condition, the variation of the associated Lagrangian function has to be computed. This procedure yields

$$\delta \mathcal{L}(\beta^{\text{diss}}, \mu^{\text{diss}}) = \langle \delta \mathbf{s}^{\text{diss}}, \mathbf{M} \mathbf{s}^{\text{diss}} + \mu^{\text{diss}} \mathbf{M}(\mathbf{v} - \mathbf{u}) \rangle$$

$$+ \delta \mu^{\text{diss}} (\langle \mathbf{s}^{\text{diss}}, \mathbf{M}(\mathbf{v} - \mathbf{u}) \rangle - \tilde{\mathcal{D}}_s(\mathbf{u}, \mathbf{v})). \quad (77)$$

Noting that $\delta \mathbf{s}^{\text{diss}} = \delta \beta^{\text{diss}} \mathbf{s}^{\text{cons}}$, the stationarity condition of the Lagrangian can be written explicitly as

$$\begin{pmatrix} A_{11}^s & A_{12}^s \\ A_{12}^s & 0 \end{pmatrix} \begin{bmatrix} \beta^{\text{diss}} \\ \mu^{\text{diss}} \end{bmatrix} = \begin{bmatrix} 0 \\ b_2^{s, \text{diss}} \end{bmatrix}, \quad (78)$$

with

$$A_{11}^s = 2T(\mathbf{w}), \quad (79)$$

$$A_{12}^s = T(\mathbf{v}) - T(\mathbf{u}), \quad (80)$$

and

$$b_2^{s, \text{diss}} = \tilde{\mathcal{D}}_s(\mathbf{u}, \mathbf{v}). \quad (81)$$

The solution of this linearly constrained quadratic program is

$$\beta^{\text{diss}} = \frac{\tilde{\mathcal{D}}_s(\mathbf{u}, \mathbf{v})}{T(\mathbf{v}) - T(\mathbf{u})} \quad (82)$$

and

$$\mu^{\text{diss}} = -\frac{T(\mathbf{w}) \tilde{\mathcal{D}}_s(\mathbf{u}, \mathbf{v})}{(T(\mathbf{v}) - T(\mathbf{u}))^2}. \quad (83)$$

Finally, the formula for the dissipative part of the algorithmic velocity takes the following explicit form:

$$\mathbf{s}^{\text{diss}} = \frac{\tilde{\mathcal{D}}_s(\mathbf{u}, \mathbf{v})}{T(\mathbf{v}) - T(\mathbf{u})} \frac{\mathbf{v} + \mathbf{u}}{2}. \quad (84)$$

Assuming an additive composition of the algorithmic approximation of the velocity, that is,

$$\mathbf{s} = \mathbf{s}^{\text{cons}} + \mathbf{s}^{\text{diss}}, \quad (85)$$

we can write

$$\mathbf{s}(\mathbf{u}, \mathbf{v}) = \left(1 + \frac{\tilde{\mathcal{D}}_s(\mathbf{u}, \mathbf{v})}{T(\mathbf{v}) - T(\mathbf{u})} \right) \frac{\mathbf{v} + \mathbf{u}}{2}. \quad (86)$$

This formula is identical to the formula proposed in [9,31] that was derived by employing only geometric arguments. This time, it can be clearly interpreted as an optimal approximation.

3.7 Final equations

The combination of all ingredients discussed here yields the full discrete formulation of the dynamic equilibrium for non-linear mechanical systems. These consist of two residuals,

one for the generalized velocities and another for the generalized coordinates, namely,

$$\begin{bmatrix} r_s \\ r_q \end{bmatrix}_{n+1/2} = \begin{bmatrix} \pi(s_n, s_{n+1}) - p(q_n, q_{n+1}) \\ \dot{\pi}(s_n, s_{n+1}) + \mathbf{f}(q_n, q_{n+1}) - \mathbf{f}^{\text{ext}}(q_{n+1/2}) \end{bmatrix}, \tag{87}$$

where both residuals have to be minimized at every time step. This task is accomplished by means of a Newton-Raphson algorithm.

The generalized-velocity-based momentum term in its algorithmic form is

$$\pi(s_n, s_{n+1}) = \mathbf{M} \left(1 + \frac{\tilde{D}_s(s_n, s_{n+1})}{T(s_{n+1}) - T(s_n)} \right) \frac{s_{n+1} + s_n}{2}. \tag{88}$$

The generalized-coordinate-based momentum term in its discrete version becomes

$$p(q_n, q_{n+1}) = \mathbf{M} \frac{q_{n+1} - q_n}{\Delta t_n}. \tag{89}$$

The generalized-coordinate-based momentum rate term in its algorithmic form is

$$\dot{\pi}(s_n, s_{n+1}) = \mathbf{M} \frac{s_{n+1} - s_n}{\Delta t_n}. \tag{90}$$

Finally, the generalized internal force becomes

$$\begin{aligned} \mathbf{f}(q_n, q_{n+1}) &= \frac{\mathbf{f}(q_n) + \mathbf{f}(q_{n+1})}{2} \\ &+ \frac{\tilde{C}_f(q_n, q_{n+1}) + \tilde{D}_f(q_n, q_{n+1})}{\langle \mathbf{f}(q_{n+1}) - \mathbf{f}(q_n), q_{n+1} - q_n \rangle} (\mathbf{f}(q_{n+1}) - \mathbf{f}(q_n)). \end{aligned} \tag{91}$$

In the case of accommodating the preservation of linear and angular momenta, we require the G -equivariant version given by

$$\begin{aligned} \mathbf{f}^G(q_n, q_{n+1}) &= D\Pi_{n+1/2}^T \left(\frac{\mathbf{f}(\Pi_{n+1}) + \mathbf{f}(\Pi_n)}{2} \right. \\ &\left. + \alpha(\Pi_n, \Pi_{n+1})(\mathbf{f}(\Pi_{n+1}) - \mathbf{f}(\Pi_n)) \right) \end{aligned} \tag{92}$$

where

$$\alpha(\Pi_n, \Pi_{n+1}) = \frac{\tilde{C}_f(\Pi_{n+1}, \Pi_n) + \tilde{D}_f(\Pi_{n+1}, \Pi_n)}{\langle \mathbf{f}(\Pi_{n+1}) - \mathbf{f}(\Pi_n), \Pi_{n+1} - \Pi_n \rangle} \tag{93}$$

and $\Pi_n = \Pi(q_n)$. The discrete conservation function is given by

$$\begin{aligned} \tilde{C}_f(q_n, q_{n+1}) &= (V(q_{n+1}) - V(q_n)) \\ &- \left\langle \frac{\mathbf{f}(q_n) + \mathbf{f}(q_{n+1})}{2}, q_{n+1} - q_n \right\rangle, \end{aligned} \tag{94}$$

and its G -equivariant version given by

$$\begin{aligned} \tilde{C}_f^G(\Pi_n, \Pi_{n+1}) &= (V(\Pi_{n+1}) - V(\Pi_n)) \\ &- \left\langle \frac{\mathbf{f}(\Pi_n) + \mathbf{f}(\Pi_{n+1})}{2}, \Pi_{n+1} - \Pi_n \right\rangle. \end{aligned} \tag{95}$$

The most basic discrete dissipation function at the level of the generalized internal force that can be chosen is

$$\tilde{D}_f(q_n, q_{n+1}, \tilde{q}_n) = \frac{1}{2} \langle q_{n+1} - q_n, \mathbf{D}(\tilde{q}_n - q_n) \rangle, \tag{96}$$

or its G -equivariant counterpart expressed as

$$\tilde{D}_f^G(\Pi_n, \Pi_{n+1}, \tilde{\Pi}_n) = \frac{1}{2} \langle \Pi_{n+1} - \Pi_n, \mathbf{D}(\tilde{\Pi}_n - \Pi_n) \rangle, \tag{97}$$

where \tilde{q}_n could correspond to an intermediate configuration, and \mathbf{D} is constant, symmetric and positive semi-definite. The dissipation function for the velocity is of the form

$$\tilde{D}_s(s_n, s_{n+1}, \tilde{s}_n) = \frac{1}{2} \langle s_{n+1} - s_n, \mathbf{M}(\tilde{s}_n - s_n) \rangle, \tag{98}$$

or its G -equivariant version given by

$$\tilde{D}_s^G(s_n, s_{n+1}, \tilde{s}_n) = \frac{1}{2} (\|s_{n+1}\|_{\mathbf{M}} - \|s_n\|_{\mathbf{M}}) (\|\tilde{s}_n\|_{\mathbf{M}} - \|s_n\|_{\mathbf{M}}), \tag{99}$$

where \tilde{s}_n could correspond to an intermediate configuration. With this setting, unconditional stability in the nonlinear sense can be achieved. The chosen dissipation functions correspond to those proposed in [9,31] for the EDMC-1/2.

4 Numerical results

In this section, we present four numerical examples which were chosen to show the potentialities of the proposed approach. With these, we do not pretend to test the new approach exhaustively, but at rather provide some insight on its properties. For this purpose, we study first two examples involving two-mass systems with potential functions that can arise in the context of reduced-order models, and then two examples of nonlinear elastic shell structures employing a neo-Hookean material. Additionally, we briefly discuss the dissipation properties of the proposed scheme in the high-frequency range.

4.1 Reduced-order models

The first example is a mechanical system with two degrees of freedom whose potential function possesses polynomial complexity. The second one considers another mechanical system with also two degrees of freedom, but whose potential function shows non-polynomial complexity. Here, we adopt the most basic discrete dissipation functions at the level of the generalized internal force and at the level of the generalized velocity that are given by

$$\tilde{D}_f(\mathbf{q}_n, \mathbf{q}_{n+1}) = \frac{\chi_f}{2h} \|\mathbf{q}_{n+1} - \mathbf{q}_n\|_D^2, \tag{100}$$

in which D is a constant symmetric semi-positive definite matrix, and

$$\tilde{D}_s(s_n, s_{n+1}) = \frac{\chi_s}{h} \left(\sqrt{T(s_{n+1})} - \sqrt{T(s_n)} \right)^2, \tag{101}$$

where χ_f and χ_s in $\mathbb{R}_{\geq 0}$ are merely dissipation parameters. For both examples, four cases are considered: *i*) fully conservative, i.e., $\chi_f = \chi_s = 0$; *ii*) dissipative at the level of the generalized internal force, i.e., $\chi_f \neq 0$ and $\chi_s = 0$; *iii*) dissipative at the level of the generalized velocities, i.e., $\chi_f = 0$ and $\chi_s \neq 0$; and, *iv*) fully dissipative, i.e., $\chi_f \neq 0$ and $\chi_s \neq 0$. Additionally, to numerically gain some insight about the accuracy of the method, we provide for these two examples and all cases the second quotient of precision $Q_{II}(t)$ computed on the basis of the corresponding states $\xi \in W$, namely $\xi = (\mathbf{q}, s)$. The definition of $Q_{II}(t)$ is presented in the ‘‘Appendix’’.

4.1.1 Two-mass system with a polynomial potential

Here, we consider a nonlinear oscillatory mechanical system with potential function

$$V(\mathbf{q}) = \frac{1}{2} V_{ab}^{II} q^a q^b + \frac{1}{3} V_{abc}^{III} q^a q^b q^c + \frac{1}{4} V_{abcd}^{IV} q^a q^b q^c q^d. \tag{102}$$

This kind of systems naturally arises in the context of reduced-order models, see for instance [36,37]. To perform our computations, we adopt a model with two degrees of freedom used as a demonstrator in [36]. The non-zero mechanical properties are $M_{11} = M_{22} = 1$ Kg, $V_{11}^{II} = V_{22}^{II} = 16$ N/m, $V_{12}^{II} = V_{21}^{II} = -15$ N/m and $V_{1111}^{IV} = 15$ N/m³. The simulation parameters are initial time $t_i = 0$ s, final time $t_f = T$ s, simulation time $T = 50$ s, time step $\Delta t = 0.001$ s and relative iteration tolerance $\varepsilon = 10^{-10}$. Additionally, for the dissipative cases, we set $\chi_f = 0.0025$ and $\chi_s = 0.008$ as

well as $D = V^{II}$. The initial conditions employed are

$$\mathbf{q}_0 = \begin{bmatrix} 1.00000 \\ 0.91800 \end{bmatrix} \quad \text{and} \quad \mathbf{s}_0 = \begin{bmatrix} 0.00000 \\ 0.00000 \end{bmatrix}.$$

Figure 1 shows the idealized mechanical system under consideration and Fig. 2 presents a plot of the potential function, which is clearly convex within the region where the dynamics of the system takes place. Figure 3 shows different plots for the solution of the fully conservative case. We can observe the very complex and nonlinear oscillatory behavior, which is also in excellent agreement with those results presented in [36].

On the left of Figs. 4, 5, 6 and 7, the evolution of the kinetic, potential, and total energies is shown. On the right of these figures, we show the second precision quotient also as a function of time. Figure 4 evidently corresponds to the fully conservative case. Figure 5 shows the dissipative case at the level of the generalized internal forces. Figure 6 corresponds to the dissipative case at the level of the generalized velocities. Finally, Fig. 7 corresponds to the fully dissipative case. In the latter, the energy decay is larger than the two previous cases.

For all cases the second quotient of precision is almost constant and its value is approximately 4. Therefore, as expected, the numerical method is second-order accurate. According to Eq. (115), a method of a given order is unable to produce solutions with higher quotients of precision. In [38], it is stated that even if the method is correctly implemented, it is not trivial to find the right set of parameters

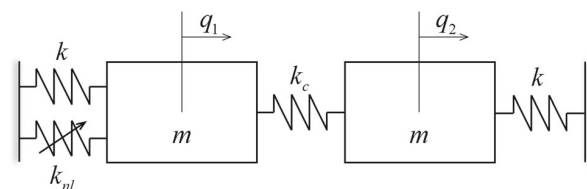


Fig. 1 Two masses connected by linear springs between two walls. The first mass is also connected to the left wall through a nonlinear spring

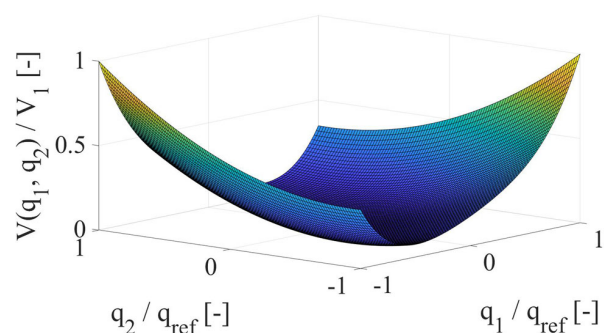


Fig. 2 Potential function with polynomial complexity

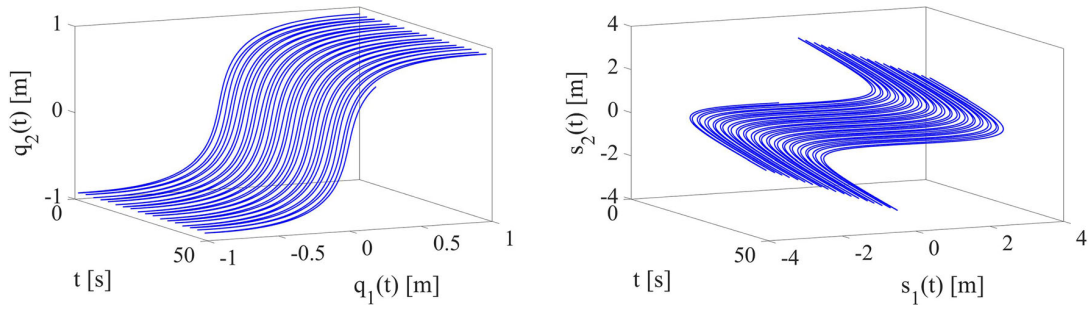


Fig. 3 Fully conservative case; extended configuration and velocity diagrams

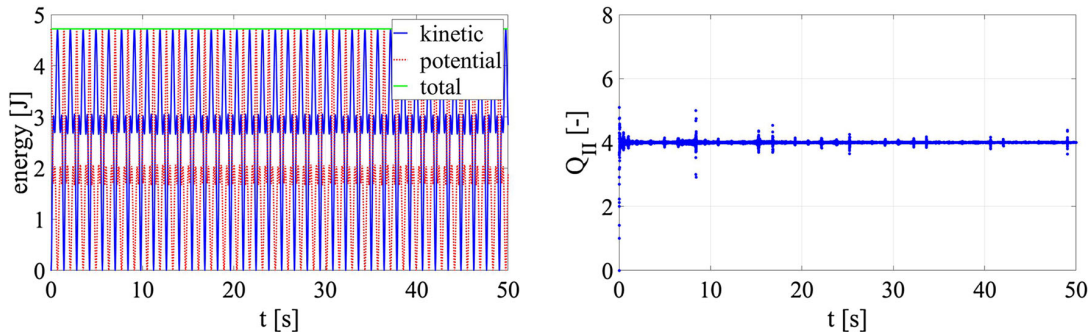


Fig. 4 Fully conservative case; energy and Q_{II}

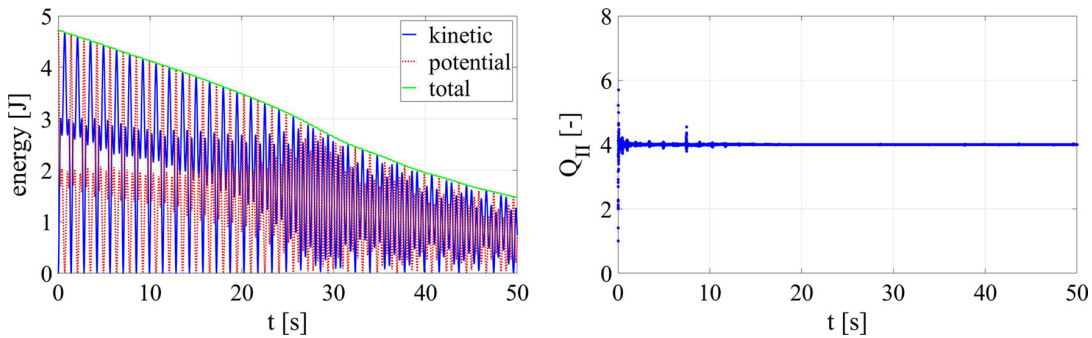


Fig. 5 Dissipative case at the level of internal forces; energy and Q_{II}

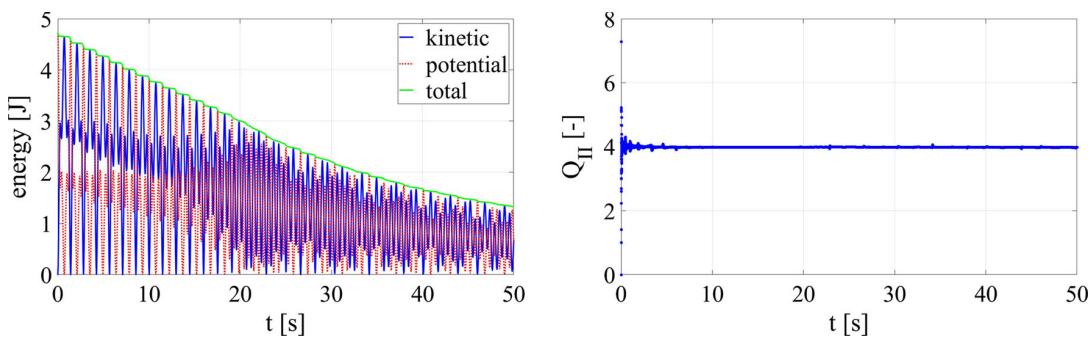


Fig. 6 Dissipative case at the level of generalized velocities; energy and Q_{II}

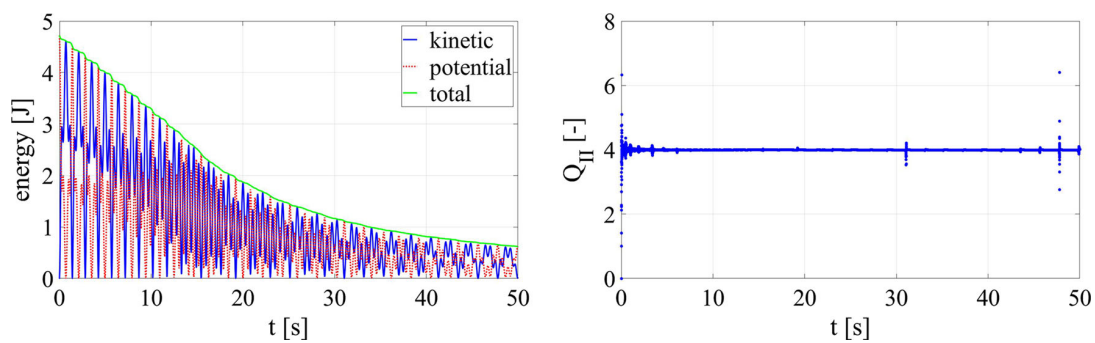


Fig. 7 Fully dissipative case; energy and Q_{II}

in order to numerically obtain precision quotients of a high quality like the one presented herein.

4.1.2 Two-mass system with a non-polynomial potential

Next, we consider a nonlinear oscillatory mechanical system whose potential function is

$$V(\mathbf{q}) = \frac{1}{2} \left[V_{ab}^{II} + \frac{V_{ab}^N}{(1 + V_{ab}^D q^a q^b)^n} \right] q^a q^b, \quad (103)$$

in which the conditions $V_{ab}^{II} = V_{ba}^{II}$, $V_{ab}^N = V_{ba}^N$ and $V_{ab}^D = V_{ba}^D$ are used for the sake of simplicity. This kind of systems could arise in the context of Euler-Bernoulli beams [39,40] or for structures with softening behavior [41].

To perform our computations, we adopt a model with two degrees of freedom. The non-zero constants of the model are $M_{11} = M_{22} = 1$ Kg, $V_{11}^{II} = V_{22}^{II} = 10$ N/m, $V_{11}^N = V_{22}^N = -V_{12}^N = -V_{21}^N = 300$ N/m, $V_{11}^D = V_{22}^D = -V_{12}^D = -V_{21}^D = 5$ N/m² and $n = 3$.

The simulation parameters are initial time $t_i = 0$ s, final time $t_f = T$ s, simulation time $T = 50$ s, time step $\Delta t = 0.0001$ s, and relative iteration tolerance $\varepsilon = 10^{-10}$. Additionally, for the dissipative cases, we set $\chi_f = 0.001$ and $\chi_s = 0.001$ as well as $\mathbf{D} = \mathbf{V}^{II}$. The initial conditions employed are

$$\mathbf{q}_0 = \begin{bmatrix} -0.41726 \\ -0.49840 \end{bmatrix} \quad \text{and} \quad \mathbf{s}_0 = \begin{bmatrix} -2.53182 \\ -2.79761 \end{bmatrix}.$$

Figure 8 shows the idealized mechanical system under consideration and Fig. 9 depicts the potential function, which is clearly non-convex within the region where the dynamics of the system takes place, see Fig. 10. This feature pushes the numerical method to its limits. On the left of Figs. 11, 12, 13 and 14 the kinetic, potential and total energies are plotted. On their right, these show the second precision quotient also as a function of time. Figure 11 depicts the energies in the conserving solution. Figures 12 and 13 plot the ener-

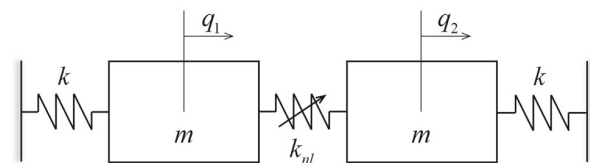


Fig. 8 Nonlinear system with two masses connected by linear springs to two walls. Both masses are connected to each other by a nonlinear spring

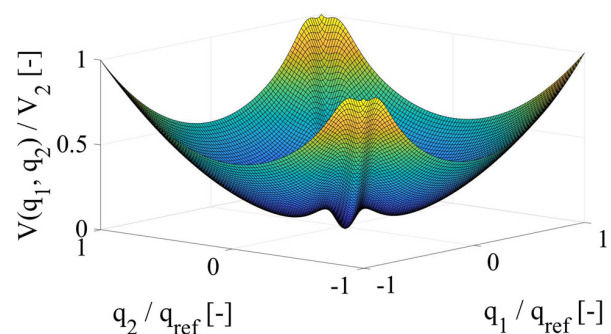


Fig. 9 Potential function with non-polynomial complexity

gies when dissipation is introduced in the internal forces and generalized velocities, respectively. Last, Fig. 14, provides the results obtained when both dissipation functions are employed, resulting in a larger dissipation of energy. In all cases, the second quotient of precision is very close to 4 for all time, confirming the second order accuracy of the method in all the simulations.

4.2 Finite elasticity models

Here we analyze two finite elasticity models. The first one is a tumbling cylinder and the second one is a free-flying, single-layer, shell. In both cases, the spatial discretizations are based on a four-node shell element [34,42], i.e., an extensible-director-based solid-degenerate shell model, in which the shear locking and the artificial thickness strains are controlled

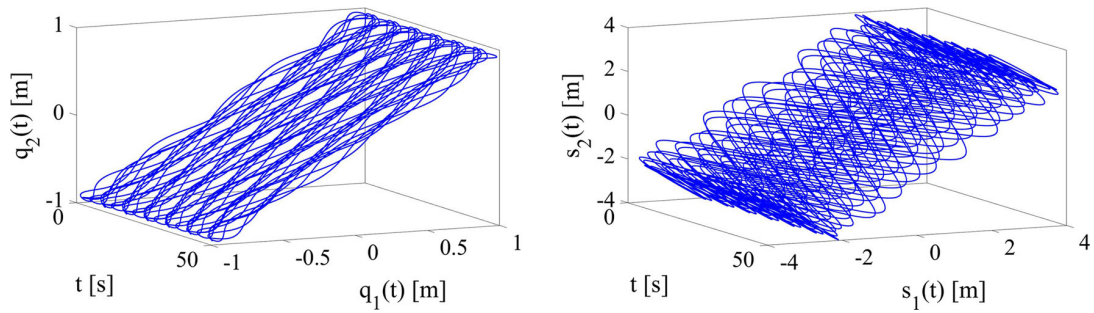


Fig. 10 Fully conservative case; extended configuration and velocity diagrams

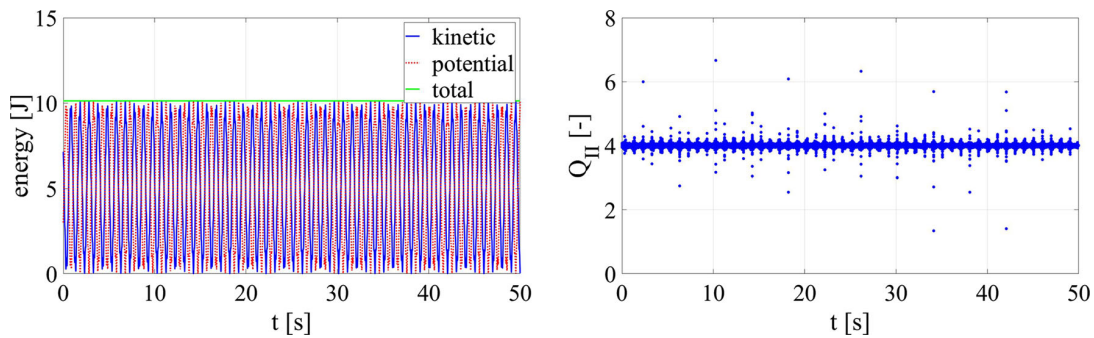


Fig. 11 Fully conservative case; energy and Q_{II}

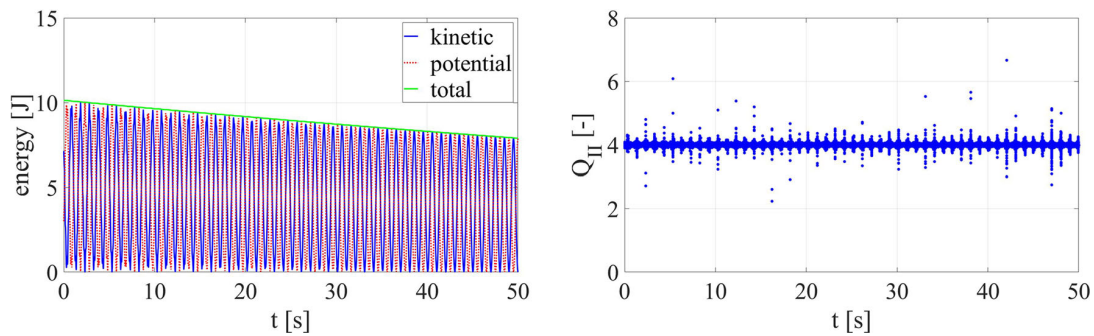


Fig. 12 Dissipative case at the level of internal forces; energy and Q_{II}

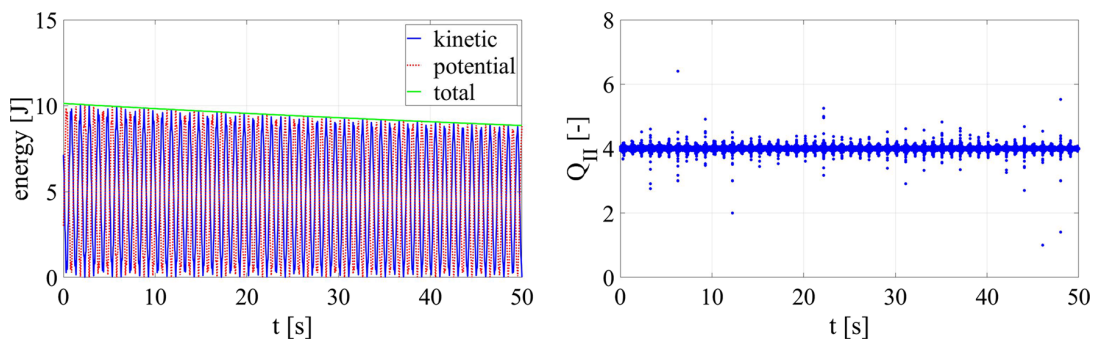


Fig. 13 Dissipative case at the level of generalized velocities; energy and Q_{II}

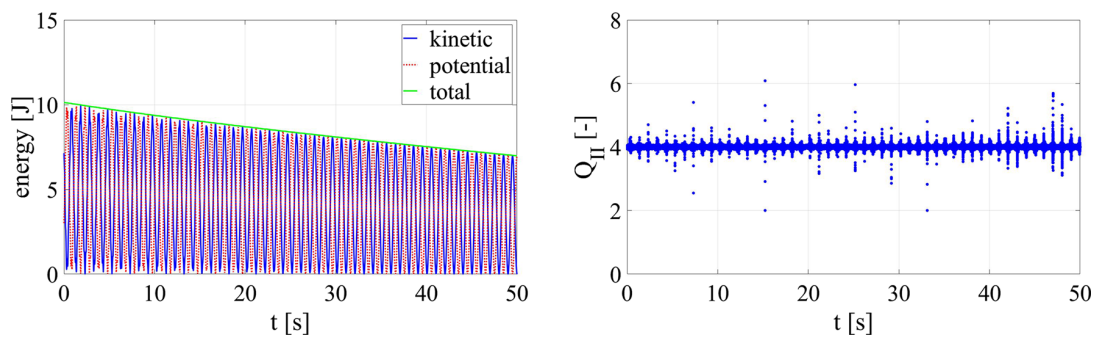


Fig. 14 Fully dissipative case; energy and Q_{II}

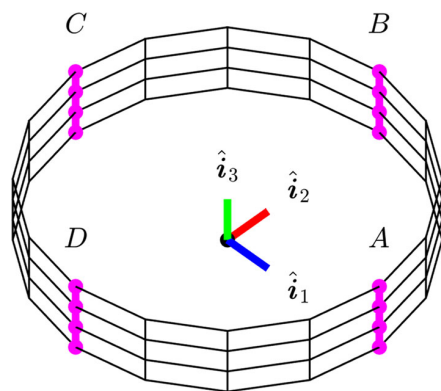


Fig. 15 Tumbling cylinder—finite element representation

Table 1 Tumbling cylinder—spatial loads per length unit in N/m

	A	B	C	D
f_1	0	1	1	0
f_2	-1	1	1	-1
f_3	-1	1	1	-1

by means of the assumed natural strain method. Also, the enhancement of the strain field in the thickness direction and the cure of the membrane locking are achieved by means of the enhanced assumed strain method. Such element allows to consider unmodified three-dimensional constitutive laws. For the current study, we adopt the neo-Hookean hyperelastic material model, whose strain energy density is given by

$$\tilde{W}(\mathbf{C}) = \frac{\lambda}{2} \log^2(J) + \frac{\mu}{2} (I_1 - 3) - \mu \log(J), \quad (104)$$

with \mathbf{C} , the right Cauchy–Green deformation tensor, $J = \sqrt{\det(\mathbf{C})}$, $I_1 = \text{trace}(\mathbf{C})$, and λ and μ are the first and second Lamé parameters, respectively.

4.2.1 Tumbling cylinder

This structure is a cylindrical shell subject to body loads with a prescribed time variation and was already investi-

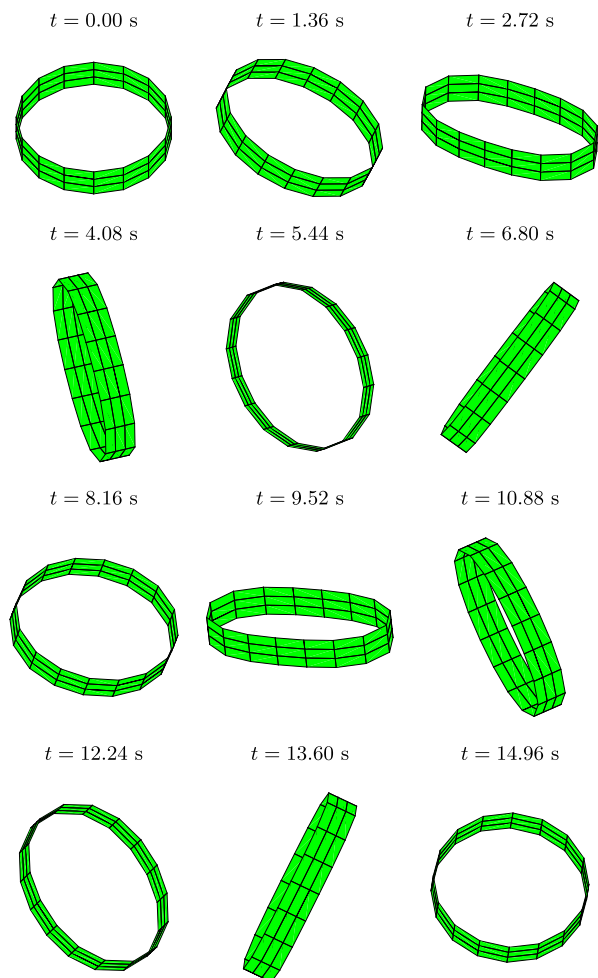


Fig. 16 Tumbling cylinder (conservative)—sequence of motion

gated, for instance, in [5,42,43] and in many other works. The geometrical and material properties are the following: mean radius 7.5 m, height 3.0 m, thickness 0.02 m, first Lamé parameter 80 MPa, second Lamé parameter 80 MPa and mass density per volume unit 1.0 Kg/m³. The cylinder is dis-

Table 2 Tumbling cylinder—stationary values

$t > t_{load}$ (1.0 s)	l_1 (Kg m/s)	l_2 (Kg m/s)	l_3 (Kg m/s)	j_1 (Kg m ² /s)	j_2 (Kg m ² /s)	j_3 (Kg m ² /s)	$T + V$ (J)
Cons.	20.00000	0.00000	0.00000	122.00960	147.20774	− 178.26475	445.22767
Diss.	20.00000	0.00000	0.00000	121.62771	147.28455	− 178.14972	−

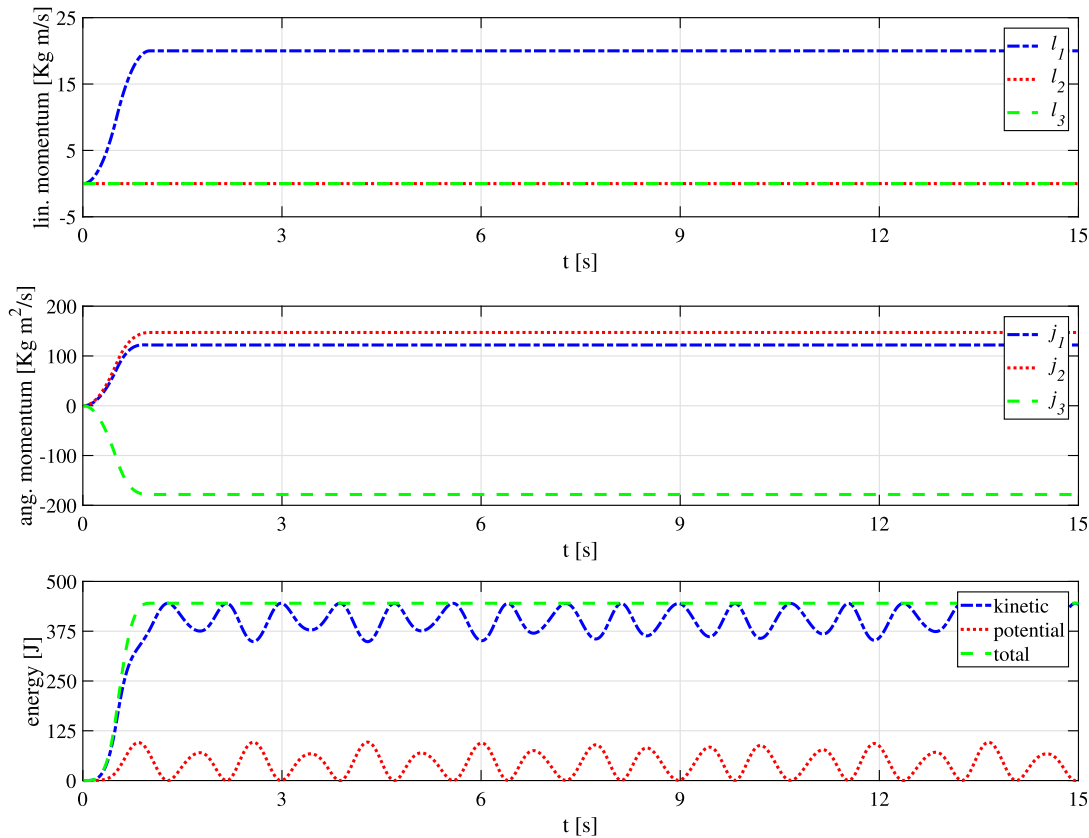


Fig. 17 Tumbling cylinder (conservative)—momenta and energy

cretized with 48 elements, in which 16 elements are located along the circumference and 3 elements along the height. The total number of nodes is 60. Moreover, no kinematic boundary conditions are enforced. For the dissipative case we set $\chi = 0.25$. Figure 15 shows the finite element model of the tumbling cylinder. Additionally, the line segments *A*, *B*, *C* and *D*, to which the spatial loads are applied, are indicated in magenta. Table 1 presents the values for the loads that are applied to the structure. The loads are then multiplied with a function that describes the variation of the applied force over the time, which is defined in Eq. (105). Then $f_0^{ext} = f_1\hat{i}^1 + f_2\hat{i}^2 + f_3\hat{i}^3$ and $f^{ext}(t) = f(t)f_0^{ext}$, in which the last expression is the applied load.

$$f(t) = \begin{cases} 10t & \text{for } 0 \leq t < 0.5 \\ 5 - 10t & \text{for } 0.5 \leq t < 1 \\ 0 & \text{for } t \geq 1 \end{cases} \quad (105)$$

Figure 16 shows a motion sequence for the conservative case, where the original configuration is located at the upper-left corner of the plot, and some deformed configurations are sequentially shown from left to right and from the top to the bottom. Table 2 provides the stationary values for momenta and energy computed with the current method for both the conservative and the dissipative cases. Figure 17 shows the time history of momenta and energy for the conservative case. It can be observed that the linear momentum, angular momentum and total energy vary during the time in which the external load is active, i.e., the first 1 s. After the external loads vanish, these three quantities are identically preserved

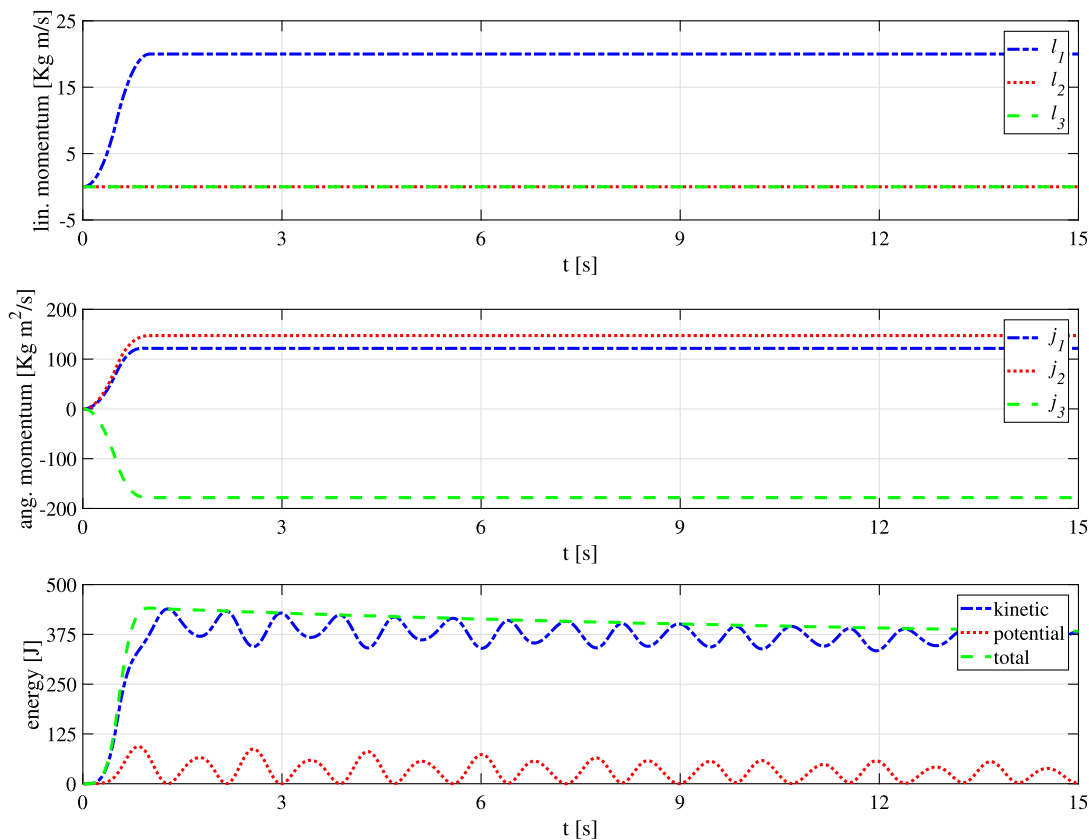


Fig. 18 Tumbling cylinder (dissipative)—momenta and energy

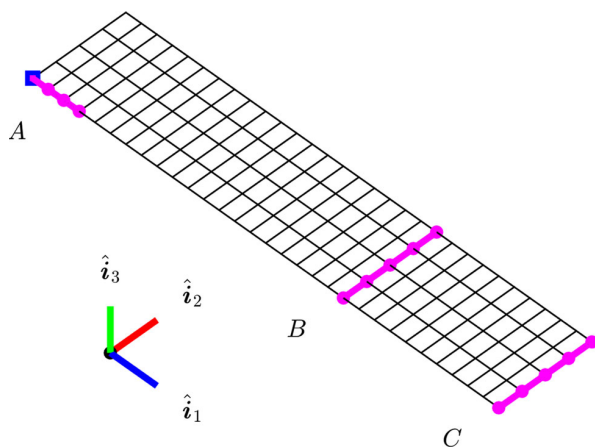


Fig. 19 Free-flying single-layer plate—finite element representation

through the time. These results confirm that the newly proposed integration scheme preserves momenta and energy. Although the total energy remains constant, the potential and kinematic energies vary in time, complementing each other in such a way that the total energy is perfectly constant. Fig-

Table 3 Free-flying single-layer plate—force density per length unit in N/m

	A	B	C
f_1	0	0	40,000
f_2	40,000	0	0
f_3	40,000	-40,000	40,000

ure 18 shows the time history of momenta and energy for the dissipative case. Clearly, the momenta is identically preserved and energy is dissipated.

4.2.2 Free-flying single-layer plate

The structure considered in this last example is a rectangular flat plate, which consisting of a single material layer, subject to spatial loads with a prescribed time variation and was considered, for example, in [26,42,44] and in many other works. The geometrical and material properties are the following: length 0.3 m, width 0.06 m, thickness 0.002 m, first Lamé parameter 0.0 Pa, second Lamé parameter 103.0 GPa and mass density per volume unit $7.3 \times 10^3 \text{ Kg/m}^3$. The plate is then discretized with 120 elements, 30 elements being

Fig. 20 Free-flying single-layer plate (conservative)—sequence of motion

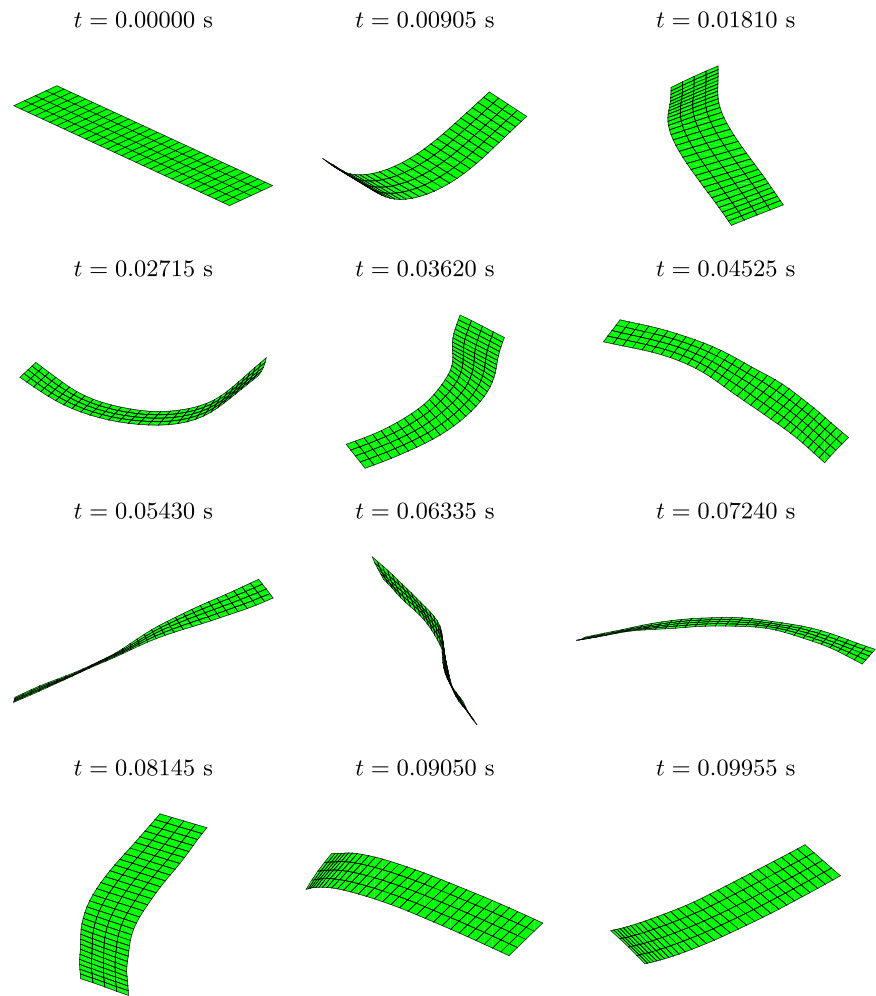


Table 4 Free-flying single-layer plate—stationary values

$t > t_{load}$ (0.004 s)	l_1 (Kg m/s)	l_2 (Kg m/s)	l_3 (Kg m/s)	j_1 (Kg m ² /s)	j_2 (Kg m ² /s)	j_3 (Kg m ² /s)	$T + V$ (J)
Cons.	4.80000	3.20000	3.20000	0.02880	− 0.38690	− 0.03596	246.53283
Diss.	4.80000	3.20000	3.20000	0.02896	− 0.38701	− 0.03597	–

located along the largest dimension and 4 elements along the smallest dimension. The total amount of nodes is 155 and for the dissipative case we set $\chi = 0.5$. Figure 19 depicts the finite element discretization of this structure. The loads are applied over the line segments *A*, *B* and *C*, indicated in magenta on the figure. The reference point for the angular momentum is indicated with the symbol \square . Table 3 gathers the values for the loads that are applied to the structure and Eq. (106) defines their scaling factor.

$$f(t) = \begin{cases} 500t & \text{for } 0 \leq t < 0.002 \\ 2 - 500t & \text{for } 0.002 \leq t < 0.004 \\ 0 & \text{for } t \geq 0.004 \end{cases} \quad (106)$$

Figure 20 shows a motion sequence for the conservative case. The linear momentum, angular momentum and energy during the simulation are constant once reached the stationary state, and their values are provided in Table 4 for both the conservative and the dissipative cases. Momenta and energy values in time are plotted in Fig. 21 for the conservative case, proving that after the removal of the force, they all remain constant. Figure 22 shows the values in time of momenta and energy for the dissipative case. Once again, momenta is perfectly preserved and energy is artificially dissipated.

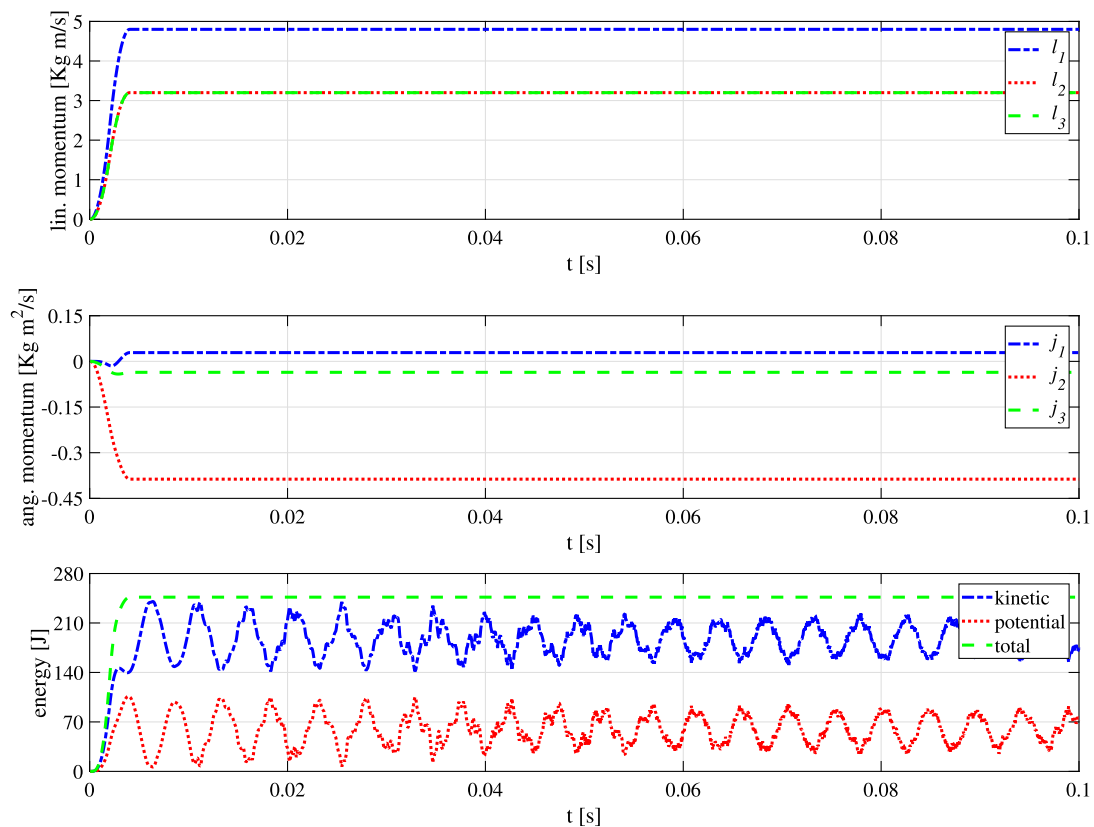


Fig. 21 Free-flying single-layer plate (conservative)—momenta and energy

4.2.3 On the dissipation properties

Dissipative schemes would be of little interest if the energy dissipation did not take place mostly in the high-frequency range. It is well-known that the dissipation of the high frequencies results in enhanced stability for the integration of stiff differential equations. Therefore, we could conclude that the only useful dissipative schemes are those that can annihilate the high-frequency content of the response without radically affecting the low frequency content of the response. In a nonlinear mechanical context, and to the best of our knowledge, there exists no dissipation function that only eliminates the high-frequency content and leaves untouched the low-frequency content. Dissipation always takes place along the whole frequency range. Moreover, there is no formal proof that the dissipation can be split in that sense for nonlinear problems and thus, we can only claim that some dissipation functions seem to be effective to address the high-frequency problem, fact that is mainly justified by experience. Further detailed analysis regarding intrinsic features of dissipation functions would fall outside the scope of the current work that addresses the derivation of a new structure preserving schema that is enriched

with the inclusion of numerical dissipation. The choice of a particular dissipation function is left to the structural analyst based on the special demands of the problem to be solved.

Keeping these limitations in mind, the free-flying single-layer plate turns to be a suitable example to show the good dissipation properties of the new proposed scheme. Figure 23, to the left, presents the amplitude spectrum based on the fast Fourier transform of the potential energy for both, the conservative and dissipative cases within the time range 0.06–0.1 s such that the direct influence of the initial transient is avoided. The subsequent analysis corresponds to the frequency range 100–2000 Hz and to the energy amplitude range 0–20 J. Figure 23, to the right, presents the same information, but for the energy amplitude range 0–2 J. Clearly, the dissipative algorithm works very effectively beyond 600 Hz. For the kinetic energy, Fig. 24, to the left and to the right, shows almost identical dissipative properties. Up to 600 Hz, even if slightly different due to some dissipation within 200–210 Hz, the behavior for the conservative and dissipative cases looks similar. Thus, we can claim that the proposed scheme seems to have very interesting dissipation properties.

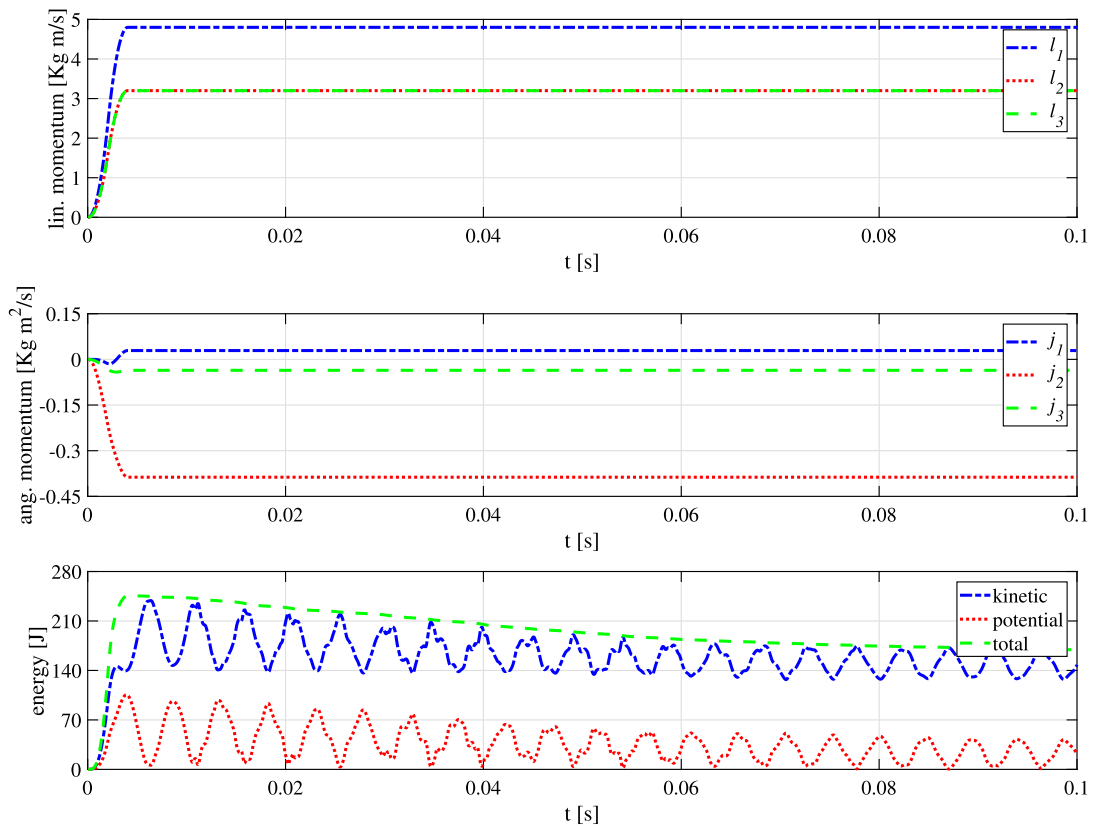


Fig. 22 Free-flying single-layer plate (dissipative)—momenta and energy

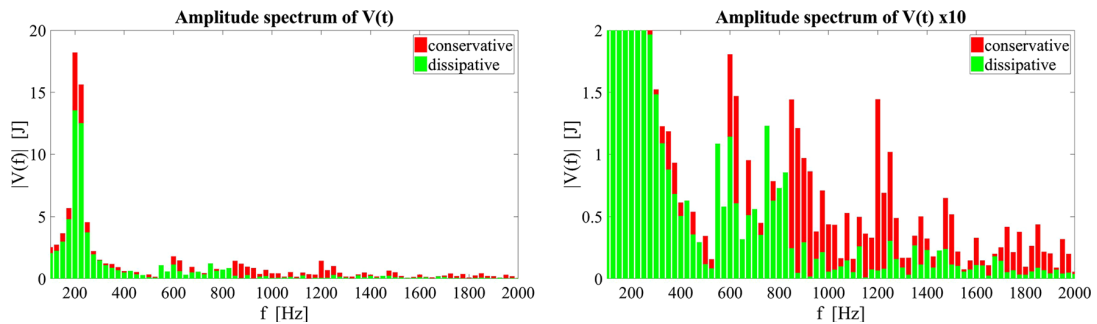


Fig. 23 Effectiveness of the dissipative scheme at the potential energy level

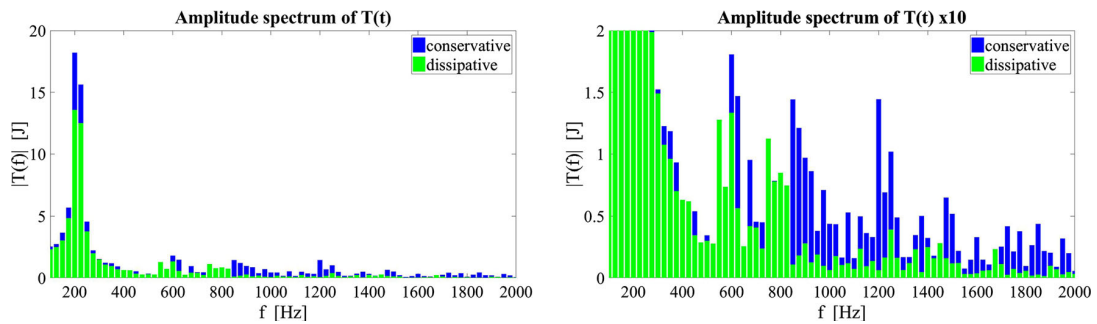


Fig. 24 Effectiveness of the dissipative scheme at the kinetic energy level

5 Concluding remarks

We considered the conservative/dissipative time integration in the context of nonlinear mechanical systems. A systematic approach to derive algorithmic internal forces and generalized velocities that ensure the preservation or the controlled dissipation of energy was presented. As a main concrete result, we proposed a new second-order formula for the algorithmic internal forces. Moreover, this formula was investigated from a geometric point of view and also interpreted for the fully conservative case in terms of a general approach available in the literature.

In contrast with conservative/dissipative methods available in the literature and based on the midpoint rule, the proposed formulas are perturbations of averaged evaluations, and thus not equivalent to existing ones.

The proposed methods are able to preserve the total energy of conservative equations, or add artificial dissipation in a controllable fashion, while preserving, in both cases, the linear and angular momenta of the system. Numerical tests verify all the previous assertions.

The proposed methods could be extended to integrate differential-algebraic equations or to include consistently dissipation functions involving derivatives with fractional orders, among others. The reformulation in the context of polyconvex large strain elasticity as well as of Lie Groups may yield interesting results. Beyond that, rigorous mathematical proofs on the robustness are still necessary.

Acknowledgements Cristian Guillermo Gebhardt and Raimund Rolfes acknowledge the financial support of the Lower Saxony Ministry of Science and Culture (research project *ventus efficiens*, FKZ ZN3024) and the German Federal Ministry for Economic Affairs and Energy (research project *Deutsche Forschungsplattform für Windenergie*, FKZ 0325936E) that enabled this work.

A Precision quotient

It is very useful to have means for checking the correctness of integration algorithms during their development and implementation. Therefore, we introduce here two tests that can be applied once an integration scheme has been numerically implemented. According to Kreiss and Ortiz [38], the numerical solution of an initial value problem can be expanded as

$$\begin{aligned} \xi(t, h, k) &= \xi(t) + \left(\frac{h}{k}\right) \psi_1(t) + \left(\frac{h}{k}\right)^2 \psi_2(t) + \dots \\ &\quad + \left(\frac{h}{k}\right)^n \psi_n(t) + \mathcal{O}(h^{n+1}), \end{aligned} \quad (107)$$

where $\xi(t)$ is the exact solution of the given initial value problem and ψ_i for $i = 1, \dots, n$ are smooth functions of the time t that do not depend on the reference time step h .

A positive integer number k allows to define finer solutions based on the original resolution given by the time step h that are necessary to compute precision coefficients, a tool that may be very effective to check the correctness of a running program.

A first precision quotient can be defined as

$$Q_I(t) = \frac{\|\xi(t, h, 1) - \xi(t)\|}{\|\xi(t, h, 2) - \xi(t)\|}, \quad (108)$$

where the numerator is computed as

$$\|\xi(t, h, 1) - \xi(t)\| = \left(\frac{h}{1}\right)^n \|\psi_n(t)\| + \mathcal{O}(h^{n+1}), \quad (109)$$

and the denominator is given by

$$\|\xi(t, h, 2) - \xi(t)\| = \left(\frac{h}{2}\right)^n \|\psi_n(t)\| + \mathcal{O}(h^{n+1}). \quad (110)$$

It is possible to show that for sufficiently small time steps, the first precision quotient can be directly approximated by 2^n , where n denotes the order of accuracy of the integration method, namely

$$Q_I(t) = \frac{\left(\frac{h}{1}\right)^n \|\psi_n(t)\| + \mathcal{O}(h^{n+1})}{\left(\frac{h}{2}\right)^n \|\psi_n(t)\| + \mathcal{O}(h^{n+1})} = 2^n + \mathcal{O}(h^{n+1}) \approx 2^n. \quad (111)$$

The main issue with this definition is that the exact solution of the initial value problem is required and, in general, is not available, especially in the context of mechanical systems involving nonlinear constitutive relations. To circumvent this drawback, it is possible to define a second precision quotient as

$$Q_{II}(t) = \frac{\|\xi(t, h, 1) - \xi(t, h, 2)\|}{\|\xi(t, h, 2) - \xi(t, h, 4)\|}, \quad (112)$$

where the numerator is computed as

$$\begin{aligned} &\|\xi(t, h, 1) - \xi(t, h, 2)\| \\ &= \left\| \left(\frac{h}{1}\right)^n \psi_n(t) - \left(\frac{h}{2}\right)^n \psi_n(t) + \mathcal{O}(h^{n+1}) \right\| \\ &= \left(\frac{2^n - 1}{2^n}\right) h^n \|\psi_n(t)\| + \mathcal{O}(h^{n+1}) \end{aligned} \quad (113)$$

and the denominator is given by

$$\begin{aligned} &\|\xi(t, h, 2) - \xi(t, h, 4)\| \\ &= \left\| \left(\frac{h}{2}\right)^n \psi_n(t) - \left(\frac{h}{4}\right)^n \psi_n(t) + \mathcal{O}(h^{n+1}) \right\| \\ &= \left(\frac{2^n - 1}{4^n}\right) h^n \|\psi_n(t)\| + \mathcal{O}(h^{n+1}). \end{aligned} \quad (114)$$

Notice that this concept removes intrinsically the need for the exact solution of the considered initial value problem. Once again, it is possible to show that for sufficiently small time steps, the second precision quotient can be approximated by 2^n as well as in the case of the first precision quotient, namely

$$Q_{II}(t) = \frac{\left(\frac{2^n-1}{2^n}\right) h^n \|\psi_n(t)\| + \mathcal{O}(h^{n+1})}{\left(\frac{2^n-1}{4^n}\right) h^n \|\psi_n(t)\| + \mathcal{O}(h^{n+1})} = 2^n + \mathcal{O}(h^{n+1}) \approx 2^n. \quad (115)$$

For the integration scheme considered in this work (an energy-conservative/dissipative method), accuracy of second order can be guaranteed, meaning that $\log_2[Q_I(t)] \approx 2$ and $\log_2[Q_{II}(t)] \approx 2$. Let us note that for the calculation of precision quotients, h has to be chosen small enough, and the choice may vary from case to case. In addition, if $\|\psi_n(t)\|$ is very small, both tests may fail even if the implementation is right. For this reason it is sometime necessary to experiment with several initial conditions and time step sizes in order to achieve correct pictures. As a general rule, the quotients of accuracy show better performance when the trajectories are periodic or quasi-periodic.

References

- Arnold VI (1989) *Mathematical methods of classical mechanics*. Springer, Berlin
- Hairer E, Lubich C, Wanner G (2006) *Geometric numerical integration*, 2nd edn. Springer, Berlin
- Stuart AM, Humphries AR (1996) *Dynamical systems and numerical analysis*. Cambridge University Press, Cambridge
- Simo JC, Tarnow N (1992) The discrete energy-momentum method. Conserving algorithms for nonlinear elastodynamics. *Z Angew Math Phys* 43:757–792
- Simo JC, Tarnow N (1994) A new energy and momentum conserving algorithm for the non-linear dynamics of shells. *Int J Numer Methods Eng* 37:2527–2549
- Gonzalez O (1996) Time integration and discrete Hamiltonian systems. *J Nonlinear Sci* 6:449–467
- Kane C, Marsden JE, Ortiz M (1999) Symplectic-energy-momentum preserving variational integrators. *J Math Phys* 40:3353–3371
- McLachlan RI, Quispel GRW, Robideux N (1999) Geometric integration using discrete gradients. *Philos Trans Math Phys Eng Sci* 357:1021–1045
- Armero F, Romero I (2001) On the formulation of high-frequency dissipative time-stepping algorithms for nonlinear dynamics. Part I: low-order methods for two model problems and nonlinear elastodynamics. *Comput Methods Appl Mech Eng* 190:2603–2649
- Marsden JE, West M (2001) Discrete mechanics and variational integrators. *Acta Numer* 10:357–514
- Simo JC, Tarnow N, Doblaré M (1995) Non-linear dynamics of three-dimensional rods: exact energy and momentum conserving algorithms. *Int J Numer Methods Eng* 38:1431–1473
- Romero I, Armero F (2002) An objective finite element approximation of the kinematics of geometrically exact rods and its use in the formulation of an energy-momentum conserving scheme in dynamics. *Int J Numer Methods Eng* 54:1683–1716
- Armero F, Petocz E (1998) Formulation and analysis of conserving algorithms for frictionless dynamic contact/impact problems. *Comput Methods Appl Mech Eng* 158:269–300
- Goicolea JM, García Orden JC (2000) Dynamic analysis of rigid and deformable multibody systems with penalty methods and energy-momentum schemes. *Comput Methods Appl Mech Eng* 188:789–804
- Betsch P, Hesch C, Sängler N, Uhlar S (2010) Variational integrators and energy-momentum schemes for flexible multibody dynamics. *J Comput Nonlinear Dyn* 5:031001-1–031001-11
- Gonzalez O (2000) Exact energy-momentum conserving algorithms for general models in nonlinear elasticity. *Comput Methods Appl Mech Eng* 190:1763–1783
- Laursen TA, Meng XN (2001) A new solution procedure for application of energy-conserving algorithms to general constitutive models in nonlinear elastodynamics. *Comput Methods Appl Mech Eng* 190:6300–6309
- Gotusso L (1985) On the energy theorem for the Lagrange equations in the discrete case. *Appl Math Comput* 17:129–136
- Itoh T, Abe K (1988) Hamiltonian-conserving discrete canonical equations based on variational difference quotients. *J Comput Phys* 76:85–102
- Romero I (2012) An analysis of the stress formula for energy-momentum methods in nonlinear elastodynamics. *Comput Mech* 50:603–610
- Harten A, Lax B, Leer P (1983) On upstream differencing and Godunov-type schemes for hyperbolic conservation laws. *SIAM Rev* 25:35–61
- French DA, Schaeffer JW (1990) Continuous finite element methods which preserve energy properties for nonlinear problems. *Appl Math Comput* 39:271–295
- Groß M, Betsch P, Steinmann P (2005) Conservation properties of a time fe method. Part IV: higher order energy and momentum conserving schemes. *Int J Numer Methods Eng* 63:1849–1897
- Betsch P, Janz A, Hesch C (2018) A mixed variational framework for the design of energy-momentum schemes inspired by the structure of polyconvex stored energy functions. *Comput Methods Appl Mech Eng* 335:660–696
- García Orden JC (2018) Energy and symmetry-preserving formulation of nonlinear constraints and potential forces in multibody dynamics. *Nonlinear Dyn* 95:823–837
- Kuhl D, Ramm E (1996) Constraint energy momentum algorithm and its application to nonlinear dynamics of shells. *Comput Methods Appl Mech Eng* 136:293–315
- Kuhl D, Crisfield MA (1999) Energy-conserving and decaying algorithms in non-linear structural dynamics. *Int J Numer Methods Eng* 45:569–599
- Bottasso CL, Borri M (1997) Energy preserving/decaying schemes for non-linear beam dynamics using the helicoidal approximation. *Comput Methods Appl Mech Eng* 143:393–415
- Bottasso CL, Borri M, Trainelli L (2001) Integration of elastic multibody systems by invariant conserving/dissipating algorithms. II. Numerical schemes and applications. *Comput Methods Appl Mech Eng* 190:3701–3733
- Romero I (2016) High frequency dissipative integration schemes for linear and nonlinear elastodynamics. In: Betsch P (ed) *Structure-preserving integrators in nonlinear structural dynamics and flexible multibody dynamics*. Springer, Berlin, pp 1–30
- Armero F, Romero I (2001) On the formulation of high-frequency dissipative time-stepping algorithms for nonlinear dynamics. Part II: second-order methods. *Comput Methods Appl Mech Eng* 190:6783–6824
- Romero I, Armero F (2002) Numerical integration of the stiff dynamics of geometrically exact shells: an energy-dissipative momentum-conserving scheme. *Int J Numer Methods Eng* 54:1043–1086

33. Armero F, Romero I (2003) Energy-dissipative momentum-conserving time-stepping algorithms for the dynamics of nonlinear Cosserat rods. *Comput Mech* 31:3–26
34. Gebhardt CG, Hofmeister B, Hente C, Rolfes R (2019) Nonlinear dynamics of slender structures: a new object-oriented framework. *Comput Mech* 63:219–252
35. Gebhardt CG, Steinbach MC, Rolfes R (2019) Understanding the nonlinear dynamics of beam structures: a principal geodesic analysis approach. *Thin-Walled Struct* 140:357–372
36. Kerschen G, Golinval J-C, Vakakis AF, Bergman LA (2005) The method of proper orthogonal decomposition for dynamical characterization and order reduction of mechanical systems: an overview. *Nonlinear Dyn* 41:147–169
37. Jansen EL (2005) Dynamic stability problems of anisotropic cylindrical shells via simplified analysis. *Nonlinear Dyn* 39:349–367
38. Kreiss H-O, Ortiz OE (2014) Introduction to numerical methods for time dependent differential equations. Wiley, London
39. Kopmaz O, Gündoğdu O (2003) On the curvature of an Euler–Bernoulli beam. *Int J Mech Eng Educ* 31:132–142
40. Nayfeh AH, Pai PF (2008) Linear and nonlinear structural mechanics. Wiley, London
41. Ye F, Zi-Xiong G, Yi-Chao G (2018) An unconditionally stable explicit algorithm for nonlinear structural dynamics. *J Eng Mech* 144:04018034-1–04018034-8
42. Gebhardt CG, Rolfes R (2017) On the nonlinear dynamics of shell structures: combining a mixed finite element formulation and a robust integration scheme. *Thin-Walled Struct* 118:56–72
43. Betsch P, Sängner N (2009) On the use of geometrically exact shells in a conserving framework for flexible multibody dynamic. *Comput Methods Appl Mech Eng* 198:1609–1630
44. Vu-Quoc L, Tan XG (2003) Optimal solid shells for non-linear analyses of multilayer composites. II. Dynamics. *Comput Methods Appl Mech Eng* 192:1017–1059

Publisher's Note Springer Nature remains neutral with regard to jurisdictional claims in published maps and institutional affiliations.

6. Closure

6.1. Conclusions

In this work, we considered the nonlinear dynamics of beam and shell structures from a purely computational point of view. This investigation was carried out by means of the derivation and implementation of finite-element models for the discrete representation of geometrically exact beams and solid-degenerate shells. Due to its great wealth in kinematic concepts, we considered the rigid body as well. With these *canonical models*, we could study the behavior of relatively simple slender structures that are challenging enough for the purpose of showing the potentialities of the procedures proposed. The setting adopted is such that the rotational degrees of freedom were elegantly circumvented through the choice of a differential-algebraic approach, also known as multibody formalism. The unifying representation, was also consistently combined with robust integration methods, which were formulated to retain up to a certain extent the underlying mechanical features. Such integration schemes beyond preserving linear and angular momenta allow to conserve the total energy of the system, for the purely conservative case, or to artificially dissipate energy, when necessary to compute long-term responses and thus, rendering nonlinear unconditional stability. By inclusion of dissipation functions at the level of coordinates or at the level of velocities, we could investigate long-term response of structures exhibiting strong nonlinear behavior.

Among the original contributions, we can highlight the following ones: *i*) a director-based finite-element formulation to investigate the nonlinear dynamics of geometrical exact beams with general cross-section properties; *ii*) a director-based finite-element formulation to investigate the nonlinear dynamics of solid-degenerate shells made of hyperelastic multilayer composite materials; *iii*) the unifying description of rigid bodies, geometrically exact beams and solid-degenerate shells and their combination with kinematic pairs; *iv*) the development of a robust integration scheme based on the *average vector field*; *v*) the particularization of the *principal geodesic analysis* to identify motion patterns exhibited by beam structures in a purely nonlinear setting; *vi*) the derivation of a new conservative/dissipative integration method that relies on high order correction terms that modify, in the minimal possible way, the well-know midpoint rule, and, *vii*) the implementation of all the methods and algorithms into a new object-oriented framework.

6.2. Future work

Even provided that the current work is rather comprehensive, the proposed unifying approach can be further enhanced and improved by addressing the following suggestions:

- Enrichment of the beam formulation with torsion- and shear-warping modes to improve the estimation of strain and stress states.
- Enrichment of the shell formulation with high-order-shear and zig-zag functions to improve the estimation of strain and stress states across the thickness.
- Derivation and implementation of variational links among beams and shells to allow the energetically optimal deformation of the coupling interfaces.
- Inclusion of contact models among point, line and surface representations to enable the intermittent interaction of each *canonical models* with itself and with the remaining ones.
- Implementation of optimal reduction techniques (hyper reduction) to reduce the number of unknowns and thus, to accelerate the computation time.
- Derivation and implementation of fractional-order dissipation functions to render complex damping mechanisms.
- Combination with fluids to investigate fluid-structure interactions.
- Embedding of optimal control techniques for studying intelligent structures.
- And, many others.

A. Articles between July 2015 and June 2019

This appendix lists, in reverse chronological order, the journal articles written between July 2015 and June 2019 and published in regular issues, in which I participated either as main author or as coauthor. These fall directly or indirectly within the field of structural analysis (*Statik und Dynamik*).

21. HENKEL, M., HÄFELE, J., WEIJTJIENS, W., DEVRIENDT, C., GEBHARDT, C. G., AND ROLFES, R. Strain estimation for offshore wind turbines with jacket substructures using dual-band modal expansion. *Marine Structures* 71 (2020), 102731.
20. ROMERO, I., AND GEBHARDT, C. G. Variational principles for nonlinear Kirchhoff rods. *Acta Mechanica* 231 (2020), 625–647.
19. GEBHARDT, C. G., ROMERO, I., AND ROLFES, R. A new conservative/dissipative time integration scheme for nonlinear mechanical systems. *Computational Mechanics* 65 (2020), 405–427.
18. HÜBLER, C., PIEL, J.-H., STETTER, C., GEBHARDT, C. G., BREITNER, M., AND ROLFES, R. Influence of structural design variations on economic viability of offshore wind turbines: An interdisciplinary analysis. *Renewable Energy* 145 (2020), 1348–1360.
17. HENTE, C., GEBHARDT, C. G., PACHE, D., AND ROLFES, R. On the modal analysis of nonlinear beam and shell structures with singular mass and stiffness matrices. *Thin-Walled Structures* 144 (2019), 106310.
16. GEBHARDT, C. G., STEINBACH, M. C., AND ROLFES, R. Understanding the nonlinear dynamics of beam structures: a principal geometric analysis approach. *Thin-Walled Structures* 140 (2019), 357–372.
15. HÜBLER, C., WEIJTJIENS, W., GEBHARDT, C. G., ROLFES, R., AND DEVRIENDT, C. Validation of improved sampling concepts for offshore wind turbine fatigue design. *Energies* 12 (2019), 603.
14. HÄFELE, C., GEBHARDT, C. G., AND ROLFES, R.: A comparison study on jacket substructures for offshore wind turbines based on optimization. *Wind Energy Science* 4 (2019), 23–40.
13. GEBHARDT, C. G., HOFMEISTER, B., HENTE, C., AND ROLFES, R. Nonlinear dynamics of slender structures: a new object-oriented framework. *Computational Mechanics* 63 (2019), 219–252.
12. HÜBLER, C., GEBHARDT, C. G., AND ROLFES, R. Methodologies for fatigue assessment of offshore wind turbines considering scattering environmental conditions and the uncertainty due to finite sampling. *Wind Energy* 21 (2018), 1092–1105.

-
11. HÄFELE, J., DAMIANI, R. R., KING, R. N., GEBHARDT, C. G., AND ROLFES, R. A systematic approach to offshore wind turbine jacket predesign and optimization: geometry, cost, and surrogate structural code check models. *Wind Energy Science* 3 (2018), 553–572.
 10. GEBHARDT, C. G., MATUSEVICH, A. E., AND INAUDI, J. A. Coupled transverse and axial vibrations including warping effect in asymmetric short beams. *Journal of Engineering Mechanics* 144 (2018), 04018043.
 9. SCHRÖDER, K., GEBHARDT, C. G., AND ROLFES, R. A two-step approach to damage localization at supporting structures of offshore wind turbines. *Structural Health Monitoring* 17 (2018), 1313–1330.
 8. HÄFELE, J., HÜBLER, C., GEBHARDT, C. G., AND ROLFES, R. A comprehensive fatigue load set reduction study for offshore wind turbines with jacket substructures. *Renewable Energy* 118 (2018), 99–112.
 7. ALBANESI, A., BRE, F., FACHINOTTI, V., AND GEBHARDT, C.. Simultaneous ply-order, ply-number and ply-drop optimization of laminate wind turbine blades using the inverse finite element method. *Composite Structures* 184 (2018), 894–903.
 6. HÜBLER, C., HÄFELE, J., GEBHARDT, C. G., AND ROLFES, R. Experimentally supported consideration of operating point dependent soil properties in coupled dynamics of offshore wind turbines. *Marine Structures* 57 (2018), 18–37.
 5. HÜBLER, C., GEBHARDT, C. G., AND ROLFES, R. Development of a comprehensive data basis of scattering environmental conditions and simulation constraints for offshore wind turbines. *Wind Energy Science* 2 (2017), 491–505.
 4. GEBHARDT, C. G., AND ROLFES, R. On the nonlinear dynamics of shell structures: combining a mixed finite element formulation and a robust integration scheme. *Thin-Walled Structure* 118 (2017), 56–72.
 3. HÜBLER, C., GEBHARDT, C. G., AND ROLFES, R. Hierarchical four-step global sensitivity analysis of offshore wind turbines based on aeroelastic time-domain simulations. *Renewable Energy* 111 (2017), 878–891.
 2. ALBANESI, A., FACHINOTTI, V., PERALTA, I., STORTI, B. AND GEBHARDT, C.. Application of the inverse finite element method to design wind turbine blades. *Composite Structures* 161 (2017), 160–172.
 1. HÄFELE, J., HÜBLER, C., GEBHARDT, C. G., AND ROLFES, R. An improved two-step soil-structure interaction modeling method for dynamical analyses of offshore wind turbines. *Applied Ocean Research* 55 (2016), 141–150.

Bibliography

- [1] ANTMAN, S. S. *Nonlinear problems of elasticity*. Springer, 1995.
- [2] ARMERO, F., AND PETŐCZ, E. Formulation and analysis of conserving algorithms for frictionless dynamic contact/impact problems. *Computer Methods in Applied Mechanics and Engineering* 158 (1998), 269–300.
- [3] ARMERO, F., AND ROMERO, I. On the formulation of high-frequency dissipative time-stepping algorithms for nonlinear dynamics. Part I: Low-order methods for two model problems and nonlinear elastodynamics. *Computer Methods in Applied Mechanics and Engineering* 190 (2001), 2603–2649.
- [4] ARMERO, F., AND ROMERO, I. On the formulation of high-frequency dissipative time-stepping algorithms for nonlinear dynamics. Part II: Second-order methods. *Computer Methods in Applied Mechanics and Engineering* 190 (2001), 6783–6824.
- [5] ARMERO, F., AND ROMERO, I. Energy-dissipative momentum-conserving time-stepping algorithms for the dynamics of nonlinear Cosserat rods. *Computational Mechanics* 31 (2003), 3–26.
- [6] ARNOLD, V. I. *Mathematical methods of classical mechanics*. Springer, 1989.
- [7] ARNOLD, V. I., KOZOLOV, V. V., AND NEISHTADT, A. I. *Mathematical Aspects of Classical and Celestial Mechanics*. Springer, 2006.
- [8] AURICCHIO, F., CAROTENUTO, P., AND REALI, A. On the geometrically exact beam model: A consistent, effective and simple derivation from three-dimensional finite-elasticity. *International Journal of Solids and Structures* 45 (2008), 4766–4781.
- [9] BATHE, K.-J., AND BOLOURCHI, S. Large displacement analysis of three-dimensional beam structures. *International Journal for Numerical Methods in Engineering* 14 (1979), 961–986.
- [10] BATHE, K.-J., AND DVORKIN, E. N. A formulation of general shell elements – The use of mixed interpolation of tensorial components. *International Journal for Numerical Methods in Engineering* 22 (1986), 697–722.
- [11] BETSCH, P., GRUTTMANN, F., AND STEIN, E. A 4-node finite shell element for the implementation of general hyperelastic 3d-elasticity at finite strains. *Computer Methods in Applied Mechanics and Engineering* 130 (1996), 57–79.
- [12] BETSCH, P., HESCH, C., SÄNGER, N., AND UHLAR, S. Variational integrators and energy-momentum schemes for flexible multibody dynamics. *Journal of Computational and Nonlinear Dynamics* 5 (2010), 031001.
- [13] BETSCH, P., AND STEIN, E. An assumed strain approach avoiding artificial thickness straining for a non-linear 4-node shell element. *Communications in Numerical Methods in Engineering* 11 (1995), 899–909.
- [14] BETSCH, P., AND STEIN, E. A nonlinear extensible 4-node shell element based on continuum

- theory and assumed strain interpolations. *Journal of Nonlinear Sciences* 6 (1996), 169–199.
- [15] BETSCH, P., AND STEINMANN, P. Constrained dynamics of geometrically exact beams. *Computational Mechanics* 31 (2003), 49–59.
- [16] BISCHOFF, M., AND RAMM, E. Shear deformable shell elements for large strains and rotations. *International Journal for Numerical Methods in Engineering* 40 (1997), 4427–4449.
- [17] BOTTASSO, C. L., AND BORRI, M. Energy preserving/decaying schemes for non-linear beam dynamics using the helicoidal approximation. *Computer Methods in Applied Mechanics and Engineering* 143 (1997), 393–415.
- [18] BOTTASSO, C. L., BORRI, M., AND TRAINELLI, L. Integration of elastic multibody systems by invariant conserving/dissipating algorithms. II. numerical schemes and applications. *Computer Methods in Applied Mechanics and Engineering* 190 (2001), 3701–3733.
- [19] BOYER, F., AND PRIMAULT, D. Finite element of slender beams in finite transformations: a geometrically exact approach. *International Journal for Numerical Methods in Engineering* 59 (2004), 669–702.
- [20] BRAUN, M., BISCHOFF, M., AND RAMM, E. Nonlinear shell formulations for complete three-dimensional constitutive laws including composites and laminates. *Computational Mechanics* 15 (1994), 1–18.
- [21] BUCALEM, M. L., AND BATHE, K.-J. Higher-order mitc general shell elements. *International Journal for Numerical Methods in Engineering* 36 (1993), 3729–3754.
- [22] BÜCHTER, N., AND RAMM, E. Shell theory versus degeneration - a comparison in large rotation finite element analysis. *International Journal for Numerical Methods in Engineering* 34 (1992), 39–59.
- [23] BÜCHTER, N., RAMM, E., AND ROEHL, D. Three-dimensional extension of non-linear shell formulation based on the enhanced assumed strain concept. *International Journal for Numerical Methods in Engineering* 37 (1994), 2551–2568.
- [24] CALIRI JR., M. F., FERREIRA, A. J. M., AND TITA, V. A review on plate and shell theories for laminated and sandwich structures highlighting the finite element method. *Composite Structures* 156 (2016), 63–77.
- [25] CARDONA, A., AND GÉRADIN, M. A beam finite element non-linear theory with finite rotations. *International Journal for Numerical Methods in Engineering* 26 (1988), 2403–2438.
- [26] CARRERA, E., CINEFRA, M., AND NALI, P. MITC technique extended to variable kinematic multilayered plate elements. *Composite Structures* 92 (2010), 1888–1895.
- [27] CHOI, C. K., AND PAIK, J. G. An effective four node degenerated shell element for geometrically nonlinear analysis. *Thin-Walled Structures* 24 (1996), 261–283.
- [28] CIARLET, P. *Mathematical elasticity - Volume 1: three dimensional elasticity*. North-Holland, 1993.
- [29] CONDE MARTÍN, S., AND GARCÍA ORDEN, J. C. An energy-consistent integration scheme for flexible multibody systems with dissipation. *Proceedings of the Institution of Mechanical Engineers, Part K: Journal of Multi-body Dynamics* 230 (2016), 268–280.
- [30] DE MIRANDA, S., GUTIÉRREZ, A., MELCHIONDA, D., AND PATRUNO, L. Linearly elastic constitutive relations and consistency for GBT-based thin-walled beams. *Thin-Walled Structures* 92 (2015), 55–64.

- [31] DVORKIN, E. N., AND BATHE, K.-J. A continuum mechanics based four-node shell element for general non-linear analysis. *Engineering Computations* 1 (1984), 77–88.
- [32] EISENBERG, M., AND GUY, R. A proof of the hairy ball theorem. *The American Mathematical Monthly* 86 (1979), 571–574.
- [33] EPSTEIN, M. *The Geometrical Language of Continuum Mechanics*. Cambridge University Press, 2010.
- [34] EUGSTER, S., HESCH, C., BETSCH, P., AND GLOCKER, C. Director-based beam finite elements relying on the geometrically exact beam theory formulated in skew coordinates. *International Journal for Numerical Methods in Engineering* 97 (2014), 111–129.
- [35] GARCÍA ORDEN, J. C. Energy and symmetry-preserving formulation of nonlinear constraints and potential forces in multibody dynamics. *Nonlinear Dynamics* 95 (2019), 823–837.
- [36] GAY NETO, A. Simulation of mechanisms modeled by geometrically-exact beams using Rodrigues rotation parameters. *Computational Mechanics* 59 (2017), 459–481.
- [37] GEBHARDT, C. G., MATUSEVICH, A. E., AND INAUDI, J. A. Coupled transverse and axial vibrations including warping effect in asymmetric short beams. *Journal of Engineering Mechanics* 144 (2018), 04018043.
- [38] GENOVESE, D. A two-director Cosserat rod model using unconstrained quaternions. *European Journal of Mechanics - A/Solids* 43 (2014), 44–57.
- [39] GHOSH, S., AND ROY, D. A frame-invariant scheme for the geometrically exact beam using rotation vector parametrization. *Computational Mechanics* 44 (2009), 103–118.
- [40] GOICOLEA, J. M., AND GARCÍA ORDEN, J. C. Dynamic analysis of rigid and deformable multibody systems with penalty methods and energy-momentum schemes. *Computer Methods in Applied Mechanics and Engineering* 188 (2000), 789–804.
- [41] GONZÁLEZ, O. Time integration and discrete Hamiltonian systems. *Journal of Nonlinear Sciences* 6 (1996), 449–467.
- [42] GONZÁLEZ, O. Exact energy-momentum conserving algorithms for general models in nonlinear elasticity. *Computer Methods in Applied Mechanics and Engineering* 190 (2000), 1763–1783.
- [43] GOTUSSO, L. On the energy theorem for the Lagrange equations in the discrete case. *Applied Mathematics and Computation* 17 (1985), 129–136.
- [44] GRUTTMANN, F., SAUER, R., AND WAGNER, W. A geometrical nonlinear eccentric 3d-beam element with arbitrary cross-sections. *Computer Methods in Applied Mechanics and Engineering* 60 (1998), 383–400.
- [45] HARTEN, A., AND LAX, P. LEER, B. On upstream differencing and Godunov-type schemes for hyperbolic conservation laws. *SIAM Review* 25 (1983), 35–61.
- [46] HAUPTMANN, R., AND SCHWEIZERHOF, K. A systematic development of 'solid-shell' element formulations for linear and non-linear analyses employing only displacement degrees of freedom. *International Journal for Numerical Methods in Engineering* 42 (1998), 49–69.
- [47] HEARD, W. B. *Rigid Body Mechanics: Mathematics, Physics and Applications*. Wiley, 2006.
- [48] HODGES, D. H. A mixed variational formulation based on exact intrinsic equations for dynamics of moving beams. *International Journal of Solids and Structures* 26 (1990),

- 1253–1273.
- [49] IBRAHIMBEGOVIC, A., AND MAMOURI, S. Energy conserving / decaying implicit time-stepping scheme for nonlinear dynamics of three-dimensional beams undergoing finite rotations. *Computer Methods in Applied Mechanics and Engineering* 191 (2002), 4241–4258.
- [50] ITOH, T., AND ABE, K. Hamiltonian-conserving discrete canonical equations based on variational difference quotients. *Journal of Computational Physics* 76 (1988), 85–102.
- [51] KLINKEL, S., GRUTTMANN, F., AND WAGNER, W. A continuum based three-dimensional shell element for laminated structures. *Computers & Structures* 71 (1999), 43–62.
- [52] KLINKEL, S., GRUTTMANN, F., AND WAGNER, W. A robust non-linear solid shell element based on a mixed variational formulation. *Computer Methods in Applied Mechanics and Engineering* 195 (2006), 179–201.
- [53] KO, Y., LEE, P.-S., AND BATHE, K.-J. The mitc4+ shell element and its performance. *Computers & Structures* 169 (2016), 57–68.
- [54] KO, Y., LEE, P.-S., AND BATHE, K.-J. A new mitc4+ shell element. *Computers & Structures* 182 (2017), 404–418.
- [55] KUHL, D., AND CRISFIELD, M. A. Energy-conserving and decaying algorithms in non-linear structural dynamics. *International Journal for Numerical Methods in Engineering* 45 (1999), 569–599.
- [56] KUHL, D., AND RAMM, E. Constraint energy momentum algorithm and its application to nonlinear dynamics of shells. *Computer Methods in Applied Mechanics and Engineering* 136 (1996), 293–315.
- [57] LANDAU, L. D., AND LIFSHITZ, E. M. *Mecánica - Volúmen I*. Reverté, 1993.
- [58] LAURSEN, T. A., AND MENG, X. N. A new solution procedure for application of energy-conserving algorithms to general constitutive models in nonlinear elastodynamics. *Computer Methods in Applied Mechanics and Engineering* 190 (2001), 6300–6309.
- [59] LAVRENČIČ, M., AND BRANK, B. Simulation of shell buckling by implicit dynamics and numerically dissipative schemes. *Thin-Walled Structures* 132 (2018), 682–699.
- [60] LURIE, A. I. *Analytical Mechanics*. Springer, 2002.
- [61] MÄKINEN, J. Total lagrangian Reissner’s geometrically exact beam element without singularities. *International Journal for Numerical Methods in Engineering* 70 (2007), 1009–1048.
- [62] MARSDEN, J. E., AND HUGES, T. J. R. *Mathematical foundation of elasticity*. Dover Publication, 1994.
- [63] MATA, P., OLLER, S., AND BARBAT, A. H. Dynamic analysis of beam structures considering geometric and constitutive nonlinearity. *Computer Methods in Applied Mechanics and Engineering* 197 (2008), 857–878.
- [64] MCLACHLAN, R. I., QUISPÉL, G. R. W., AND ROBIDEUX, N. Geometric integration using discrete gradients. *Philosophical Transactions: Mathematical, Physical and Engineering Sciences* 357 (1999), 1021–1045.
- [65] MOREIRA, R. A. S., ALVES DE SOUSA, R. J., AND VALENTE, R. A. F. A solid-shell layerwise finite element for non-linear geometric and material analysis. *Composite Structures* 92 (2010), 1517–1523.

- [66] NGUYEN, T. L., SANSOUR, C., AND HJIAJ, M. Long-term stable time integration scheme for dynamic analysis of planar geometrically exact timoshenko beams. *Journal of Sound and Vibration* 393 (2017), 144–171.
- [67] NOELS, L., STAINIER, L., AND PONTHOT, J.-P. On the use of large time steps with an energy momentum conserving algorithm for non-linear hypoelastic constitutive models. *International Journal of Solids and Structures* 41 (2004), 663–693.
- [68] ORTIGOSA, R., GIL, A. J., BONET, J., AND HESCH, C. A computational framework for polyconvex large strain elasticity for geometrically exact beam theory. *Computational Mechanics* 57 (2016), 277–303.
- [69] PAI, P. F. Energy-consistent formulation and order deficiency of linear and nonlinear shear-deformable beam theories. *Thin-Walled Structures* 65 (2013), 7–13.
- [70] PAI, P. F. Problems in geometrically exact modeling of highly flexible beams. *Thin-Walled Structures* 76 (2014), 65–76.
- [71] PIMENTA, P. M., CAMPELLO, E. M., AND WRIGGERS, P. An exact conserving algorithm for nonlinear dynamics with rotational dofs and general hyperelasticity. part 1: Rods. *Computational Mechanics* 42 (2008), 715–732.
- [72] RAH, K., VAN PAEPEGEM, W., AND DEGRIECK, J. A novel versatile multilayer hybrid stress solid-shell element. *Computational Mechanics* 51 (2017), 825–841.
- [73] REINOSO, J., AND BLÁZQUEZ, A. Application and finite element implementation of 7-parameter shell element for geometrically nonlinear analysis of layered CFRP composites. *Composite Structures* 139 (2016), 263–276.
- [74] REISSNER, E. On one-dimensional finite-strain beam theory: The plane problem. *Journal of Applied Mathematics and Physics* 23 (1972), 795–804.
- [75] ROJAS, J., LIU, T., AND KAVAN, L. Average vector field integration for st. venant-kirchhoff deformable models. *IEEE Transactions on Visualization and Computer Graphics* (2018), 1–10.
- [76] ROMERO, I. The interpolation of rotations and its application to finite element models of geometrically exact rods. *Computational Mechanics* 34 (2004), 121–133.
- [77] ROMERO, I. A comparison of finite elements for nonlinear beams: the absolute nodal coordinate and geometrically exact formulations. *Multibody System Dynamics* 20 (2008), 51–68.
- [78] ROMERO, I. An analysis of the stress formula for energy-momentum methods in nonlinear elastodynamics. *Computational Mechanics* 50 (2012), 603–610.
- [79] ROMERO, I. High frequency dissipative integration schemes for linear and nonlinear elastodynamics. In *Structure-preserving integrators in nonlinear structural dynamics and flexible multibody dynamics*, P. Betsch, Ed. Springer, 2016, pp. 1–30.
- [80] ROMERO, I., AND ARMERO, F. Numerical integration of the stiff dynamics of geometrically exact shells: An energy-dissipative momentum-conserving scheme. *International Journal for Numerical Methods in Engineering* 54 (2002), 1043–1086.
- [81] ROMERO, I., AND ARMERO, F. An objective finite element approximation of the kinematics of geometrically exact rods and its use in the formulation of an energy-momentum conserving scheme in dynamics. *International Journal for Numerical Methods in Engineering* 54 (2002),

- 1683–1716.
- [82] RUBIN, M. B. *Cosserat Theories: Shells, Rods and Points*. Springer, 2000.
- [83] SANSOUR, C., FEIH, S., AND WAGNER, W. On the performance of enhanced strain finite elements in large strain deformations of elastic shells: Comparison of two classes of constitutive models for rubber materials. *Engineering Computations* 20 (2003), 875–895.
- [84] SANSOUR, C., WAGNER, W., WRIGGERS, P., AND SANSOUR, J. An energy-momentum integration scheme and enhanced strain finite elements for the non-linear dynamics of shells. *International Journal of Non-Linear Mechanics* 37 (2002), 951–966.
- [85] SANSOUR, C., WRIGGERS, P., AND SANSOUR, J. Nonlinear dynamics of shells: Theory, finite element formulation, and integration schemes. *Nonlinear Dynamics* 13 (1997), 279–305.
- [86] SCHWARZE, M., AND REESE, S. A reduced integration solid-shell finite element based on the eas and the ans concept - geometrically linear problems. *International Journal for Numerical Methods in Engineering* 80 (2009), 1322–1355.
- [87] SCHWARZE, M., AND REESE, S. A reduced integration solid-shell finite element based on the eas and the ans concept - large deformation problems. *International Journal for Numerical Methods in Engineering* 85 (2011), 289–329.
- [88] SIMMONDS, J. G. *A Brief on Tensor Analysis*. Springer, 1994.
- [89] SIMÓ, J. C. A finite strain beam formulation. The three-dimensional dynamic problem. Part I. *Computer Methods in Applied Mechanics and Engineering* 49 (1985), 55–70.
- [90] SIMÓ, J. C., AND RIFAI, M. S. A class of mixed assumed strain methods and the method of incompatible modes. *International Journal for Numerical Methods in Engineering* 29 (1990), 1595–1638.
- [91] SIMÓ, J. C., AND TARNOW, N. The discrete energy-momentum method. conserving algorithms for nonlinear elastodynamics. *Zeitschrift für Angewandte Mathematik und Physik* 43 (1992), 757–792.
- [92] SIMÓ, J. C., AND TARNOW, N. The discrete energy-momentum method. conserving algorithms for nonlinear elastodynamics. *Zeitschrift für Angewandte Mathematik und Physik* 43 (1992), 757–792.
- [93] SIMÓ, J. C., AND TARNOW, N. A new energy and momentum conserving algorithm for the non-linear dynamics of shells. *International Journal for Numerical Methods in Engineering* 37 (1994), 2527–2549.
- [94] SIMÓ, J. C., TARNOW, N., AND DOBLARÉ, M. Non-linear dynamics of three-dimensional rods: exact energy and momentum conserving algorithms. *International Journal for Numerical Methods in Engineering* 38 (1995), 1431–1473.
- [95] SONNEVILLE, V., BRÜLS, O., AND BAUCHAU, O. Interpolation schemes for geometrically exact beams: A motion approach. *International Journal for Numerical Methods in Engineering* 112 (2017), 1129–1153.
- [96] SONNEVILLE, V., CARDONA, A., AND BRÜLS, O. Geometric interpretation of a non-linear beam finite element on the lie group SE(3). *Archive of Mechanical Engineering* 61 (2014), 305–329.
- [97] SUSSMAN, T., AND BATHE, K.-J. 3d-shell elements for structures in large strains. *Computers & Structures* 122 (2013), 2–12.

- [98] SZE, K. Y., CHAN, W. K., AND PIAN, T. H. H. An eight-node hybrid-stress solid-shell element for geometric non-linear analysis of elastic shells. *International Journal for Numerical Methods in Engineering* 55 (2002), 853–878.
- [99] TAN, X. G., AND VU-QUOC, L. Efficient and accurate multilayer solid-shell element: non-linear materials at finite strain. *International Journal for Numerical Methods in Engineering* 63 (2005), 2124–2170.
- [100] TONTI, E. The reason for analogies between physical theories. *Applied Mathematical Modelling* 1 (1976), 37–50.
- [101] TRUESDELL, C., AND NOLL, W. *The Non-Linear Field Theories of Mechanics*. Springer, 2004.
- [102] VU-QUOC, L., AND TAN, X. G. Optimal solid shells for non-linear analyses of multilayer composites. II. Dynamics. *Computer Methods in Applied Mechanics and Engineering* 192 (2003), 1017–1059.
- [103] VU-QUOC, L., AND TAN, X. G. Efficient hybrid-eas solid element for accurate stress prediction in thick laminated beams, plates, and shells. *Computer Methods in Applied Mechanics and Engineering* 253 (2013), 337–355.
- [104] YOON, K., AND LEE, P.-S. Nonlinear performance of continuum mechanics based beam elements focusing on large twisting behaviors. *Computer Methods in Applied Mechanics and Engineering* 281 (2014), 106–130.
- [105] YU, W., LIAO, L., HODGES, D. H., AND VOLOVOI, V. V. Theory of initially twisted, composite, thin-walled beams. *Thin-Walled Structures* 43 (2005), 1296–1311.
- [106] ZUPAN, D., AND SAJE, M. Finite-element formulation of geometrically exact three-dimensional beam theories based on interpolation of strain measures. *Computer Methods in Applied Mechanics and Engineering* 192 (2003), 5209–5248.

Curriculum vitae

Personal details

Name: Cristian Guillermo Gebhardt
Date of birth: 24.01.1983
Place of birth: Córdoba, Argentina
Nationality: Argentine (*ius soli*) and German (*ius sanguinis*)
Family status: Married, two kids

Education

2007-2012: Doctor in Engineering Sciences, *Universidad Nacional de Córdoba*, Córdoba, Argentina
2001-2005: Diploma in “Mechanical and Aeronautical Engineering”, *Instituto Universitario Aeronáutico*, Córdoba, Argentina
1989-2000: Primary and secondary school education, Córdoba, Argentina

Scientific career

2018: Visiting Professor at IMDEA Materials Institute, Madrid, Spain
Since 2015: Head of the Group “Coupled Dynamical Systems” at Institute of Structural Analysis, *Leibniz Universität Hannover*, Hannover, Germany
2012–2015: Research Associate at Fraunhofer Institute for Wind Energy and Energy System Technology, Bremerhaven, Germany
2007–2012: Several teaching and research positions at *Universidad Nacional de Córdoba*, Córdoba, Argentina

Awards

2019: Elected member of the Young BWG (*Braunschweigische Wissenschaftliche Gesellschaft*), Germany
2011: Green Talent Award, Federal Ministry of Education and Research, Germany
2006: Several best graduate awards, Argentina
2000: Several awards to the excellence at high school, Argentina

